Mandrel-based Polishing of Single-Crystal Diamond and Ceramics for Fabrication of Micro-endmills: Analysis of the Polishing Characteristics and the Error Motions of Ultra-High-Speed Micromachining Spindles

Submitted in partial fulfillment of the requirements for

the degree of

Doctor of Philosophy

in

Mechanical Engineering

Krishna Prashanth Anandan

B.Tech, Mechanical Engineering, Indian Institute of Technology Madras

M.S., Mechanical Engineering, University of Minnesota, Twin Cities

Carnegie Mellon University

CARNEGIE INSTITUTE OF TECHNOLOGY

Pittsburgh, PA

May 2012

To my parents,

Girija and Anandan,

and

my wife,

Shruthi.

Acknowledgements

During the course of my Ph.D., there have been a number of people who have supported me in various ways. It is a pleasure to express my heartfelt gratitude and sincere appreciation to all of them.

First and foremost, I would like to thank my advisor Prof. Burak Ozdoganlar for his support, guidance, and mentoring during the past six years. His work ethic, limitless-energy and expectations for a high standard of excellence have helped me to constantly push myself to deliver my best effort. His constructive criticisms and feedback while conducting research, writing papers and preparing presentations, have really guided me to develop as an independent researcher. I am also very thankful for his patience in letting me explore deeper into research problems, not necessarily of immediate interest, and his supportive attitude during hard times.

I wish to thank my committee members, Dr. M. Alkan Donmez, Prof. C. Fred Higgs, III, Prof. William C. Messner for serving on my committee and providing helpful suggestions regarding my research and its presentation. I also want to thank them for helping me obtain an important perspective on the applicability of my research.

I would like to thank Mr. Michael Hunter and Mr. Pete Kawalec of Chardon Tools for their valuable time in educating me about polishing and fabrication of single-crystal diamond micro-tools.

I wish to acknowledge the financial support from the National Science Foundation. I also would like to thank Chardon Tools for providing us some equipment and material during the initial phase of the research and Fischer Precise USA, Inc. for providing a UHS spindle that was actively used during this research.

I want to thank Jim Dillinger, John Fulmer and Ed Wojciechowski of the Mechanical Engineering machine shop and Larry Hayhurst of the Chemical Engineering machine shop for their practical guidance and help in fabrication of various components and fixtures. I want to thank Joseph Suhan and Tom Nuhfer for their assistance with scanning electron microscopy. I also want to thank Dolores Smiller, Bobbi Kostyak, Chris Zeise, Chris Hertz and OIE Staff (specifically Neslihan Ozdoganlar and Carly Shane) for their assistance in various administrative aspects. I want to thank Jon Ledonne and Andy Schultz for their assistance in various materials science related experimental procedures.

The Ph.D. experience would not have been memorable without the company of my labmates and friends. Thanks to Nithya and Arda for their great company and support they provided during the past six years. I will always cherish the great discussions, both technical and otherwise, that were quite refreshing and fruitful. Thanks to Sid, Shin Hyung, Sinan, Alex, Abhinandan, Juen, Bekir, Emrullah and Rakesh for their company during the course of my Ph.D. Special thanks to Gerardo for adding a social flavor by creating opportunities for socializing. Also, I would like to specially thank Recep and Sudhanshu for being patient with me and helping me with my experiments and various aspects related to research. I want to thank my friends Mukund, Balakumar, Allumallu, Kamal, Bhanu, Balaji, Nisha, Hari and Santosh for offering a listening ear and keeping me motivated during my PhD. I want to also thank all the other friends, members of the CMU ultimate frisbee group, and members of the PittPunters Cricket Club who gave me good company and added an extra-curricular flavor during my graduate student life.

I want to greatly thank my uncle, Dr. Narasinga Rao, aunt Shobha Rao, and aunt Indira for their encouragement and support throughout my academic life. I would like to thank special family friends, Dr. K. Chandrasekaran and Dr. R. Balakrishnan, and all other relatives (especially Rajan Sethurao and Seshadri Rao Sahib) who have morally supported and motivated me during the course of my graduate study.

I want to thank my in-laws, late Shrish Mohan and Suman Shrish, who have been very supportive during the past three years of my Ph.D. Lastly, and most importantly, I want to thank my parents, Girija and Dr. S. Anandan, and my wife, Shruthi for everything that they have done. Without my parents' sacrifices, their prayers, and their unconditional love, support and encouragement throughout my life, it would not have been possible to have come all this way. Without my wife's diligent support, sacrifices, love, encouragement and understanding during the past three years, it would have been much more difficult to complete my Ph.D. I would like to especially thank her for tolerating me during these years. I gratefully dedicate this thesis to my parents and my wife.

Abstract

The demand for miniature devices and parts has increased significantly over the past decade. During this period, research and development of mechanical micromachining processes, including micromilling and microdrilling, have enabled fabrication of intricate three-dimensional micro- and meso-scale components and features on a broad range of materials. One of the key concerns in micromilling is related to the cutting tool. The currently available carbide micro-endmills have the following issues: (a) relatively large cutting edge radius (typically 2 μm - 5 μm) compared to commonly used uncut chip thickness levels, (b) poor tolerance in diameter (typically +/- 10%), and (c) rapid wear when used for machining of hard materials or at high-temperatures. Such non-ideal tools affect the machining process significantly and lead to both poor dimensional accuracy and rough machined surfaces, thus limiting the wide-spread application of micromachining.

This Ph.D. research addresses aforementioned issues by developing a mandrel-based precision polishing process using ultra-high-speed (UHS) miniature spindles, to fabricate single-crystal diamond and tool-grade ceramic micro-endmills which will be superior to the existing carbide micro-endmills in terms of accuracy and sharpness. The presented work has two specific aspects: The first involves the development of the mandrel-based polishing process and experimental analysis of the polishing characteristics of single-crystal diamond and tool-grade ceramics. And the second involves the design and analysis of precision polishing equipment for the mandrel-based polishing process. Together, these two aspects are aimed to provide experimental understanding of the mandrel-based polishing process and to enable identification of favorable polishing conditions that will allow accurate fabrication of micro-tools from single-crystal diamond and ceramics. A majority of the work is devoted to analyzing the (unwanted) motions of UHS spindles used for the mandrel-based polishing process, with the aim of identifying a favorable set of spindle parameters that would allow for accurate and repeatable fabrication of the micro-tools. This included developing spindle-metrology and analysis techniques applicable to measurement of axial and radial error motions of UHS spindles that currently do not exist in literature.

Initially, the effectiveness of the mandrel-based polishing process in removing single-crystal diamond is demonstrated by polishing and shaping diamond to create smooth surfaces and sharp edges (≤ 1 μm edge radius). Among others, an important issue that was identified in the mandrel-based polishing process was the poor dimensional and form accuracy during material removal. To address this issue, a dual-stage polishing test-bed was designed and constructed to include 1) a large-wheel-based traditional diamond polishing system with high material removal rates for "rough" polishing, and 2) a rigid, mandrel-based polishing configuration with capability to create intricate micro-scale

features and high-aspect-ratio structures on single-crystal diamond and ceramics.

Next, polishing characteristics of various tool-grade ceramics were experimentally analyzed to evaluate their applicability for micro-scale cutting. Almost all the ceramic materials tested yielded a better surface roughness than sub-micron grade carbide that is commonly used for micro-tools. All ceramic materials were capable of being sharpened to edge radii less than 2 μm, which is less than the edge radii of sub-micron grade carbide.

One of the most important factors governing the effectiveness of the mandrel-based polishing process in creating accurate features is the speed-dependent axial and radial error motions of the UHS spindle. Undesired motions of the UHS spindles have a direct influence on the dimensional and form accuracy, as well as the surface finish, of the polished surfaces. A thorough quantitative analysis of these motions for the specific UHS spindle used on the dual-stage polishing test-bed is essential to understand their influence on the polishing characteristics. However, there is no existing metrology technique to quantify the error motions of UHS spindles.

To address this need, a laser Doppler vibrometry (LDV)-based methodology was developed to measure the axial and radial error motions of UHS spindles from the surface of a custom-fabricated sphere-on-stem precision artifact. The measured axial and radial motions were post-processed to obtain different components of the error motions, including synchronous and asynchronous components of the axial and radial error motions in both fixed-sensitive and rotating-sensitive directions. The sources and amounts of uncertainties in measuring the motions and in calculating the error motions were then analyzed. The developed methodology is then applied to analyze the radial and axial motions of the electrically-driven hybrid-ceramic-bearing UHS spindle used on the dual-stage polishing test-bed. The measured axial and radial motions were seen to be strongly dependent upon the spindle speed, thermal-state of the spindle, and the over-hang length of the artifact (tool). Certain speed/over-hang length combinations were identified that could potentially induce significant dimensional errors, shape distortions, and surface roughness to the polished surfaces.

The developed UHS spindle-metrology technique was advanced further by implementing error-separation methods to remove the artifact form error and quantify the true spindle error motions. Two different error separation techniques were developed - Multi-Orientation Technique and a modified Donaldson Reversal Method. Both techniques were successfully demonstrated to remove artifact form error from radial motions measured at speeds up to 150 krpm.

The thesis concludes with a discussion of future work that is needed for successful fabrication of accurate single-crystal diamond and ceramic micro-endmills in a predictable fashion. Specific tasks that should be completed to ensure that the potential high-impact nature of this work is realized have been identified and described in detail.

The specific contributions of this research include: (1) Design and development of a two-stage high-precision polishing test-bed to enable accurate fabrication of micro-scale tool geometries; (2) Development of laser Doppler vibrometry (LDV)-based methodology for measurement of axial and radial error motions when using miniature ultra-high-speed (UHS) spindles; (3) An experimental characterization of the radial and axial error motions of a typical UHS spindle with hybrid-ceramic bearings, identifying the various sources of error motions and quantifying them; (4) Implementation of two different error-separation techniques (Multi-orientation technique and Donaldson reversal method) to remove the artifact form error and obtain the true spindle error motions, and (5) An experimental understanding of the mandrel-based polishing process and the polishing behavior of single-crystal diamond and various tool-grade ceramics.

Contents

List of Figures

List of Tables

Chapter 1

Introduction

1.1 Motivation

During the last decade, mechanical micromachining has emerged as an effective technique to create complex, three-dimensional micro- and meso-scale features on metals, polymers, and composites [1–7]. Mechanical micromachining uses micro-scale milling and drilling tools (as small as 10 μm in diameter) within high precision machining environments to fabricate three-dimensional features. Although micromachining is kinematically similar to its macro-scale counterpart, scaling effects, especially those arising from the large edge radius (edge sharpness) of the existing carbide tools, bring significant changes to both practical and fundamental aspects of the process [1, 8, 9].

One of the vital issues that hinder the further progress and wide application of the micromilling process is the non-ideal characteristics of the commercially available carbide micro-endmills, specifically their blunt/chipped cutting edges. A scanning electron microscopy (SEM) image of a ϕ 250 μm micro-endmill is given in Fig. 1.1. The tool material is composed of sub-micron grade tungsten carbide (WC) within a soft cobalt binder matrix (6 - 15% by weight). These micro-endmills are created by a mechanical grinding process referred to as pinch grinding which imposes fracture on the boundaries of carbide grains, rather than intra-granular fracture of carbide grains. As a result, the edges have the carbide grains pulled out, thus leading to blunt/chipped edges with the edge radius in the range of 2 - 5 μm. This range is commensurate with the feed rates typically used in micromilling. The large edge radius (as compared to the uncut chip thickness) has significant consequences in terms of both process mechanics and process performance.

Due to the large edge radius, the effective rake angle in micromachining is highly negative. This

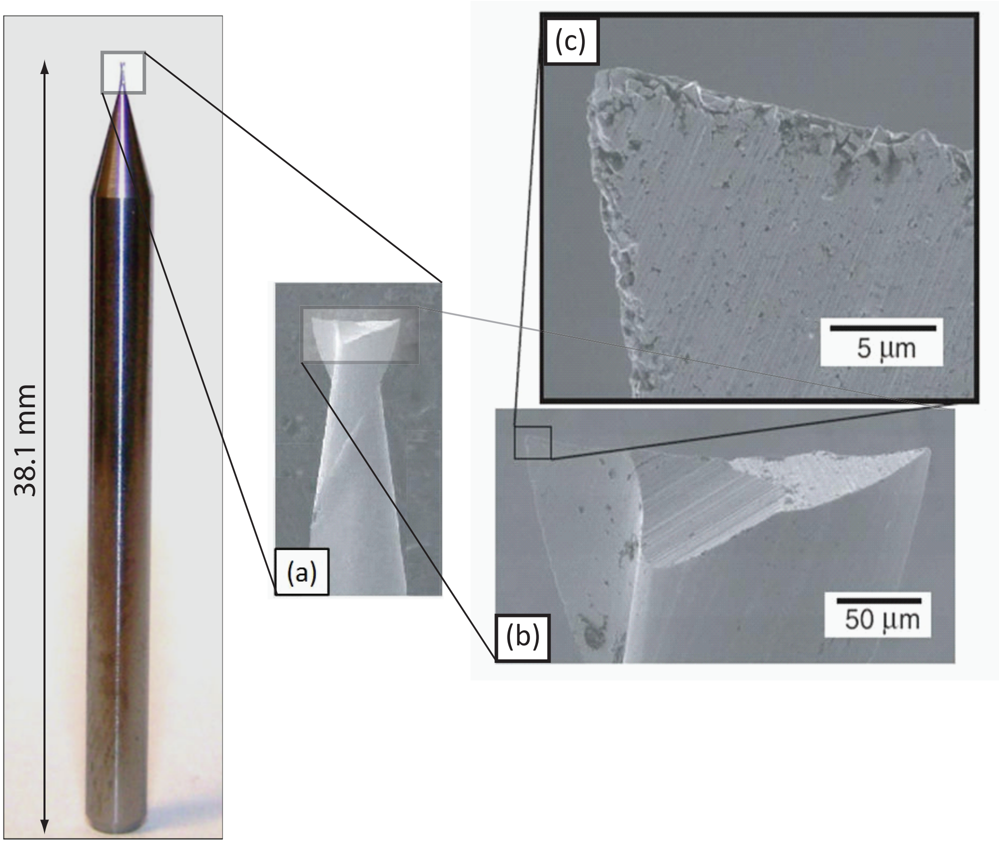

Figure 1.1: SEM images of an unused ϕ 250 μm carbide micro-endmill.

negative rake angle makes the machining process ploughing-dominated as opposed to shearing-dominated [1, 9–12]. For uncut chip thickness values below a certain ratio of the edge radius (generally 9% to 38% depending on material and tooling) no chip is generated, and the entire material is ploughed under the tool [1]. This phenomena is referred to as the *minimum chip thickness effect* and overall, it results in large and erratic forces with associated tool/workpiece deflections leading to reduced surface quality, large burr formation, rapid tool wear, and catastrophic tool failure. As a result, the micromachining process becomes unrepeatable and unpredictable.

To address the above-mentioned problems arising from the non-ideal characteristics of commercially available carbide micro-endmills, solid single-crystal diamond micro-endmills provide an excellent solution. Single-crystal diamond possesses superior mechanical and thermal characteristics that renders it as an outstanding tool material [13]. Polished diamond surfaces exhibit very low coefficients of friction. Furthermore, single-crystal diamond can be sharpened to a very high degree (with edge radii less than 10 nm) [33], and can withstand high pressures even at such levels of sharpness.

Though diamond machinable materials constitute a large and important portion of materials of interest to micromachining, diamond tools show very rapid wear with certain materials such as ferrous materials and nickel, due to thermo-chemical wear phenomenon [46] and hence cannot be used. Further, there are new applications of micromachining, such as micromachining of hardened tool steels, where diamond is not suitable. For such applications, the choice of tool-materials available for micromachining can be expanded by utilizing the large variety of tool-grade ceramic materials, currently being used for macroscale cutting [14, 15]. Due to their extreme hot-hardness and chemical inertness at high temperatures, ceramic tool materials offer unique advantages for many applications. If the tool-grade ceramics can be sharpened to edge radius values less than 2 μm without chipping and if they can retain their edge sharpness without breakage, then they could be an excellent option for micro-scale cutting. Together with single-crystal diamond, they can enable application of micromachining to a wide set of materials.

Research and development of methods to shape single-crystal diamond and ceramics precisely are critically needed to enable the fabrication of precision single-crystal diamond and ceramic micro-tools. The next section gives a brief overview of the literature on (a) fabrication of single-crystal diamond micro-tools, (b) the variety of ceramics available for use as micro-tools, as well as methods currently available to shape these ceramics precisely, and (c) new techniques and designs of micro-endmills and their evaluation.

1.2 Literature Review

1.2.1 Shaping Single-crystal Diamond

The shaping of single-crystal diamonds is accomplished through a process referred to as *diamond polishing* [16] in the diamond trade. Diamond polishing has been practiced as an art for many centuries (especially in jewelry making), and the technique of polishing diamonds has changed very little through the years.

Diamond polishing is carried out by pressing the diamond against a diamond (powder) charged rotating ferrous wheel called *scaife* with surface speeds in the range of 10 m/s to 50 m/s (see Fig. 1.2) [16]. Before the process, the cast-iron scaife is pre-machined and scored to create small grooves/pores on its surface. These grooves/pores allow embedding of the diamond grits into the scaife.

The preparation of scaife is critical to the success of the polishing process. A thin film of oil is

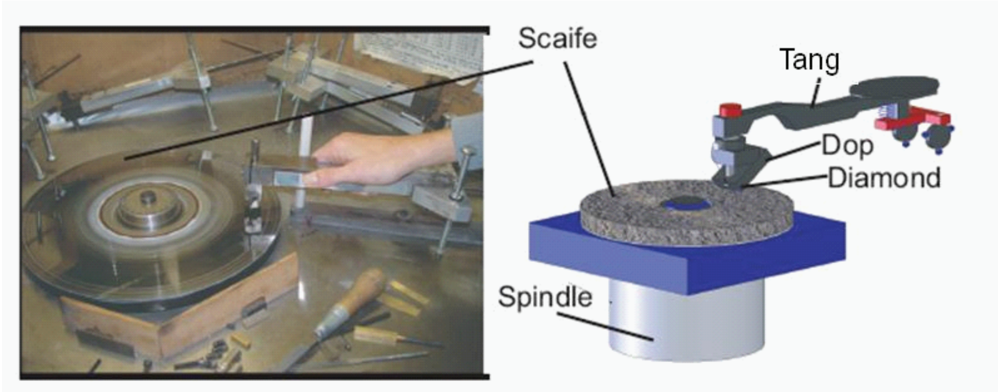

Figure 1.2: The conventional diamond-polishing process.

first rubbed onto the scaife surface. Then a small amount of diamond powder (with grit size from 0.1 μm to 20 μm) is distributed around the wheel, which turns the color of the surface to gray. The scaife is than rotated at the polishing speed (3000-6000 rpm), and a low quality diamond called *boart* (or *break-in diamond*) is used to work the powder manually into the scaife. After a period of time, the scaife surface is seen to change its color to a dark gray or black. Once this color is attained, the scaife surface is considered to be ready for polishing.

The diamond to be polished is placed on a fixture called *dop*, which is attached to a post referred to as *tang*. The tang allows obtaining the required polishing orientation. The polishing is conducted by manually pressing the diamond onto the scaife by a skilled technician. A trial-and-error process continues until the polishing is deemed complete.

One of the most important characteristics of the diamond polishing process is the anisotropy of the polishing with respect to crystallographic orientations of the diamond [13, 17–20]. On any given facet with a certain crystallographic orientation, the polishing direction was seen to make a significant difference in polishing rates. At different orientations/directions, the polishing rate under similar polishing conditions were seen to vary by as much as an order of magnitude. This was recognized centuries ago, and the easily polishable orientations/directions were referred to as "easy" (or "soft") directions. These orientations/directions are associated with high polishing rates, low vibration during polishing and result in a highly polished surface. The orientations/directions that yield very low polishing rates are referred to as "hard" (or "difficult") directions, and the polishing in these directions is associated with grating sounds, considerable vibrations and poor quality of polished surface. For instance, the cube plane {100} has four easy directions <100> and four hard directions <110>. On the other hand, the octahedral plane {111} is very resistant to wear in any direction. It was seen that the polishing rates exhibit symmetry according to the crystallographic symmetry of diamond. Furthermore, even few degrees of misorientation/tilt from the soft orientations causes the polishing rates to vary by as much as three times.

In addition to crystallographic anisotropy, a number of experimental studies in the literature have indicated that the surface speed, the powder grit size, and the applied load affect the amount of material removal and the surface roughness obtained from the process [13, 21]. Hird et al. [22] obtained the wear map of diamond polishing as a function of applied load and polishing surface speed. The wear rate of diamond is highly non-linear with respect to the polishing speed.

Although applied for centuries, there is limited fundamental understanding regarding the basic mechanisms and anisotropy of the diamond polishing process. Recently many studies have been conducted by analyzing the debris on the diamond polishing wheel (both during its preparation and during polishing) [23, 24] and studying of the morphology of the polished surfaces [25, 26] to understand the material removal mechanisms during diamond polishing and explain the anisotropy in the soft and hard directions. Several models have been proposed to explain the polishing mechanism [27–31]. The general consensus is that in the soft direction, the polished diamond undergoes a structural transformation due to the plastic deformation produced from frictional sliding. A thin layer of diamond on the surface is converted into a much softer form of sp^2 bonded carbon (as opposed to sp^3 bonded carbon in diamond). This softer layer is easily removed by the following grits of the scaife surface. This type of mechanically-induced chemical activation leads to surfaces smoother that what abrasive removal alone would achieve. In the hard directions, the polishing proceeds mainly as a result of micro- and nano-scale fracture and hence the removal rates are low and the polished diamond surfaces are rough.

The conventional diamond polishing process has been effectively used to produce single-crystal diamond cutting tools. Edge radii less than 10 nm have been demonstrated using this process [32, 33]. The basic issues and design factors involved in fabrication of diamond cutting tools for ultra-precision cutting have been studied [34, 35] and the various factors affecting the edge radius have also been analyzed [21, 36, 37]. While this conventional technique is capable of providing rapid material removal, smooth surface finish, and sharp-edge creation, its polishing configuration does not allow effective fabrication of miniature, high-aspect-ratio diamond tools. Due to its load-based nature, the feature-size control is limited. Custom-made diamond micro-endmills can be fabricated using this polishing configuration. However, due to the manual application of the process (commonly by very experienced technicians), these tools are extremely expensive (>$2000 per tool) which hinders their wider commercial applicability.

A number of alternative techniques have been attempted to fabricate miniature single-crystal diamond tools. Bonded wheels are also used as scaifes [13]. These wheels are considerably more expensive than cast-iron scaifes, and they do not show major improvement in terms of polishing rates. Non-traditional techniques, such as focused-ion beam (FIB) [38–43] and femto-second laser [44, 45] were utilized to fabricate micro-tools with sharp edges. The material removal rate and the cost of the FIB and femto-second laser processes hinder their industrial application for fabricating single-crystal diamond tools. Furthermore, these processes necessitate special configurations to make sharp, 3-D features. In another technique, thermo-chemical wear of single-crystal diamond, when rubbed against ferrous surfaces, was explored as a possible technique of diamond polishing [46]. The material removal rate, however, was significantly lower than that of the conventional polishing technique.

In conclusion, the conventional diamond polishing is the most effective and efficient process in shaping single-crystal diamond. However, this process configuration is not appropriate for fabricating micro-scale tools with more complex geometries and high-aspect-ratios.

1.2.2 Tool-grade Ceramics and Polishing

Development of tool-grade ceramic materials can be categorized under (i) monolithic forms of ceramics and ceramic composites, (ii) ceramic thin coatings and (iii) whisker-reinforced ceramic composites [14, 47]. For the purpose and scope of this thesis, we will limit the discussion to monolithic forms and whisker-reinforced composites. Within both categories, the materials can be broadly classified relative to their base material matrix - Alumina-based and Silicon Nitride-based. Alumina-based cutting tools consistently have higher chemical inertness whereas the silicon-nitride based cutting tools have a greater strength and fracture toughness. In general, the wear resistance and thermal shock resistance (a tool material property required to overcome the effects of heating and cooling cycles seen in intermittent cutting operations (like milling)) is lower in ceramic cutting tools compared to tungsten carbide tools [47, 48]. To overcome the ceramic tool material limitations and improve their cutting performance, different components - additives, particulates and whiskers [47] are added to modify the tool material composition and fabricate advanced ceramic composites. TiC, TiN, ZrO_2 particulates and SiC whiskers are added to alumina to improve its fracture toughness and/or thermal shock resistance. Silicon nitride-based ceramics can be classified into three different families based on their composition - silicon nitride containing sintering additives, silicon-nitride-aluminum-oxygen solutions(SiAlONs) and particulate-based silicon nitride ceramic composites. The material composition along with the processing and densification techniques [49] significantly affect the material properties of these tools. Sialons have excellent thermal shock resistance, while silicon-carbide whisker reinforced alumina-based ceramic composite has excellent fracture toughness. Variations of these alumina-based and silicon-nitride based ceramic composites are active areas of research [50–57], and new composite materials are being developed at a rapid pace to significantly enhance the properties and applicability of the ceramic tool materials.

Due to their inherent material properties, ceramics are used in high-speed machining of hard and difficult-to-machine materials. Ceramic tools, in general, can be used to machine many different types of steels, cast-iron, Ni, Co and Fe based superalloys and many nonferrous alloys and composites [58]. Particulate-toughened alumina-based cutting tools have a lower fracture toughness and thermal shock resistance. In general they are only used for continuous high-speed finish machining without coolants. Sialon and SiC whisker-reinforced ceramic composites, due to their high fracture resistance, are commonly used to machine high strength superalloys at high material removal rates. These tool materials are also used for interrupted cutting of superalloys. However, due to excessive chemical reactivity between silicon nitride or silicon carbide and steel, silicon nitride-based cutting tools and SiC whisker-reinforced ceramic composites are not suited for steel machining [59, 60].

The choice of the specific tool material depends on the workpiece to be machined, the particular machining process - turning, milling etc. and the type of operation - finishing or roughing. Some of these tools have been used in interrupted cutting operations like endmilling [61] and face milling [62, 63] as well, and have been demonstrated to show a better cutting performance compared to carbide tools in certain applications [63, 64].

In addition to the above tool selection criteria, for a given tool material to be used for micromachining, the tool should be fabricated to have smooth surfaces and sharp, un-serrated cutting edges with edge radii less than 2 μm. This capability combines both the *smoothability*, *sharpenability*, and *edge retention capability* of the given ceramic material and the ability of the tool-fabrication process to maximize surface smoothness, minimize edge-rounding / edge-chipping and prescribe a certain edge profile (edge preparation). The edge preparation determines the strength of the cutting edge [48,60]. Typically, ceramic tools are used with a negative rake angle to utilize the high compressive strength and overcome the low transverse rupture strength of these materials [48, 60]. The sharpenability, smoothability, and edge retention capability are hypothesized to be directly related to (a) the size and shape of the different components forming the ceramic-matrix composite, (b) the mechanical properties- transverse rupture strength and fracture toughness, of the ceramic composite, which quantify the ease of brittle fracture and the propagation of cracks within the material, and (c) the processing technique used during fabrication of the ceramic composite, which governs the density of packing of the different components and the porosity of the ceramic [49].

Grinding and polishing of structural ceramics have been the focus of many studies [65]. These processes have been known to be the most efficient methods to shape tool-grade ceramic materials and create polished surfaces. Different types of grinding wheels, mostly with diamond abrasives have been used. The selection of the appropriate grinding wheel plays an important role in the grinding efficiency and surface finish of the polished ceramics. The bond type (resinoid, metal, vitrified and electroplated), the diamond grit type, the grit size and concentration are the various critical parameters that need to be taken into account to make the right choice of the grinding wheel for polishing a given ceramic material [66]. Porous cast-iron bonded grinding wheels were also used to demonstrate a much improved grinding efficiency [67].

One of the main issues in grinding ceramic materials has been the surface defects induced during the grinding process [68–71]. These defects tend to reduce the strength of the ceramic tool material significantly. The grinding parameters have a significant effect on the grinding forces, type of defects (and hence the strength) and surface finish on different ceramic materials [66, 72–74]. Selection of grinding parameters which lead to a mode of grinding referred to as ductile mode of grinding, where plastic deformation is the major mode of material removal, is shown to produce a smooth surface finish with minimum surface defects and sub-surface damage while also reducing the overall processing time [75–79]. Ductile mode of grinding has been demonstrated on ceramic materials under both the conditions of constant pressure [80] and prescribed depths of cut [81]. The machine loop stiffness has been shown to play an important role in obtaining a good surface finish and defect-free surface [82, 83]. In addition to all these factors, the micro-structure of the specific ceramic has also been shown to affect the presence of surface defects and surface finish [84] in the grinding and polishing of ceramics. Many studies have tried to understand and summarize the grinding mechanism for ceramics [85–87]. Also, some researchers have tried to model the grinding process to predict the surface roughness and grinding damage [76, 88–90].

Based on all of the above literature, the selection of the right tool-grade ceramic for a specific micromachining application is critical to maximize the tool performance. Further, it is important to evaluate the sharpenability, smoothability and edge retention capability of the ceramic material, before it can be shaped as a micro-tool. Grinding and polishing processes are the most effective methods in shaping and polishing ceramic materials. The ceramic material's grain size, composition and properties, the grinding wheel type, the rigidity of the machine tool and the grinding parameters used - all play a critical role in affecting the surface defects, surface finish and the processing time.

1.2.3 Micro-tool Design

The single-crystal diamond and ceramic micro-tools that are intended to be fabricated during this work will be used for micro-planing and micromilling applications. The shape of the micro-planing tools is in the form of a monolithic block rigidly attached to a base, with the desired rake and clearance angles. The micro-endmills are rotary tools (with 3 mm shank diameter) and have fluted or straight cutting edges at the tool-tip.

There are two categories of micro-endmills - ball end-mills and flat end-mills. For the purpose of this work, we limit the scope to fabrication of flat end-mills. Conventionally, tungsten carbide micro-endmills shapes are just scaled-down versions of the macro-scale endmills with fluted edges. Recent studies have shown that the fluted design is not necessary and simple straight cutting edge design will be more effective for micro-endmills [91–94]. A variety of new micro-endmill designs are actively being proposed and fabricated [91, 94–98]. New technologies to fabricate micro-tools such as Wire Electro Discharge Machining (WEDM) or Wire Electro-Discharge Grinding (WEDG) [96, 99–104] and Electrolytic In-process Dressing (ELID) [105] are topics of active research. In all these studies, the tool materials used were either sintered Poly-crystalline diamond (PCD) or sub-micron or ultra-fine grade tungsten carbide.

1.3 Research Objectives

The literature review presented above has clearly identified that a mechanical polishing process, such as the one used for conventional diamond-polishing, is one of the most effective methods to create smooth surfaces and sharp cutting edges on single-crystal diamond and ceramics. However, effective application of polishing to fabricate high-precision micro-tool geometries requires a different polishing configuration with an ability to create complex micro-scale geometries with high-aspect-ratios, smooth surfaces, and sharp cutting edges in a predictable fashion on single-crystal diamond and ceramics.

To address this need, this Ph.D. thesis research focuses on precision fabrication of single-crystal diamond and ceramic micro-tools for micromilling using a precision polishing (lapping) process, referred to as the *mandrel-based polishing*. The mandrel-based polishing process utilizes mandrel-type polishing tools (electroplated, bonded or diamond-paste charged cast-iron mandrels) with shank diameter of 3 mm (or 0.125 in.) and a precision micromachining platform. The polishing tool is mounted on a ultra-high-speed (UHS) miniature spindle that can run at speeds up to 200 krpm, and the tool material (single-crystal diamond or a tool-grade ceramic) to be polished is mounted on precision XYZ slides. The desired shape and edges are obtained through accurately prescribed XYZ motions of the slides with respect to the rotating mandrel.

The overarching research objective of this Ph.D. research is to gain an understanding of the mandrel-based polishing process and equipment to enable identifying favorable polishing conditions that will lead to accurate fabrication of micro-tools from single-crystal diamond and ceramics in a predictable fashion. We will address this goal through the following specific objectives:

- To analyze the mandrel-based polishing process and the polishing characteristics of single-crystal diamond and tool-grade ceramics through experimental studies. Addressing this need requires design and construction of a precision polishing test-bed.
- To develop spindle-metrology and analysis techniques applicable to measurement of axial and radial error motions of UHS spindles in order to identify a favorable set of spindle parameters for accurate and repeatable fabrication of the micro-tools.

1.4 Research Contributions

The specific contributions of this thesis research include

1. An experimental understanding of the mandrel-based polishing process and the polishing behavior of single-crystal diamond and various tool-grade ceramics.
2. Design and development of a two-stage high-precision polishing test-bed to enable accurate fabrication of micro-scale tool geometries.
3. Development of laser Doppler vibrometry (LDV)-based methodology for measurement of axial and radial error motions when using miniature ultra-high-speed (UHS) spindles.
4. An experimental characterization of the radial and axial error motions of a typical UHS spindle with hybrid-ceramic bearings, identifying the various sources of error motions and quantifying them.
5. Implementation of two different error-separation techniques (Multi-orientation technique and Donaldson reversal method) to remove the artifact form error and obtain the true spindle error motions.

1.5 Thesis Organization

Chapter 2 provides a description of the mandrel-based polishing configuration. Experimental studies to understand the effect of some of the process parameters on the polishing behavior of single-crystal diamond are also given. Chapter 3 presents the design and construction of the dual-stage polishing test-bed. Details of the design and features of the test-bed are illustrated. Chapter 4 describes an experimental evaluation of various tool-grade ceramics to understand their polishing behavior and assess their applicability for micro-scale cutting. Chapter 5 describes the LDV-based methodology for measurement of axial and radial error motions of UHS spindles. Chapter 6 presents a thorough quantitative analysis and characterization of the radial and axial error motions of a typical UHS spindle with hybrid-ceramic bearings. Chapter 7 presents implementation of two error-separation techniques (Multi-orientation technique and Donaldson reversal method) on UHS spindles to measure the true spindle error motions. Chapter 8 summarizes the conclusions from the presented research. Chapter 9 discusses the future work that is needed for successful fabrication of accurate single-crystal diamond and ceramic micro-endmills in a predictable fashion.

Chapter 2

Mandrel-based Polishing Process and Experimental Studies on Single-crystal Diamond

2.1 Introduction

To address the need for an efficient process to fabricate precise and accurate single-crystal diamond and ceramic micro-endmills, the mandrel-based polishing process was conceived and developed. An evaluation of this process in terms of creation of smooth surfaces, creation of sharp edges (less than 2 μm), and ability to shape micro-scale features precisely and accurately on tool-materials is essential before its application towards tool fabrication.

In this chapter, the mandrel-based polishing configuration and the effectiveness of the process in polishing and shaping single-crystal diamond at the micro-scale is evaluated. Further, studies are conducted to understand the influence of some of the important polishing parameters, including powder grit size, polishing path and boart material in polishing single-crystal diamond. Edges are created by polishing two adjacent faces. The quality of the polished surfaces, sharpness and condition of the created edges, and the ease of material removal are qualitatively and quantitatively evaluated.

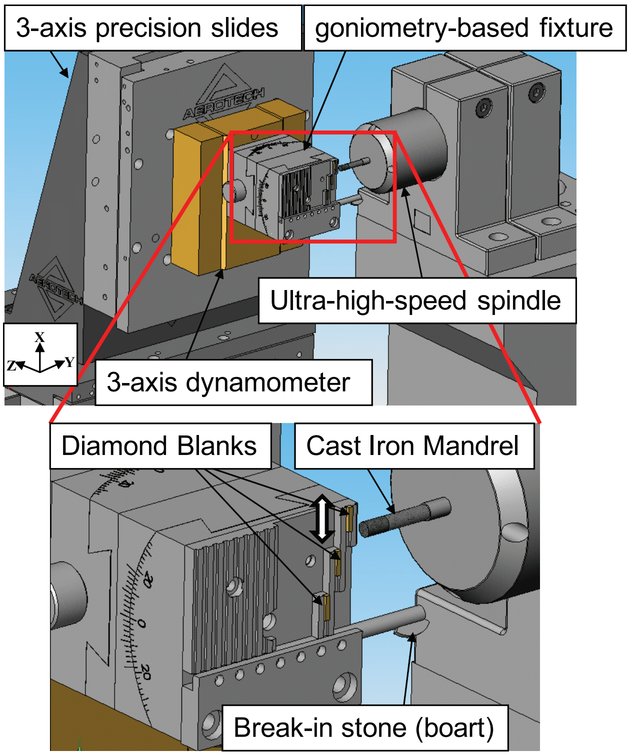

Figure 2.1: The setup for the mandrel-based diamond polishing configuration.

2.2 Description of the Mandrel-based Polishing Configuration

Figure 2.1 shows the setup of the mandrel-based polishing configuration. It uses a small-diameter mandrel (typically $\approx \phi$ 3 mm or 0.125 in.) rotated at ultra-high speeds (up to 200 krpm) on an UHS spindle as the polishing tool. The small diameter of the mandrel provides access to create high-aspect-ratio features. In addition to the polishing tool, the main components of the setup include 3-axis precision slides, a mandrel-preparation subsystem, and a goniometry-based fixture for holding (and aligning) single-crystal diamond workpieces. A 3-axis force dynamometer (Kistler 9256C1 MiniDyn) is used to measure the polishing forces. An optical microscope allows viewing the initial approach and progression of the polishing.

Electroplated, bonded or diamond-paste charged cast-iron mandrels could be used as the polishing tool. All the studies conducted in this chapter use a diamond-charged cast-iron mandrel. Figure 2.2 describes the procedure followed in the mandrel-based polishing process when using the cast-iron mandrel. The diameter of the mandrel used is 3.125 mm. The preparation of the mandrel, i.e., charging of the mandrel with diamond particles, is critical to the success of the polishing process. The mandrel is first scored with a rough sand paper to create sites for embedding the

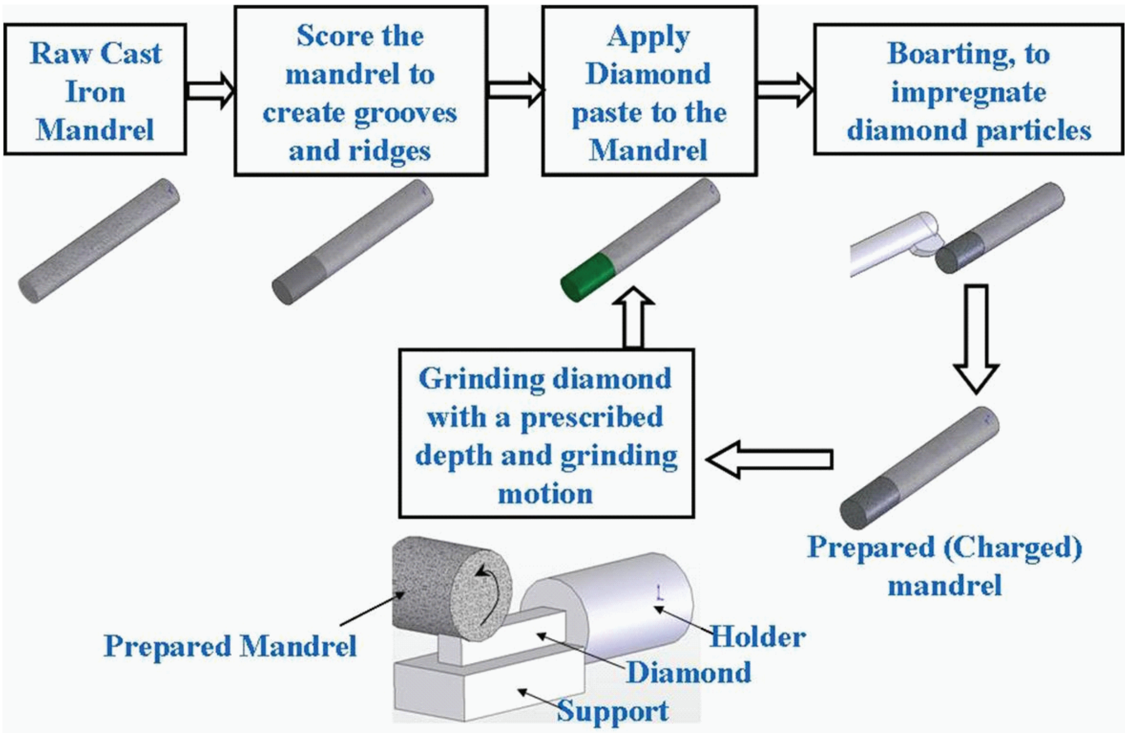

Figure 2.2: Overview of mandrel-based polishing process when using cast-iron mandrel.

diamond particles. An oil-based diamond paste that includes powdered diamond particles with a specific grit-size range is applied on the mandrel to be prepared, while rotating the mandrel at relatively low speeds. A break-in stone (also called a boart), which is either a low-quality single-crystal diamond or a polycrystalline cubic-boron nitride (PCBN) stone, is pressed on the mandrel surface to facilitate embedding the diamond particles on the mandrel surface. The stone is moved back and forth on the mandrel surface along mandrels axial direction. This process is continued until the surface of the mandrel darkens to a dark-gray color.

The single-crystal diamond workpieces are attached to the fixture using super-glue. The channels pre-fabricated on the fixture facilitate rough positioning, while the goniometers provide the fine positioning and orientating of the workpieces. Since the polishing rates are highly dependent on the crystallographic orientation of the single-crystal diamond, the orientation of the workpieces with respect to the mandrel is critical. To confirm the crystallographic orientation specified by the manufacturer, Laue X-ray diffraction technique is used. It was seen that the orientation specified by the manufacturer was correct within the resolution of the measurement (approximately 1^o).

Next, the spindle speed is increased to the polishing speeds. Generally, speeds above 10 m/s are needed to obtain sufficient levels of polishing rate since the material removal increases considerably with increase in speed. For this reason, an air turbine-driven UHS spindle with hydrostatic air bearings is used to rotate the mandrel. A specific polishing path, in-feed/polishing depth, and cross-feed are then provided by prescribing the motion of the precision slides using a G-code. In this preliminary study a simple (back-and-forth) and a complex ("figure-8" type loops) polishing path are tested. The cross-feed direction is also prescribed as desired. As the polishing process continues, the diamond particles on the mandrel dislodge, causing material removal to seize. For this reason the mandrel preparation is repeated periodically during the process. This cycle of preparation and polishing is continued until the desired amount of material is removed.

2.2.1 Feasibility Studies of the Mandrel-based Polishing Process

To demonstrate the basic capability of the new diamond-polishing configuration, four sides of a synthetic single-crystal diamond workpiece with approximately 1.1 mm x 1 mm cross-section and 4 mm length were polished. The raw diamond workpiece was first brazed onto a carbide shaft to gain access to all four sides. Another fixture was designed to hold the carbide shaft (rather than the fixture described above).

During this feasibility study, a set of polishing conditions were selected. Two different diamond pastes with grit sizes of 0-2 μm and 20-40 μm were used. Only the straight polishing path with front-to-back motion was utilized. At each step, a polishing depth of 0.5 to 2.0 μm was provided. The cross-feeding direction was chosen to be along the axial direction of the carbide shaft on which the diamond workpiece is mounted. The single-crystal diamond workpiece was oriented to set the polishing surfaces to be the $\{100\}$ planes and polishing direction to be the [010] direction. During polishing, the workpiece was moved along the mandrel axis to use a larger area of the mandrel surface, and thereby to reduce the frequency of the mandrel preparation. The polishing speed was maintained at approximately 16 m/s by setting the spindle speed to be 100 krpm. At a set polishing depth, the front-to-back motion was repeated 15 times. After the completion of five polishing-depth steps, the mandrel was re-charged with diamond particles.

Figures 2.3(a) and 2.3(b) show the raw and removed portions on the diamond workpiece after the polishing operation. Approximately 250 μm of diamond was removed from each of the four sides of the workpiece. It is clear from the figures that the polishing process is capable of removing considerable amount of material. Furthermore, it is shown that small structure can be created on single-crystal diamond (the final size of the created feature is approximately 500 μm.) The SEM images of two surfaces polished using 20-40 μm grit size (with 2 μm polishing-depth steps) and

0-2 μm grit size (with 0.5 μm polishing depth) are given in Figs. 2.3(d) and 2.3(e), respectively. While the material removal rate was higher for the larger grit size, the surface roughness was also higher. The large grit size was seen to leave grooves on the surface, with approximately 40 μm separation. However, the surface created using the small grit size is considerably smoother. In addition, the material removal with the smaller grit size seems to be ductile (rather than brittle) in nature, resulting in crack-free surface. The edges that were created along the intersection of the polished surfaces were also examined under SEM. Figure 2.3(c) shows a portion of the edge created during this study. The edge radius for the region shown can be estimated to be considerably below 1 μm.

This preliminary study demonstrated that the mandrel-based diamond polishing configuration has the basic capability of creating miniature structures on single-crystal diamond. It was also shown that the smooth surfaces and sharp edges can be attained.

2.2.2 Effect of Grit Size, Polishing Path and Boart Material

A number of polishing parameters, including the powder grit size, crystallographic orientation of the workpiece, mandrel preparation process (including the boart material), polishing path, polishing speed, cross-feed rate, cross-feed direction, and incremental polishing depth, have a significant effect in performance of the mandrel-based polishing process. In this work, two of the parameters, including diamond grit size and the polishing path and boart material are investigated. The surface roughness, the actual amount of material removed and the edges created while using three different grit sizes were examined.

2.2.3 Experimental Parameters and Setup

During this experimental investigation, three (diamond powder) grit sizes, including 0-2 μm, 5-10 μm, 20-40 μm, were considered. For each grit size, a simple (back-and-forth) and a complex ("figure-8" type loops) polishing path were tested. Two boart materials, including (low-quality) diamond and polycrystalline cubic-boron nitride are also considered.

Each single-crystal diamond workpiece was fixed on the goniometer-based fixture as in Fig. 2.1. For each grit size, a separate diamond workpiece was used. Two distinct regions were polished on each workpiece surface corresponding to the two polishing paths. The cross-feed (along the X-direction in Fig. 2.4) was prescribed as 600 μm along the [010] direction on {001} orientations. A single polishing pass involves cross-feed motion in both forward (-X) and backward directions

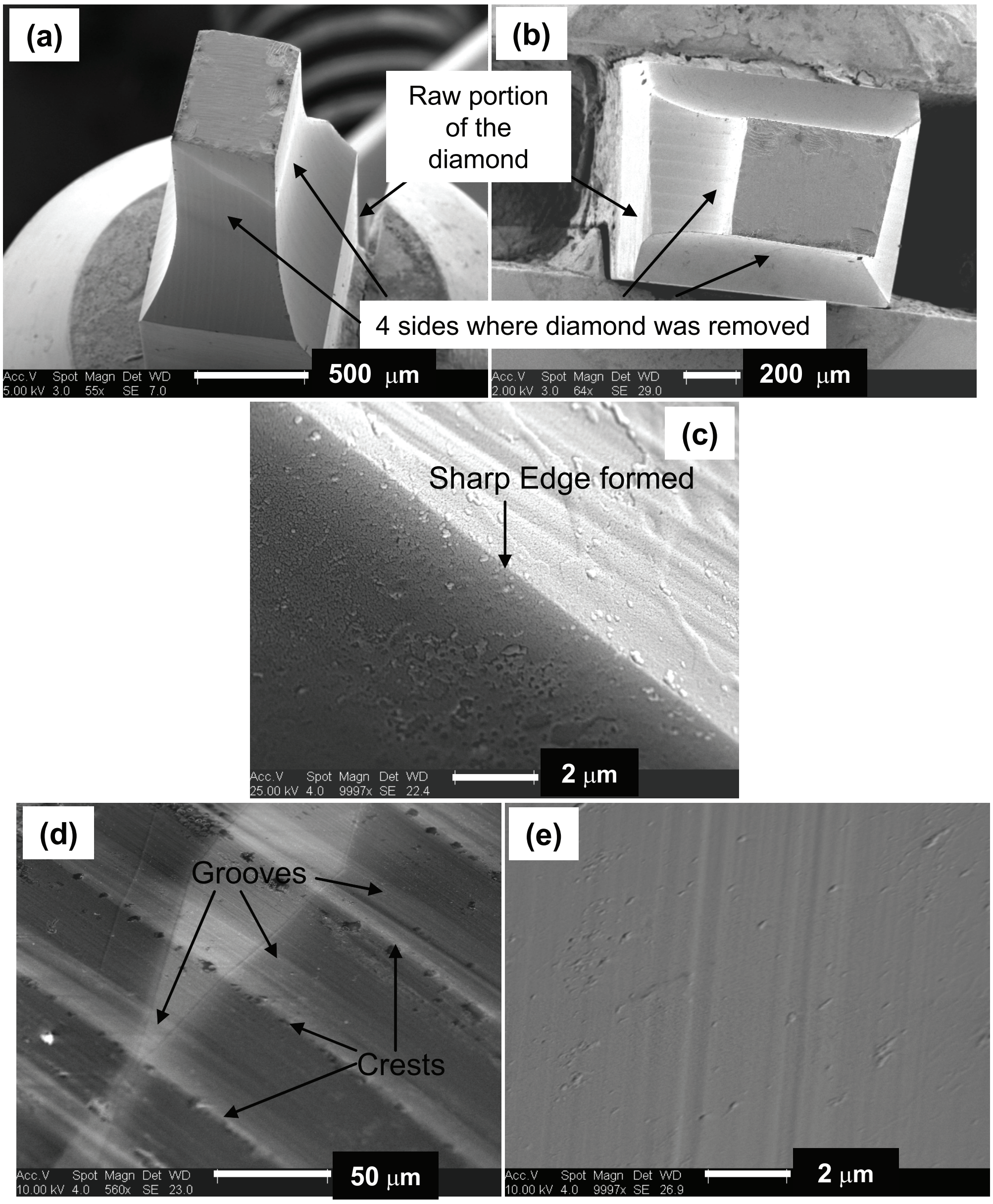

Figure 2.3: A single-crystal diamond polished using the mandrel-based polishing configuration.

($+X$). To reduce the number of mandrel-preparation steps, the workpiece was moved along the axis of the mandrel ($\pm$ Y) by 130 μm (step-feed) for each polishing pass. For every alternate polishing pass, a polishing depth of 25 nm (along the -Z-direction) was prescribed. The mandrel preparation frequency is set to be every 2 μm and every 1.2 μm of prescribed polishing depth for the simple and complex polishing paths, respectively. For all cases, the preparation removal cycle was repeated for a total prescribed depth of removal of 120 μm. Except for the manual application

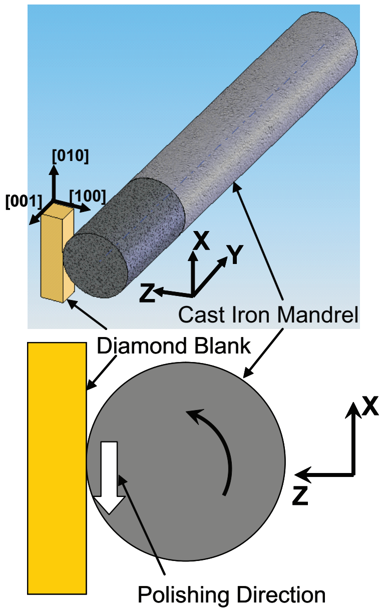

Figure 2.4: Sketch of the polishing configuration.

of paste, all motions for mandrel preparation and diamond polishing were automated using G-code programming.

2.2.4 Results and Observations

Figure 2.5 shows the SEM image of all the blanks on which the experiments were conducted. Note the individual blanks used for different grit sizes. Also note the two regions on each blank, corresponding to the two polishing paths, where material was removed.

Polishing Forces: A sample force signature collected during polishing is given in Fig. 2.6. During each polishing cycle the forces were seen to fluctuate within a certain range. It was seen that the forces in the Y-direction were the highest for any of the tests conducted. The X- and Z-forces were similar in magnitude (the Z-forces were slightly less than the X-forces). Typically, the force ranges of 5 N to 15 N were experienced. The forces experienced during the complex motion were lower than those for the simple motion. For both simple and complex tool paths, the forces were seen to reduce with increased grit size.

Surface Roughness: To assess the surface roughness, the polished surfaces of the diamonds were measured using white-light interferometry (WYKO). Before the measurement, the polished surfaces were cleaned thoroughly with alcohol. Without using a reflective coating, it was difficult and time-consuming to obtain sufficient reflection from the polished surfaces. Accordingly, the surfaces to be

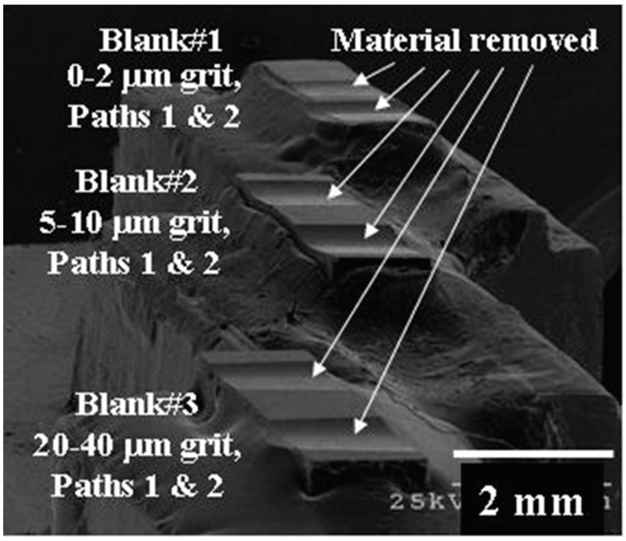

Figure 2.5: Diamond blanks used for experimentation showing the material removed in various cases.

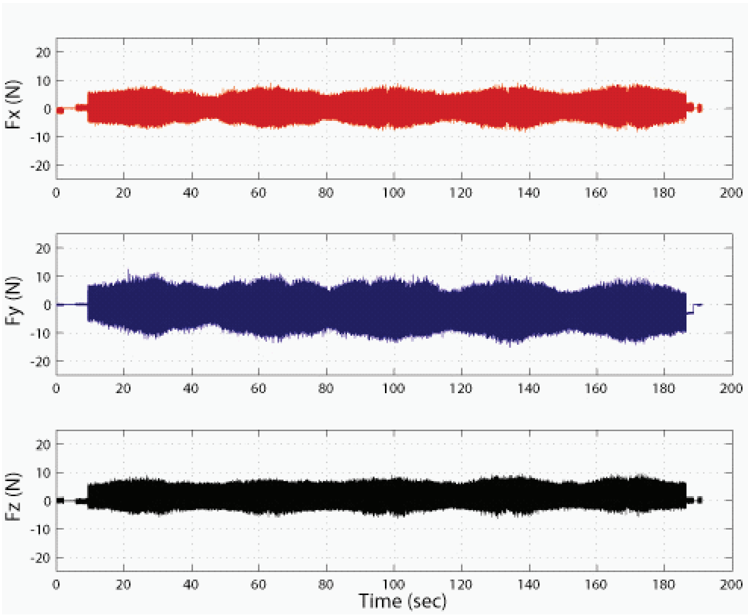

Figure 2.6: Typical polishing-force data.

measured were sputtered with a conformal layer (approximately 5 nm) of gold to attain sufficient optical reflectivity. The surface roughness values were obtained from four regions on the polished surface along the location of maximum material removal. Each measurement region was 60 μm by 46 μm.

Figure 2.7 shows the surface roughness parameters (Ra, Rz) with grit size and polishing path

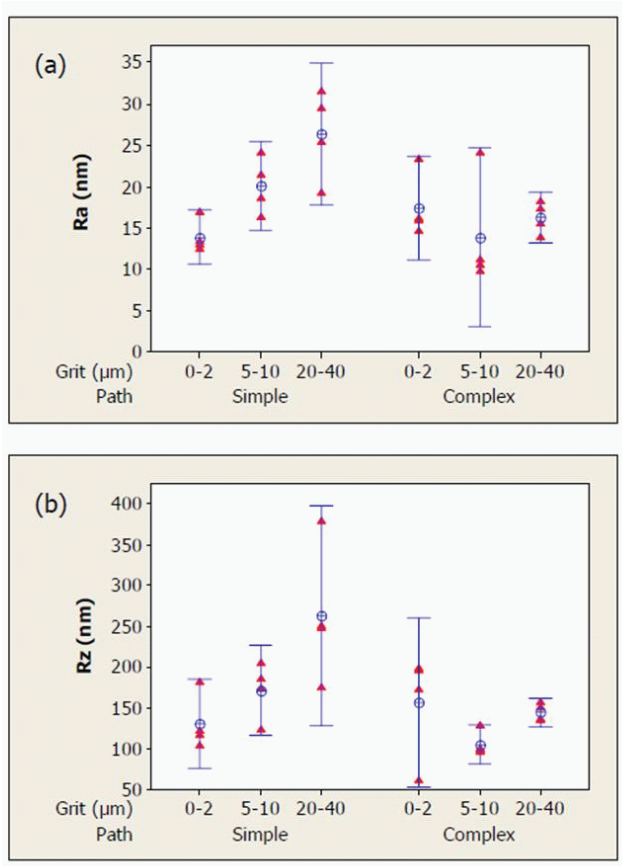

Figure 2.7: The variation of R_a, R_z with grit size and polishing path.

when using the diamond boart. The triangles indicate values for each of the four measurement regions. The hollow circles indicate the average of the four values. Error bands for the 95% confidence interval are also included in the figures. While Ra gives an estimate of the average deviation from the mean surface, Rz provides an estimate of the average peak-to-valley deviations. For this work, Rz is calculated as $Rz = 6\text{x}Rq$, where Rq is the root mean square value of the surface roughness.

For the simple motion, the surface roughness was seen to increase with increased grit size. This result is expected since the height variation of the individual diamond particles and their spatial distribution are expected to be larger for larger grit sizes, and the simple polishing path imposes the height variation along the surface. For the complex motion, such a correlation was not observed. Indeed, the average surface roughness did not vary significantly with grit size, and the lowest value was observed with the intermediate grit size. In the case of the complex motion, the surface roughness is determined by the combination of the grit size and polishing path, rather than by only

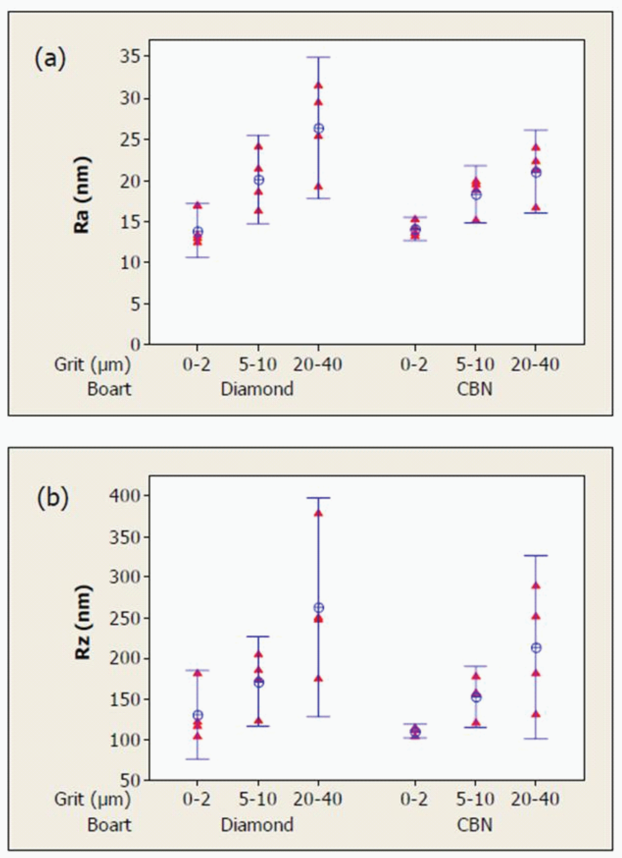

Figure 2.8: The variation of R_a, R_z for two different boarts.

the grit size. Generally, the surface roughness obtained from the complex motion was lower than that obtained from the simple motion.

Figure 2.8 compares the Ra and Rz values for the simple polishing path when the mandrel preparation was completed using diamond and CBN boarts, while all other conditions remained the same. The trend of increasing Ra and Rz with grit size is observed in both cases. In addition, the surface roughness values were seen to be comparable. This indicates that the polishing tests were repeatable, and the surface roughness was insensitive to the boart material.

Actual Depth of Material Removed: While a certain depth of material removal was prescribed during the experiments, the actual material removal amount could be different from the prescribed amount. The actual depth of material removal was determined by measuring the maximum depth with respect to an unpolished region of the workpiece using the WYKO. Figure 2.9 shows the actual depth of removal for both polishing paths and the three grit sizes and for a prescribed total depth of 120 μm. As expected, the actual material removal is less than the prescribed one. The largest

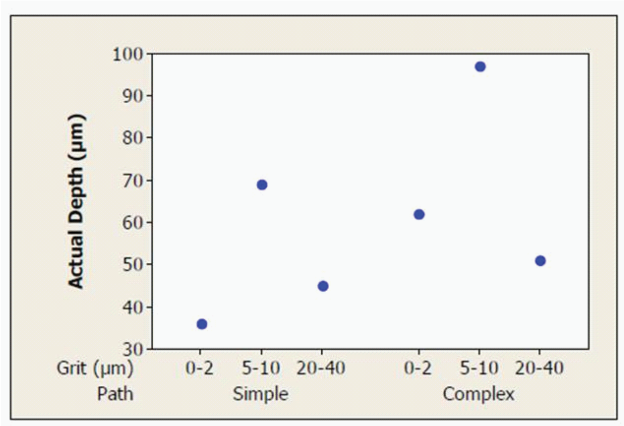

Figure 2.9: Effect of grit size and polishing path on actual depth of removal.

removal was observed for the medium grit size (5-10 μm). In addition, the complex polishing path led to higher material removal than the simple polishing path.

The prescribed removal depth includes not only the depth of actual material removed, but also the mandrel-wear, dynamic runout of the spindle (which includes the axis of rotation errors of the spindle) and the elastic deflections within the structural-loop (including deflection of the mandrel, deflection of the spindle due to it radial stiffness and deflection of the precision slides). In assessing the feasibility of the mandrel-based polishing technique, it is important to understand the actual depth of material removal versus the prescribed depth.

To get a better understanding of this, actual depth of removal versus prescribed depth was studied with two different grit sizes as the polishing process progressed. Figure 2.10 shows a plot obtained through these studies of the actual depth versus the prescribed depth of removal while polishing. The 45^{o} red line represents an ideal case where the actual depth of material removed is equal to the prescribed depth. Difference from the ideal case accumulates as more material is prescribed to be removed. In the case of 20-40 μm grit size, the actual depth is lower by up to 75-80 μm when the prescribed depth is 150 μm. Such large differences can lead to significant errors in the fabricated shapes and will render the micro-tool unusable. A fundamental approach is sought to understand this issue and to identify and quantify the possible sources that cause this issue.

Mandrel wear is estimated using SEM images (Fig. 2.11). It was seen that the mandrel radius was reduced by 10-25 μm for different cases. Even in the worst case scenario, a mandrel wear of 25 μm is estimated.

For the polishing forces measured, the elastic deflection of a 3 mm mandrel with an overhang

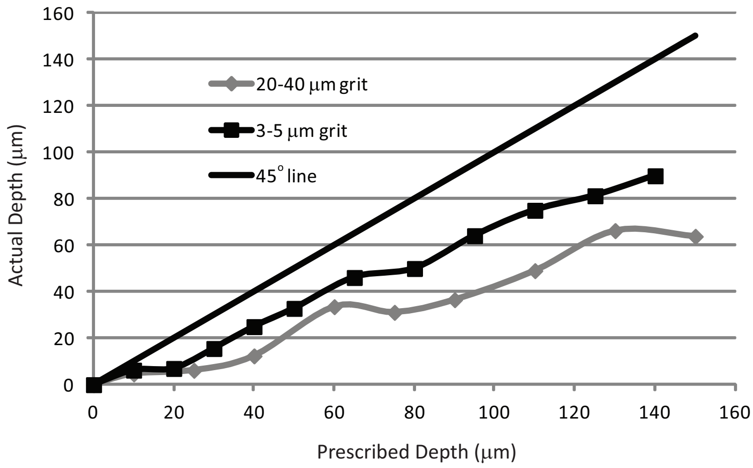

Figure 2.10: Actual depth vs. Prescribed depth.

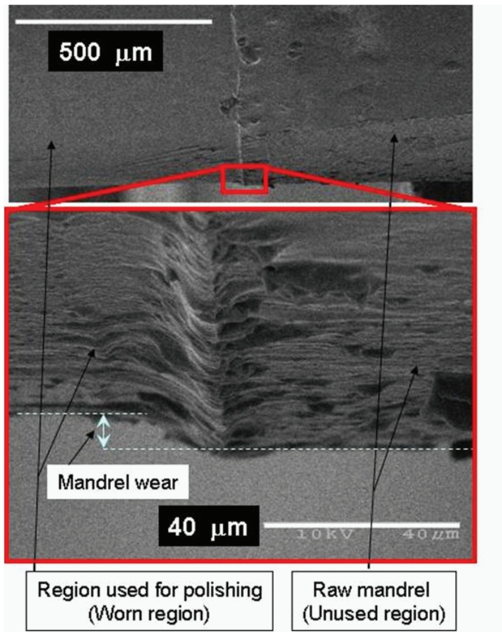

Figure 2.11: Estimation of mandrel wear.

length of 15 mm is calculated using beam theory to be up to 30 μm. Furthermore, the deflection of slides was estimated to be 5 μm. Thus the sum total of mandrel wear and elastic deflections of the mandrel and slides account for up to 60 μm of the difference between the prescribed depth and actual depth of removal. The remainder 15-20 μm of the difference is still unaccounted for.

Due to the ultra-high rotational speeds and relatively low stiffness of the miniature UHS air-bearing spindle used in these studies, the dynamic radial and axial motions when using the UHS

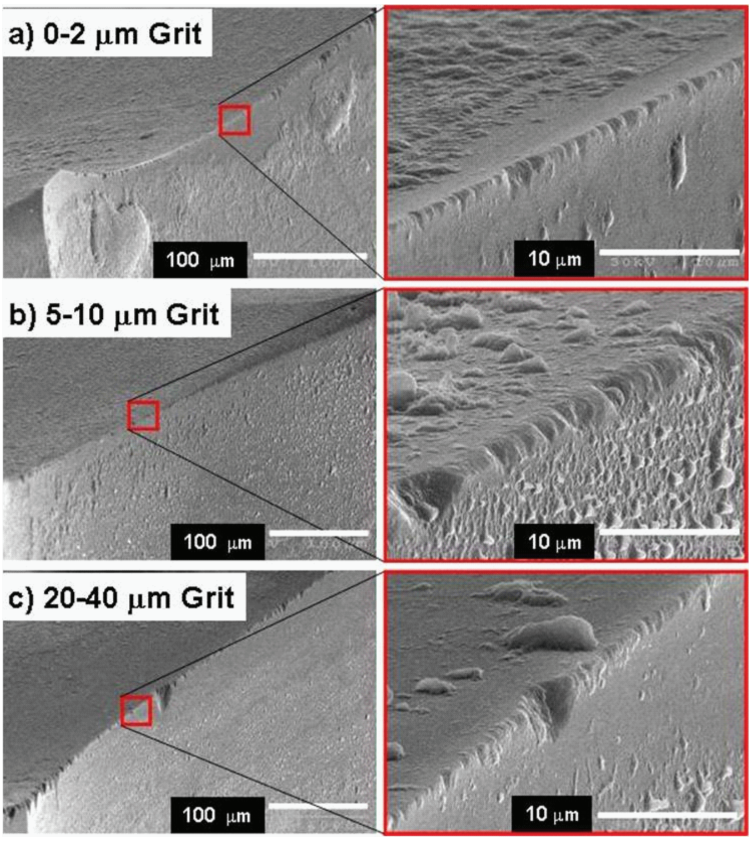

Figure 2.12: Edges created with different grit sizes.

spindle will be the next most significant contributor. Axis of rotation errors of the spindle are a component of these motions. It is also hypothesized that the synchronous axis of rotation errors can lead to shape (form) errors on the polished surfaces while the asynchronous axis of rotation errors can lead to increased surface roughness of the polished surfaces.

Edge Condition and Sharpness: To qualitatively assess the edge quality, the edges created by the intersection of two polished surfaces were examined under SEM. Figure 2.12 shows the edges formed for the different grit sizes with the simple path. In all cases, the edges were chipped at various locations. The edge radius was approximated to be 1 μm for 0-2 μm grit size, and few micrometers for the two larger grit sizes.

It is considered that the polishing path had an important influence on the edge quality. During the use of straight (simple) polishing path with the cross-feed direction aligned with the created edge, only a set of diamond grits are interacting with the edge location. It is therefore expected that smoother and sharper edges may be created if the polishing tool is fed normal to the axis of the edge to be created.

2.3 Summary

This chapter presented the mandrel-based diamond polishing process for fabricating miniature, high aspect ratio structures with smooth surfaces and sharp edges required for micro-endmills. Preliminary studies were conducted to investigate the effects of grit size, polishing path and boart material on the performance of the mandrel-based diamond polishing configuration. The feasibility of the configuration is demonstrated by removing approximately 250 μm depth of material on each of the four facets of a single-crystal diamond workpiece (the final size of the created feature was approximately 500 μm). Sharp edges ($\leq$ 1 μm edge radius) and smooth surfaces were attained during this preliminary study. It was seen that the mandrel-based diamond polishing configuration is capable of removing considerable amount of material, creating sharp edges and attaining smooth surfaces.

It is seen that the surface roughness depends on both the grit size and polishing path. For the simple polishing path, the average surface roughness was seen to be proportional to the grit size. This dependence was insensitive to the boart material used. For the complex polishing path, the surface roughness was seen to be insensitive to the grit size. As compared to the simple motion, the complex motion produced smoother surfaces. Chipping was observed along the created edges, extent and severity of which was seen to be correlated to the grit size and polishing path.

The actual depth of material removal was seen to be less than the prescribed depth in every case. In addition to mandrel-wear and the elastic deflections within the structural-loop (including deflection of the mandrel, deflection of the spindle due to it radial stiffness and deflection of the precision slides), the dynamic axial and radial motions of the miniature UHS air-bearing spindle (due to its relatively low stiffness) could be the dominant factors causing this difference. In addition to affecting the accuracy of material removal, all these factors could affect the form errors of the polished surface.

To address some of these important issues, a rigid polishing test-bed is designed and constructed. The details of the design and various features of the test-bed are described in the next chapter.

Chapter 3

Dual-stage Polishing Test-bed for Fabricating Single-crystal Diamond and Ceramic Micro-endmills

3.1 Motivation

In the previous chapter, a few disadvantages of the mandrel-based configuration itself and further specifically related to the setup used in the previous study were identified. One of the issues related to the previous setup was the stiffness of the miniature UHS spindle. The spindle used had aero-static air-bearings whose radial stiffness is quite low. This, in addition to the low-stiffness of the mandrel and mandrel-wear, contributed to significant differences between the actual removal depth and the prescribed removal depth. Also, the spindle was air-turbine driven and had very low power (14 W). During the diamond polishing experiments, it was seen that the spindle slowed down significantly and hence the polishing speed, which is a significant parameter in diamond polishing, could not be controlled accurately. To address and overcome these issues, there was a need to design a rigid platform to allow for accurate fabrication of single-crystal diamond and ceramic micro-endmills. This need was satisfied through the conception of a dual-stage polishing test-bed.

This chapter presents the design and construction of the dual-stage polishing test-bed. The two stages of the machine include: 1) the large-wheel based traditional diamond polishing system for "rough" polishing with high material removal rates, and 2) the mandrel-based polishing configuration (discussed in the previous chapter) with capability to create intricate micro-scale features and high-aspect-ratio structures on single-crystal diamond and ceramics. Diamond-paste charged cast-iron wheels/mandrels or resin-bonded wheels/mandrels could be used on either systems. Other sub-systems such as the automated paste application system were simultaneously developed to be included as part of the machine to facilitate automation of the polishing process.

3.2 Machine Design

The first step in the design of the new test-bed was to list down all the basic capabilities required from the machine. The diamond/ceramic being polished should be able to access the individual polishing stages in an automated fashion. Apart from these polishing stages, the diamond/ceramic should be able to access an in-situ probe-based measurement system which can be used to measure feature dimensions on the workpiece. Another basic capability is that the system should have enough space to mount a high-magnification camera for viewing the polishing process at both stages and also various sensors, including an LDV, a microphone and an acoustic emission sensor to measure different response variables.

3.2.1 Machine-design Layouts

Different machine-design layouts were considered which satisfy the basic capabilities. Finally a couple of these were short listed. The layout designs are shown in Fig. 3.1. The design shown in Fig. 3.1(a) is a gantry-based design. The diamond to be polished is mounted on a fixture and is moved between the two polishing stages and the measurement system using a precision gantry frame. The second layout, shown in Fig. 3.1(b), includes a precision XYZ assembly mounted on a motorized rotary platform. The rotary platform is used to access the individual polishing stages and the measurement system. There are many disadvantages of the gantry-based design. Firstly the gantry has to be made quite large to accommodate the physical dimensions for the two stages. The accuracy of such motion axes is much lower than the more compact stage system shown in Fig. 3.1(b). Another disadvantage is that the gantry system has a much larger inertia than the system shown in Fig. 3.1(b). This limits the maximum speeds achievable and the acceleration profiles that could be obtained. Because of the much more compact nature of the layout shown in Fig. 3.1(b), it can be designed to achieve a better system performance. Hence this layout was chosen for the machine.

The finalized design of the layout shown in Fig. 3.1(b) is shown in Fig. 3.2. As illustrated

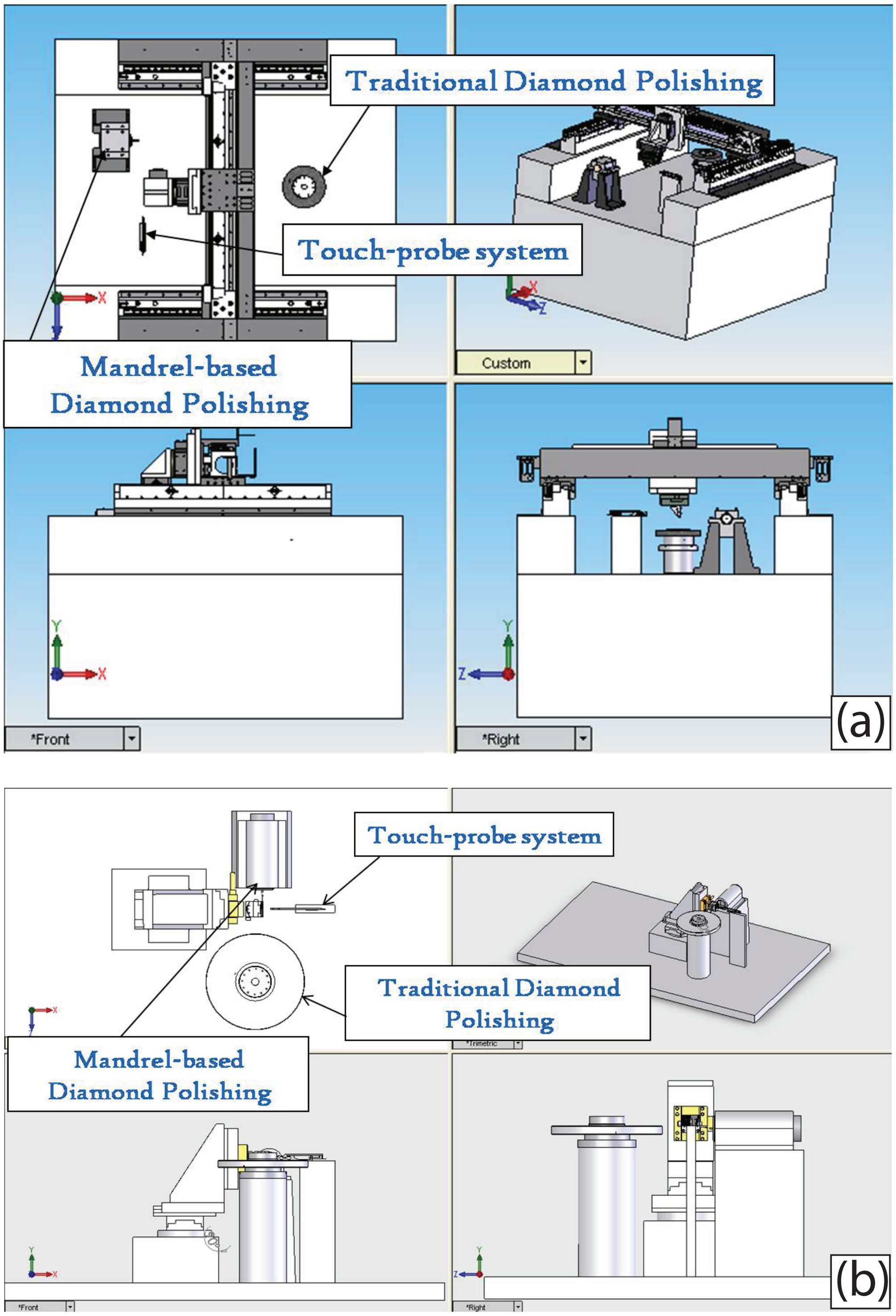

Figure 3.1: Machine design layouts.

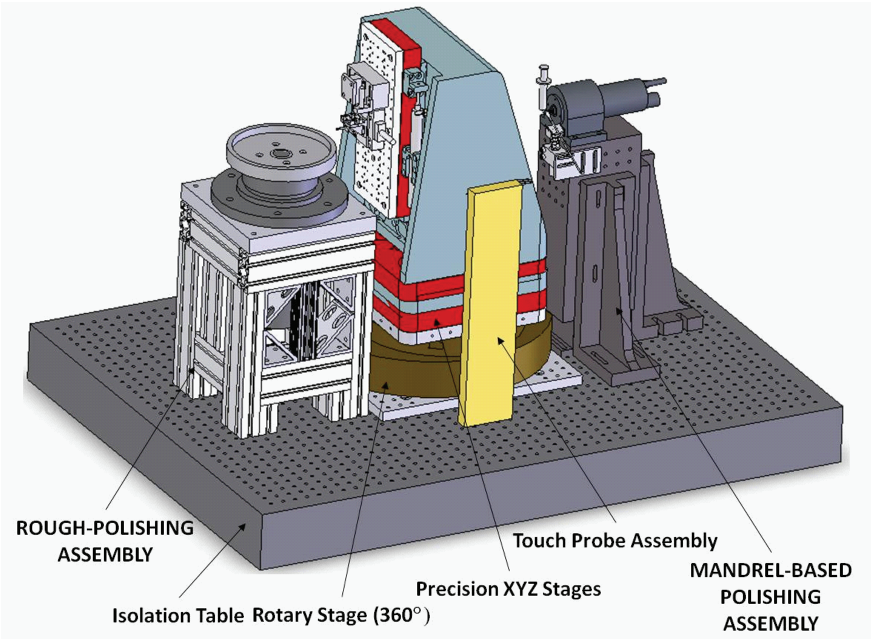

Figure 3.2: Dual-stage diamond-polishing test-bed.

in the figure, the core of the machine is a precision XYZ assembly mounted on a motorized rotary platform. The accuracy, repeatability, resolution and continuous force specifications of the precision XYZ stages and the motorized rotary stage will determine the system capability to accurately fabricate miniature features on diamond. These requirements were listed and presented to many precision stage manufacturers. Custom XYZ stage designs were obtained from a couple of these manufacturers to meet the specified requirements. The chosen precision XYZ stage met the specifications shown in Fig. 3.3. The custom XYZ stage required a high-stiffness custom design of the angle bracket to support the Z-stage. Many designs were evaluated using FEA by applying a unit load at a typical diamond mounting location to determine the bending stiffness in all three axes as shown in Fig. 3.4. Among these, the one with highest stiffness for a given mass was chosen.

The main requirements of the rotary platform are repeatability of motion, high stiffness to provide a stable and rigid mounting platform and large load capacity with sufficient power to rotate the XYZ assembly. The motorized rotary platform that was finally selected is a stepper-motor controlled worm-gear based design with a ratio of 450:1 from the motor to the rotary platform. Due its solid steel construction, the rotation stage provides a rigid platform for the XYZ assembly

	Axes Specifications		
Specification Met	X	Y	Z
Accuracy (µm)	+/- 0.12	+/- 0.07	+/- 0.13
Repeatability (µm)	+/- 0.085	+/- 0.06	+/- 0.097
Straightness (µm)	+/- 0.1	+/- 5	+/- 1.25
Flatness (µm)	+/- 0.13	+/- 1.5	+/- 1.25
Pitch (arc-sec)	+/- 8.9	+/- 11	+/- 8.8
Yaw (arc-sec)	+/- 4.8	+/- 11	+/- 2.9
Dither (nm)	+/- 15	+/- 15	+/- 20
Continuous Force (N)	30	30	30
Travel (mm)	+/- 60	+/- 60	+/- 60

Figure 3.3: Custom designed precision XYZ stage specifications.

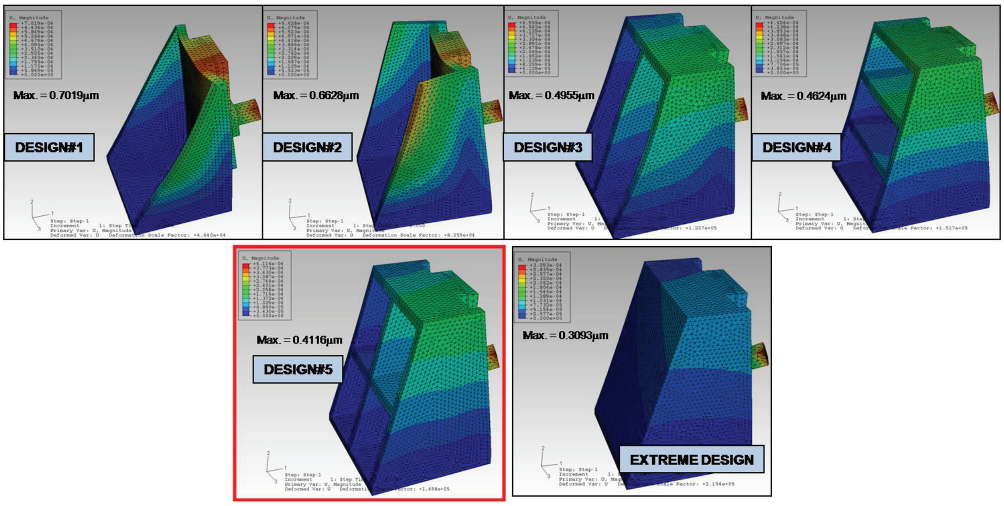

Figure 3.4: FEA of angle-bracket designs.

with a high load capacity. Also, because of its precision assembly and fine tuning, backlash is minimized and a very high repeatability of motion is guaranteed. High-precision limit switches (with a repeatability of $\leq$0.5 μm) located at both polishing stages ensure that the rotary platform consistently positions the XYZ stage accurately at the same physical location.

The rotation platform with the XYZ assembly mounted on it is fixed on an active pneumatic isolation table. The adapter plates between the rotary platform and the table and between the XYZ assembly and rotary platform are made of stress-relieved high strength aluminum adapter plates which are ground to within 0.0005 inch flatness. This ensures a flat mating of the XYZ assembly to the rotation platform and of the platform to the isolation table.

Figure 3.5 shows a closer view of the rough-polishing stage with the large wheel. A resin-bonded

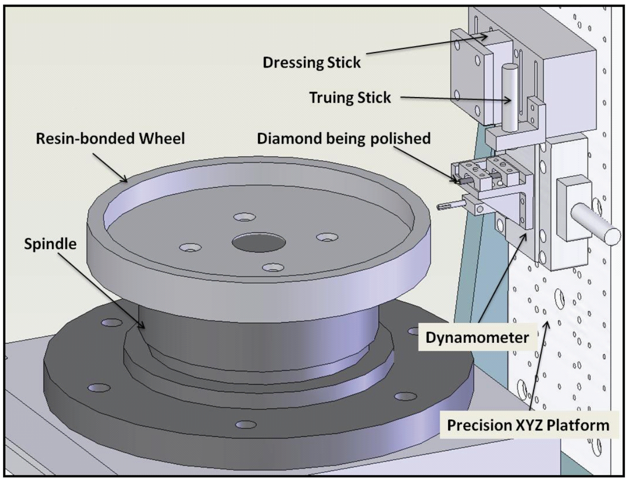

Figure 3.5: Large-wheel based polishing configuration for rough polishing.

wheel (or a traditional cast-iron wheel) is mounted on a large spindle which can be spun up to 3600 rpm. To true and dress the wheel, truing and dressing sticks are mounted on the stage. The diamond to be polished is mounted on a special fixture, which is fixed to a dynamometer that measures the forces during polishing.

Figure 3.6 shows a detailed view of the mandrel-based polishing configuration along with the other sub-systems that were developed to automate the process. An UHS spindle is used to rotate the 3 mm (or 0.125 inch) polishing mandrel at speeds up to 160 krpm, to provide the necessary polishing speeds required for material removal. Automated diamond-paste application and spreading systems are used to replenish the cast-iron mandrel with diamond particles, whenever it gets depleted. The break-in stone is used to press the diamond particles onto the mandrel so that the mandrel gets charged with diamond particles that hold on to the pores in the cast-iron mandrel. Figure 3.7 shows a closer view of the polished diamond indicating the micro-scale shape.

3.3 UHS Spindle for Mandrel-based Polishing

The required specifications for the UHS spindle were first listed. These are mainly the required torque rating at a given speed, axial and radial stiffness of the bearings and maximum dynamic run out of the spindle. Based on these, three different spindle manufacturers were short-listed who manufacture products which met some of the specifications. These manufacturers were requested to run dynamic analysis of their spindles to evaluate the mandrel deflections with different over-hang lengths. The specifications for the UHS spindle that was finally chosen to be part of the system

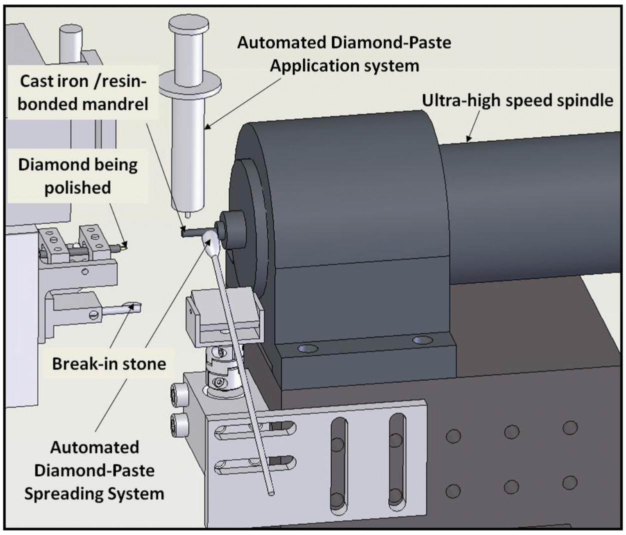

Figure 3.6: Mandrel-based polishing configuration for finish polishing.

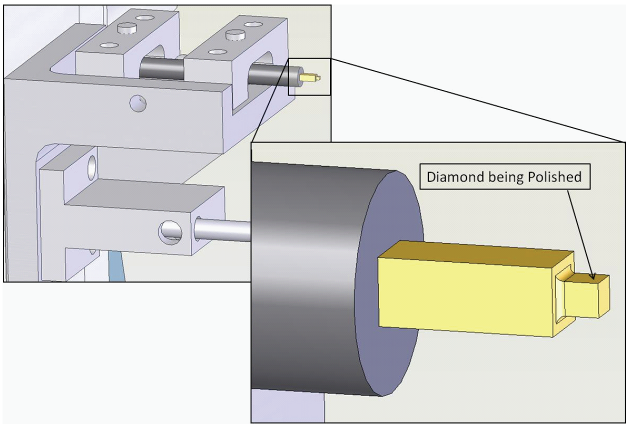

Figure 3.7: Closer view of the polished diamond.

design are given in Fig. 3.8. As can be seen, this spindle has significantly higher power and torque rating compared to the existing air-turbine spindle (peak power of 500 W compared to the existing peak power of 14 W). Hence it should be quite capable of reaching high speeds during polishing without slowing down. Another nice feature of this spindle is that it has hybrid-ceramic bearings which have a much higher axial and radial stiffness values compared to the air-bearing spindle that was part of the older setup. The support structure for the UHS spindle shown in Fig. 3.2 is made of solid cast-iron. This ensures rigidity of the mounting as well as provides sufficient damping of any vibrations from the spindle to the table.

Spindles' Specifications	
Rough Polishing	
Speed Range	1200 - 3400 rpm
Power	~ 1 hp
Mandrel-Based Polishing	
Speed Range	60, 000 - 160,000 rpm
Torque (S1-100%)	0.03 Nm
Power (S1-100%)	500 W
Radial Shaft Stiffness	25 N/micron
Axial Shaft Stiffness	17 N/micron

Figure 3.8: UHS spindle specifications.

3.4 Spindle for Rough Polishing

The basic torque and speed requirements for the traditional polishing spindle were first listed. The spindle that was finally used is one which is used in the diamond-tool making industry. Its power rating is 1 hp and it has an adjustable frequency inverter that allows adjusting the spindle speed from 1200 - 3600 rpm. The support frame for this spindle was designed with 80/20 structures. The frame was designed with many over-constraining pieces to ensure rigidity of the design.

3.5 Other Sub-systems

Another feature of the machine is to eliminate the need for manual intervention during polishing as much as possible. As mentioned in the previous chapter, there is a need to replenish the diamond particles on the mandrel frequently to ensure that effective polishing of the diamond will occur and this was done manually in the previous setup. To automate this process, both the diamond-paste release and spreading have been automated. This diamond-paste release from a syringe is automated by electronically controlling the opening/closing of a pneumatic valve which controls the air pressure to the back-side of the syringe. When the valve is opened, a set pressure is applied to the piston in the syringe which starts releasing the diamond-paste at a certain rate. Based on the pressure and time for which the valve is opened, the total quantity of paste released is controlled. For spreading the released paste evenly on the mandrel, a mini-motor with a swab attached to it is activated (Fig. 3.9). A +/-5 V pulse voltage to the motor provided a sweeping motion which distributes the paste on the mandrel. The speed of this motion can be controlled by the frequency of the pulse voltage.

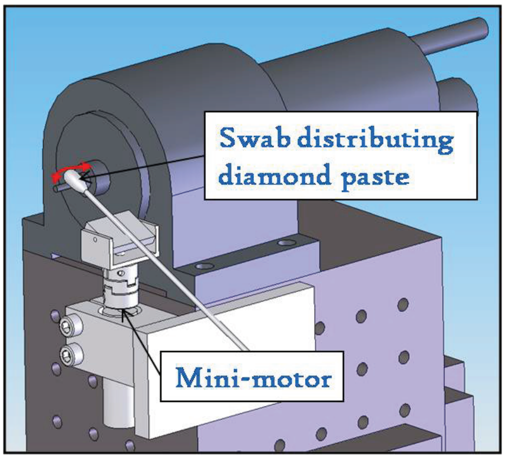

Figure 3.9: Paste spreading system.

3.6 Controller

The motion of the XYZ axes and the rotary platform is controlled by a 4-axis Delta Tau Controller. The X-, Y- and Z-stages have high-resolution encoders which provide position feedback from sensors mounted on the moving platform. The rotary is an open-loop stepper motor controlled platform. However, the controller ensures that the rotary platform is accurately positioned at either of the polishing stages using the signals from the high-precision limit switches.

Another feature of the machine design is the usage of the +/-10 V analog output from Delta Tau controller to drive either of the spindles. The frequency inverters of both the spindles allow speeds to be set using analog voltage inputs. Since only one of the spindles is active at any given point of time, speed setting of both the spindles can be controlled separately using a double-pole single-throw relay which is energized using the digital signals from the Delta Tau controller. The dual poles allow switching feedback signals also from any speed sensors mounted on the spindles, if closed-loop spindle speed control is desired.

Also, the opening/closing of the pneumatic valve for diamond-paste release and sweeping motion of the mini-motor are controlled by digital signals from the Delta Tau controller. Using a common timing base, the entire process can be automated to go between both polishing stages and do polishing independently at each stage without manual intervention.

3.7 Summary

This chapter presented the design and construction of a dual-stage polishing test-bed for fabricating micro-scale features on single-crystal diamond and ceramics. The new test-bed combines the advantages of both the traditional polishing and the mandrel-based polishing configurations by having the capability to remove material at a high rate and at the same time being able to create accurate and precise meso-and micro-scale geometries.

Many issues with the setup used in the previous chapter were identified. These issues have been addressed and overcome in the dual-polishing test-bed. The layout chosen makes the system design quite compact. The XYZ precision stages have superior performance specifications than the precision slides used in the previous setup. The rotary platform is quite rigid and provides a flat and stable base for the XYZ assembly.

The UHS spindle that is chosen has significantly higher power and torque capacity than the one used on the earlier setup and hence should be able to maintain the speeds during polishing. Also, due to the hybrid-ceramic bearings used, this spindle has much higher radial and axial stiffness than the air-bearing spindle used earlier. Also, the angle bracket for the XYZ assembly has been designed to ensure high-stiffness. Both these aspects of the design will ensure that the effective structural deflection is lower than what was seen in the earlier setup.

By having different sub-systems that work independently and by automating them using one controller, the polishing processes at both the stages can occur without any manual intervention. Overall, the test-bed can be used to automate the entire process of fabricating micro-scale features on single-crystal diamond and ceramics. Starting from a relatively large-sized roughly cut diamond to the finishing of meso- and micro-scale features with smooth surfaces and sharp edges- all of this can be accomplished in one single test-bed with almost complete automation.

The next chapter describes an experimental evaluation of various tool-grade ceramics to assess their applicability for micro-scale cutting. The qualitative and quantitative evaluation that is presented allows in understanding the polishing characteristics of tool-grade ceramic materials under conservative conditions.

Chapter 4

Evaluation of Tool-grade Ceramics for Micro-scale Cutting

4.1 Motivation

For any tool-grade ceramic to be used for micro-scale cutting, one of the most important requirements is the creation of uniform un-serrated cutting edges with sharp edge radii and smooth surfaces (rake faces for lower friction). This capability is related to the ability to create smooth surfaces and sharp, high-quality cutting edges on ceramic materials, including the ability of the tool-fabrication process to minimize edge-rounding/edge-chipping and maximize surface smoothness. While the tool-fabrication process is dependent on various process parameters, the edge and surface quality of the fabricated tools are hypothesized to be directly related to the (1) the size and shape of the different phases that form the ceramic composite and the binding strength between them, (2) the mechanical properties-transverse rupture strength and fracture toughness-of the ceramic composite, which quantify the ease of brittle fracture and the propagation of cracks within the material, and (3) the processing technique used during fabrication of the ceramic composite, which governs the density of packing of the different phases and the porosity of the ceramic.

The aim of this work is to assess the potential of tool-grade ceramics as tool material for micro-scale cutting operations. This is done by an edge/surface quality-based evaluation of various tool-grade ceramics. Sharp (cutting) edges are created by lapping two adjacent surfaces of various tool materials using a two-stage lapping process under conservative conditions. The surface roughness of the lapped faces and the edge sharpness of the created edges are measured using white-light in-

	Composition	Label
Alumina-based	99.9% Al_2O_3	A
	Al_2O_3 + TiC	B
	Al_2O_3 + TiC+TiN	C
	SiC whisker-reinforced Al_2O_3	D
Silicon Nitride-based	Si_3N_4+Er_2O_3+SiO_2	E
	Sialon	F
Sub-micron grade Carbide	WC + Co	G

Figure 4.1: Composition of the materials evaluated.

terferometry (WLI) and atomic force microscopy (AFM), respectively. Lapped surfaces are further examined using an environmental scanning electron microscope (ESEM) to examine the existence of voids and edge serrations.

4.2 Tool-grade Ceramics Evaluated

Tool-grade ceramics can be categorized under (i) monolithic forms of ceramics and ceramic composites, (ii) ceramic thin coatings and (iii) whisker-reinforced ceramic composites. The materials that have been evaluated are limited to monolithic forms and whisker-reinforced composites. Within both categories, the materials can be broadly classified relative to their base material matrix: Alumina-based and Silicon Nitride-based. Alumina-based cutting tools consistently have higher chemical inertness whereas the silicon-nitride based cutting tools have a greater strength and fracture toughness. To span the wide variety of ceramic tool materials, five different commercially available tool-grade ceramics were chosen for this study. As a reference, sub-micron grade tungsten carbide with cobalt binder and 99.9% pure alumina were also studied. The materials chosen and their respective composition are listed in Fig. 4.1.

4.3 Experimental Procedure

All the materials were first diced into small blocks with rough dimensions of 3 mm x 4 mm x 3 mm using a diamond saw. Each block was mounted and cured in an epoxy resin system. The cured epoxy, with the block encased inside, was cut to dimensions of approximately 10 mm x 10 mm x 5 mm to make a sample for lapping. The 10 mm x 10 mm face closest to the block surface was first lapped on a lapping machine using a certain lapping recipe. Then the sample was removed and cleaned in an ultrasonic cleaner for 30 minutes with a 50-50 mixture of acetone and DI water. The lapped surface on the block was then analyzed by first measuring the surface roughness using a WYKO NT3300 WLI and then imaging the surface using a Quanta 600 ESEM.

After analysis, a piece of cured epoxy (cut to size and shape close to the sample's dimensions) was glued to the back surface of the sample parallel to the lapped front surface, to increase the sample's thickness. This glued assembly was diced perpendicular to the lapped surface to a thickness of approximately 5 mm such that another surface of the block was barely exposed. The sample was remounted and this surface was now lapped using the same lapping recipe as the first surface.

The material block encased in the epoxy now has two adjacent surfaces lapped and a sharp edge formed at the intersection of the two surfaces. The sample was now removed and ultrasonically cleaned as before. Then the second surface's roughness was measured using the WLI. The second surface and the edge were imaged using the ESEM. Further, the sharpness of the created edge was measured using a Nanoscope Dimension 3100 AFM.

4.4 Lapping Process

Figure 4.2 shows the Logitech PM5 Precision Lapping and Polishing machine that is used for lapping of all the materials. The lapping machine consists of a spindle on which different types of ϕ12-inch lapping plates can be mounted.

The lapping recipe used to lap both faces of each material includes two stages- (1) rough-lapping with 9 μm calcined alumina powder suspended in DI water followed by (2) finish-lapping with 0.02 μm colloidal silica solution. A cast-iron lapping plate is used for rough lapping and a polyurethane padded lapping plate is used for finish lapping. The machine has different reservoirs for the two different types of abrasive slurries and different flow channels made near the reservoirs that allow the abrasive slurries to drip onto the lapping plate. Drip rates of both the alumina and silica solutions were kept constant during lapping of all materials such that there is a visibly similar concentration of the slurry on the surface of the plate.

Before rough-lapping the sample, the cast-iron plate is first conditioned using a conditioner with radial grooves. The conditioning is done at a spindle speed of 70 rpm for approximately 20

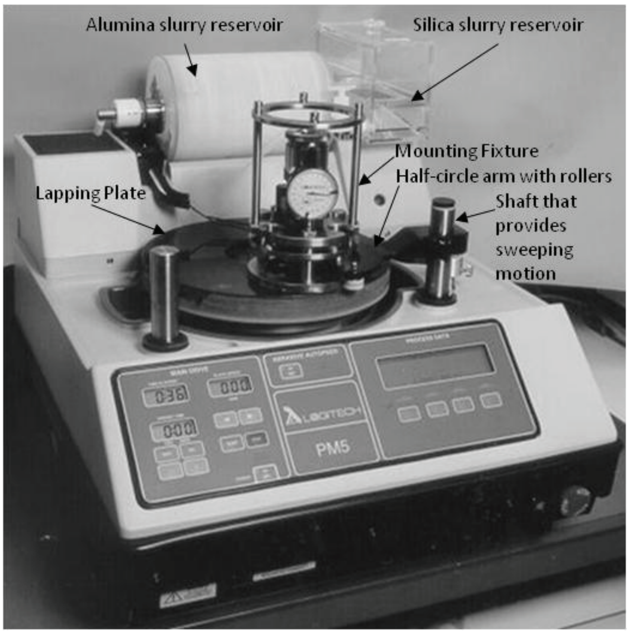

Figure 4.2: Precision lapping and polishing machine.

minutes. The conditioner with a loading weight is placed within a half-circle shaped arm with rollers on it. This arm is mounted on a shaft that can provide a sweeping motion to move the conditioner back-and-forth across the plate to ensure uniform conditioning across the surface of the plate. For finish-lapping, the cast-iron plate is replaced with the polyurethane-padded plate. A conditioner with a different surface structure is used and conditioning of this plate is done at a spindle speed of 35 rpm for approximately 10 minutes.

The sample to be lapped is mounted on a ϕ3-inch glass plate using molten wax. The glass plate with the sample is vacuum-mounted on a mounting fixture. The fixture has a spring inside, whose preload can be adjusted to provide a constant load on the sample during lapping. It also has a reference flat annular surface that comes into contact with the lapping plate surface during the lapping process. The fixture is designed to fit against the rollers of the half-circle shaped roller arm.

For rough-lapping, the sweeping motion of the roller arm is turned off and the roller arm is positioned such that the fixture is centered on the lapping surface of the cast-iron plate. The sweeping motion is kept on for finish-lapping. When the lapping plate rotates at a set speed, due to the friction between the flat annular surface on the fixture and the abrasive-laden plate, the mounting fixture rotates between the rollers on the half-circle arm, thus randomizing the lapping process-kinematics. This prevents a fixed pattern of scratch marks from occurring on the lapped surface and ensures a more uniform polish throughout the sample surface thus improving the surface finish. On each surface, rough lapping is done for 1 hour after the entire surface of the sample is lapped flat and finish lapping is done for 75 minutes.

4.5 Results and Discussion

4.5.1 Scanning Electron Microscope Images

The ESEM images of the different lapped surfaces are shown in Fig. 4.3. All the scanning electron microscope images were taken in the Low Vac mode of the ESEM which allowed the samples to be imaged without depositing a conductive coating. None of the lapped surfaces show the presence of any scratches induced due to lapping. This provides evidence that the lapping process was well randomized in direction and also validates the assumption that under the conservative lapping conditions used, the process was close to ideal for creating flat lapped surfaces.

These images show the presence of various phases in each material. In a few materials (C, F), the packing of the various phases is such that there are no visible voids at the scale shown. However, voids can be observed on the lapped surfaces in the case of a few ceramics (A, D). Sample A (99.9% Al_2O_3) does not have a binder phase and is formed by hot isostatic-pressing (HIPing), as stated by the manufacturer, which is supposed to provide a bulk density close to the theoretical density of alumina. However, this final processing still allows the formation of voids at the intersection of certain grains. Sample D (whisker-reinforced ceramic) also shows voids which might be related to the processing technique used during its fabrication.

As mentioned earlier, edges are created by lapping two adjacent faces on each material. The edge length is about 3-4 mm. Figure 4.4 shows the ESEM images of the edges at a certain location along the edge which is representative of the general characteristic observed for that material.

Note that in all the materials, at the scale shown, the lapping process did not cause grains of any phase of the material to be pulled out and that the grains on the edge have been lapped from both sides. Further, the different phases can be more clearly observed than on the surfaces, since these images give a three-dimensional perspective.

The voids seen on the surface of ceramics A and D show as gaps on the edge. This may not be beneficial for micro-scale cutting since these gaps act as cracks at the micro-scale. This can cause a higher stress at the base of the grains that are physically active in the cutting process and hence lead to fracture of the edge. Furthermore, poor edge quality will also result in reduced machined

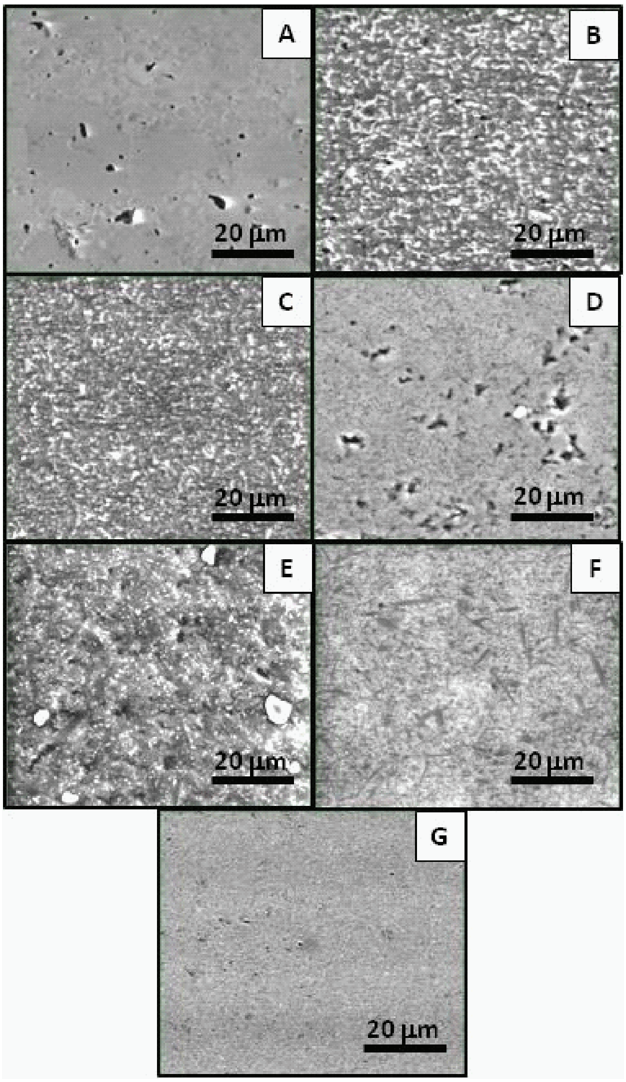

Figure 4.3: Examination of lapped surfaces using ESEM.

surface quality.

The sharpness of the edges can be qualitatively discerned as the thickness of an imaginary line that is drawn to define the edge. Qualitatively it can hypothesized that SiN based ceramics (E and F) have the sharpest edges and also that the edge of the sub-micron grade carbide (G) is rounded and does not seem to be as sharp as some of the ceramics.

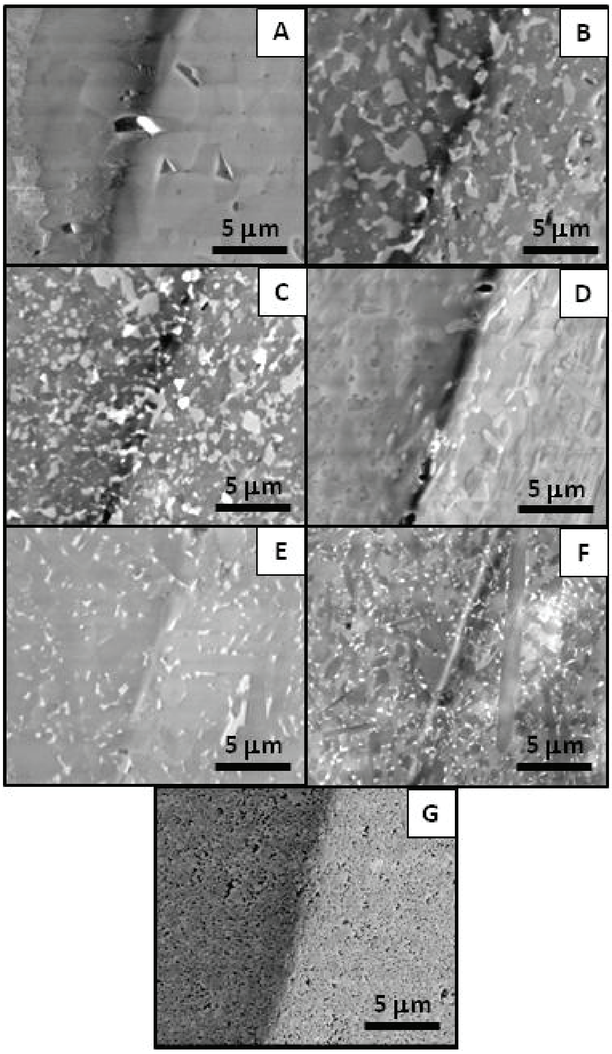

Figure 4.4: Examination of edges using ESEM.

4.5.2 Surface Roughness

In order to quantify the large-area and small-area surface characteristics, the surface roughness of the lapped surfaces was measured for two different sizes of sampling areas. The sizes of the large and small sampling areas were 237 μm x 181 μm and 61 μm x 46 μm respectively. For each size, ten sample areas were measured spanning the entire lapped region. Depending on the measured roughness, the appropriate scanning mode (PSI/VSI) was used to record the data.

The cylindricity and tilt errors in the data were removed by post-processing and the average and root-mean squared roughness parameters, Ra and Rq respectively, were calculated for each sampling area. The average and standard deviation of Ra and the root-mean-squared average

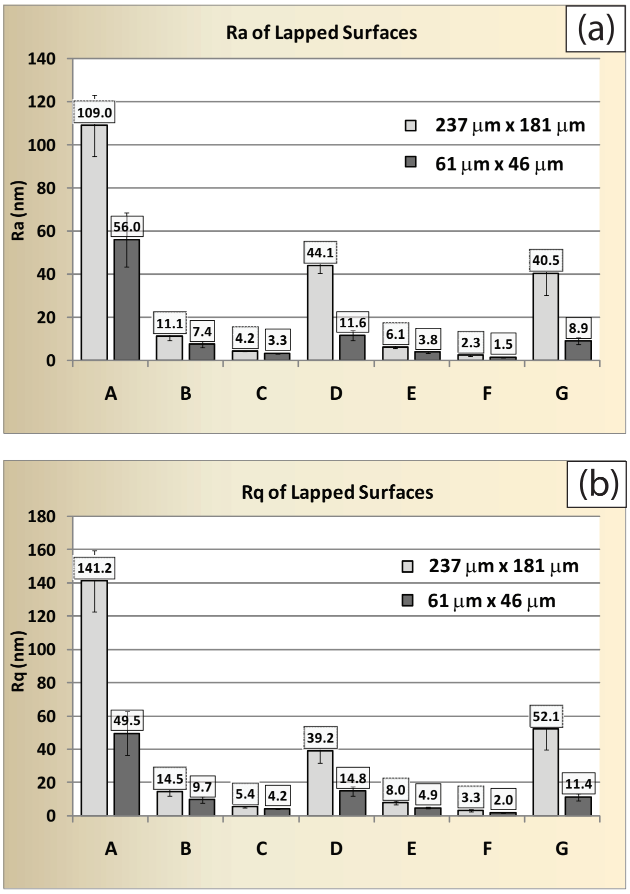

Figure 4.5: Surface Roughness: (a) R_a, (b) R_q.

and standard deviation of Rq across the ten sample areas and the two lapped surfaces for a given material are calculated. These values are used to compare the roughness on various materials.

Figures 4.5(a) and 4.5(b) show the plot of the average Ra and the root-mean-squared average Rq respectively for both the sampling areas. The error bars represent $\pm$ one standard deviation of the respective parameter. Except for the materials A, D and G, all the other materials have large-area and small-area Ra less than 12 nm.

For materials A, D and G, there is a large difference between the large-area roughness and small-area roughness. Materials A and D are known to have voids, as seen in the images of their surfaces. The significant increase in the roughness parameters at the larger scale could be directly related to the presence of a greater number of voids in the larger sampling area. However, in the case of G, the large difference may be attributed to the presence of residual form errors after cylindricity and tilt removal.

Using a two-sample t-test for unequal variances, different pairs of materials are tested for the difference in Ra and Rq. Based on this analysis, for the large-area roughness, the following statistically significant inequalities can be established.

$$Ra\text{: F} < \text{C} < \text{E} < \text{B} < \text{G} \approx \text{D} < \text{A}$$

$$Rq\text{: F} < \text{C} < \text{E} < \text{B} < \text{D} < \text{G} < \text{A}$$

For the small-area roughness, the statistically significant inequalities are:

$$Ra\text{: F} < \text{C} < \text{E} < \text{B} < \text{G} < \text{D} < \text{A}$$

$$Rq\text{: F} < \text{C} < \text{E} < \text{B} < \text{G} < \text{D} < \text{A}$$

From a point of view of surface roughness, it can be concluded that except for SiC whisker-reinforced Al_2O_3 (D), all the other ceramic materials tested are better than sub-micron grade tungsten carbide (G) and alumina (A). Further, the silicon-nitride based ceramic SiAlON (F), and alumina-based ceramic (Al_2O_3+TiC+TiN) (C) have small-area and large-area Ra less than 5 nm, which would make them the most favorable ceramic tool materials for micro-scale cutting.

4.5.3 Edge Radius

The edge length on all the materials ranged from 3-4 mm. Through the AFM microscope, the edge to be scanned was first aligned perpendicular to the cantilever tip. The scanning direction was set to be perpendicular to the edge. The edge profile was scanned in the contact-mode of the AFM. Four to seven different locations along the edge are scanned with up to twenty five different scans around each location to ensure local repeatability. The scan lengths used ranged from 5 μm to 10 μm.

Algorithms have been developed in literature [106] to characterize the edge radius. In this work, for each edge profile, edge radius was determined using two methods. Both methods fit straight lines on either side of the edge and a circle to the edge through least squares minimization. In either method, the data used for each of the fits is varied by changing the locations corresponding to the transition from circle to straight line on both sides. A range of locations are searched on either side, to find the transition locations which minimize the sum total of the normalized residual errors of the straight line and circle fits. The radius of the fitted circle in this case is defined as the edge radius.

The main difference between the two methods is that in the first method, there is no specific relation between the straight lines and the circle, whereas in the second method, the straight lines

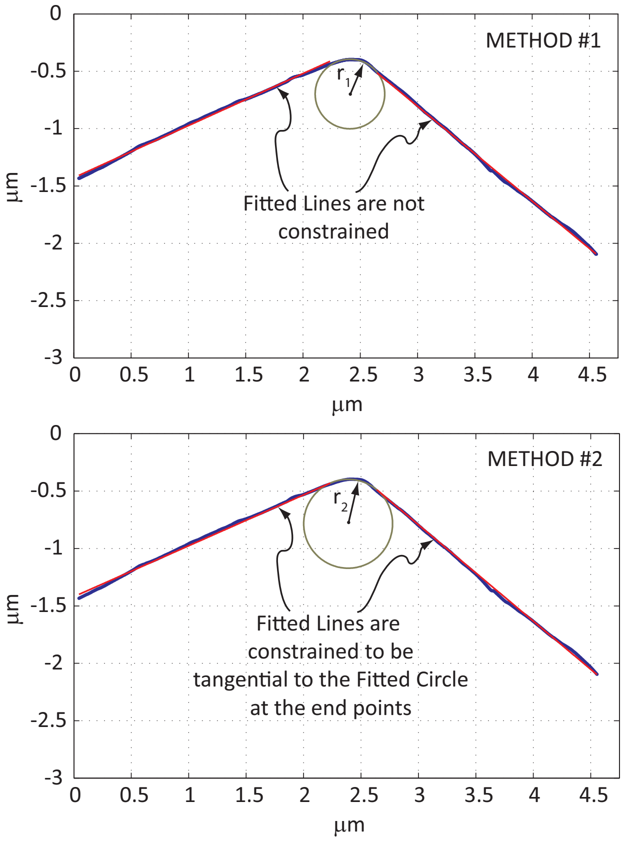

Figure 4.6: Methods to estimate edge radius.

are constrained to be tangential to the circle at their end points. Figures 4.6(a) and 4.6(b) illustrate the application of these methods respectively to find the edge radius.

Figure 4.7 shows the average edge radii of the various materials determined using the above methods. The error bars represent ± one standard deviation. The difference between the two methods is within a maximum of 0.2 μm.

All the lapped materials have an edge radius of less than 3.5 μm. In the case of SiC whisker-reinforced Al_2O_3 (D), the standard deviation across the different locations was 0.6 μm, which is at least double of what is observed on the other materials. This could be related to the fact that scans at locations where silicon-carbide whiskers are present could be significantly different from those on base material matrix due to the differences in their morphology.

Using a two-sample t-test for unequal variances, different pairs of materials are tested for the difference in their edge radii calculated using both methods. The following statistically significant inequalities can be established for the radii calculated using both methods.

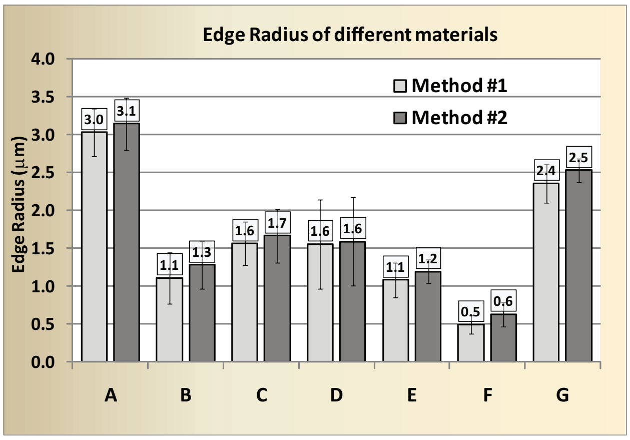

Figure 4.7: Edge radius of different materials.

Edge Radius: F $<$ E $\approx$ B $\approx$ D $\approx$ C $<$ G $<$ A

Based on this data, SiAlON (F) is the most sharpenable material. It has a radius of approximately 0.5 μm with low variability across different locations on the edge. The other four tool-grade ceramics have edge radii less than 2 μm and are all statistically similar. The edge radii of all tool-grade ceramics are less than that of sub-micron grade carbide (G) and 99.9% alumina (A).

4.5.4 Summary

The sharpenability and smoothability of five different tool-grade ceramic materials, sub-micron grade tungsten carbide and 99.9% pure alumina was evaluated. A dual-stage lapping process under conservative conditions is used to lap two adjacent faces and create an edge to evaluate these materials. In SiAlON (F) and (Al_2O_3+TiC+TiN) (C) the packing of the various phases was observed to be very dense with no visible voids. However, voids were seen on the lapped surfaces of pure alumina and SiC whisker-reinforced Al_2O_3 (D). These were believed to be present due to the processing technique used during their fabrication. In all the materials, the lapping process does not cause grains of any phase of the material to be pulled out and it was observed that the grains on the edge were lapped from both sides. The voids seen on the surfaces show as gaps on the edge.

Except for SiC whisker-reinforced Al_2O_3 (D), all the other ceramic materials tested had a better surface roughness than sub-micron grade WC+Co (G) and pure alumina (A). Also these materials had large-area and small-area *Ra* less than 12 nm. SiAlON (F) and (Al_2O_3+TiC+TiN) (C) have small-area and large-area *Ra* less than 5 nm.

Edge radius was measured using two different methods. The results from both the methods were quite similar. All ceramic materials have edge radii less than 2 μm, which is less than the edge radii of sub-micron grade WC+Co (G) and pure alumina (A).

The next set of chapters are devoted to development of spindle-metrology techniques for UHS spindles and analysis of the UHS spindle used for mandrel-based polishing. Chapter 5 describes the development of an LDV-based spindle-metrology technique to measure the speed-dependent axial and radial error motions of miniature UHS spindles. Chapter 6 utilizes the developed technique to analyze the axial and radial motions of the specific UHS spindle used on the dual-stage polishing test-bed. Chapter 7 describes further advancement of the metrology technique by implementing error-separation methods to remove the artifact form error and quantify the true spindle error motions.

Chapter 5

An LDV-based Methodology for Measuring Axial and Radial Error Motions when using Miniature Ultra-High-Speed (UHS) Micromachining Spindles

5.1 Introduction

As mentioned in Chapter 2, one of the most important factors governing the effectiveness of the mandrel-based polishing process in creating accurate features is the speed-dependent axial and radial error motions of the UHS spindle. The undesired motions of the UHS spindle have a direct influence on the dimensional and form accuracy as well as the surface finish of the polished surfaces. A thorough quantitative analysis of these motions for the specific UHS spindle used on the dual-stage polishing test-bed is essential to understand their influence on the polishing characteristics. However, there is no existing metrology technique to quantify the error motions of UHS spindles.

Measurement and characterization of error motions of ultra-precision spindles used in precision machining have been the subject of many works in the literature, e.g., [107–113]. Two international standards [114, 115] have been published for characterization of axes of rotation. These standards define the concept of error motions (of the axis of rotation, of the spindle and of the structural loop), outline the test procedures for their measurement, and describe the measurement configurations and measurement artifacts. Most of the works in the literature share certain basic measurement concepts (to measure error motions) that include the use of non-contact displacement sensors to measure displacements from the surface of a precision artifact mounted on the spindle, e.g., [107], or from the surface of the stator of a master axis of rotation [110], and then eliminate the artifact roundness/master axis errors from the data to calculate the true error motions of the spindle. The shape of the precision artifact is either a simple high-precision cylinder [114, 115], or, more commonly, a sphere-on-stem that has a cylindrical stem with one or two spherical targets [114, 115]. Although majority of research was conducted when the spindle rotated at very low speeds (sometimes manually), some works considered the measurement of spindle vibrations from the surface of a rotating tool blank at higher rotational speeds (up to 24 krpm) [116–118]. In addition to commonly used non-contact capacitive sensors, e.g., in [107, 110, 111], various other instruments using non-contact optical sensors have also been proposed and developed to measure the error motions of spindles [109, 119–124]. LDVs [116–118] have also been used for measuring tool vibrations from a milling spindle.

Although well-established for large sized precision spindles and for relatively low rotational speeds, measurement of error motions of UHS miniature spindle poses various challenges. *First*, most UHS miniature spindles can only accommodate tool shanks with 3 mm (or 0.125 in.) diameter, and thus, available sphere-on-stem artifacts used in measuring error motions of larger spindles cannot be utilized. The need for small precision artifacts imposes limitations to displacement-measurement sensors by increasing the curvature errors and sensor nonlinearities. For instance, the capacitive measurements (even with the smallest sensor sizes available) would induce relatively large measurement errors [125,126] when measuring from a 3 mm spherical target. *Second*, UHS spindles cannot be operated at near-zero speeds. The ultra-high-speed operation and miniature size of the UHS spindles could result in increased dynamic effects, and thus, considerably change the nature and magnitude of the error motions with speed. For this reason, measurement instrumentation should possess sufficient bandwidth (greater than 30 kHz) to enable measurement of high frequency motions from the surface of a rotating artifact. And *third*, a majority of UHS miniature spindles do not have a built-in tachometer or encoder, which is required for accurate angular synchronization of data from successive revolutions in the presence of spindle speed fluctuations.

To address some of the aforementioned challenges, we recently developed an LDV-based methodology to measure radial and tilt error motions when using UHS miniature spindles [127]. The methodology uses a precision cylindrical artifact, and enables determining the radial and tilt error motions when using a UHS spindle through radial motion measurements in two mutually-orthogonal directions from two axial locations of the artifact. The measurements are conducted with the LDV sensor heads mounted on a metrology frame with no significant resonant frequencies above 800 Hz. The advantages of this approach include a high measurement bandwidth, good measurement accuracy, and the use of small precision artifacts. Despite the fact that the effectiveness of LDV-based spindle-error measurements of UHS spindles was proven, the methodology was only applicable to measuring error motions in radial directions, i.e., the use of cylindrical artifact did not allow measurement of axial error motions. In addition, relatively large uncertainties (as compared to the measured error motions) were contributed from the large out-of-roundness of the precision artifact (a Class-XX gage pin), and from the compounded effects of laser misalignments and curvature.

Significant improvements that have been realized compared to our previous work by (i) incorporating the *axial measurement capability*, (ii) developing a new *three-dimensional* precision laser-beam alignment technique, (iii) incorporating a method to determine the absolute angular (rotation) position, and (iv) reducing the uncertainties (through the use of a custom fabricated sphere-on-stem artifact, better laser-beam alignment, and improved data processing). Although the uncertainty in the measurement of error motions is significantly reduced by using a high-precision artifact, in this work, artifact form errors are still considered as a source of measurement uncertainty and no attempt is made to separate the form errors to obtain the true error motions.

This chapter presents the enhanced LDV-based methodology for measurement of axial and radial error motions when using miniature UHS spindles used for micromachining applications. The new methodology measures three-dimensional displacements from the surface of a custom-fabricated sphere-on-stem precision artifact using three mutually-orthogonal laser beams. A precision alignment technique is developed to configure the three laser beams mutually orthogonal to one another. An infra-red sensor is used to provide a reference for the rotational angle of the spindle. The axial and radial motion data measured at operational speeds is then post-processed to obtain the synchronous and asynchronous components of the error motions in both directions. The presented approach enables obtaining error motions along both fixed-sensitive and rotating-sensitive directions. The methodology is then demonstrated by measuring axial and radial error motions when using a miniature UHS spindle at four different speeds. Analysis of the measured data indicated the significant effect of spindle speed on the error motions along both fixed-sensitive and the rotating-sensitive directions. Finally, an uncertainty analysis is presented to quantify the overall combined uncertainty on the error measurements when using the new methodology.

5.2 Background

Ideally, when rotated on a spindle, the tool-tip trajectory (e.g., of a micro-endmill) should be circular—with a diameter equal to that of the tool diameter—in a plane perpendicular to the coinciding tool and rotational axes. However, the actual tool-tip trajectory deviates from the ideal (nominal) trajectory along the radial and axial directions due to (1) tool-spindle centering errors (i.e., eccentricity and tilt arising from the attachment of the tool to the spindle), (2) tool-profile errors (i.e., misalignment of tool-tip with respect to the tool-shank axis), (3) spindle error motions (radial, axial, and tilt, as defined in [114]), which are the axis of rotation error motions due to bearing error motions and the noise and vibration from within the spindle, and (4) structural vibrations of the structure supporting the spindle. These axial and radial motions of the tool tip could significantly affect the dimensional accuracy, surface quality, and form accuracy of micromachined features. The deviations of the tool tip from the ideal trajectory are sometimes referred to as the tool-tip *runout*. Based on the standards [114, 115], the definition of runout (or equivalently the total indicator reading (TIR)) is limited to a single value representing the peak-to-peak amplitude of the motions sensed by an indicator during one or more revolutions of the spindle. An analysis of the motions of the tool-tip (except tool-profile errors) is best conducted through the measurement of axial and radial motions from the surface of a precision artifact.

A *perfect* spindle is described in the standards [114,115] as one that "has no motion of its axis of rotation with respect to a reference coordinate axes". Based on these standards, *error motion* refers to any motion, relative to the reference coordinate axes, of the surface of a geometrically "perfect" artifact*, with the artifact centerline coincident with the axis of rotation. The main sources of the error motions are (a) *spindle error motions*, which are error motions measured from the spindle stator to the spindle rotor and (b) *structural error motions*, which are the error motions measured from the stator to the displacement measurement sensor.

To describe these error motions, first an *axis average line* is defined as the average location of the axis of rotation over one or more revolutions. An XYZ cartesian reference frame is set up such that the Z axis coincides with the axis average line. Error motions perpendicular to the Z axis (i.e., motions projected to the $X-Y$ plane) are defined as radial error motions and those along the Z axis are defined as the axial error motions.

To describe the tool-tip trajectory, we will refer to the schematic illustration given in Fig. 5.1. The ideal trajectory (T_I) is traced when a "perfect" tool (i.e., one that has no tool-profile errors) is

*Geometrically perfect artifact is a rigid body having a perfect surface of revolution about a centerline.

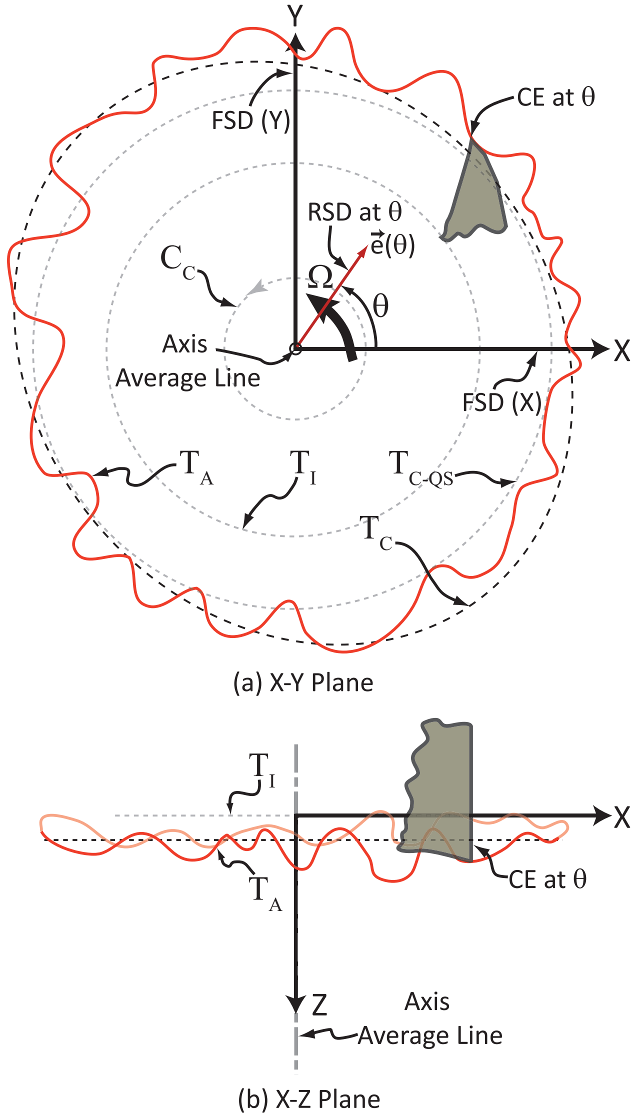

Figure 5.1: Depiction of Ideal and Actual cutting edge trajectories. CE: Cutting Edge; FSD: Fixed-Sensitive Direction; RSD: Rotating-Sensitive Direction; T_I: Ideal tool trajectory; C_C: Tool-axis trajectory due to centering errors from a quasi-static perspective; T_{C-QS}: Tool trajectory due to centering errors from a quasi-static perspective; T_C: Tool trajectory with only centering errors (quasi-static and dynamic effects included); T_A: Actual tool trajectory

attached (with no attachment errors) on a perfect spindle with its geometric axis coincident with the axis average line. The trajectory T_I is circular in the $X-Y$ plane with a diameter equal to the tool diameter.

When the perfect tool is attached to a perfect spindle through a collet, the inaccuracy in attachment can radially displace and/or tilt the geometric axis of the tool with respect to the axis of rotation. These errors in attachment are referred to as the *centering errors.* From a quasi-static perspective, the centering errors cause the tool axis to rotate orbitally about the axis average line in a circular path (C_C) on the $X - Y$ plane, resulting in a circular tool-tip trajectory (T_{C-QS}) with a diameter larger than the diameter of the tool. From a dynamic perspective, however, the eccentricity (rotating unbalance) caused by the centering errors alters the tool-tip trajectory further. A circular tool-tip trajectory (yet, with a larger diameter than that of the quasi-static one) can only be attained when the radial stiffness of the spindle is distributed in a uniform axisymmetric fashion. In reality, however, the radial stiffness of the spindle, the housing, the collet and the tool are non-uniform, causing the tool-tip trajectory to differ from a circular one. For instance, considering the stiffness variations in two principal directions, the axis of rotation rotates orbitally about the axis average line, resulting in an elliptical tool-tip trajectory, whose major and minor axes are aligned with the principal axes. A sample trajectory for the case with only the centering errors, including both the quasi-static and dynamic effects, is indicated as T_C in Fig. 5.1(a). It should be noted that the effect of the tool-profile errors of the actual (imperfect) tool can be accounted for in a manner similar to that of the quasi-static perspective of the centering errors.

In addition to the centering errors, the actual tool-tip trajectory, T_A, includes the tool-profile errors of the actual tool, the spindle error motions and structural vibrations of the structure supporting the spindle arising from the spindle operation. The trajectory T_A is shown for only one revolution of the spindle. If the motions of the tool tip include only the rotational frequency (i.e., the *fundamental frequency*) and its harmonics, the same trajectory would repeat every revolution. However, due to the non-harmonic components of the tool tip motions, the trajectory deviates from one revolution to another both radially and axially.

The tip of a milling tool as it moves along the actual trajectory during rotation is shown in Fig. 5.1 at a rotation angle $\theta = \Omega t$, where Ω is the rotational frequency corresponding to the nominal spindle speed. This rotation angle is defined based on a unit radial vector ($\vec{e}(\theta)$) that rotates at the nominal spindle speed. Without the loss of generality, $\vec{e}(\theta)$ can be defined to be aligned with the X axis at the rotational orientation corresponding to $\theta = 0$.

For processes such as turning, where the tool tip is stationary and the workpiece rotates, characterizing the error motions along a *fixed-sensitive direction* is sufficient. For rotating-tool processes such as micromilling, however, the interest is the undesired motions of the cutting edge relative to the ideal trajectory at a given angular location: The direction of interest is referred to as the *rotating-sensitive direction.* Referring to Fig. 5.1(a), measurements conducted along X- and Y- directions (with a stationary sensor) are fixed-sensitive, and the measurement along the unit radial vector, $\vec{e}(\theta)$, is rotating-sensitive. An accepted method of measuring motions along the rotating-sensitive radial direction is to conduct simultaneous radial motion measurements along two orthogonal fixed-sensitive radial directions, and then project these motions onto $\vec{e}(\theta)$ [114,115]. This method will be adopted in this work.

In addition to the above sources, the measured axial and radial motions include the form (error) of the artifact. When the artifact is mounted without any centering errors and rotated on a "perfect" axis of rotation, its form around the circumference will be measured at frequencies that repeat every revolution along a fixed-sensitive radial direction. In general, the artifact's form can be expressed as

$$S(\theta) = \sum_{i=1}^{n} A_i sin(i\theta + \phi_i), \tag{5.1}$$

where θ is the angle around the circumference or the rotation angle, n is the number of harmonics contributing to the shape and ϕ_i is the phase of the i^{th} harmonic relative to an arbitrary reference. Furthermore, in the presence of centering errors, the artifact form errors will also be measured along the axial direction.

The measured axial and radial motions can be analyzed by separating them based on their frequency content. In the $X-Y$ plane, the fixed-sensitive radial motions measured at the fundamental (spindle) frequency (i.e., the once-per-revolution, or once-per-rev, component) arise from (a) the centering errors, (b) the fundamental component of the artifact form errors (i.e., with $i = 1$ in Eq. (5.1)), and (c) the structural error motions from the spindle stator to the LDV sensor head due to vibrations at the fundamental frequency. The radial motions that occur at the harmonics of the fundamental frequency (referred to as the synchronous frequencies) include (a) the radial *spindle* error motions at synchronous frequencies, (b) the radial *structural* error motions at synchronous frequencies, (c) the artifact form errors other than the once-per-revolution component, and (d) the radial motions due to the curvature effects. In this work, these motions are referred to as the *synchronous radial error motions* since the curvature effects are removed and the artifact form error is separately considered as a source of measurement uncertainty. The frequencies other than the fundamental frequency and its harmonics are referred to as the asynchronous frequencies. In this thesis, the radial motions that occur at the asynchronous frequencies are considered as the *asynchronous radial error motions*. Asynchronous radial error motions mainly arise from the radial spindle error motions at asynchronous frequencies (which are composed of asynchronous bearing error motions and the noise and vibrations from within the spindle with respect to its stator in the radial direction), and the radial structural error motions at asynchronous frequencies. The structural vibrations of the frame at the asynchronous frequencies that are included in those motions are considered as motion measurement uncertainties, which are quantified separately.

For the axial motions, the axial components of the spindle error motions and structural error motions both contribute to the motions that occur (and measured) at the fundamental frequency and its multiples (harmonics). In addition, due to the centering errors, the artifact form errors contribute to the motions that occur at the fundamental frequency and its multiples. In this thesis, the entire axial motions that occur at the fundamental frequency and its multiples are referred to as the *synchronous axial error motions*. The artifact form's contribution included in this measurement is considered to be a source of measurement uncertainty, which is quantified separately. The motions at the fundamental frequency are referred to as the *fundamental axial error motions* and the motions at harmonics of the fundamental frequency are referred to as the *residual synchronous axial error motions*. Similar to the radial error motions, axial motions at the asynchronous frequencies are referred to as the *asynchronous axial error motions* with a measurement uncertainty due to the axial structural vibrations of the frame at the asynchronous frequencies. Asynchronous axial error motions are composed of asynchronous axial spindle error motions and asynchronous axial structural error motions.

The range of synchronous error motions is quantified by a *synchronous error motion value*, which is defined as the difference between the maximum and minimum synchronous error motions within a full revolution. For the radial error motions, this value is equivalent to calculation of the difference in radii between two concentric circles, centered at the least-squares circle center, that are just sufficient to contain the entire synchronous radial error motions. For the axial error motions, this value is equivalent to calculation of the difference in radii between two concentric circles, centered at the polar-chart center, that are just sufficient to contain the entire synchronous axial error motions.

Typically, as per the standards [114, 115] the range of asynchronous error motions is quantified by an *asynchronous error motion value*, which is defined as "the maximum scaled width of the asynchronous error motion polar plot, measured along a radial line through the polar chart center." However, this metric is susceptible to outliers in the data and can overestimate the range. When the asynchronous error motions have a *normal* distribution, the standard deviation (σ) can be used as an alternative measure for the axial error motions in lieu of the maximum scaled width [111]. In this case, the 6σ band centered around zero provides a more robust estimate of the range of asynchronous error motions by containing 99.7% of the motion values. Since the asynchronous

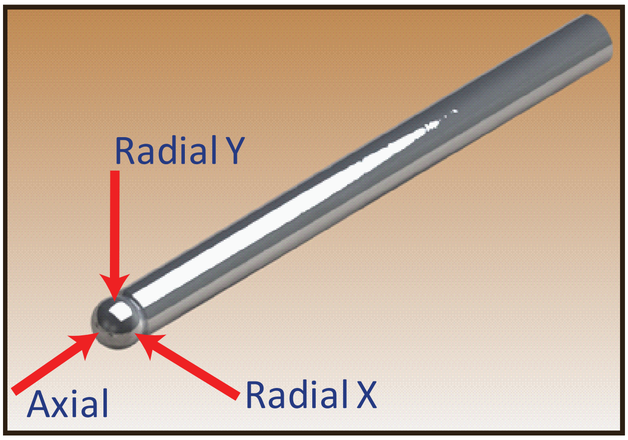

Figure 5.2: A model of the 3 mm (or 0.125 in.) diameter sphere-on-stem precision artifact fabricated to conduct the axial and radial motion measurements.

error motions are normally distributed for the spindle that was tested, we will use the standard deviation of the asynchronous error motions measured across multiple revolutions as the metric to obtain an overall assessment of the asynchronous error motions.

5.3 Measurement Methodology

In this section, we describe the technique developed for measuring axial and radial motions, including the data processing steps to determine the radial and axial error motions. The procedure is described by considering "ideal properties", such as perfect alignment of lasers and perfect artifact geometry. The *uncertainties* arising from the measurement equipment and procedure are then quantified thoroughly in Section 5.5.

As described above, simultaneous measurement of the axial and radial motions necessitate use of a sphere-on-stem type precision artifact. Since small precision artifacts are not available commercially, we fabricated a sphere-on-stem precision artifact (see Fig. 5.2) by assembling (using a high-strength glue) a Grade 3 hardened steel sphere to the end of a stem (a Class-XX gage pin). By rotating the artifact on an UHS spindle, and comparing the peak-to-peak radial motion amplitude measured from the sphere to that measured from the stem (at a position about 1 mm from its end), an (upper-bound) estimate of the relative eccentricity is obtained to be approximately 1 μm. It should be noted that the dominant effect of this eccentricity is revealed in the measurements as a component at the fundamental frequency, and thus, will be removed and will not effect the error calculations.

5.3.1 Measurement Setup

The configuration of the LDV-based three-dimensional error measurement setup for measuring radial and axial motions is illustrated in Fig. 5.3. An aluminum frame is constructed around the spindle under test, and the entire setup is placed on an vibration-isolation (optical) table. Two independent laser sources, each with differential fiber-optic carriers, are used for the measurements. The laser beams used for measurement are mounted on a six-degree-of-freedom kinematic mount attached to the measurement frame. The kinematic mounts that provide independent translational and angular positioning within $\pm$ 1 mm and $\pm 5^o$ ranges, respectively, are used during the alignment procedure. To obtain the rotational angle of the artifact during measurements, the voltage output from an infrared (IR) sensor is used. The IR sensor senses the passing of a black mark painted on the artifact surface as the artifact rotates, thus providing an angular reference for every revolution.

The laser beam from each of the two laser sources is transmitted through a fiber-optic cable with a split end, providing two laser beams from the same laser source. The LDV can be used in an absolute measurement mode by using one of the two laser beams of the same source as the measurement beam and the other as the reference beam, which is obtained by shining the laser beam onto a stationary mirror surface. This measurement mode is referred to here as the *single-point measurement mode*. Alternatively, when both of the laser beams from the same laser source are used simultaneously, relative motion between the two points are measured. This measurement mode is referred to as the *differential measurement mode*.

Since only two displacement measurements can be simultaneously conducted using the two independent laser sources available, to obtain both axial and radial motions, the tests are performed by pairwise measurements of (X, Y) and (Z, Y) motions. The modifications to the measurement setup for conducting each of the (X, Y) and (Z, Y) pairwise motion measurements are shown in Figs. 5.3(a) and 5.3(b), respectively. A single-point measurement mode for the Y-direction is obtained by attaching one of the split fiber-optic carriers (for the measurement beam) to the kinematic mount in the Y-direction, and by blocking the other split fiber-optic carrier (for the reference beam) using a mirror cap. The split fiber-optic carriers from the other laser source are attached to the X- and Z- direction mounts. To perform single-point measurements along one of the X or Z axis, the other laser beam is used as the reference beam by diverting it to a mirror surface using a pentaprism.

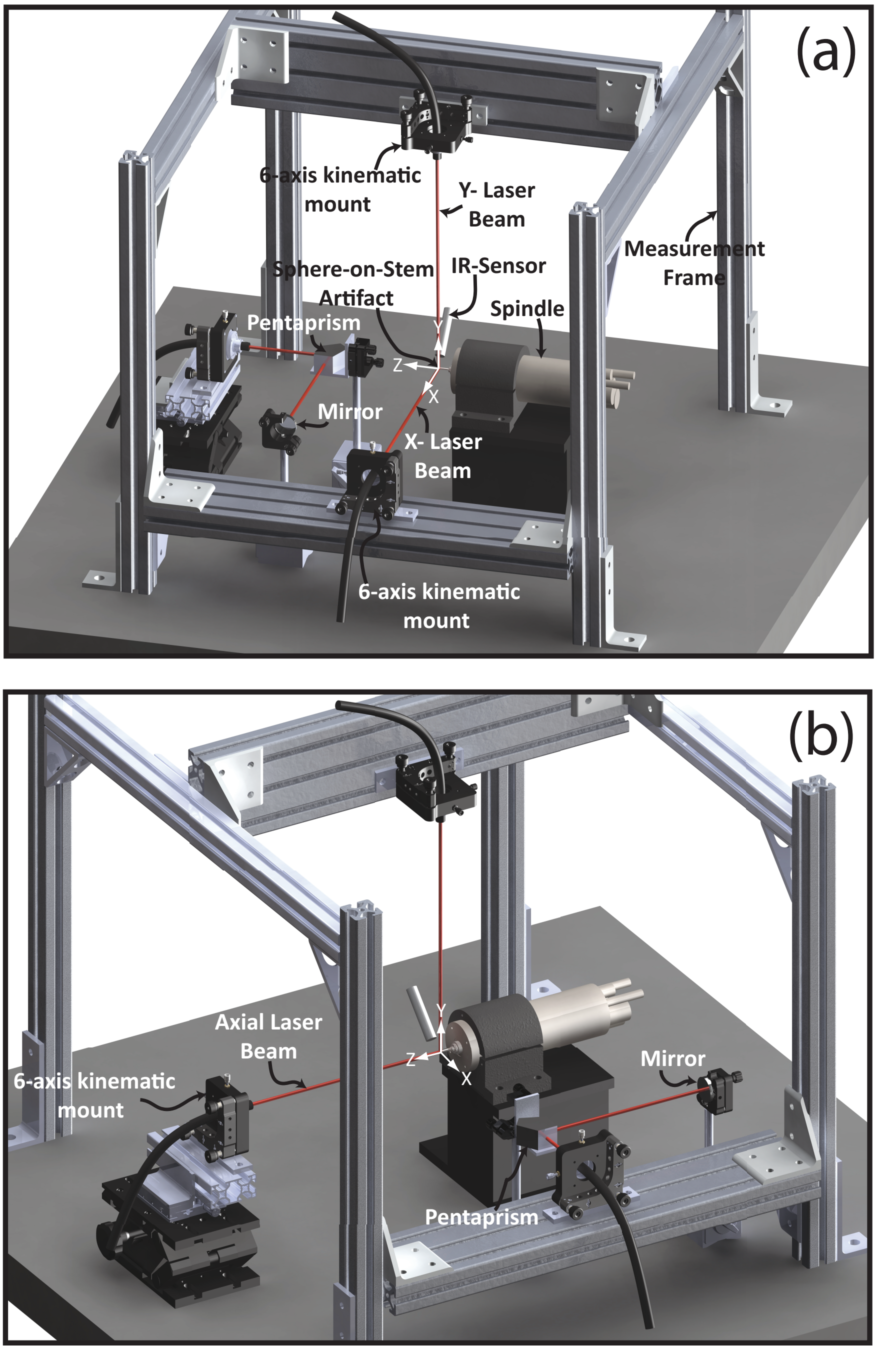

Figure 5.3: Measurement setup used for obtaining (a) the (X, Y) motion measurements, and (b) the (Z, Y) motion measurements.

5.3.2 Three-Dimensional Alignment of the Laser Beams

The alignment of the three laser beams in a mutually-orthogonal fashion is critical for conducting measurements of radial and axial motions accurately. This section describes the alignment procedure used for aligning the three laser beams mutually orthogonal and incident to the spherical target on the sphere-on-stem artifact attached to the spindle.

The alignment procedure uses the voltage signals provided by the laser controller that correspond to the intensity of the reflected laser beam. The reflected-laser intensity, and hence, the magnitude of the voltage reading, depends upon the perpendicularity of the incident laser beam to the surface at the point of incidence, the reflectivity of the surface, and the focus of the incident beam onto the surface. When the laser beam is focused on a highly reflective (non-diffusive) surface, the changes in the voltage amplitude are directly correlated with the changes in the angular orientation of the laser beam with respect to the local surface normal: The voltage reaches its maximum level (for a given surface) when the beam is perpendicular to the surface. Furthermore, focusing can also be monitored from the laser intensity, and the optimum focus yields the maximum intensity level. It should be noted that the laser reflection from highly-reflective (mirror-like) surfaces are not very sensitive to the focusing, but very sensitive to the angular orientation. By maximizing the voltage levels at each step of the alignment procedure, the laser beams can be focused and made perpendicular to the surfaces of interest.

The steps of the alignment procedure are described in Figs. 5.4(a)-5.4(e). A measurement cartesian frame of reference $[XYZ]$ is considered; after the completion of the alignment procedure, each laser beam axis is coincident with one of the axes of the reference frame. The Z laser beam is aligned to coincide nominally with the axis average line, and the other two (X and Y) laser beams are aligned perpendicular to the Z axis.

The *initial* alignment of the three laser beams is completed when the spindle is rotated at 40 krpm. First, each of the laser beams are shined onto the sphere, and roughly aligned using the kinematic mounts to obtain sufficient reflection. Subsequently, the optimal focus for each laser beam is obtained by moving a focusing objective attached to the end of the fiber-optic carrier to maximize the reflected-laser intensity (see Fig. 5.4(a)).

Several steps are completed to make the laser beam axes coincide with the axes of the reference frame: **(1)** The X and Y laser beams are moved to the cylindrical portion of the artifact, and the six-axis kinematic mounts are used to perform translational and angular movements iteratively until the voltage level corresponding to reflected-laser intensity is maximized (see Fig. 5.4(b)). This step makes each laser beam perpendicular to the axis average line. **(2)** The X and Y laser beams are then moved back to the sphere using only the translational degrees of freedom of the kinematic mounts. Subsequently, a rhomboid prism[†] is used to deflect each laser beam to a corner

[†]A rhomboid prism shifts an incident laser beam parallel to its original axis by a fixed distance (for this case, by

cube[‡], which is then placed in front of the artifact (displaced in the Z-direction)(see Fig. 5.4(c)). The corner cube is mounted on a fixture to enable translational and rotational adjustments. The orientation of the corner cube and the fine angular movements of the kinematic mounts (about an axis approximately parallel to the axis average line) are then adjusted until the maximum reflected-laser strength is obtained. After this step, the two radial laser beams become mutually perpendicular to each other, and normal to the axis average line. The rhomboid prisms are then removed, and both the radial laser beams are moved to the cylindrical portion of the artifact to confirm that their perpendicularity with respect to the axis average line is retained. **(3)** The laser beams are then moved to the sphere, and using only the translational degrees of freedom of the kinematic mounts, the signal levels are maximized. When this step is completed, the X and Y laser beams become mutually orthogonal, lie on the same plane normal to the axis average line, and intersect at the sphere center. **(4)** Next, the axial (Z) laser beam is aligned to be perpendicular to the plane formed by the X and Y laser beams by shining the Z laser beam on the third face of the corner cube (Fig. 5.4(d)). Without disturbing the orientation of the corner cube, the angular orientations of the Z laser beam are adjusted using the kinematic mount until the reflected-laser strength (voltage signal) is maximized. This makes all the three laser beams perpendicular to the corresponding three faces of the corner cube, and hence, renders them to be mutually orthogonal to each other. **(5)** The corner cube is then removed to shine the Z laser beam on the sphere. By using only the translational movements of the kinematic mounts, the reflecting-laser strength is maximized for the Z laser beam. As a result, a set of three mutually orthogonal laser beams is obtained that intersects at the sphere center with the Z laser beam coincident with the axis average line.

When the spindle speed is changed, axial-, radial-, and tilt-axis shifts (of the axis average line) could occur. If those shifts reduce the reflected-signal strength, the laser beams can be moved using only the translational degrees of freedom of the kinematic mounts to regain the optimal signal strength. Due to the spherical shape of the target, those movements would enable finding positions on the sphere such that the incident laser beams are perpendicular to the measurement surface. In addition, the translational movements do not disturb the mutual orthogonality of the three laser beams.

---

35 mm).

[‡]The corner cube is fabricated by sputter-coating the back side of a commercial retroreflector with a thin layer of aluminum.

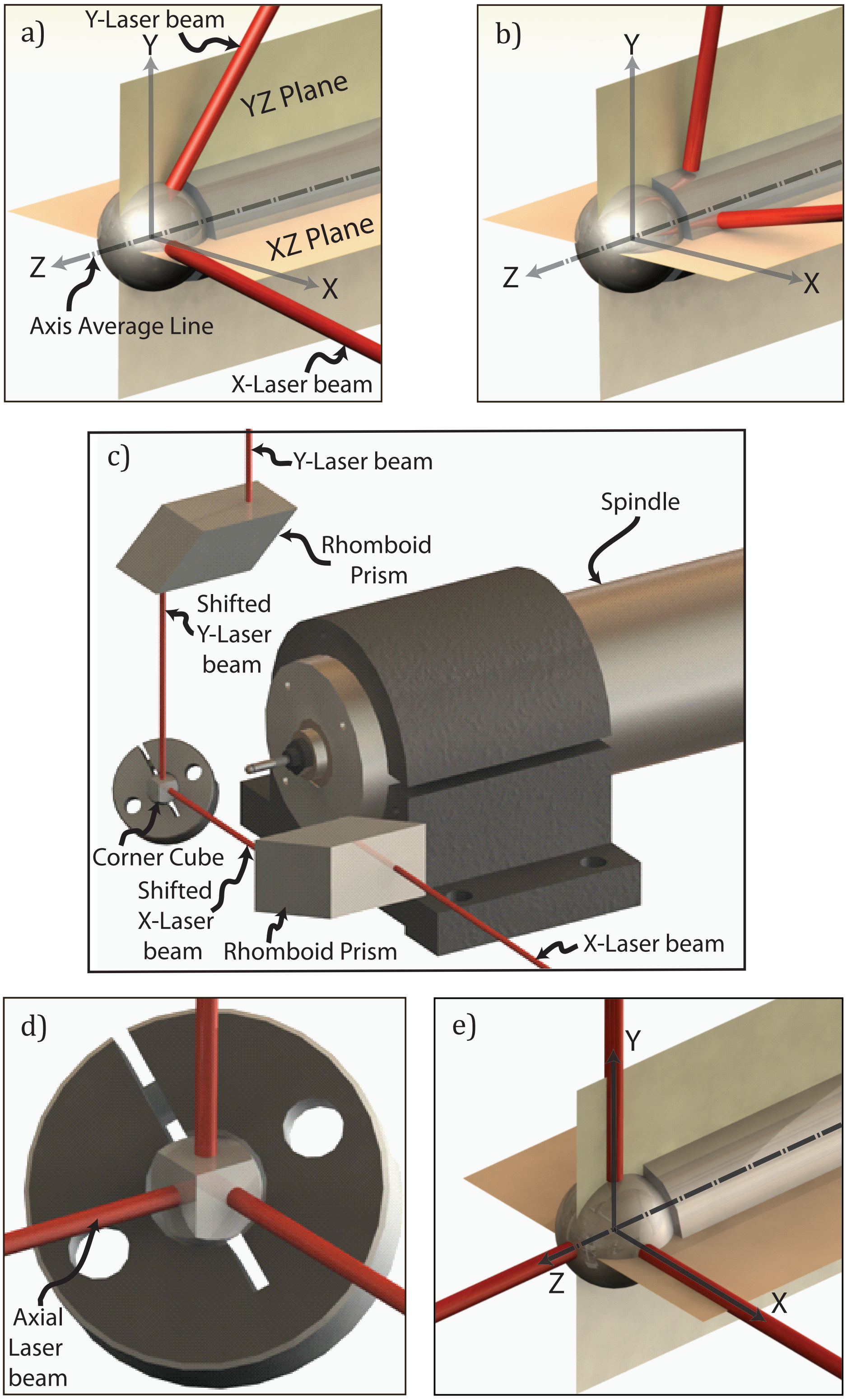

Figure 5.4: The procedure used for the alignment: (a)-(e) illustrate the various steps described in the text.

5.3.3 Data Acquisition and Post-Processing

Data acquisition and post-processing steps are critical to performing accurate measurements and decomposition of axial and radial motions. The LDV systems output voltages that are correlated linearly with the measured motions. To obtain high-resolution motion data, a 16-bit data acquisition card (National Instruments NI-6259) is used at a sampling rate of 500 kHz. To eliminate the low-frequency (< 15 Hz) drift inherent to the LDV system, the motion data is filtered using a zero phase-shift high-pass filter with a cut-off frequency of 50 Hz.

Once the test setup is completed, the physical location of the IR sensor is fixed, and the artifact is not removed from the spindle. Hence, the 5-volt pulse signal that the IR sensor outputs when the black mark painted on the artifact is sensed corresponds to the same physical rotational orientation, and can be used as the reference signal. To more accurately capture the "sharpness" of the pulse signal, and thus to resolve the reference angular position accurately (i.e., the zero degree rotational orientation), the IR sensor voltage is measured with a data acquisition card with 5 MHz sampling rate (National Instruments NI-6115). The angle at which the trailing edge of the pulse crosses 2.5 V amplitude is chosen as the beginning of each revolution, which is $\theta = 0$ for every revolution, where θ is the rotation angle. A LabView$^{\mathrm{TM}}$code is used to synchronize the LDV data with the IR voltage using a common clock signal. For each pairwise motion measurements ((X, Y) or (Z, Y)), two sets of voltage data corresponding to the motions from the two LDV systems and the pulse signals from the IR sensor are simultaneously acquired.

The speed of the spindles could exhibit (albeit slight) fluctuations about the nominal (set) spindle speed, which could be as much as $\pm$ 200 rpm for most UHS spindles. Thus, the time taken between successive marker locations may vary. To obtain the motion data at the same angular locations across multiple revolutions, data corresponding to each revolution is mapped from the time domain to an angular domain. For this purpose, the angular speed Ω_i for the i^{th} revolution is calculated as $\Omega_i = 1/T_i$, where T_i is the time it takes between i^{th} and $(i+1)^{\mathrm{th}}$ pulses from the IR sensor. Subsequently, the angular location $\theta_i(t)$ corresponding to each time increment t within the i^{th} revolution is determined. Using the data at $\theta_i(t)$, a shape-preserving piecewise cubic interpolation is used to obtain the motion data corresponding to the same angular orientations for each revolution. These angular orientations correspond to a set of fixed angles that are chosen by dividing one rotation into fixed number of intervals, magnitude of which is determined based on the spindle speed. This value is calculated as

$$\Delta\theta = \frac{2\pi}{\mathcal{I}[360/\Delta\theta_{nom}]n}, \tag{5.2}$$

where $\mathcal{I}$ is a function that determines the integer portion of a number, $\Delta\theta_{nom}$ is the angular resolution at the nominal spindle speed and n (an over-sampling factor) is an integer which determines the level of over-sampling within a revolution. The reason for over-sampling is to minimize the interpolation errors later, when the data from the angular domain is mapped back to the time domain. $\Delta\theta_{nom}$ is calculated as

$$\Delta\theta_{nom} = \frac{2\pi}{T_{nom}f_s}. \tag{5.3}$$

where T_{nom} is the time per revolution at the nominal speed and f_s is the sampling rate. To accurately interpolate the motion data at the beginning and the end of each revolution, the data from the previous and next revolutions are used. Using this approach for every revolution, the motion data is now obtained at the same angular locations across the entire data set with multiple revolutions. It should be noted that this analysis assumes the variations of the spindle speed *within a revolution* to be negligible. If the motion data needs to be mapped back to the time domain from the angular domain, the motion data at the fixed angular locations is interpolated to the angles $\theta_i(t)$ that correspond to the physical time increments (as calculated above) for the i^{th} revolution. By repeating this for each revolution, the motion data in the time domain across all revolutions can be retrieved. The processed motion data ($X(\theta)$,$Y(\theta)$,$Z(\theta)$) from a test at 80 krpm spindle speed for 1000 revolutions is shown in Fig. 5.5 in the angular domain as an example.

From the radial motion data given in Fig. 5.5, it can be observed that there are sharp notches present in both the X and Y measurements at two angular locations ($\approx 30^{\text{o}}$ and $\approx 260^{\text{o}}$ as seen in Radial X) which occur at the same angular orientation across all revolutions. Also, the angular locations of the notches in the X data are shifted by exactly 90^{o} from those in the Y data. These notches correspond to physical scratches on the surface of the sphere that were possibly created during the artifact fabrication. The scratches were imaged using white light interferometry, and were seen to be approximately 200 μm wide and 250 nm deep. These notches are individually removed from the data and replaced with data interpolated using the motion values at the beginning and end of the notch locations before further post-processing. It should be noted that, instead of IR sensor data, the notches could also be used as the angular reference for the rotational orientation of the artifact.

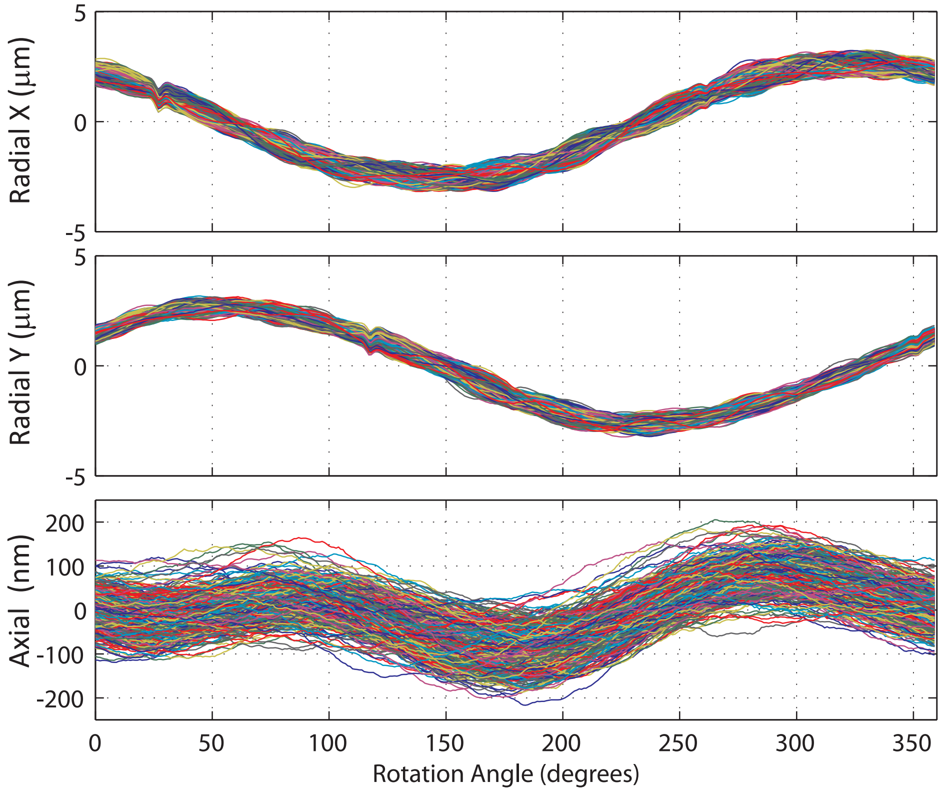

Figure 5.5: (X, Y, Z) motions for 1000 revolutions at 80 krpm.

5.3.3.1 Removal of Curvature Effects

Due to the small diameter of the sphere (3 mm or 0.125 in.), the axial and radial motions include displacements measured due to the effect of curvature. Since the curvature effects do not contribute to the actual tool-tip trajectory, their removal is critical to obtain more accurate measurements of motions, and thus, to determine the tool-tip trajectory.

To quantify the contribution of curvature to the measured motions, a computer code is written to simulate measurements of the displacements from the surface of a sphere that moves following a certain trajectory (see Figure 5.6). In particular, the trajectory of the sphere is specified as the motions measured during the experimentation, and the curvature effect is calculated as the difference between the simulated measurements and the measured motions. This approach provides a good approximation of the curvature effect so long as the curvature effect is considerably smaller than the measured motions.

The determination of the curvature effect, and thus the simulations of measurements, requires consideration of the finite spot size of the laser beam, and the distribution of the laser light intensity

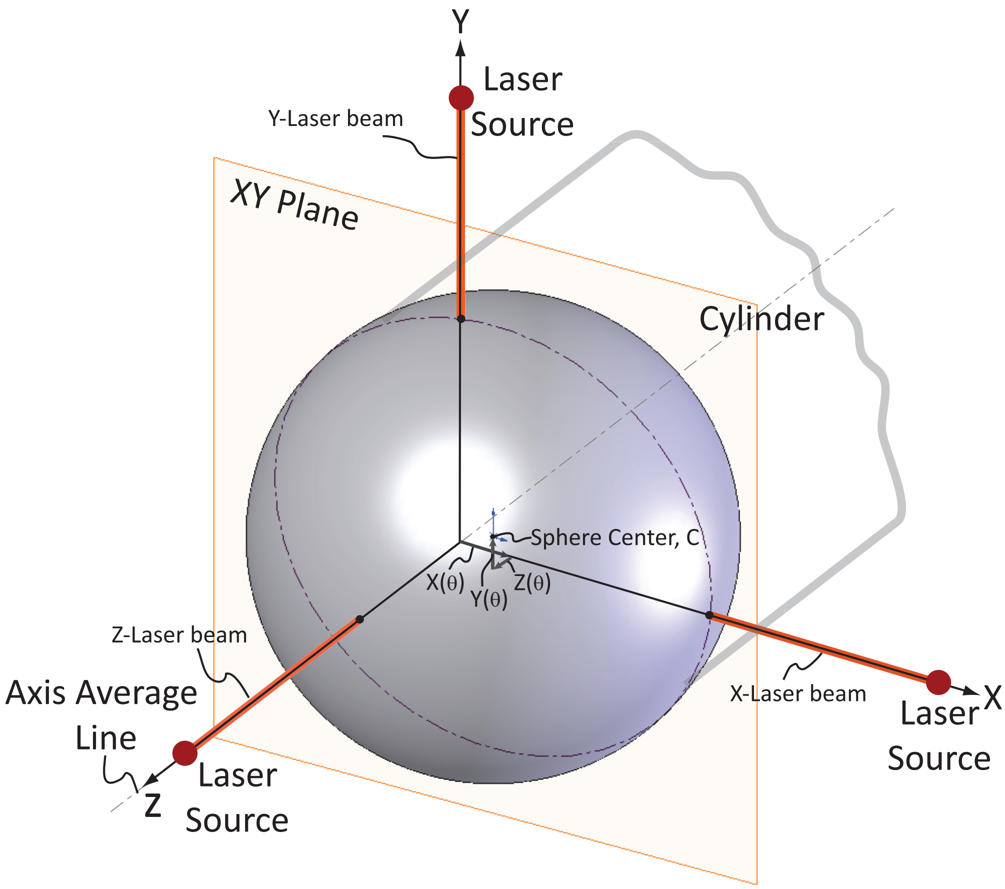

Figure 5.6: Simulation configuration to assess the curvature effects.

within the spot. In the simulations, we used a spot with a 50 μm diameter, and modeled the laser light intensity distribution within the spot to be Gaussian. A finite number of "rays" (50) within the spot size are used for the simulation, where the measurement from each ray provides the displacement of the sphere surface measured along the ray axis. The total displacement is obtained from the weighted average of the measurements from all the rays, where the weighing factors for each ray are chosen based on the Gaussian distribution.

Measured radial and axial motion data in the angular domain ($X(\theta)$,$Y(\theta)$,$Z(\theta)$) are used as the trajectory of the sphere center, and the simulated displacements ($X_{sim}(\theta)$,$Y_{sim}(\theta)$,$Z_{sim}(\theta)$) are calculated.

The difference between the simulated and experimental (input) motions ($X_{sim}(\theta)$-$X(\theta)$,$Y_{sim}(\theta)$-$Y(\theta)$,$Z_{sim}(\theta)$-$Z(\theta)$) are then calculated as the displacements due to the curvature effects. For each set of measured data, this procedure is completed, and the calculated curvature effect is removed from measured motion data to obtain the motion data without curvature, which is used for further post-processing.

5.3.3.2 Decomposition of Measured Motion Data

The decomposition of the motion data into its various components is explained in this section, using the data given in Fig. 5.5 (after removing the notches and the curvature effects) as an example.

The processed data (after removal of curvature) is first averaged across all revolutions to calculate the *average motions*. The average motions include all the frequency components which are at integer number of cycles-per-revolution. The once-per-rev component can be obtained by fitting a sine function of the form $A\sin(\theta + \phi)$ to the average motions, where the amplitude A and the phase ϕ are calculated using least squares minimization within a tolerance of 1x10^{-8}.

The synchronous *radial* error motions along the two orthogonal fixed-sensitive radial directions (X, Y) are obtained by removing the once-per-rev component from the average motions. On the other hand, the synchronous *axial* error motions are equal to the average motions measured along the axis average line. The fundamental component of the synchronous axial error motions is subtracted from the average motion data to obtain the residual synchronous axial error motions. Figure 5.7(a) shows the decomposition of the average radial (X) motions into the fundamental component and the synchronous radial error motions. Figure 5.7(b) shows the decomposition of the synchronous axial error motions into the fundamental component and the residual synchronous axial error motion components. The synchronous error motions calculated in this manner span one complete revolution and, by definition, repeat every revolution. Hence, before transforming the data, to obtain a higher frequency resolution, the total (angular) duration of the data is expanded by duplicating and appending the single revolution data over the total number of revolutions.

To analyze the different frequency components of the synchronous error motions, the error motions are transformed into the frequency domain from the angular domain using the Fourier transform. Since the synchronous error motion data is in the angular domain, the unit of frequency is cycles-per-revolution (cpr). Although this analysis could also be performed using the time-domain data, the spindle-speed fluctuations would distort the spectral content of the signal, and would make it harder to interpret the synchronous error motions. Figures 5.8(a) and 5.8(b) show the magnitude of the Fourier transforms of synchronous error motions in the X- and Z- directions, respectively.

Asynchronous error motions for each revolution are obtained in the angular domain by sub-

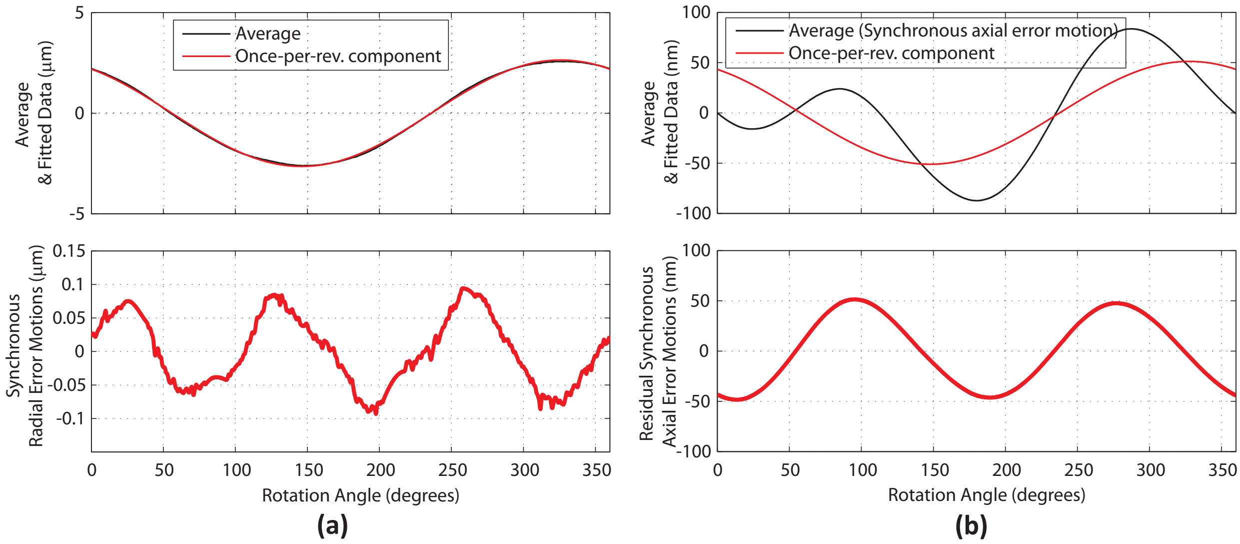

Figure 5.7: Decomposition of average motions into once-per-revolution component and the other integer multiples of fundamental frequency for measurements obtained at a spindle speed of 80 krpm: (a) along the fixed-sensitive X-direction, and (b) along the Z-direction.

tracting the average motion data from the total motion data. The major sources of asynchronous error motions are the asynchronous spindle error motions and structural error motions. Since these motions have direct relevance to the physical time, it may be preferred to analyze and interpret asynchronous error motions in the time domain rather than in the angular domain. To perform the time-domain analysis, asynchronous error motions in each revolution are mapped from the angular domain to the time domain. The frequency content of the asynchronous error motion data is performed by transforming the time-domain data to the frequency domain, where the units of frequency are cycles per sec (Hz). Figures 5.9(a) and 5.9(b) show the magnitude of the Fourier transforms of asynchronous error motions in the X- and Z- directions, respectively.

Figures 5.10(a) and 5.10(b) show the measured motions, average motions, and the asynchronous error motions in the time domain for the X- and Z- directions, respectively.

The *rotating-sensitive* motion data $R(\theta)$ for the angular location θ can be calculated by projecting data measured along two orthogonal fixed-sensitive directions onto the direction of the rotating unit radial vector $\vec{e}(\theta)$ as

$$R(\theta) = X(\theta)\cos(\theta) + Y(\theta)\sin(\theta). \tag{5.4}$$

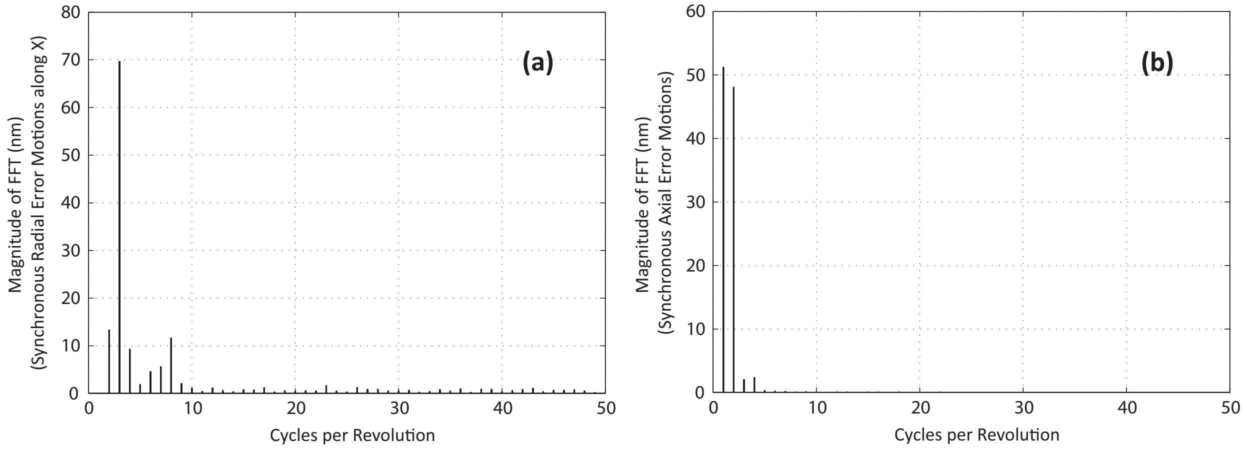

Figure 5.8: Magnitude of the Fourier transforms of synchronous error motions for measurements obtained at a spindle speed of 80 krpm: (a) along the fixed-sensitive X-direction, and (b) along the Z-direction.

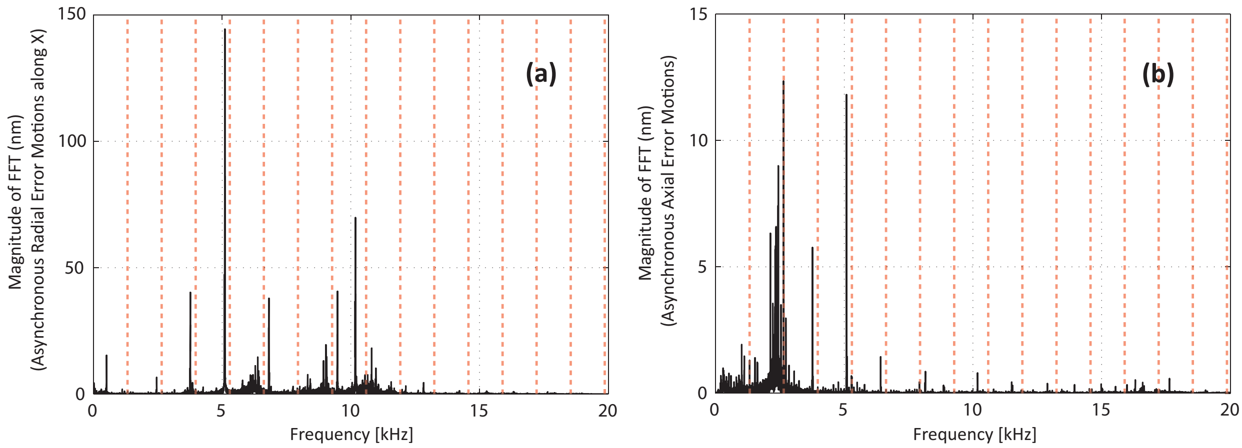

Figure 5.9: Magnitude of the Fourier transforms of asynchronous error motions for measurements obtained at a spindle speed of 80 krpm: (a) along the fixed-sensitive X-direction, and (b) along the Z-direction.

Determination of synchronous and asynchronous components of the rotating-sensitive motions and their analysis in the frequency domain are performed by following the same procedure used for processing the motions along fixed-sensitive directions.

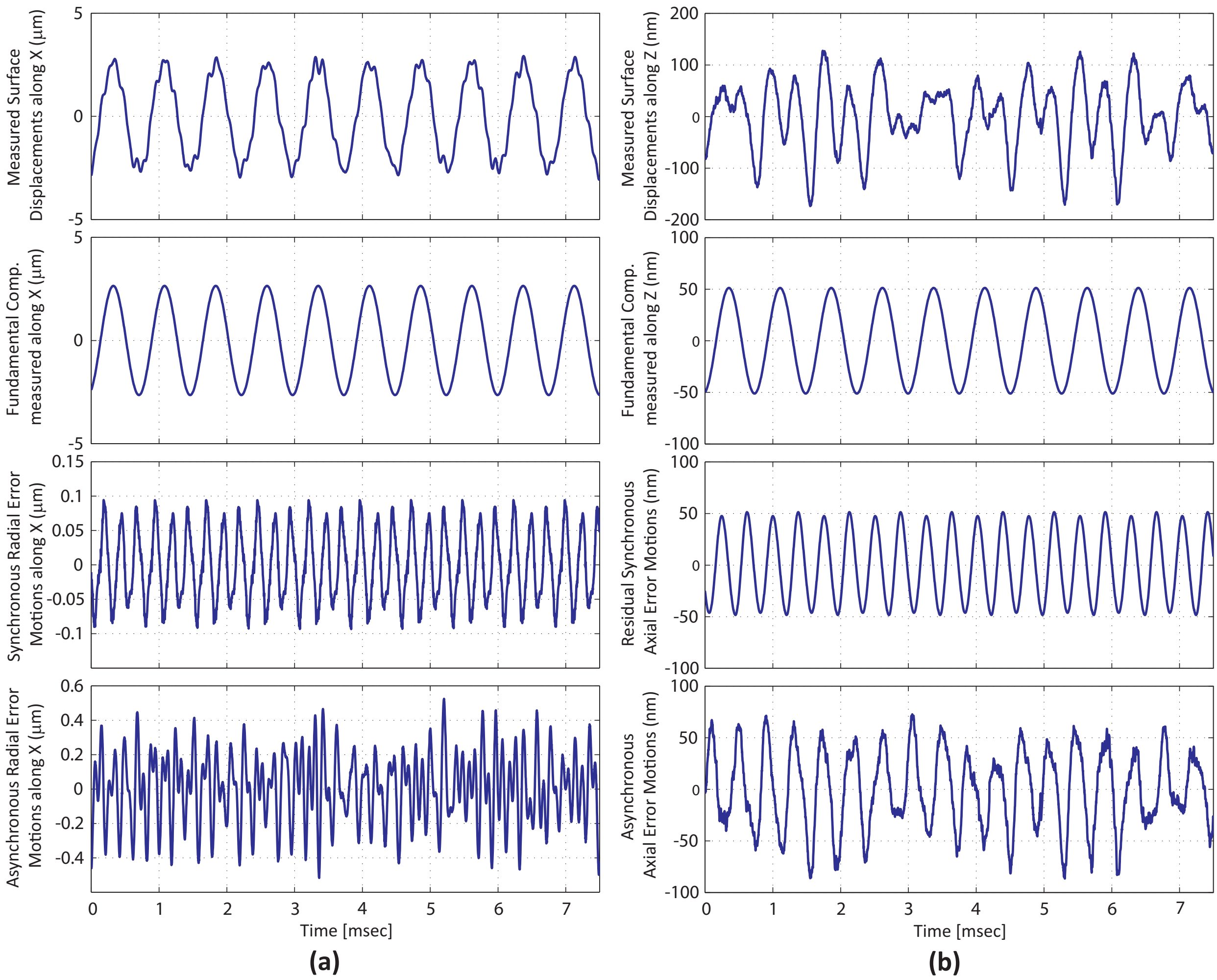

Figure 5.10: Decomposition of measured motions into different components for measurements obtained at a spindle speed of 80 krpm: (a) along the fixed-sensitive X-direction, and (b) along the Z-direction.

5.4 Demonstration of Methodology

In this section, we demonstrate the presented methodology by conducting measurements on an electrically-driven UHS spindle with hybrid-ceramic bearings (Fischer-Precise SC1060A). After completing the alignment procedure, the radial and axial error measurements are conducted at spindle speeds of 40, 80, 100, and 160 krpm. The spindle is cooled through continuous circulation of a water-based coolant, which ensures that the internal temperature of the spindle is controlled to within $\pm 1^{\circ}$C of the set temperature of 20°C. Before the collection of the data, the spindle was allowed to continuously run at the test speed for at least 15 minutes to obtain the thermal equilibrium, thus minimizing the influence of thermal-effects on the measured displacements.

Since the sampling rate for the motion measurements is kept at 500 kHz, the angular resolution of the measured data is different at different spindle speeds. For instance, the angular resolutions are 0.5^o and 1.9^o for the nominal speeds of 40 krpm and 160 krpm, respectively. The time duration of each data capture is also kept constant throughout the tests at 750 ms, corresponding to 500 and 2,000 revolutions for the speeds of 40 krpm and 160 krpm, respectively. The sampling rate for the IR sensor is also kept constant at 5 MHz, which resulted in a resolution of 0.05^o for 40 krpm, and of 0.19^o for 160 krpm, for locating the angular position of the artifact. The sensitivity of the LDV is selected to be 2 μm/V for the radial measurements and 200 nm/V for the axial measurements. This corresponds to a displacement resolution of 0.6 nm in radial motions and of 0.06 nm for axial motions when using the 16-bit acquisition card.

5.4.1 Radial Motions

The *synchronous radial error motions* for the fixed-sensitive and rotating-sensitive directions are obtained using the procedure above. Figures 5.11 and 5.12 provide the polar plots of synchronous radial error motions obtained at each of the four spindle speeds for the two fixed-sensitive directions and for the rotating-sensitive direction, respectively. The variation of synchronous radial error motions with the spindle speed is clearly observed from these figures.

The frequency content of the synchronous radial error motions are given in Fig. 5.13 for the fixed-sensitive and the rotating-sensitive directions at the four different spindle speeds. As expected, the shape of the polar plots given in Figs. 5.11 and 5.12 are directly correlated to the frequency content of the synchronous radial error motions. It should be mentioned here that, during processing of the rotating-sensitive synchronous radial error motion data, the entire once-per-rev component is removed by eliminating not only the best-fit circle (which is a constant shift in $R(\theta)$ versus θ plot, equal to the radius of the best-fit circle), but also the sinusiodal component at the fundamental frequency [114, 115].

The frequency content of the *asynchronous radial error motions* along the two fixed-sensitive directions and the rotating-sensitive direction are given in Fig. 5.14, where the units of frequency is Hertz (Hz). The vertical lines given in Fig. 5.14 indicate the harmonics of the nominal rotational frequency. It can be seen that the same frequency components are present in both X- and Y- fixed-sensitive directions; however, the amplitude of those components vary, possibly due to the (non-uniform) operating deflection shapes of the dynamic response corresponding to those frequencies. Furthermore, the rotating-sensitive asynchronous radial error motion data exhibits responses at

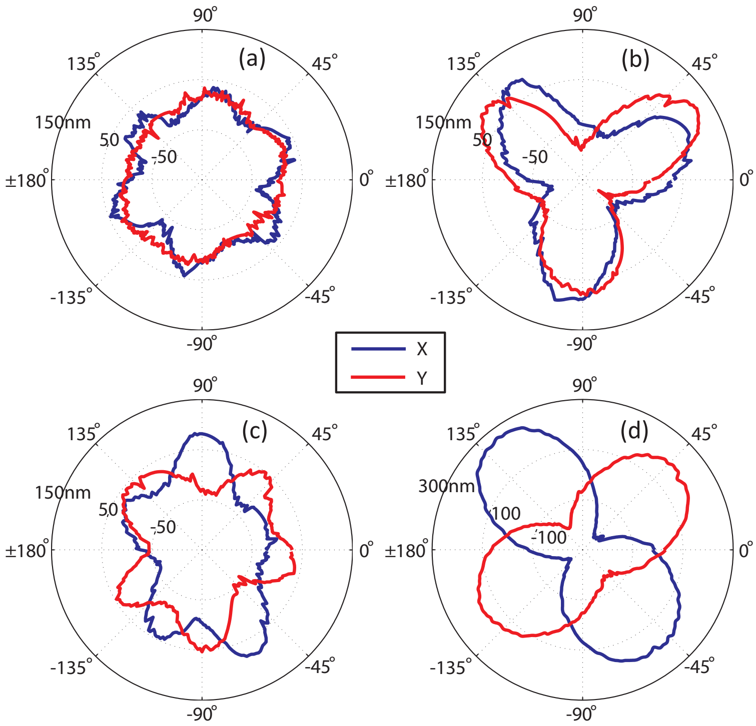

Figure 5.11: Synchronous radial error motions along the X- and Y-fixed-sensitive directions at spindle speeds of (a) 40 krpm, (b) 80 krpm, (c) 100 krpm, and (d) 160 krpm.

frequency that are not present in the fixed-sensitive asynchronous radial error motion data. These differences could be arising from the well-known phenomenon in rotating system dynamics, where the frequency content of the same motion differs whether the motion is observed by a fixed observer or by a rotating observer [128].

To quantify the ranges of radial error motions, the *synchronous radial error motions values* and the *standard deviation of the asynchronous radial error motions* are calculated. Figure 5.15(a) provides the synchronous error motion values for the radial error motions at the four test speeds. The standard deviation (1σ) of the asynchronous radial error motions is given in Fig. 5.15(b). Again, the large effect of spindle speed on the radial error motions is clearly observed in this data.

5.4.2 Axial Motions

As described earlier, in the case of axial measurements, the motions at all integer multiples of the fundamental frequency (including the fundamental frequency) are considered inherent to the synchronous axial error motions. Figure 5.16 shows the polar plots of the *synchronous axial error motions* at the four test speeds and Fig. 5.17(A) shows the corresponding frequency content (Fourier

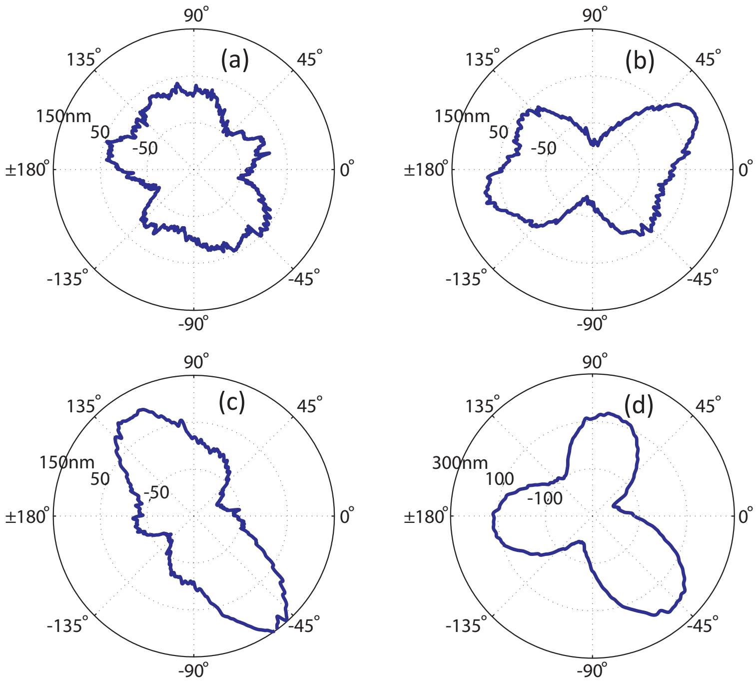

Figure 5.12: Synchronous radial error motions along the rotating-sensitive direction at spindle speeds of (a) 40 krpm, (b) 80 krpm, (c) 100 krpm, and (d) 160 krpm.

transform amplitudes). The significance of the spindle speed on the synchronous axial error motions is observed from the figures. Furthermore, it is also seen that the relative magnitude of once-per-revolution component (compared to the other components) increases significantly as the speed increases. This could plausibly be due to the influence of the residual unbalance couple on the axial error motion [129].

The frequency content of the *asynchronous axial error motions* is given in Fig. 5.17(B) for the four test speeds. Also shown are lines representing the integer multiples of the nominal rotation frequency for each case. Furthermore, the *synchronous axial error motions values* and the (1σ) *standard deviation of the asynchronous axial error motions* are presented in Fig. 5.18.

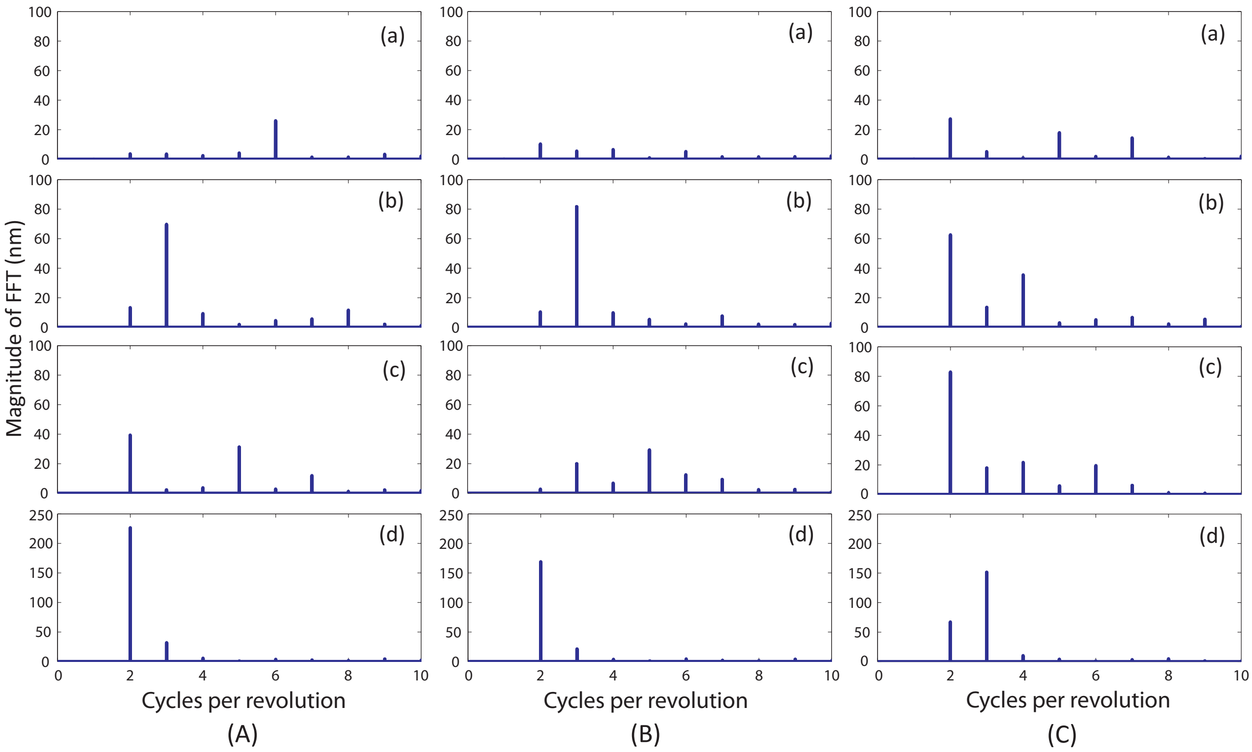

Figure 5.13: Magnitude of the Fourier transforms of synchronous radial error motions: (A) along the fixed-sensitive X-direction, (B) along the fixed-sensitive Y-direction, and (C) along the rotating-sensitive direction at spindle speeds of (a) 40 krpm, (b) 80 krpm, (c) 100 krpm, and (d) 160 krpm.

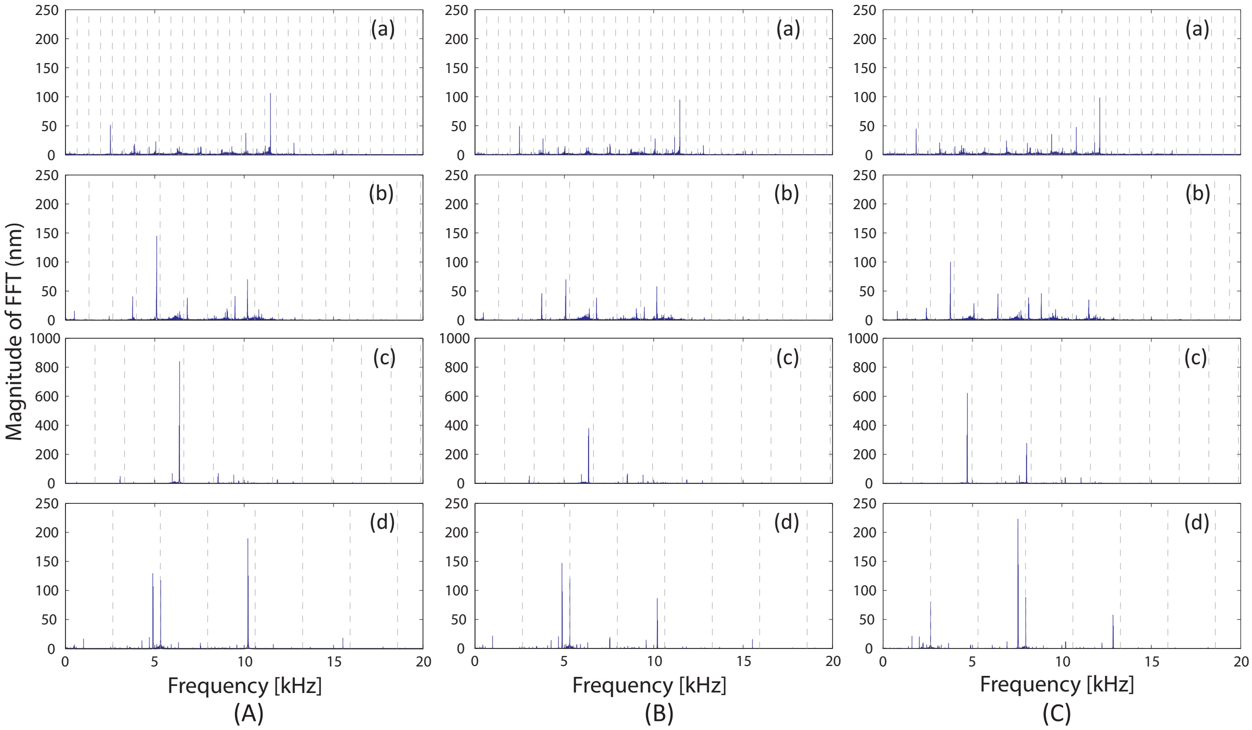

Figure 5.14: Magnitude of the Fourier transforms of asynchronous radial error motions: (A) along the fixed-sensitive X-direction, (B) along the fixed-sensitive Y-direction, and (C) along the rotating-sensitive direction at spindle speeds of (a) 40 krpm, (b) 80 krpm, (c) 100 krpm, and (d) 160 krpm.

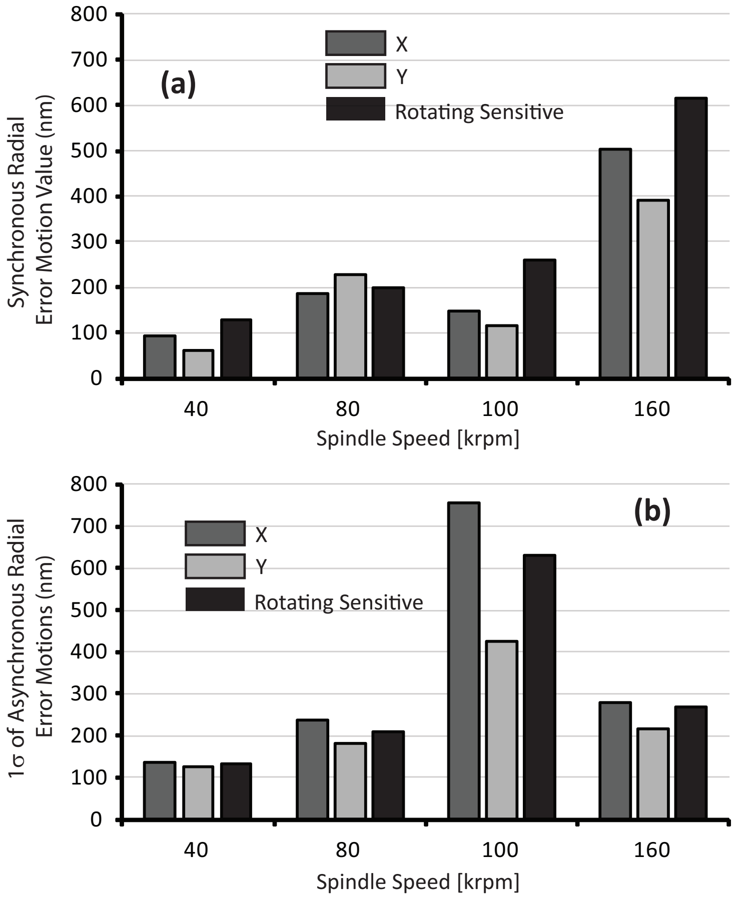

Figure 5.15: The radial error motions: (a) The synchronous radial error motion value, and (b) 1σ of the asynchronous error motions.

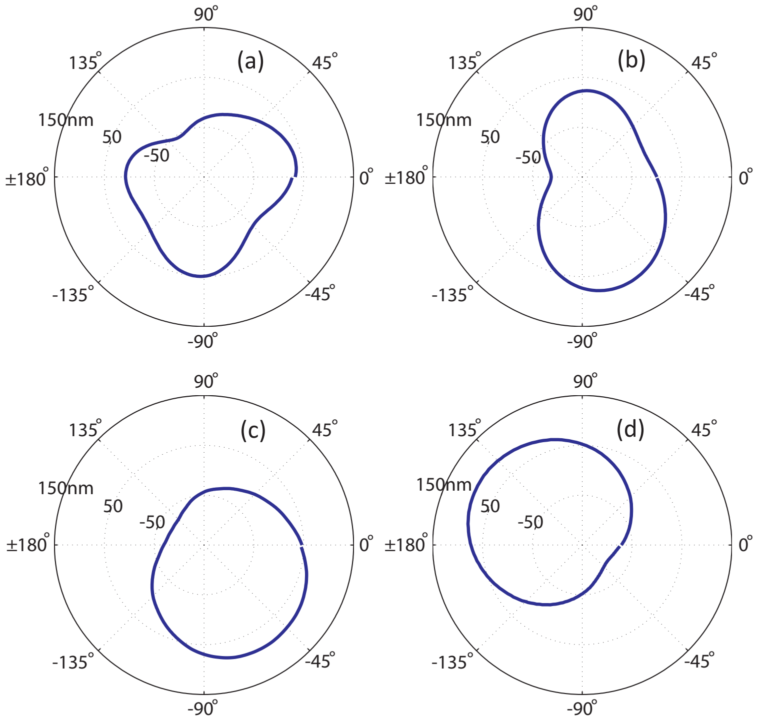

Figure 5.16: Synchronous axial error motions at spindle speeds of (a) 40 krpm, (b) 80 krpm, (c) 100 krpm, and (d) 160 krpm.

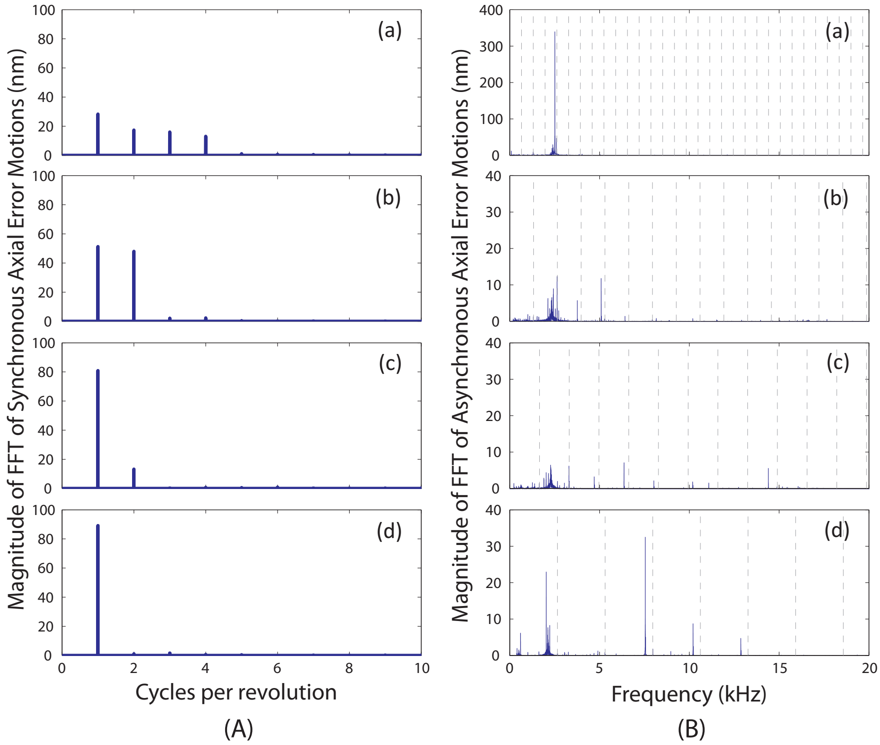

Figure 5.17: Magnitude of the Fourier transforms of (A) synchronous axial error motions, and (B) asynchronous axial error motions at spindle speeds of (a) 40 krpm, (b) 80 krpm, (c) 100 krpm, and (d) 160 krpm.

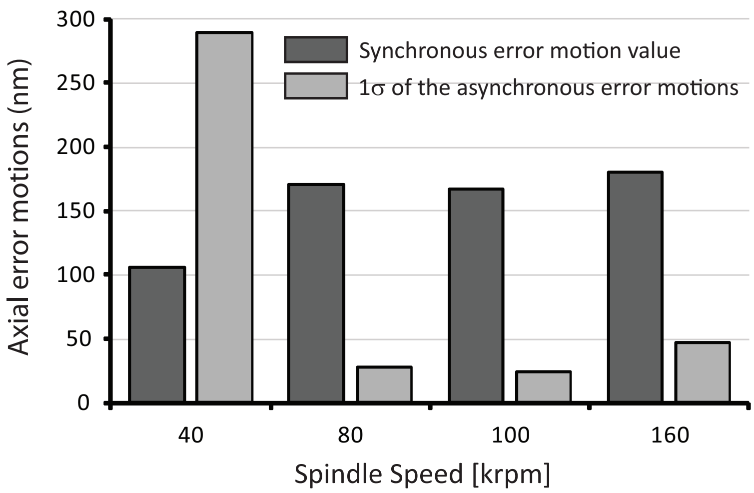

Figure 5.18: The axial error motions showing both the synchronous axial error motion value and 1σ of the asynchronous error motions.

5.5 Quantification of Uncertainty of Motion Measurements

This section presents quantification of uncertainties in the radial and axial motion measurements when performed using the presented methodology. The uncertainty quantification follows the procedure outlined in the Guide to the Expression of Uncertainty in Measurement (GUM) document [130]. The total uncertainty is considered to arise from four major sources, each with multiple contributors: (1) the measurement device and artifacts, (2) the environmental effects, (3) the laser beam-alignment procedure and curvature effects, and (4) the data processing.

5.5.1 Calculation of Uncertainties

For the uncertainty analysis, each contributor i is assumed to have either a *Normal* (Gaussian), a *U-Shaped*, or a *Rectangular* statistical distribution. The range value associated with the variation of the contributor can be converted to a standard uncertainty u_i by multiplying the range value by a factor f corresponding to the distribution type. The rounded values of the factor f are 0.25, 0.35 and 0.29 for the *Normal*, *U-shaped* and *Rectangular* distributions, respectively.

Under the assumption that each contributor is independent from the others, the square root of the sum of squares of the individual standard uncertainties yields the *combined standard uncertainty* u_c as

$$u_c = \left(\sum_{i=1}^{n} u_i^2 \right)^{1/2}, \qquad \text{for n contributors.} \tag{5.5}$$

Furthermore, to provide a measure of the overall uncertainty of a measurement, an interval is defined around the motion measurements by using an *expanded uncertainty* U as

$$U = k\, u_c, \tag{5.6}$$

where k is the *coverage factor*. As such, the motion measurements are expected to lie within $\pm U$ with a specified level of confidence. For the uncertainty analysis presented here, the combined effect of all the different contributors of a particular source is assumed to have a normal distribution. By using a coverage factor $k = 2$, the motions lie within $\pm U$ with a level of confidence of approximately 95%.

5.5.2 Measurement Uncertainty due to Measurement Device and Artifacts

The nominal resolution of LDV systems depends upon the type of displacement decoder and the laser sensitivity setting used for measurements. The nominal resolution is realized provided that the strength levels of the reflected beam are above 60% of the full strength. For all the measurements conducted during this work, the strength levels were 90% or above, and hence, the measurements have the nominal resolution.

For the measurements shown in this thesis, DD-500 displacement decoders (Polytec, Inc.) were utilized. The laser sensitivity setting used for radial and axial measurements were 2 μm/V and 200 nm/V, respectively. This corresponds to the 0.6 nm nominal resolution for the radial measurements and 0.06 nm nominal resolution for the axial measurements. These contribute to the standard uncertainty of the LDV measurement device. Since the analog-to-digital data conversion is completed using a 16-bit data-acquisition card, the resolution of the measured data is 0.6 nm for the radial motion measurements and 0.06 nm for the axial motion measurements. Together, the uncertainty due to the LDV measurement device and the A/D card is the summation of half of the individual resolutions, which is 0.6 nm for the radial motion measurements and 0.06 nm for the axial motion measurements.

The overall noise from all the sources, including the LDV systems, the data acquisition cards and electrical noise, was measured to have a standard deviation of around 5 nm. Therefore, compared to this noise level, the uncertainty due to the effect of measurement resolution can be neglected. The noise and resolution will only contribute to uncertainty in the measured motions at asynchronous frequencies since their effect will be averaged out to a negligible level during the calculation of synchronous error motions. Assuming a normal distribution, the standard uncertainty due to system resolution and noise is 5 nm for both radial and axial motion measurements.

Another source of uncertainty arises from the precision artifacts used during the measurements. For this work, the artifact form error is considered as a source of measurement uncertainty. The sphericity of the Grade 3 hardened steel sphere used in the sphere-on-stem artifact is 76 nm, which is equal to its maximum out-of-roundness. The uncertainty caused by the out-of-roundness of the sphere affects both the synchronous radial and synchronous axial error motions. Assuming a normal distribution, the standard uncertainty due to artifact form error is calculated to be 19 nm.

The uncertainty due to the measurement device and artifacts is summarized in Table 5.1. The expanded uncertainty, U, due to the measurement device and artifacts at asynchronous frequencies is 10 nm for both radial and axial measurements. At synchronous frequencies, the expanded

Table 5.1: Measurement uncertainty due to the measurement device and artifacts.

Uncertainty Input	Contributes to Uncertainty at	Range (nm)	u_i (nm)
System Resolution and Noise	Asynchronous Frequencies (Radial, Axial)		5
Artifact Out-of-Roundness	Synchronous Frequencies (Radial, Axial)	76	19

	Expanded Uncertainty (nm) (coverage factor, k = 2)
At Asynchronous Freqs. (Radial, Axial)	10, 10
At Synchronous Freqs. (Radial, Axial)	38, 38

uncertainty for radial and axial measurements is 38 nm.

5.5.3 Measurement Uncertainty due to Environmental Effects

The environmental effects that could cause measurement uncertainty are mainly composed of the thermal effects and the structural vibrations of the aluminum frame due to the excitation from the rotating unbalance and noise from the spindle. If the temperature inside an UHS spindle is not controlled, relatively small temperature changes may cause considerable variations in the error motions. The electrically-driven UHS spindle used in this work for demonstrating the methodology has a temperature controller that continually circulates a water-based coolant. The controller keeps the temperatures within $\pm 1^{\circ}$C. Furthermore, to attain a steady-state temperature distribution, the spindle was run for a period of time before the data was collected. Due to these reasons, the thermal effects are considered negligible for the presented data.

In order to estimate the vibrations of the structural frame during testing, displacements (along the axial and radial directions) were measured from the surface of a large steel block (300 mm x 160 mm x 100 mm) that is bolted down to the isolation table while the spindle is running at various operating speeds. Due to the high rigidity and large mass of the steel block, it is assumed that the measured motions arise only from the structural vibrations of the frame. The measured motions were decomposed into their synchronous and asynchronous components to estimate the uncertainty in each frequency component (see Fig. 5.19).

It was seen that the peak-to-peak amplitude of structural vibrations at synchronous frequencies is below 7 nm at any speed along either the radial or the axial directions. For the asynchronous frequencies above 50 Hz, the root-mean-square amplitude of structural vibrations are below 15 nm at any speed along any direction. These maximum values were taken as conservative estimates for

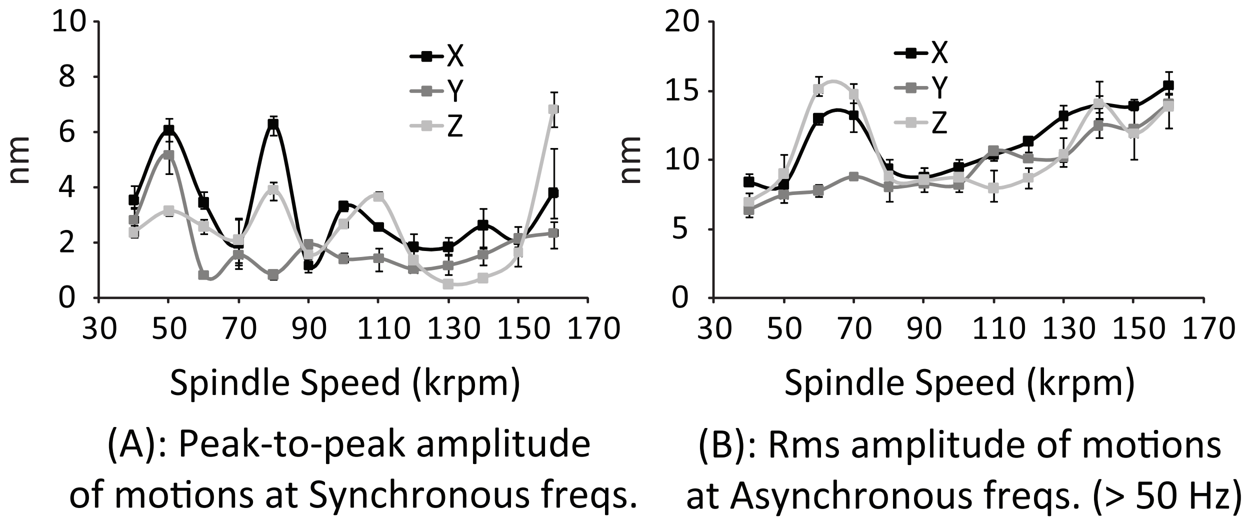

Figure 5.19: Decomposition of structural vibrations of the aluminum frame into motion components at synchronous and asynchronous frequencies to evaluate the measurement uncertainty.

the uncertainty values for the respective frequency components.

5.5.4 Measurement Uncertainty due to Laser Beam Alignment and Curvature Effects

The curvature effects of the artifact and the alignment procedure outlined in Section 5.3.1 are critical contributors to the overall measurement uncertainties. When the laser beam is well-focused on a highly reflective surface, the changes in the reflected-laser intensity directly correspond to the variations in the *relative angular orientation* of the incident light with respect to the local-surface normal. The sensitivity of the reflected-laser strength (voltage) to the changes in relative angular orientation depends upon the stand-off distance between the reflective surface and the laser source. The sensitivity is determined experimentally by shining a laser beam to a mirror mounted on a 2-axis goniometer. The stand-off distance between the mirror and the laser source (the end of the fiber-optic carrier) was arranged to be in the vicinity of the stand-off distances used during the motion measurements. After the laser beam is focused on the mirror, and the orientation of the mirror is adjusted to maximize the voltage reading, one of the axes of the goniometer is rotated to change the relative angular orientation by a specific amount. The voltage change corresponding to this new orientation is noted. This experiment is repeated for a number of relative angular orientations about the normal. The relative angular orientation that results in the minimum (robustly) detectable voltage change of 0.01 V was seen to be 0.04^o. Since the surface of the spherical (and the cylindrical) target is highly reflective and since the first step of the alignment procedure is to focus the laser beam onto the surface, it can be concluded that the alignment method can be used to obtain a relative angular orientation of 90^o within a resolution of 0.04^o.

Optical components used during the alignment procedure may also induce angular misalignments. As per the manufacturer's specifications, the rhomboid prisms could deviate the angle of the incoming light by up to an angle of 30 seconds, and the faces of the corner cube are orthogonal to each other within an angle of 10 seconds. All these possible angular misalignments cause an uncertainty in the alignment of the X, Y and Z laser beams with respect to the XYZ reference frame. Figure 5.20 shows the misaligned laser beams and the misalignment angles δ_X, δ_Y, δ_Z and β which quantify the misalignments. By following the steps of the alignment procedure and summing up the contributions from the various sources, the maximum values of the misalignment angles are estimated as δ_{X-max}=0.04^o, δ_{Y-max}=0.04^o, δ_{Z-max}=0.13^o and β_{max}=0.1^o.

The simulation that is used earlier for estimating the curvature effects can be utilized to estimate the uncertainty in the motion measurements due to the convolved effects of laser beam misalignments, the curvature of the sphere, and the motions of the sphere (see Fig. 5.20). Since the components at the fundamental frequency are significantly larger than the others for both the radial and axial motion measurements, it is sufficient to calculate the uncertainty levels only due to the fundamental motion components of the sphere. To assess the uncertainty, simulations are performed using three different amplitudes of fundamental components in the radial directions (2.5 μm, 4.5 μm, 6.5 μm, which span the range seen during the experimentation above). The fundamental amplitude along the Z-direction was kept constant at 75 nm, which represents the average amplitude of the fundamental component in the axial error motions during the experiments.

The misalignment of each laser beam can be represented by considering the laser beam to lie within a cone about the nominal laser orientation, with a cone angle equal to the maximum misalignment angle for that laser beam, and with an apex that passes through the origin of the XYZ reference frame. For each amplitude, 12 different orientations (lying on the outer surface of the cone) of each laser beam are simulated. Figure 5.20 shows the nominal orientation and the sample orientations of each of the laser beams.

At a given rotation angle, the differences between the nominal curvature effects (calculated for the nominal laser beam orientations) and the maximum and minimum curvature effects (calculated across all the 12 orientations) are evaluated. These differences represent the positive and negative ranges of the uncertainty in the motions arising from the convolved effects of laser beam misalignments, curvature of the sphere, and the motions of the sphere.

Figure 5.21 shows the simulation results for the various levels of fundamental amplitudes across one full revolution of the sphere. For a given spindle speed, the uncertainties are repeated in every revolution, and thus, they only contribute an uncertainty to the synchronous error motions. The uncertainty graphs for the X and Y measurements are seen to have a phase difference due to the effect of the misalignment angle β, i.e., Figs. 5.21(a) and 5.21(b) are offset by $(90 \pm \beta_{max})$. It is also seen that the uncertainty in axial measurements varies with the amplitude of fundamental radial motions, but does not vary with the rotation angle.

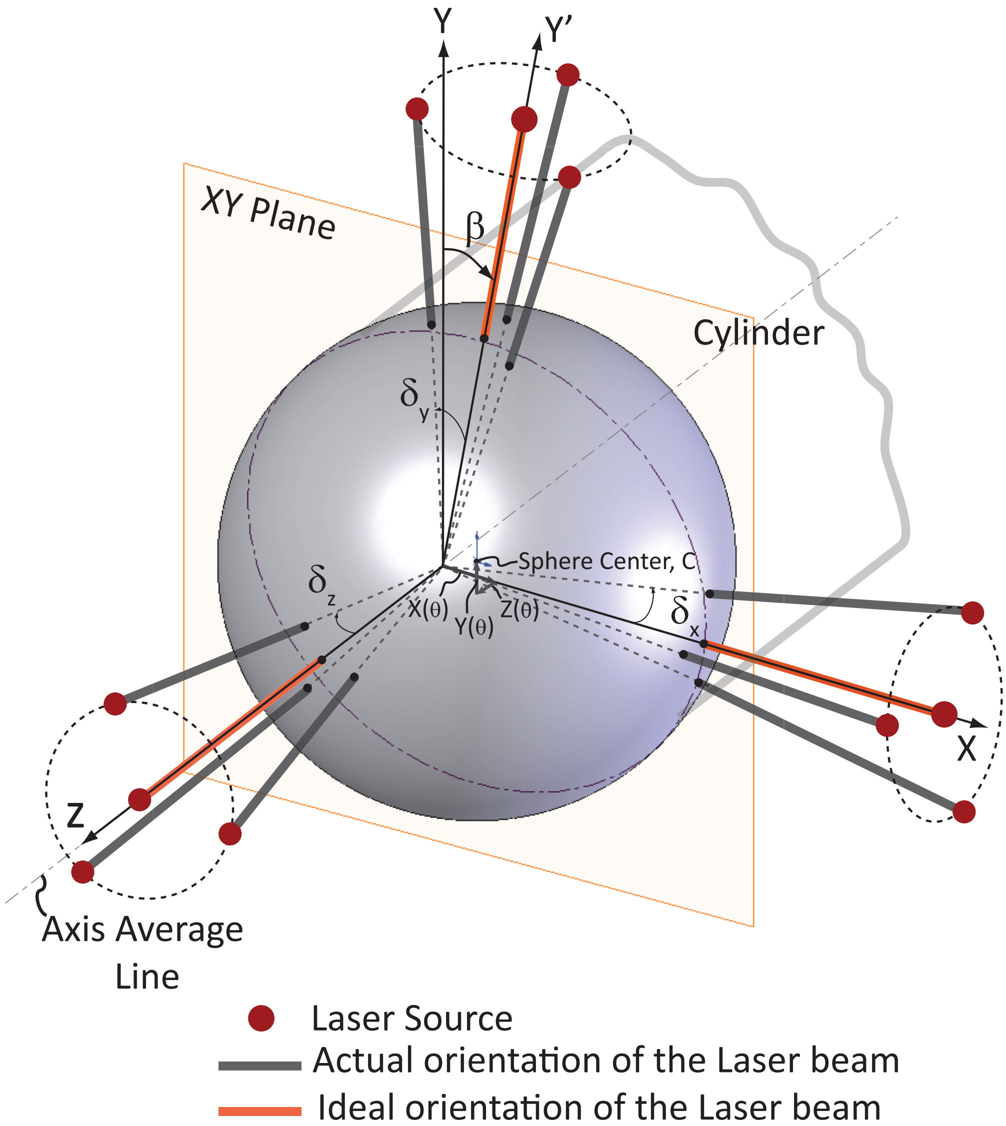

Figure 5.20: Simulation setup to calculate the uncertainties due to the convolved effects of laser beam misalignments, curvature of the sphere, and the motion levels (radial and axial) of the center of the sphere from the origin.

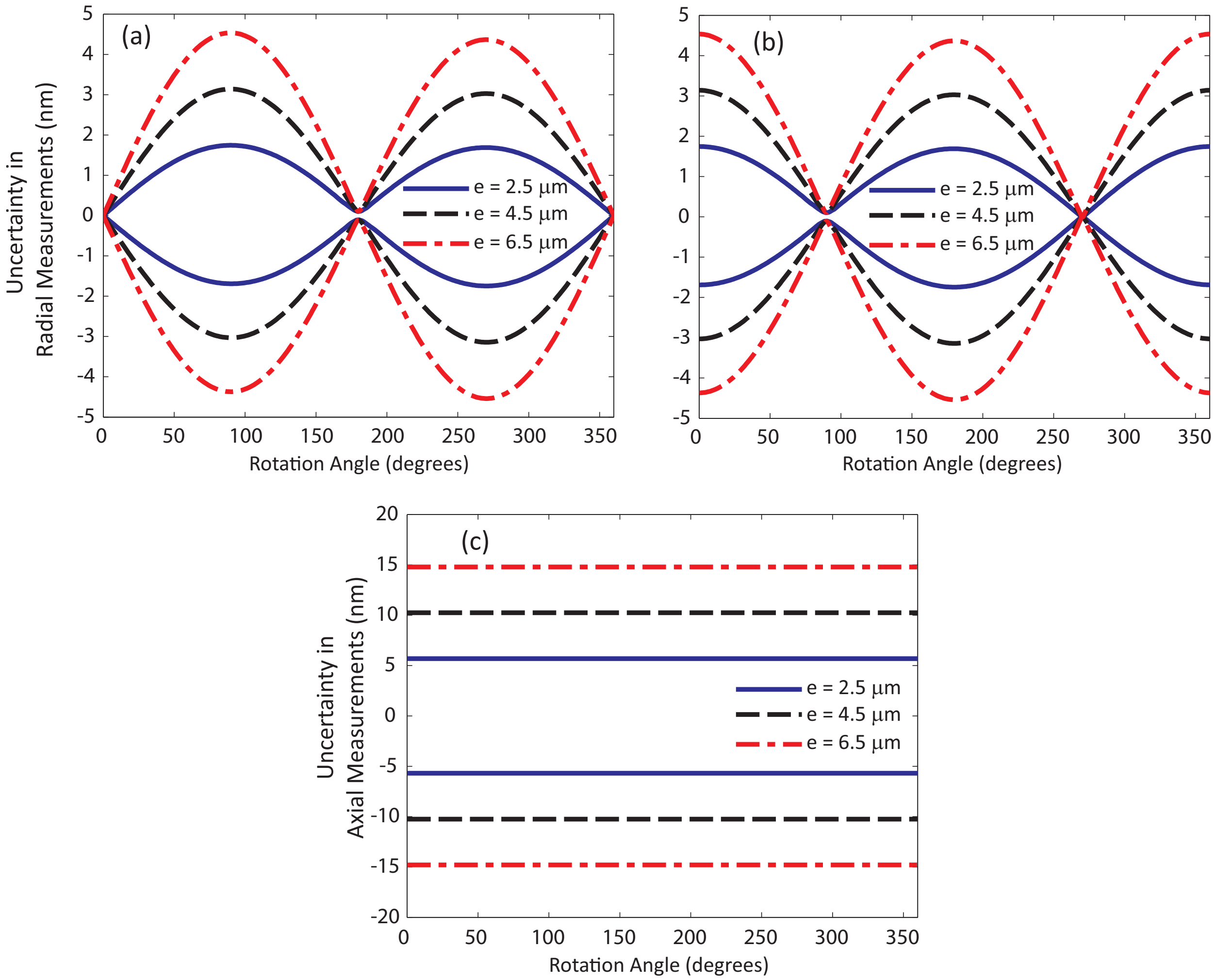

Figure 5.21: Calculated measurement uncertainties due to the convolved effects of laser beam misalignments, curvature of the sphere, and the motion levels (radial and axial) of the center of the sphere from the origin: (a) and (b) the uncertainty in the radial motion measurements along the X- and Y-fixed-sensitive directions, respectively; and (c) the uncertainty in the axial motion measurements.

5.5.5 Uncertainty due to Data Acquisition and Post-processing

As mentioned in Section 5.3.3, when using a sampling rate of 5 MHz to sample the IR sensor signal, the beginning of a revolution can be resolved to within 0.05^o and 0.19^o at the nominal spindle speeds of 40 krpm and 160 krpm, respectively. This angular resolution causes an uncertainty by an equivalent amount in the determination of the rotation angle. This uncertainty will propagate into the overall uncertainty in the radial motions along a rotating-sensitive direction. Its effect is coupled with the effect from other uncertainties and is analyzed in the next section.

During post-processing, the data is mapped from the time domain to the angular domain, and then back to the time domain in the case of asynchronous error motions. This process involves application of either one or two sets of data interpolations, which could cause uncertainties in accurately separating synchronous and asynchronous error motions. This uncertainty is dependent upon the over-sampling factor (n) chosen during interpolation. For all the data presented in this chapter, we have chosen n=*10*, which results in a low value of uncertainty due to interpolations.

To evaluate this uncertainty, all measurement data sets were interpolated from the time domain to the angular domain and re-interpolated back to the time domain. The maximum peak-to-peak value of the difference between the measurement data and the processed data across all spindle speeds was found to be 1 nm. This value is considered as the contribution of the data processing to the expanded uncertainty in both synchronous and asynchronous error motions. The spindle-speed variations do not cause any additional uncertainty in separating synchronous and asynchronous error motions, since the procedure of mapping from the time domain to the angular domain appropriately accounts for the correct rotation angle within the angular resolution of the IR sensor.

The procedure for curvature removal assumes that the input to the simulation are purely motions of the sphere center, without any curvature effects. However, the measured motion data already includes the motions measured due to curvature effects of the sphere. This gives rise to an uncertainty in our calculation of the contribution due to curvature effects. To estimate this uncertainty, after subtracting the effect of curvature from the measured motion data, the modified data is input to the simulation again. The modified simulated data are now subtracted from the modified input data to obtain a second estimate of the motions due to curvature. The two estimates of the displacements due to curvature are compared and their difference is quantified as the uncertainty due to the procedure of curvature removal. For all the spindle speeds tested, the maximum difference between the two estimates is found to be within 1 nm (peak-to-peak) for both axial and radial measurements. This is considered as the expanded uncertainty due to the curvature removal procedure.

5.5.6 Total Combined Standard Uncertainty of the Motion Measurements

Taking into account the combined standard uncertainties from all four sources (Measurement device and artifacts (MDA), Environmental Effects (EE), Laser Beam Alignment and Curvature Effects (LACE) and Data Acquisition Parameters and Post-processing Steps (DAPPS)), a total combined standard uncertainty (u_{Total}) can be calculated as

$$u_{Total} = \left(u_{MDA}^2 + u_{EE}^2 + u_{LACE}^2 + u_{DAPPS}^2\right)^{1/2}. \tag{5.7}$$

Using a coverage factor $k = 2$, the total expanded uncertainty can be given as

$$U_{Total} = 2\, u_{Total}. \tag{5.8}$$

Since a normal distribution was assumed for the combined errors of each sources, the assumption of normality would hold for the total errors from all the sources as well. Therefore, including contributors from all the four sources, the measured motions are within $\pm U_{Total}$ with a level of confidence of approximately 95%.

Tables 5.2 and 5.3 show the expanded uncertainties for the individual sources and the total expanded uncertainty for the motions measured at synchronous frequencies (excluding the fundamental frequency for radial measurements) and asynchronous frequencies, respectively. For the calculations presented in Tables 5.2 and 5.3, maximum uncertainty levels due to laser beam alignment and curvature (removal) effects are used: For a once-per-rev amplitude of 6.3 μm seen at 160 krpm, an uncertainty of 5 nm occurs in the radial motions (at a rotation angle of 90^o) and of 15 nm occurs in the axial motions. A rectangular distribution is assumed to determine the standard uncertainty due to this source. Overall, it was seen that the total expanded uncertainty for the fixed-sensitive radial and axial motions at synchronous frequencies are 38 nm and 15 nm, respectively. At asynchronous frequencies, the total expanded uncertainty due to all the sources in both fixed-sensitive radial and axial motions is found to be 32 nm.

Table 5.2: The expanded uncertainty for the motions measured at the synchronous frequencies.

Contributing Sources	**Expanded Uncertainty (nm) (coverage factor, k = 2)**
• **Radial**	
Measurement device and artifacts	38
Environmental Effects	3.5
Laser Beam Alignment and Curvature	5
Data Analysis	0.7
• **Axial**	
Measurement device and artifacts	38
Environmental Effects	3.5
Laser Beam Alignment and Curvature	15
Data Analysis	0.5

Total Expanded Uncertainty including all sources, U_{Total} (nm) (coverage factor, k = 2)	
Radial	**38**
Axial	**41**

Table 5.3: The expanded uncertainty for the motions measured at the asynchronous frequencies.

Contributing Sources	**Expanded Uncertainty (nm) (coverage factor, k = 2)**
• **Radial**	
Measurement device and artifacts	10
Environmental Effects	30
Laser Beam Alignment and Curvature	0
Data Analysis	0.7
• **Axial**	
Measurement device and artifacts	10
Environmental Effects	30
Laser Beam Alignment and Curvature	0
Data Analysis	0.5

Total Expanded Uncertainty including all sources, U_{Total} (nm) (coverage factor, k = 2)	
Radial	**32**
Axial	**32**

5.5.7 Uncertainty in the Rotating-Sensitive Direction Measurements

The overall uncertainty in the radial motions measured along the rotating-sensitive direction can be calculated using the *Law of Propagation of Uncertainty* (*LPU*) as outlined in [130]. The uncertainty in the radial motions along both X- and Y- fixed-sensitive directions (tabulated in Tables 5.2 and 5.3), the angular uncertainty (β) between the X and Y laser beams, and the uncertainty in the rotation angle are propagated through a modified version of Eq. (6.1) given below (Eq. (5.9)).

$$R(\theta) = X(\theta)\,\cos(\theta) + Y(\theta)\,\sin(\theta + \beta). \tag{5.9}$$

Assuming that the uncertainties in each of the individual quantities are independent, according to the *LPU*, the overall uncertainty in R(θ) can be written as

$$\delta R = \left(\left(\frac{\partial R}{\partial X}\delta X\right)^2 + \left(\frac{\partial R}{\partial \theta}\delta \theta\right)^2 + \left(\frac{\partial R}{\partial Y}\delta Y\right)^2 + \left(\frac{\partial R}{\partial \beta}\delta \beta\right)^2 \right)^{1/2}, \tag{5.10}$$

where δX and δY are the uncertainties in the radial motions along the X- and Y- directions that are functions of the rotation angle, $\delta\theta$ is the uncertainty in the rotation angle (i.e., the angular resolution of the zero degree angle), and $\delta\beta$ is β_{max}. The uncertainties δX and δY are calculated by root sum square of the total expanded uncertainties at the fundamental frequency, synchronous frequencies and asynchronous frequencies of the motion measurements along the X- and Y- fixed-sensitive directions, respectively. The uncertainties δX and δY are functions of rotation angle because the uncertainties arising from the compounded effect of laser beam misalignments, curvature of the sphere, and the motions of the sphere are all dependent upon the rotation angle. Since Eq. (5.10) couples uncertainties from different frequency components, the uncertainties for the synchronous and asynchronous components along the rotating sensitive direction cannot be separated when using this procedure.

5.6 Summary and Conclusions

This chapter presented an LDV-based methodology for calculation of axial and radial error motions when using UHS miniature spindles through measurement of motions from the surface of a sphere-on-stem precision artifact. A measurement setup and an alignment procedure are used to align three laser beams in a mutually orthogonal fashion, where the axial laser beam was aligned to coincide with the axis average line. The measured motion data are post-processed, including the removal of artifact-curvature effects, to obtain the synchronous and asynchronous components of the axial and radial error motions in both fixed-sensitive and rotating-sensitive directions, as well as the synchronous error motion values and the standard deviation of asynchronous error motions. The sources and amounts of uncertainties in measuring the motions and in calculating the error motions are then analyzed.

The developed methodology is demonstrated by measuring the error motions when using a UHS spindle with hybrid-ceramic bearings at four different spindle speeds; the measurements confirmed the existence of a significant effect of spindle-speed in error motions when using UHS spindles.

An uncertainty analysis of the presented technique showed that the total expanded uncertainty ($\pm U_{Total}$ with a 95% confidence level) of the synchronous radial error motions is 38 nm in the fixed-sensitive direction. Similarly, the total expanded uncertainty of asynchronous radial error motions is calculated to be 32 nm in the fixed-sensitive directions. For the axial measurements, the total expanded uncertainty is calculated to be 41 nm and 32 nm for the synchronous and asynchronous error measurements, respectively. The most significant contribution to the uncertainties was identified to be the form error of the artifact. Therefore, it is concluded that the presented methodology can be used to determine the axial and radial error motions when using UHS miniature spindles accurately within the aforementioned uncertainty levels.

Chapter 6

Analysis of Axial and Radial Motions of the Miniature UHS Spindle

This chapter presents an experimental analysis of the radial and axial motions of the electrically-driven hybrid-ceramic-bearing miniature UHS spindle used on the dual-stage polishing test-bed. The LDV-based spindle metrology technique described in the previous chapter is used to measure radial and axial motions of the spindle from a sphere-on-stem precision artifact. The presented analysis focuses on identifying the sources of error motions and quantifying them. Since effective application of the mandrel-based polishing process requires a high level of dimensional accuracy, form accuracy, and surface finish, the (unwanted) motions of the UHS spindles must be well-understood. The influence of temperature fluctuations, dynamically-induced effects, contact-bearing defects, and tool-attachment errors on the fundamental, synchronous, and asynchronous components of motions are analyzed. The spindle speeds were varied from 40 krpm to 160 krpm, and the over-hang lengths of 15 mm and 7.5 mm were considered. The variations arising from tool attachment to the collet are also studied.

6.1 Introduction

In addition to slide motions and process mechanics/dynamics [131, 132], attainable accuracy and surface finish during machining processes that utilize spindles are dictated by (unwanted) radial and axial motions of the spindle [5, 133–135]. Although an ideal spindle provides rotation about an axis (i.e., axis of rotation) with no axial and radial motions, actual spindles exhibit error motions that result in non-ideal tool-tip trajectories. The radial tool-tip motions (amplitude of which is known as the tool-tip runout or the total indicator reading (TIR)) have been identified as the leading contributor to the overall error budget on a micro-scale machine tool [136]. Furthermore, the unwanted motions of the tool tip also affect the cutting process mechanics [5,137] and dynamics, as well as the tool wear [5, 138], e.g., by varying the nominal feed rate or depth of cut. Therefore, although there is a consensus on the significance of detrimental effects from unwanted motions of the tool-tip when rotated by a spindle, the radial and axial motions of the UHS spindle that are currently used for micromachining have not been thoroughly analyzed.

As mentioned in the previous chapter, the undesired axial and radial motions of the tool-tip arise from the centering (tool-attachment) errors, tool-profile errors, spindle error motions, and structural error motions [114, 115, 139]. In addition to the quasi-static errors (e.g., due to misalignment of the axis of rotation with the tool axis due to the centering errors), these error sources also result in speed-dependent dynamic error motions of the tool tip [139–141]. The axial and radial motions measured from the shank are also affected by the axis shift caused by the thermal drift of the spindle [114, 115, 142–145]. Thermally-induced growth of the UHS spindles have been shown to have a significant effect during micromachining [146, 147].

Figure 6.1 summarizes the various frequency components and their sources of radial motions along fixed-sensitive directions. The component of radial motion at the fundamental frequency is sometimes referred to as the once-per-revolution component. The spindle error motions do not contribute to the radial motion measured at the fundamental frequency [114, 115], i.e., the fundamental radial motion is not considered to be a property of the spindle. However, the dynamic effects (arising from the centering errors) vary not only with the spindle speed, but also with the non-uniform radial stiffness around the spindle axis as the spindle rotates.

In this chapter, the radial motions at the synchronous frequencies are referred to as the synchronous radial error motions. The two other sources of radial motion at the synchronous frequencies have been dealt with separately: the contribution from the curvature effects is removed from the measurements through simulations during post-processing, and the artifact form errors are considered as an uncertainty in the measurement of the true synchronous radial error motions. The only contributors to the radial motions at asynchronous frequencies are the spindle and structural error motions. The source of the asynchronous radial spindle error motions are the asynchronous bearing error motions and the noise and vibrations from within the spindle with respect to its stator.

Figure 6.2 shows the decomposition of the axial motion into its various frequency components and

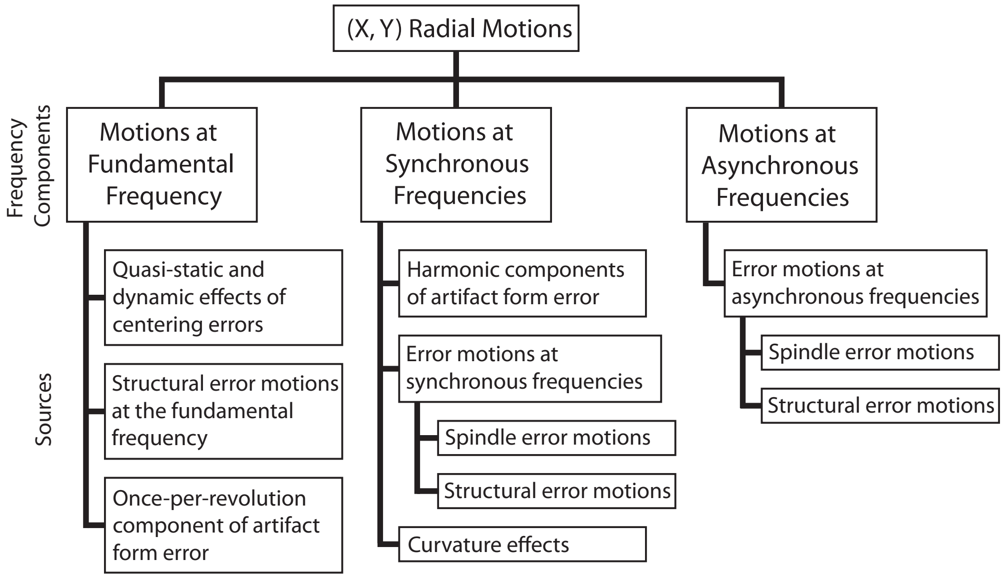

Figure 6.1: Radial motion components and the associated sources.

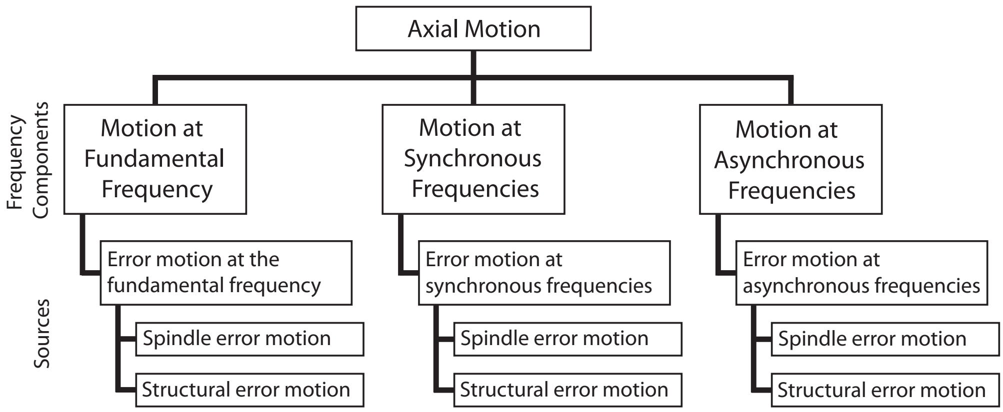

Figure 6.2: Axial motion components and the associated sources.

their sources. The axial motion at the fundamental frequency is referred to as the fundamental axial error motion and the motion at synchronous frequencies is referred to as the residual synchronous axial error motion. Both these axial motions together are referred to as the synchronous axial error motion. The axial motion at the asynchronous frequencies are referred to as the asynchronous axial error motion.

A measure of the synchronous error motion is obtained by calculating the synchronous error motion value and the asynchronous error motion is quantified by calculating its standard deviation across multiple revolutions. These metrics are used for both the radial and axial error motions. In addition, a measure of the residual synchronous axial error motion is obtained by evaluating the *residual synchronous error motion value*, which is defined as the difference between the maximum and minimum residual synchronous axial error motion within a full revolution. In general, the synchronous error motions affect mainly the form accuracy, whereas the asynchronous error motions affect mainly the roughness of the polished surfaces.

6.2 Experimental Methods

The LDV-based measurement technique used for the experimental analysis presented is described in detail in the previous chapter. The radial and axial motions are measured from the surface of a custom-fabricated sphere-on-stem precision artifact.

The UHS spindle used on the dual-stage polishing test-bed is electrically-driven, with hybrid-ceramic bearings (Fischer Precise Model SC1060A). The spindle has two angular contact-bearings with silicon nitride rolling elements and steel races. The bearings are lubricated using an oil-air lubrication system. The spindle is cooled through a continuous supply of a water-based coolant circulated through a refrigeration unit. The refrigerant unit operates through an on/off control system which maintains the coolant temperature at a set point within a certain control dead-band. This causes the coolant temperature to fluctuate about the set point by a certain value determined by the control dead-band. In order to measure the temperatures in the coolant line, miniature resistance temperature detectors (RTDs) are installed at the inlet and outlet locations of the coolant to the spindle (see Fig. 5.3). All experiments are carried out in a lab where the room temperature is controlled to within $\pm 1^{o}$C, with no external heat sources/sinks near the spindle. For all the tests, the spindle is run under no-load operating conditions with the set point temperature in the refrigeration unit set to 20.5^{o}C with a control dead-band fixed at $\pm 1.25^{o}$C around the set point.

6.2.1 Data Acquisition and Post-Processing

For each pairwise LDV measurements, a data set consisting of (X, Y) or (Z, Y) motions of the sphere surface, the pulse signal from the IR sensor, and the inlet and outlet coolant temperatures is simultaneously acquired for a short-term period of 0.75 seconds. A LabView$^{\text{TM}}$code is written to synchronize the data from the LDV systems, IR sensor and the RTDs. In addition, a separate set of measurements of the inlet and outlet coolant temperatures are conducted for relatively long durations (up to 6 minutes). As per the manufacturer's recommendation, each time the spindle

Table 6.1: Measurement parameters at the lowest and highest spindle speeds.

	Data Sampling Angular Resolution	**Zero Degree Resolution**	**Total Number of Revolutions**
Minimum Spindle Speed (40 krpm)	0.5^o	0.05^o	500
Maximum Spindle Speed (160 krpm)	1.9^o	0.19^o	2000

was first started, it was run at 40 krpm for at least 15 minutes before any data is acquired.

6.2.1.1 Radial and Axial Motion Data

The radial and axial motion data are acquired at a sampling rate of 500 kHz using a 16-bit data acquisition card (National Instruments^{TM}(NI)-6259). In order to resolve the reference angular position accurately, the 5 V pulse signal from the IR sensor is acquired at a much higher sampling rate of 5 MHz using a different data acquisition card (NI-6115). The angle at which the trailing edge of the pulse crosses 2.5 V amplitude is chosen as the beginning (i.e., $\theta = 0$) of each revolution, where θ is the rotation angle. Due to the fixed sampling rates and data acquisition period, the angular resolution of the motion data, resolution of the zero-degree orientation, and the total number of revolutions for which data is acquired will change with the spindle speed (see Table 6.1).

Accurate decomposition of the motions into their various frequency components requires careful post-processing. To eliminate the low-frequency drift due to the LDV systems and ambient conditions, the raw motion data is filtered using a zero phase-shift high-pass filter with a cut-off frequency of 50 Hz. The transient effects of the high-pass filter are removed by discarding 15% of the total revolutions at the beginning and end of the data. The reference signal from the IR sensor is used to map the motions from the time domain to an angular domain.

For the sphere-on-stem artifact used in this work, sharp notches spanning approximately 7.5^o in the angular-domain are observed in both the X- and Y-motions at two different angular locations in each revolution. By examining the sphere using a white light interferometer, these were identified as defects on the surface of the sphere that are approximately 200 μm wide and 250 nm deep. Before further post-processing, the notches are removed individually from the data and replaced with interpolated data obtained through a shape-preserving piecewise cubic interpolation of the motions at the beginning and end of the notch locations.

As described in the previous chapter, a computer code is used to simulate the axial and radial measurements by assuming nominal orientation of the laser beams. Curvature effects along the (X,Y,Z)-directions are estimated by subtracting the measured motions from their respective simulated motions. The actual motions of the sphere center are then obtained by subtracting the curvature effects from the measured motions. This is done for each revolution of the measured data, resulting in a new set of (X,Y,Z)-motions without the curvature effects.

Further processing is done to calculate (a) the centering errors, (b) the synchronous and asynchronous radial error motions along the fixed-sensitive and rotating-sensitive directions, (c) the fundamental axial error motion, (d) the residual synchronous axial error motion and (e) the asynchronous axial error motion. The asynchronous error motions have a better physical interpretation in the time domain rather than in the angular domain. Hence, those motions are mapped back to the time domain for subsequent analysis.

6.2.1.2 Temperature Data

The inlet and outlet RTDs are calibrated and the resistances of their output circuitry are chosen to maximize the overall temperature sensitivity. With this setup, the minimum detectable temperature change is 0.05°C. All temperature measurements are acquired at a sampling rate of 1 kHz. For the temperature data acquired along with the displacements signals, it is sufficient to calculate just the mean values of the inlet and outlet temperatures. However, the long-term temperature measurements require further data processing.

A typical plot of the raw long-term inlet and outlet temperature data is shown in Fig. 6.3(a). Due to the on/off cycling of the coolant refrigeration unit, the inlet and outlet temperatures of the coolant circulating through the spindle are observed to change at a certain frequency. These temperature measurements are used to determine the mean and range statistics of both the inlet and outlet temperatures within one thermal cycle. As a first step, the temperature data is passed through a zero phase-shift low-pass filter with a cut-off frequency of 10 Hz to eliminate the high-frequency temperature fluctuations. The transient effects of the low-pass filter are removed by discarding 20 seconds of the filtered data at the beginning and the end. Then, a computer code is used to identify one full thermal-cycle and compute the inlet and outlet temperature means and ranges for that cycle. Figure 6.3(b) illustrates the results for one of the cycles of the raw data shown in Fig. 6.3(a).

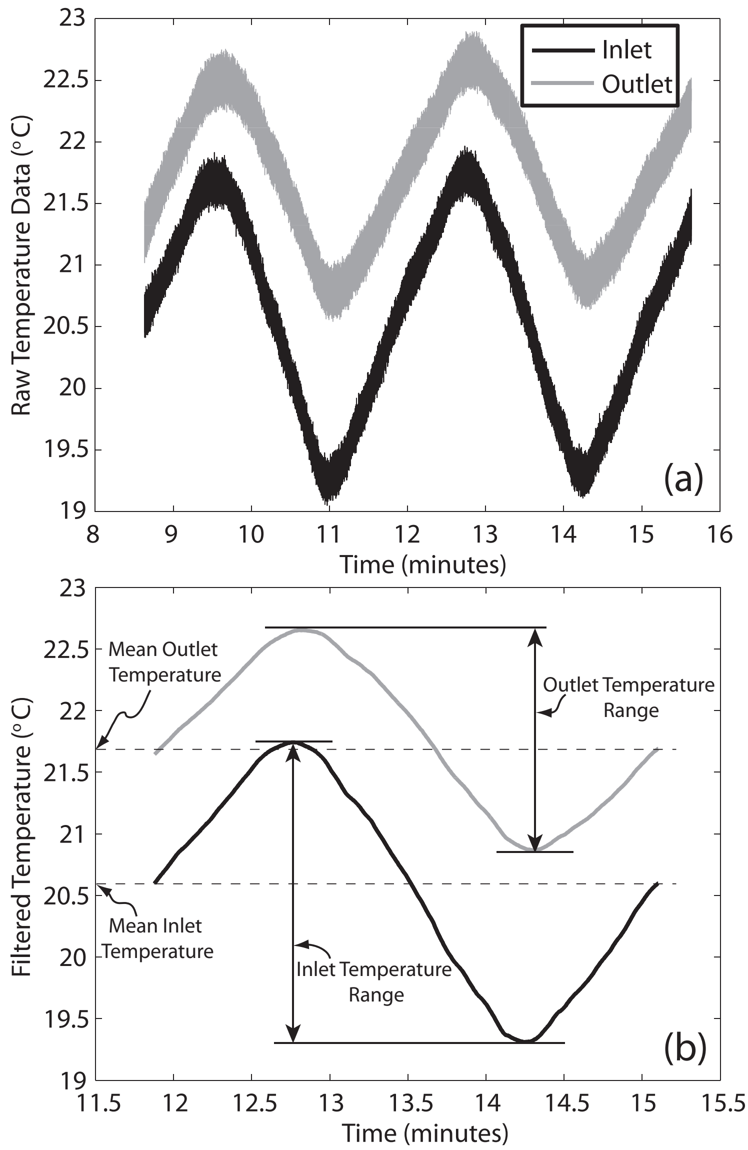

Figure 6.3: (a) Typical temperature data from the inlet and outlet, and (b) Temperature data after low-pass filtering and calculation of the mean and the range.

6.3 Thermal Characteristics of the Spindle

The inlet and outlet temperatures of the coolant are considered to be representative of the internal thermal state of the spindle. Characterization of the thermal behavior of the spindle involves (i) quantifying the time it takes for the internal thermal state of the spindle to reach a thermal equilibrium when a step change in speed occurs, and (ii) identifying the change in the internal thermal state with spindle speed. Two sets of experiments, which comprise of only long-term temperature measurements, are conducted to study these characteristics. The first set of experiments is conducted to study the thermal state of the spindle for a long duration (an hour) after a step change in spindle speed is imposed. Five different step changes are considered (40 krpm to 50 krpm, 50 krpm to 100 krpm, 100 krpm to 160 krpm, 160 krpm to 100 krpm and 100 krpm to 50 krpm), spanning the total speed range of the spindle. After each speed change, the inlet and outlet temperature data is acquired for a period of six minutes with 10 minute intervals, for a total period of an hour. The mean values and ranges of the thermal cycles are calculated and analyzed as a function of time.

For the second set of experiments, the spindle speed is changed in steps of 10 krpm spanning the entire range from 40 krpm to 160 krpm. After each speed change, the spindle is allowed to run for 5 minutes before acquiring the inlet and outlet temperature data. The mean values and the ranges of the thermal cycles are calculated to quantify the changes in thermal state as a function of spindle speed. Both sets of experiments are repeated on two different days to check repeatability.

Figure 6.4 shows the variation of mean values and ranges of the inlet and outlet temperature as a function of time for two of the five step changes studied - step up from 100 krpm to 160 krpm (Fig. 6.4(A)) and step down from 100 krpm to 50 krpm (Fig. 6.4(B)). The step changes shown represent the worst case scenarios in temperature changes as observed from the results of all the five cases. In both cases, the mean temperatures on the two different days are repeatable within 0.1°C. There is a weak transient behavior observed in the first 15 - 20 minutes after the step change in speed. However, the magnitude of the change in the mean (or range) of the outlet (or inlet) temperatures within the transient period is less than 0.3°C. The thermal equilibrium is reached after the first 20 minutes of a speed change. In the case of the smallest step change in speed (from 40 krpm to 50 krpm (not shown)), it is observed that the thermal equilibrium is reached within 5 minutes.

Figures 6.5(a) and 6.5(b) show the mean values and temperatures ranges, respectively, of the inlet and outlet temperatures as a function of spindle speed. The mean temperatures are repeatable within 0.25°C on the two different days. It is observed that while the mean inlet temperature remains constant across the entire speed range, the mean outlet temperature steadily increases with spindle speed following a certain trend, and changes by about 1°C when the speed changes from 40 krpm to 160 krpm. The range of inlet and outlet temperatures are almost constant with spindle speed.

The constant nature of the mean value of inlet temperature and the ranges of both inlet and outlet temperatures can be explained by considering the fact that these parameters are directly

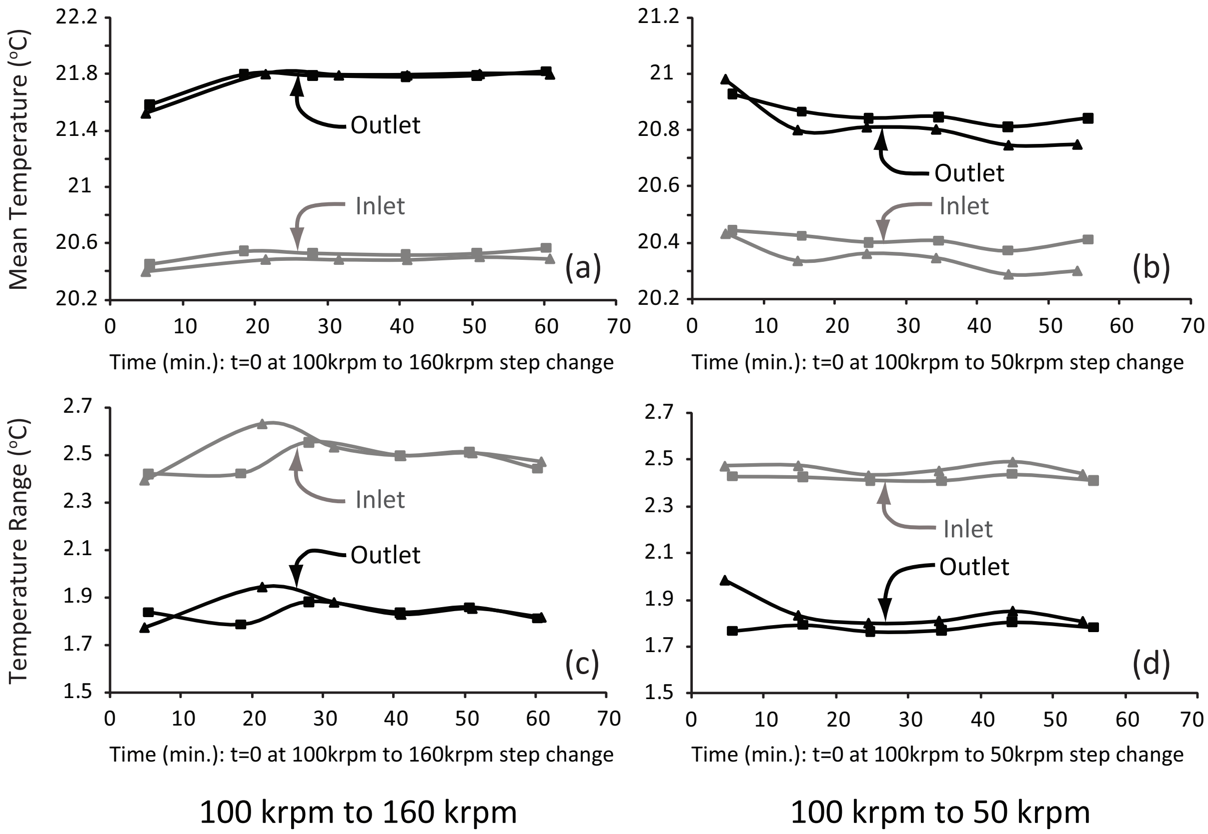

Figure 6.4: Inlet and outlet temperatures as a function of time after a step change in speed at time zero: Mean temperatures when the speed is (a) increased from 100 krpm to 160 krpm, and (b) reduced from 100 krpm to 50 krpm. The temperature ranges when the speed is (c) increased from 100 krpm to 160 krpm, and (d) reduced from 100 krpm to 50 krpm.

controlled by the coolant refrigeration unit. The set point temperature in the refrigeration unit governs the mean inlet temperature while the range of the control dead-band governs the inlet and outlet temperature ranges. The outlet temperature range being lower than the inlet temperature range is due to the large thermal mass of the spindle which would attenuate the inlet temperature swings. The mean values of the outlet temperature, however, are governed by both the mean values of the inlet temperatures as well as the heat generated from within the spindle. Since there is a greater amount of heat generated within the spindle at higher spindle speeds, the mean outlet temperatures are seen to rise with spindle speed.

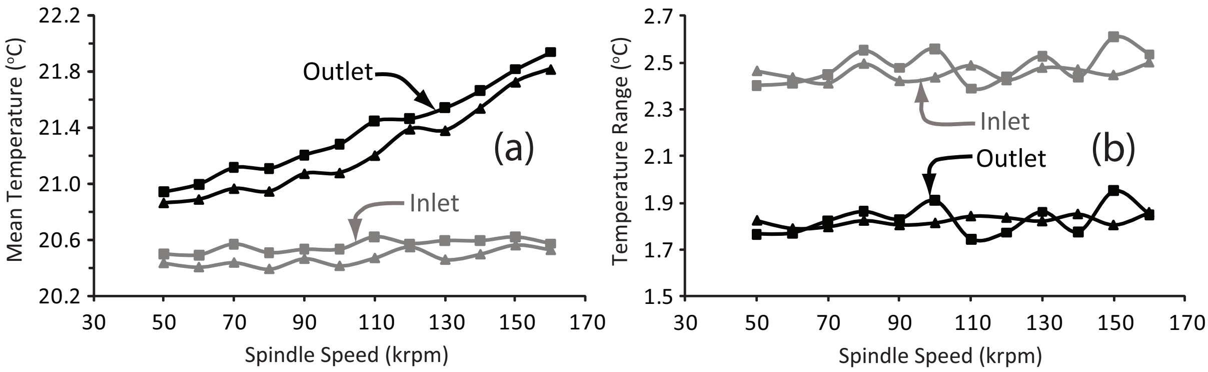

Figure 6.5: Inlet and outlet temperatures as a function of spindle speed: (a) Mean temperature, and (b) Temperature range.

6.4 Experimental Analysis of Radial and Axial Motions

6.4.1 Effect of Thermal Cycling on Radial and Axial Motions

The changes in the internal thermal state could affect the radial and axial motions of the spindle. To quantify this effect, axial and radial motions are measured at different thermal states of the spindle at a given speed by acquiring the short-term data sets (which include axial and radial motions and temperatures) for a period of 0.75 seconds, at 20 second intervals throughout at least one thermal cycle. These measurements are performed for at least two temperature cycles to ensure repeatability. The speeds studied are 40 krpm, 50 krpm, 70 krpm, 100 krpm, 130 krpm and 160 krpm.

For the subsequent experimental studies, to eliminate (or reduce) the effects of thermal cycling on the measured axial and radial motions, the inlet temperature is monitored, and the radial and axial motion measurements are conducted at the same thermal state that corresponds to the inlet temperature at its maximum value.

Figures 6.6 and 6.7 show changes in the different components of radial and axial motions, respectively, during various thermal cycles. The different components that are shown in these figures are: (A) amplitude of the fundamental frequency, (B) synchronous radial error motion value (or residual synchronous axial error motion value), and (C) 1σ of the asynchronous error motion. For each of these components, the tested speed that shows the maximum correlation between the thermal cycling and the variation of the values of that component is shown in these plots. The inlet and outlet temperatures shown are the respective mean temperatures calculated over the 0.75 seconds, during which time the displacement data was acquired.

At some spindle speeds, a high level of correlation between the radial and axial motion components and the thermal state of the spindle is observed. The thermal cycling is seen to cause up to 30 nm change in the amplitude of the fundamental component of radial motion, which is a low percentage compared to the mean value of the fundamental component observed in this work. On the other hand, the synchronous radial error motion value is seen to change by up to $\pm 30\%$, and the 1σ asynchronous radial error motion is seen to change by up to $\pm 4\%$. For the axial motions, up to $\pm 40\%$ change in fundamental axial error motion is observed. The changes in the residual synchronous error motion value and the 1σ asynchronous axial error motion are seen to be as large as $\pm 10\%$. In the synchronous radial and residual synchronous axial error motions, in addition to the error motion values, amplitudes of the dominant harmonic components are also observed to follow a cyclic pattern in correlation with the thermal cycling. Although all the effects mentioned are not present at all speeds, at certain speeds, some of the changes in radial and axial motions due to thermal cycling are significant and would affect the spindle performance when fabricating micro-scale features at those speeds.

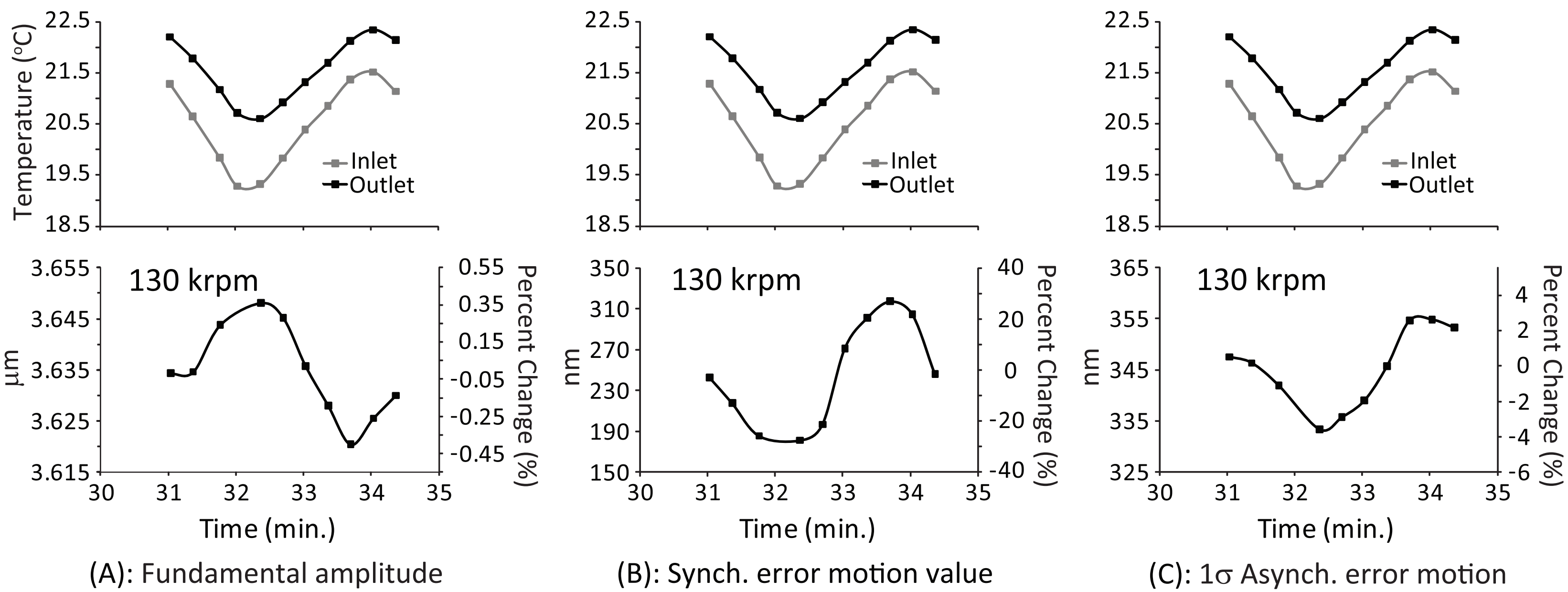

Figure 6.6: Correlation between thermal cycling and radial motion components: (A) Motion at fundamental frequency, (B) Synchronous radial error motion and (C) Asynchronous radial error motion.

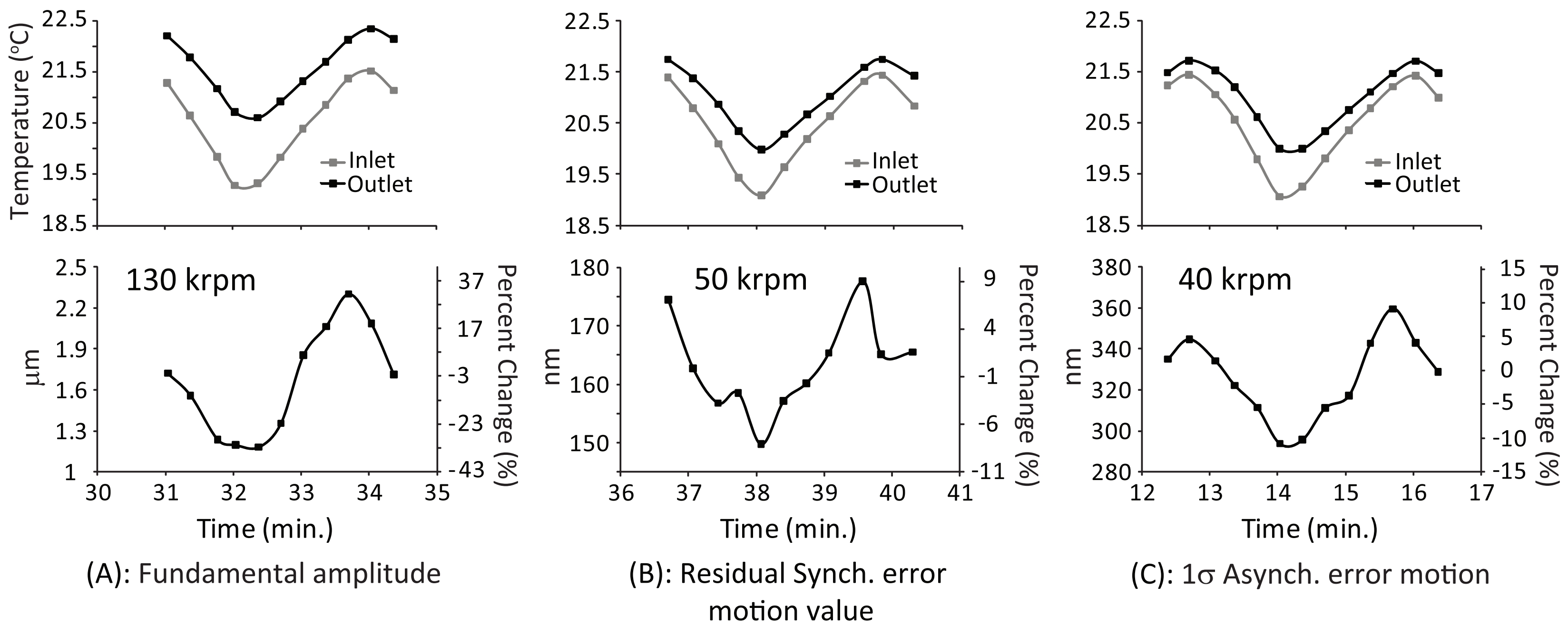

Figure 6.7: Correlation between temperature cycling and axial motion components: (A) Fundamental axial error motion, (B) Residual synchronous axial error motion and (C) Asynchronous axial error motion.

6.4.2 Effect of Spindle Speed and Over-hang Length

The dynamic behavior of the spindle directly affects its error motions. The dynamic response of the spindle depends upon the spindle speed and the artifact (tool) insertion and over-hang lengths. Further, for contact-bearing spindles, the defects in the inner and outer races of the bearings also affect the performance of the spindle as a function of speed.

To quantify the effects of the spindle speed and over-hang length, experiments are conducted at spindle speeds ranging from 40 krpm to 160 krpm in steps of 10 krpm for over-hang lengths of 7.5 mm and 15 mm. The total length of the artifact is 26 mm. It is noted that since the total artifact length is constant, when the over-hang length is changed, the insertion length also changes accordingly. After each speed change, the spindle is run for 5 minutes. Subsequently, the short-term data sets are acquired. Three sets of measurements are conducted to assess repeatability.

Unless otherwise specified, all the plots shown in this section show averaged quantities, with the average taken across the three different runs of the motion data. Further, along with the average value, error bars are shown on either side of the average to represent the minimum and maximum values measured during the three runs.

6.4.2.1 Radial Motions

Figure 6.8 shows the amplitudes of motion at the fundamental frequency along fixed-sensitive X- and Y-directions versus spindle speed at both over-hang lengths. For a given over-hang length, since all the tests were conducted in one single setup, the quasi-static portion of the centering errors does not change. It can be seen that up to 100 krpm, the fundamental amplitudes of motion are almost constant at both over-hang lengths, which may indicate dominance of the quasi-static effect. Above 100 krpm, the dynamics effects begin to dominate, resulting in the fundamental amplitudes increasing with spindle speeds. The over-hang length also plays a significant role: the longer the artifact over-hang, the faster the rate of increase of fundamental amplitude with spindle speed. As observed in the case of 7.5 mm over-hang length, it is possible that the increase will peak at a certain higher spindle speed, which may occur when the rotational frequency overlaps with a natural frequency of the system. Such a phenomena was also observed in one of the earlier works [127].

The amplitude and phase (from 90^o) differences between the X- and Y-motions at the fundamental frequency are indicative of non-axisymmetric radial stiffness of the spindle. In such cases, the dynamic effects result in elliptical trajectories at the fundamental frequency. Figure 6.9(a)

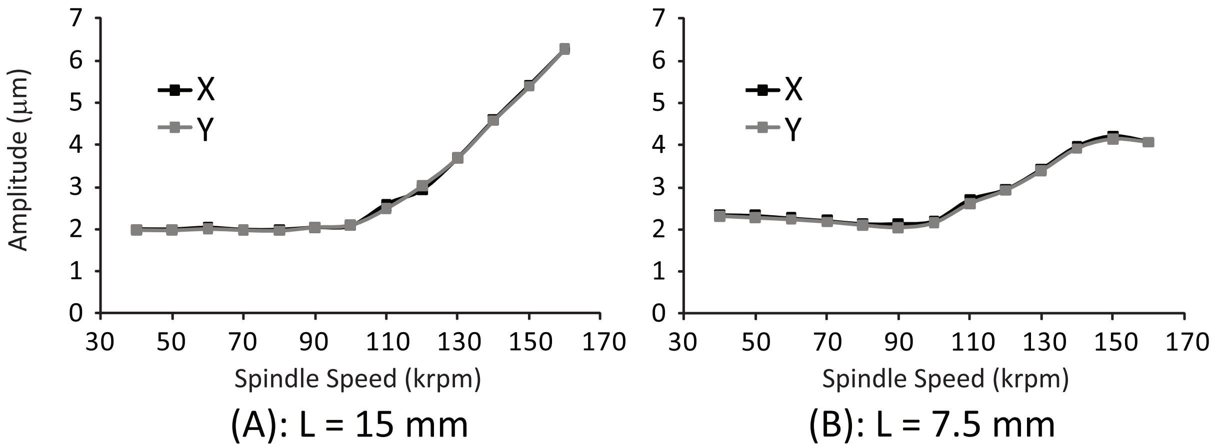

Figure 6.8: Amplitudes of motion at the fundamental frequency along fixed-sensitive X- and Y-directions versus spindle speed: (A) Over-hang length = 15 mm, (B) Over-hang length = 7.5 mm.

shows the amplitude difference between the fundamental amplitudes along fixed-sensitive X- and Y-directions versus spindle speed at both over-hang lengths. Across most speeds, at both over-hang lengths, the differences are below 75 nm, with a maximum of 100 nm. Figure 6.9(b) shows the phase difference between X- and Y-motions at the fundamental frequency versus spindle speed at both over-hang lengths. To ensure that the phase differences observed are not due to misalignment of the X- and Y-laser beams from 90^{o}, the angle between the laser beams is verified (using the phase difference between the average angular location of the notches as seen in X- and Y-data) to be within the angular resolution of the data (as indicated by the gray dashed lines). Hence, for the speeds at which the fundamental phase difference between X- and Y-motions is higher than the angular resolution, it can be concluded that the dynamic effects are prominent.

Figure 6.10 shows polar plots of synchronous radial error motions along the fixed-sensitive and rotating-sensitive directions for one of the three repetitions. Since the location of the black mark varies when the artifact is re-attached, the physical angular orientation of the spindle corresponding to the zero-degree differs between the tests conducted at different over-hang lengths. Significant differences in synchronous radial error motions are observed across various speeds for both over-hang lengths. For example, for 15 mm over-hang length, the motion along the fixed-sensitive X-direction changes from a 6-lobed pattern at 40 krpm to a 3-lobed pattern at 120 krpm. Also, the error motions along X- and Y-directions have similar shapes but different amplitudes. Further, for some speeds (e.g., 90 krpm and 160 krpm), the over-hang length changes the shape significantly. The amplitude levels at the longer over-hang length are generally higher than those at the shorter

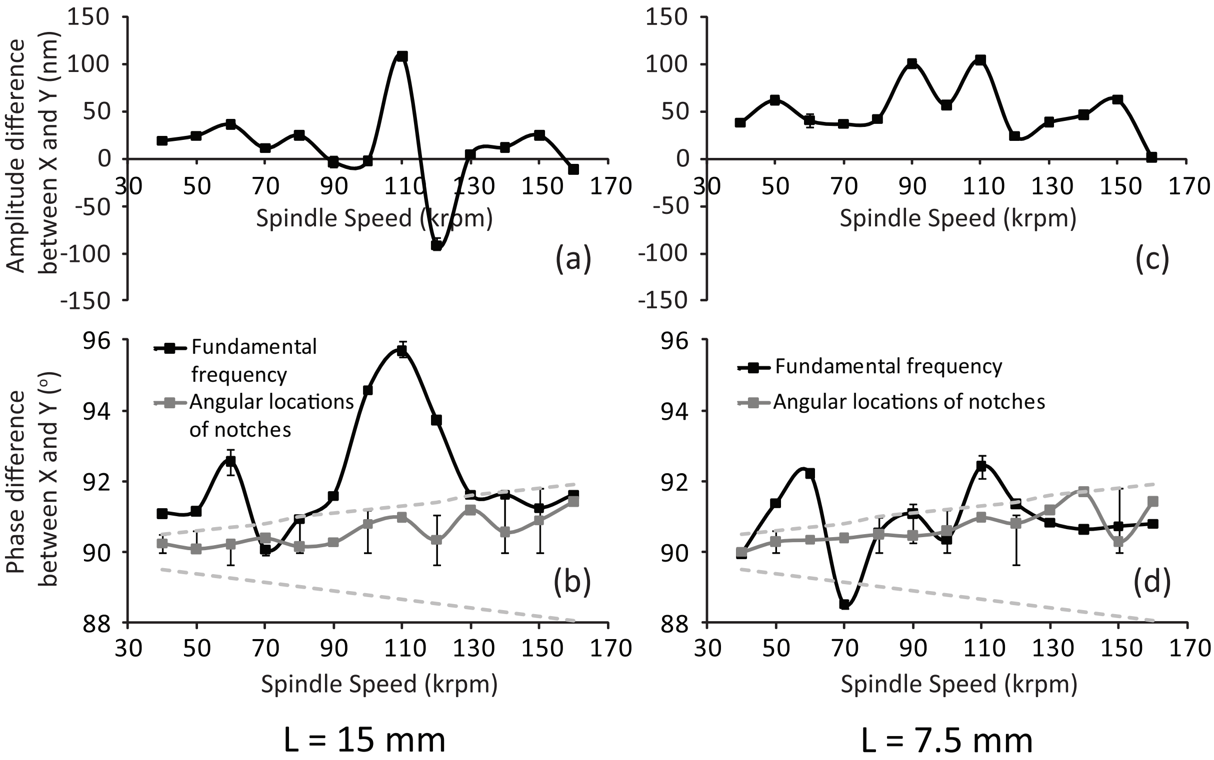

Figure 6.9: Difference between X- and Y- (a) fundamental amplitudes and (b) phases for overhang length of 15 mm; Difference between X- and Y- (c) fundamental amplitudes and (d) phases for overhang length of 7.5 mm. The average phase difference between the angular locations of notches as seen in X- and Y-data are indicated in (b) and (d).

over-hang length at most speeds. At certain speeds (e.g., 120 krpm and 160 krpm), this difference is very significant.

When calculating the synchronous radial error motions along the rotating-sensitive direction, a constant-radius least-square circle is fitted and removed from the average motion across multiple revolutions. Due to this procedure, an elliptical trajectory (caused by the fundamental frequency components along the fixed-sensitive directions) would result in a 2-lobed residual motion, as observed in the polar-plots in many cases. Figure 6.11 shows the magnitude of the Fourier transforms of the synchronous radial error motions (along fixed-sensitive and rotating-sensitive directions). The motions observed in Fig. 6.10 are equivalently seen as amplitudes of the respective harmonics corresponding to the lobed-shapes.

The significant difference in shapes of error motions along the rotating-sensitive direction compared to the fixed-sensitive directions could be explained as follows. For motions $X(\theta)$ and $Y(\theta)$ along the fixed-sensitive directions that are composed of only the n^{th} harmonic, the motion $R(\theta)$

along the rotating-sensitive direction can be written as

$$\begin{aligned} R(\theta) &= X(\theta)\cos\theta + Y(\theta)\sin\theta \\ &= A_1 \sin(n\theta+\phi_1)\cos\theta + A_2 \sin(n\theta+\phi_2)\sin\theta \\ &= K_1 \sin((n+1)\theta+\alpha) + K_2 \sin((n-1)\theta+\beta), \end{aligned} \tag{6.1}$$

where θ is the rotation angle, K_1, K_2, α and β are functions of the amplitudes (A_1, A_2) and phases (ϕ_1, ϕ_2) of the motions along the X- and Y-directions. The motions at the n^{th} harmonic along the X- and Y-directions would be observed at both $(n+1)^{th}$ and $(n-1)^{th}$ harmonics along the rotating-sensitive direction. For motion at the fundamental frequency along fixed-sensitive directions, n becomes unity. In this case, if $A_1 \neq A_2$ and/or (ϕ_1-ϕ_2) $\neq 90^o$, then $K_1 \neq 0$, implying the presence of a 2^{nd} harmonic component along the rotating-sensitive direction due to the amplitude and phase (from 90^o) differences between the X- and Y-motions at the fundamental frequency. Large 2^{nd} harmonic amplitudes can be observed in Fig. 6.11 for cases corresponding to large amplitude and phase (from 90^o) differences seen in Fig. 6.9. However, if the 3^{rd} harmonic is also present along either of the fixed-sensitive directions, it would further distort the amplitude of the 2^{nd} harmonic along the rotating-sensitive direction.

Figure 6.12 shows synchronous radial error motion values (along fixed-sensitive and rotating-sensitive directions). Similar values are observed for motions along the X- and Y-directions. At speeds of 110 - 130 krpm and 160 krpm with 15 mm over-hang length, the synchronous error motion values are greater than 250 nm and reach up to 500 - 600 nm. At all other speeds, the values are less than 250 nm. The values observed for the shorter over-hang length are 15% to 75% lower than those at the longer over-hang length for all the speeds. Overall, it can be concluded that the synchronous radial error motion shapes and values are highly dependent on the dynamic effects, and are thus affected significantly by the spindle speed and over-hang length.

Figure 6.13 shows the magnitude of the Fourier transforms of the fixed-sensitive asynchronous radial error motions along the X-direction. Many of the dominant peaks exhibit a speed-dependent shift in frequency. Although some dominant frequencies are different for different over-hang lengths, others do not vary with the over-hang length. The amplitudes of the dominant peaks are generally lower at the shorter over-hang length than those at larger over-hang length.

When the frequencies of the dominant peaks are compiled at different rotational frequencies, linear trends are observed at different slopes. Such a behavior is common to the bearing frequencies of rolling-element contact-bearings [148, 149]. Therefore, to determine whether the measured asynchronous frequencies arise from the angular contact-bearings used on the test spindle, the four characteristic bearing frequencies are calculated as,

$$\omega_t = \left[0.5 - \frac{D_b}{2D_p} cos\theta_c\right]\Omega, \tag{6.2}$$

$$\omega_s = \left[\frac{D_p}{2D_b}\left(1 - \left(\frac{D_b}{D_p} cos\theta_c\right)^2\right)\right]\Omega, \tag{6.3}$$

$$\omega_o = \left[N_b\left(0.5 - \frac{D_b}{2D_p} cos\theta_c\right)\right]\Omega, \tag{6.4}$$

$$\omega_i = \left[N_b\left(0.5 + \frac{D_b}{2D_p} cos\theta_c\right)\right]\Omega. \tag{6.5}$$

where Ω is the rotational frequency, ω_t is the fundamental train frequency, ω_s is the ball spin frequency, and ω_o and ω_i are the ball pass frequencies for outer and inner race, respectively [148,149]. Note that these frequencies are linearly related to spindle frequency, where the slopes are given in the square parentheses. For the test spindle, the ball diameter, D_b, is 3.175 mm, pitch diameter, D_p, is 13.343 mm, the number of rolling elements, N_b, is ten, and the contact angle, θ_c is 13^o. Using these bearing parameters, the slopes m_t, m_s, m_o, and m_i (corresponding to ω_t, ω_s, ω_o, and ω_i) can be calculated as 0.384, 1.988, 3.841, and 6.159, respectively. It is expected that the bearing error motions are present at frequencies not only corresponding to these slopes, but also their various combinations [149, 150].

As seen in Table 6.2, the slopes observed in the asynchronous radial error motions match very closely with the slopes calculated from various frequency combinations. Therefore, it can be concluded that most of the asynchronous radial error motions arise from the error motions of the contact-bearings. It is also expected that those frequencies do not vary with over-hang length, which is further observed from measurement results shown in Table 6.2.

To examine the complete frequency content, a surface plot of the magnitude of the Fourier transform of asynchronous radial error motion is created as a function of spindle speed as shown in Fig. 6.14. Since the same frequencies were observed in both radial directions, only the fixed-sensitive asynchronous radial error motion along the X-direction is analyzed. The identified bearing frequencies are shown as white dots and their trend is illustrated by lines (with slopes given in Table 6.2).

For the over-hang length of 15 mm, dominant peaks at three other frequencies are observed (as

Table 6.2: Comparison of frequency-speed slopes calculated from the bearing frequencies with those from the experiments for fixed-sensitive asynchronous radial error motions.

Calculated slopes using bearing frequencies		**Observed slopes**	
Frequency combination	Slope	L = 15 mm	L = 7.5 mm
m_{ω_t}	0.384	0.384	0.384
$m_{\omega_o} - 2$	1.841	1.841	1.839
$m_{\omega_o} - 1$	2.841	2.833	2.833
m_{ω_o}	3.841	3.834	3.832
$m_{\omega_t} + 2m_{\omega_s}$	4.361	4.358	4.359
$m_{\omega_o} + 1$	4.841	4.825	4.828
$16m_{\omega_t} - 1$	5.145	5.131	5.133
$2m_{\omega_o} - 2$	5.681	5.669	5.670
$m_{\omega_o} + 2$	5.841	5.821	5.822
$m_{\omega_t} + 3m_{\omega_s}$	6.349	6.344	6.347
$2m_{\omega_o} - 1$	6.681	6.682	6.682
$16m_{\omega_t} + 1$	7.145	7.121	7.125
$2m_{\omega_o}$	7.681	7.663	7.666

dark bands) between 6.5 - 11.5 kHz at speeds below 100 krpm. Above 100 krpm, two of these peaks attenuate significantly. The remaining peak shifts gradually from 6.5 kHz at 40 krpm to 5.3 kHz at 160 krpm. For the over-hang length of 7.5 mm, only two peaks (at 7.7 kHz and 10.2 kHz) are observed and they are visible only up to 80 krpm. These observed frequencies for both over-hang lengths could be related to the natural frequencies of spindle, artifact, and structural dynamics.

The frequency content of the rotating-sensitive asynchronous radial error motions is analyzed in Fig. 6.15. A significantly larger number of dominant frequencies are seen in the rotating-sensitive direction than those in the fixed-sensitive directions. This could be explained by Eq. (6.1), by considering n to be a non-integer. Hence, any asynchronous frequency ω present in the motions along the fixed-sensitive directions will give rise to two frequencies ($\omega \pm \Omega$) in the motions along the rotating-sensitive direction.

To provide a measure of the magnitude of asynchronous radial error motions, the 1σ values are calculated for both the fixed-sensitive and rotating-sensitive directions (see Fig. 6.16). Except for a few speeds, the 1σ values for the shorter over-hang length are lower by 30% to 80% than those for the longer over-hang length. The maximum 1σ values of the asynchronous error motions are seen at 60 krpm along the X-direction: This motion is mainly at 3.8 kHz, which overlaps the ball pass frequency of the outer race (ω_o) at 60 krpm. However, since the large amplitude is seen only along the X-direction (and not along the Y-direction), this motion could be arising from a structural resonance of the spindle housing, with a mode-shape having a large motion along the X-direction. For all other speeds, the 1σ values are below 800 nm and 600 nm for the 15 mm and 7.5 mm over-hang lengths, respectively.

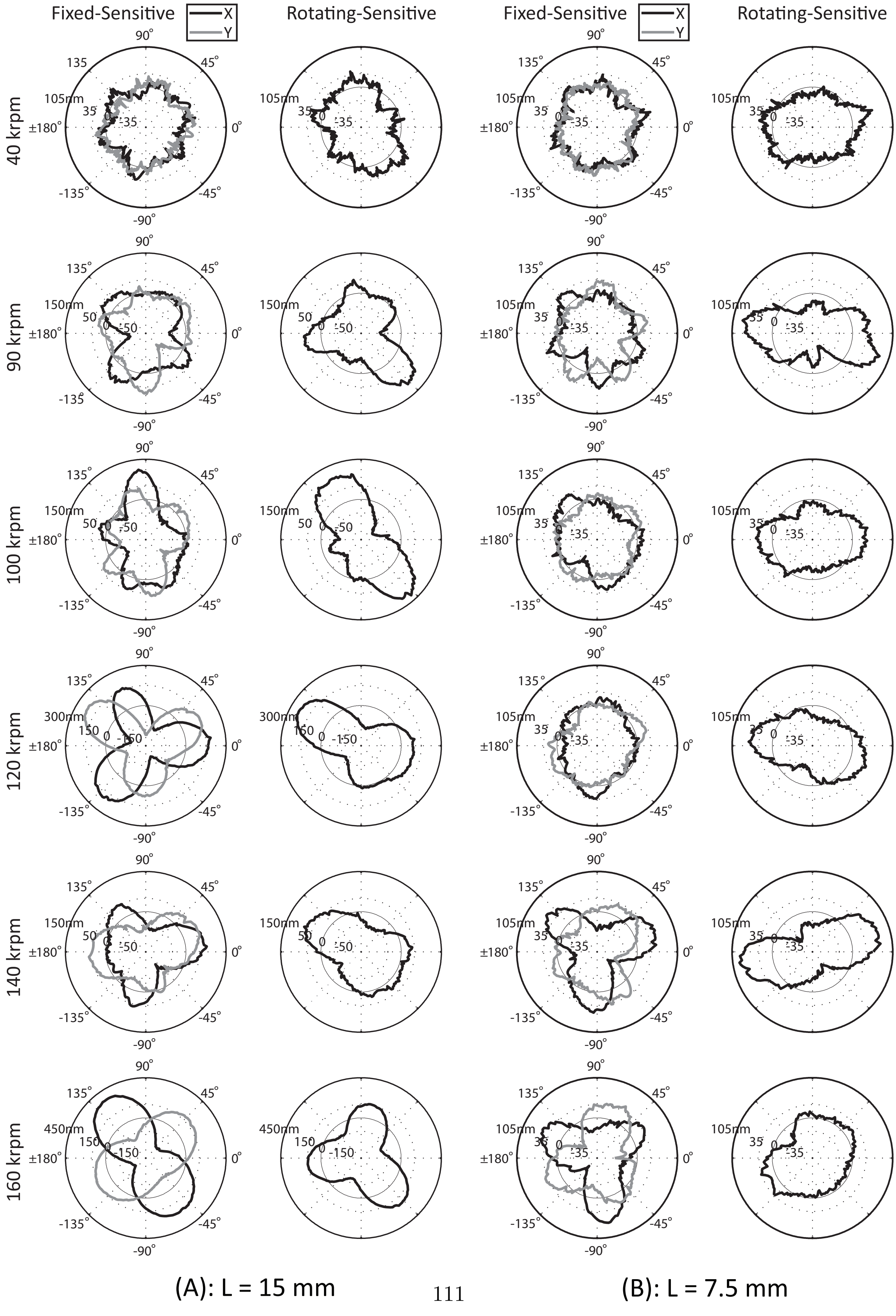

Figure 6.10: Polar plots of synchronous radial error motion along the fixed-sensitive X- and Y-directions and rotating-sensitive direction at different spindle speeds: (A) Over-hang length = 15 mm, (B) Over-hang length = 7.5 mm.

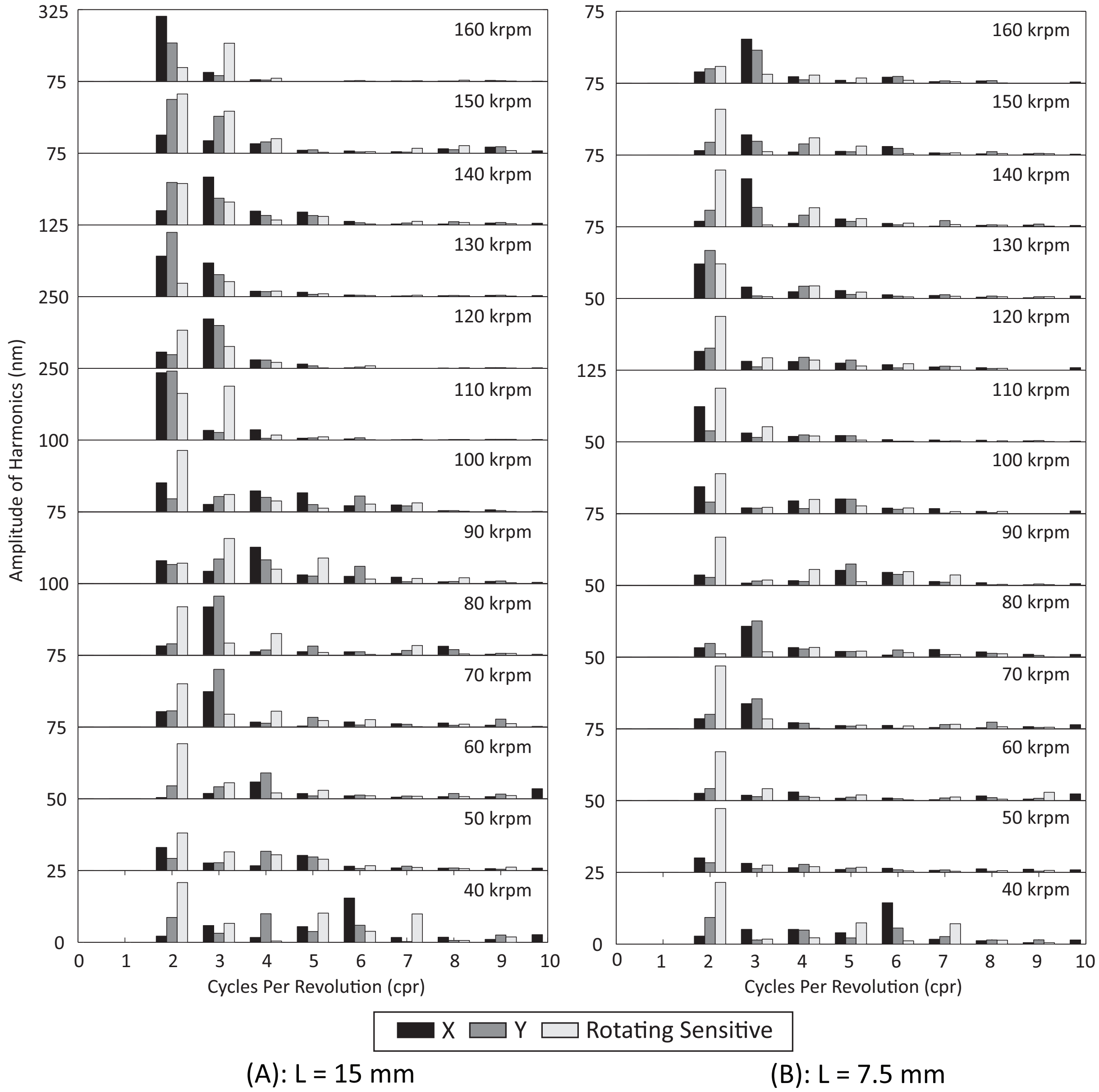

Figure 6.11: Magnitude of the Fourier transforms of synchronous radial error motion along fixed-sensitive X- and Y-directions and rotating-sensitive direction at all spindle speeds: (A) Over-hang length = 15 mm, (B) Over-hang length = 7.5 mm.

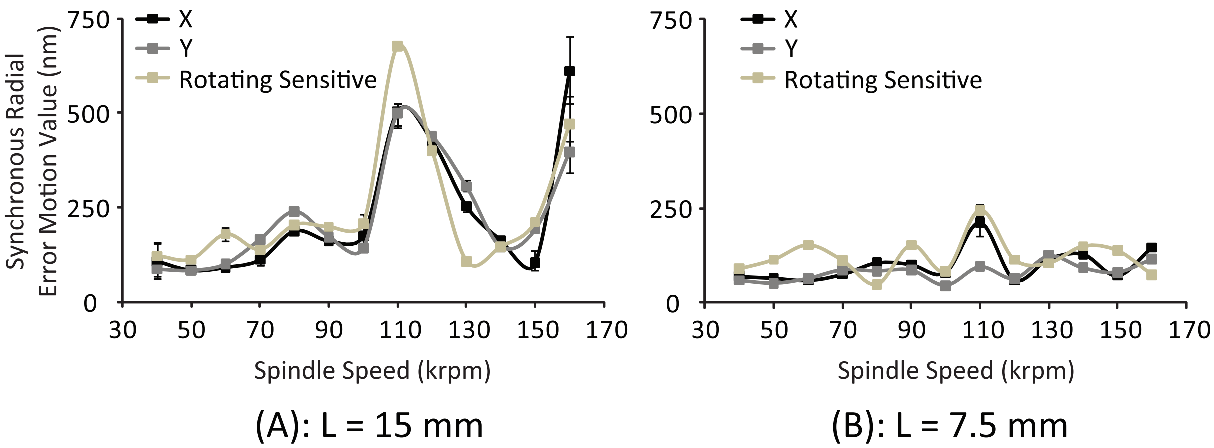

Figure 6.12: Synchronous radial error motion values along fixed-sensitive X- and Y-directions and rotating-sensitive direction versus spindle speed: (A) Over-hang length = 15 mm, (B) Over-hang length = 7.5 mm.

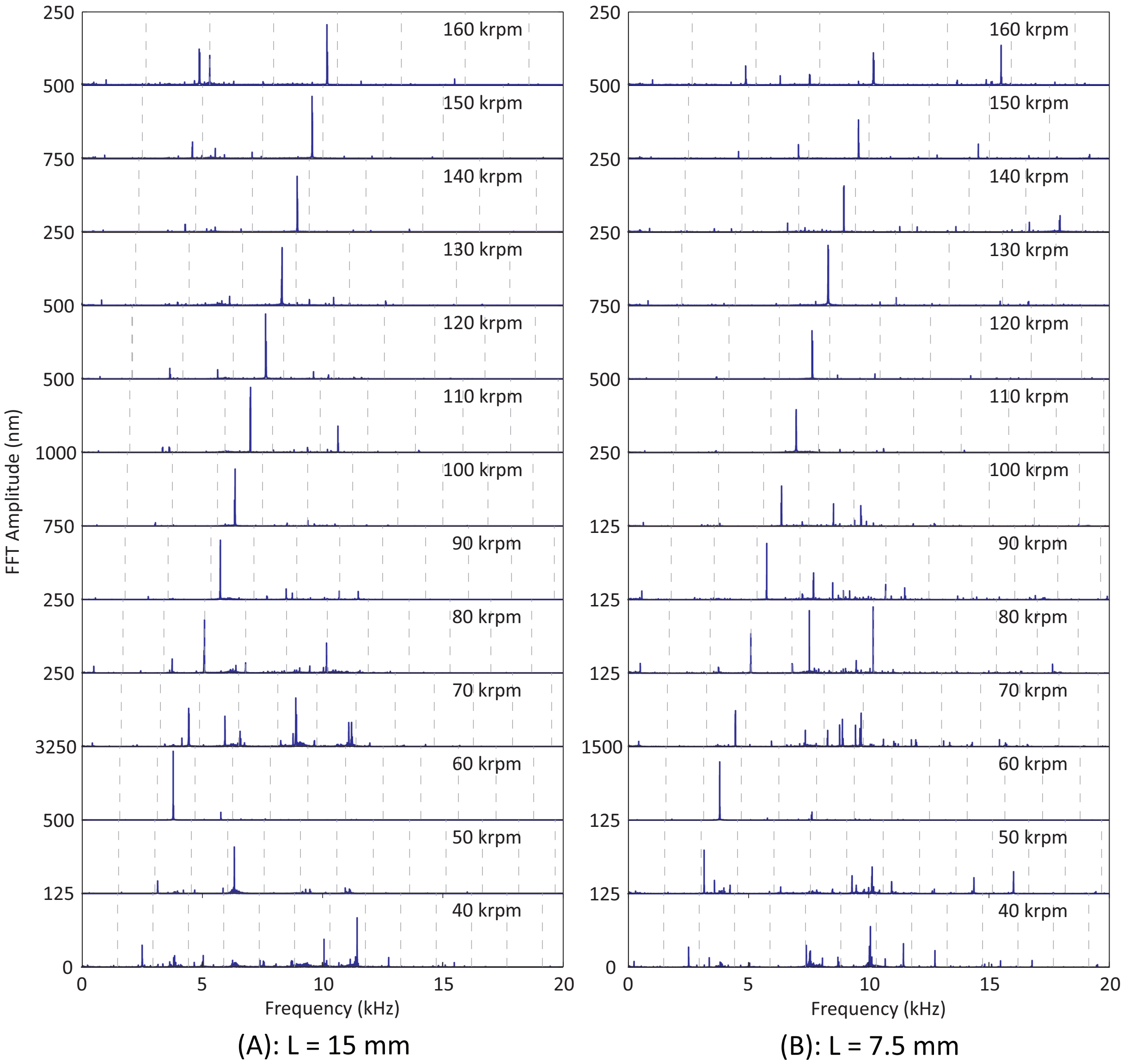

Figure 6.13: Magnitude of the Fourier transforms of asynchronous radial error motion along fixed-sensitive X-direction at all spindle speeds: (A) Over-hang length = 15 mm, (B) Over-hang length = 7.5 mm.

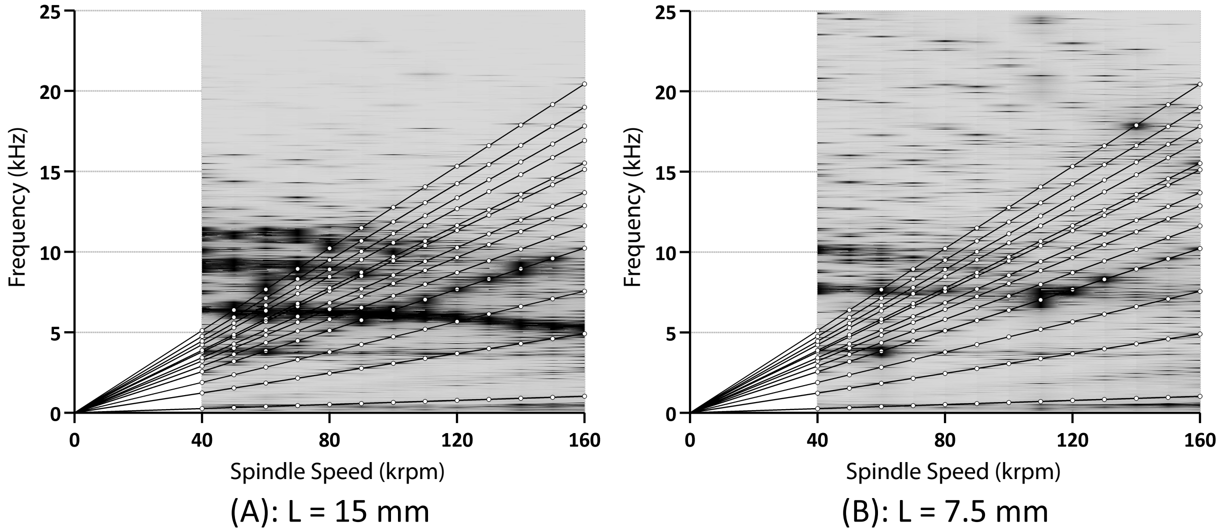

Figure 6.14: Magnitude of the Fourier transform of fixed-sensitive asynchronous radial error motion: (A) Over-hang length = 15 mm, (B) Over-hang length = 7.5 mm. Darker regions indicate higher amplitudes levels.

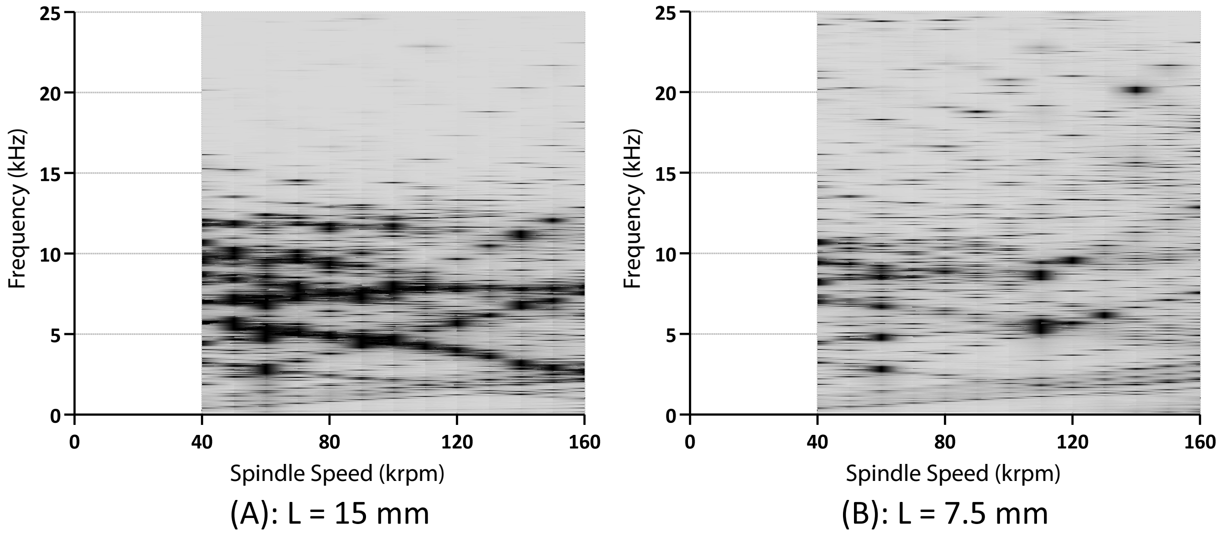

Figure 6.15: Magnitude of the Fourier transform of rotating-sensitive asynchronous radial error motion: (A) Over-hang length = 15 mm, (B) Over-hang length = 7.5 mm. Darker regions indicate higher amplitudes levels.

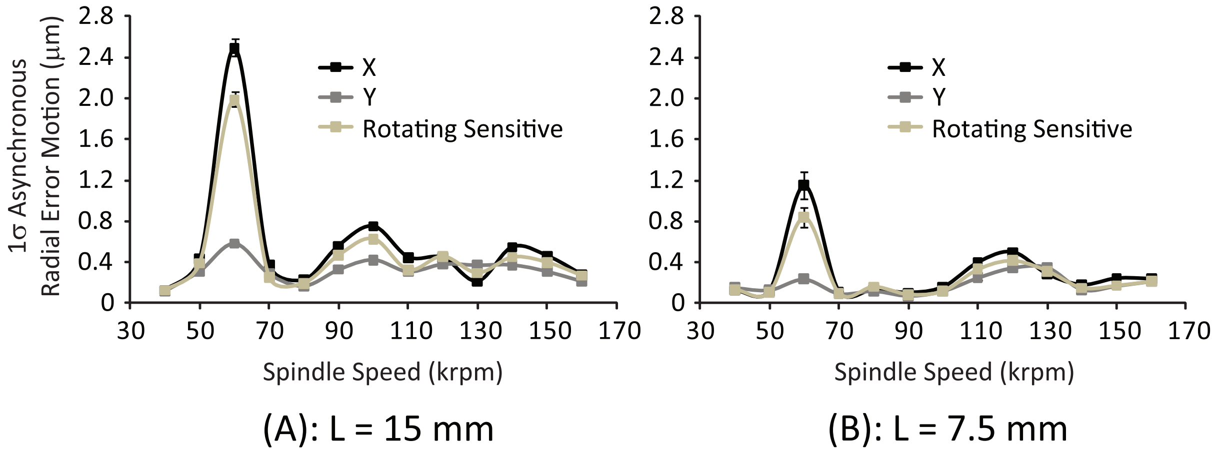

Figure 6.16: 1σ of asynchronous radial error motion along fixed-sensitive X- and Y-directions and rotating-sensitive direction versus spindle speed: (A) Over-hang length = 15 mm, (B) Over-hang length = 7.5 mm.

6.4.2.2 Axial Motions

Figure 6.17 shows polar plots of synchronous axial error motions at different speeds for both over-hang lengths. It can be observed that the synchronous axial error motions are highly sensitive to spindle speed. At speeds below 90 krpm, the motions are dominated by multiple harmonics, while above 90 krpm, the motions are dominated by the fundamental axial error motion. At all speeds, other than the fundamental frequency, 2^{nd} and 3^{rd} harmonics are the only dominant harmonics present in the synchronous axial error motions.

Figure 6.18(a) shows the amplitude of the fundamental axial error motion. The fundamental component does not vary with the over-hang length. The amplitudes are less than 400 nm at all speeds except 130 krpm, at which the amplitude increases to 1 μm. Figure 6.18(b) shows the amplitudes of the 2^{nd} and 3^{rd} harmonics. The 2^{nd} harmonic shows a peak at 70 krpm, whereas the 3^{rd} harmonic shows a peak at 50 krpm. Figure 6.19 shows the synchronous axial error motion value including the fundamental component. This value does not change with the over-hang length. Except 70 krpm and 130 krpm, at all speeds, the synchronous axial error motion value is less than 500 nm. The value increases to 750 nm and 2 μm at 70 krpm and 130 krpm, respectively.

Figure 6.20 shows the magnitude of the Fourier transforms of the asynchronous axial error motions. There are multiple dominant peaks, a few of which do not vary with spindle speed. Many of them, however, demonstrate a speed-dependent shift. Similar to the fixed-sensitive asynchronous radial error motions, the frequencies corresponding to the dominant peaks that shift (compiled at different rotational frequencies) are observed to follow linear trends with different slopes. The slopes observed in asynchronous axial error motions match closely with the slopes calculated from a combination of bearing frequencies (see Table 6.3). Also, when compared to the radial error motions, a different set of combinations are observed in the axial error motions.

Surface plots of the magnitudes of Fourier transform of the asynchronous axial error motions are shown in Fig. 6.21 to analyze the overall frequency content. The frequencies explained by the bearing frequency combinations are plotted as white dots along with their linear trends (with slopes given in Table 6.3). At both over-hang lengths, apart from the bearing frequencies, there is a single dominant peak around 2.1 - 2.5 kHz which decreases gradually with increasing speed.

To summarize and provide a measure of the asynchronous axial error motion, the 1σ values are shown in Fig. 6.22. For spindle speeds greater than 80 krpm, the 1σ value is not affected by the over-hang length and is less than 50 nm. The maximum 1σ value is observed at 70 krpm with 7.5 mm over-hang length. This value is about 425 nm, more than double of the value for 15 mm

Table 6.3: Comparison of frequency-speed slopes calculated from the bearing frequencies with those from the experiments for asynchronous axial error motions.

Calculated slopes using bearing frequencies		**Observed slopes**	
Frequency combination	Slope	L = 15 mm	L = 7.5 mm
m_{ω_t}	0.384	0.3838	0.3838
m_{ω_s}	1.988	1.9932	1.9905
$m_{\omega_o} - 1$	2.841	2.8294	2.8303
m_{ω_o}	3.841	3.8258	3.8275
$m_{\omega_o} + 1$	4.841	4.8212	4.8243
$16m_{\omega_t}$	6.145	6.1262	6.1303
$2m_{\omega_o} - 1$	6.681	6.6656	6.668
$2m_{\omega_o}$	7.681	7.6512	7.655
$2m_{\omega_o} + 1$	8.681	8.6518	8.6576

over-hang at the same speed.

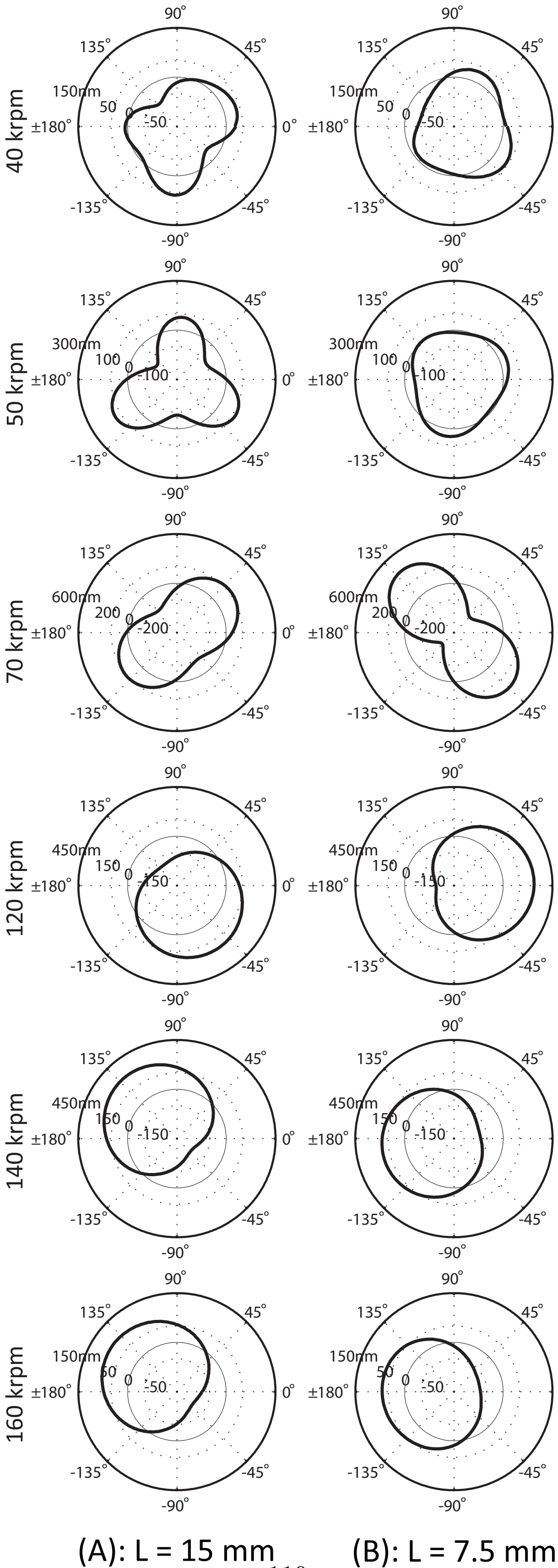

Figure 6.17: Polar plots of synchronous axial error motion at various spindle speeds: (A) Over-hang length = 15 mm, (B) Over-hang length = 7.5 mm.

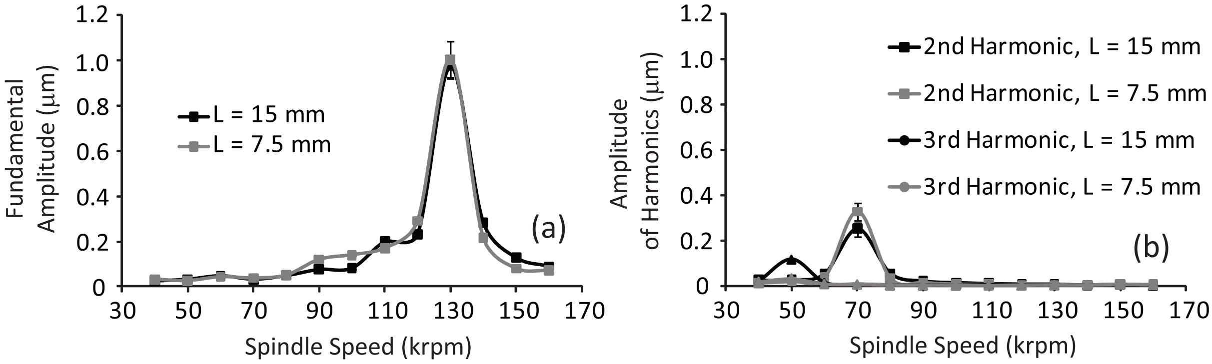

Figure 6.18: Amplitudes of various components of the synchronous axial error motion versus spindle speed at both over-hang lengths: (a) Fundamental axial error motion, (b) Amplitudes of 2^{nd} and 3^{rd} harmonics.

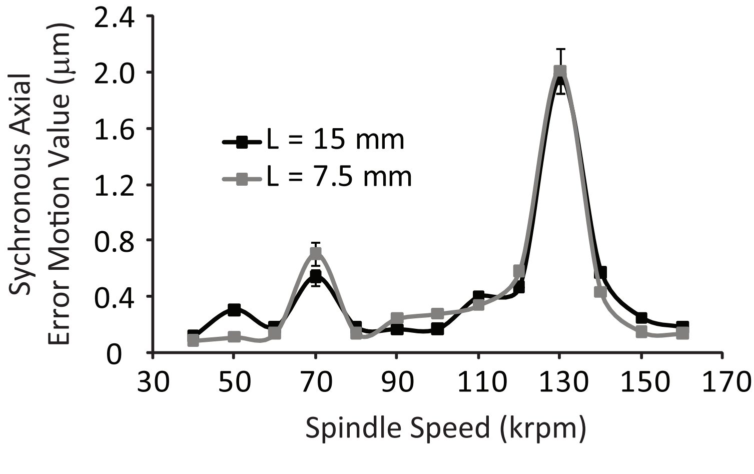

Figure 6.19: Synchronous axial error motion value versus spindle speed.

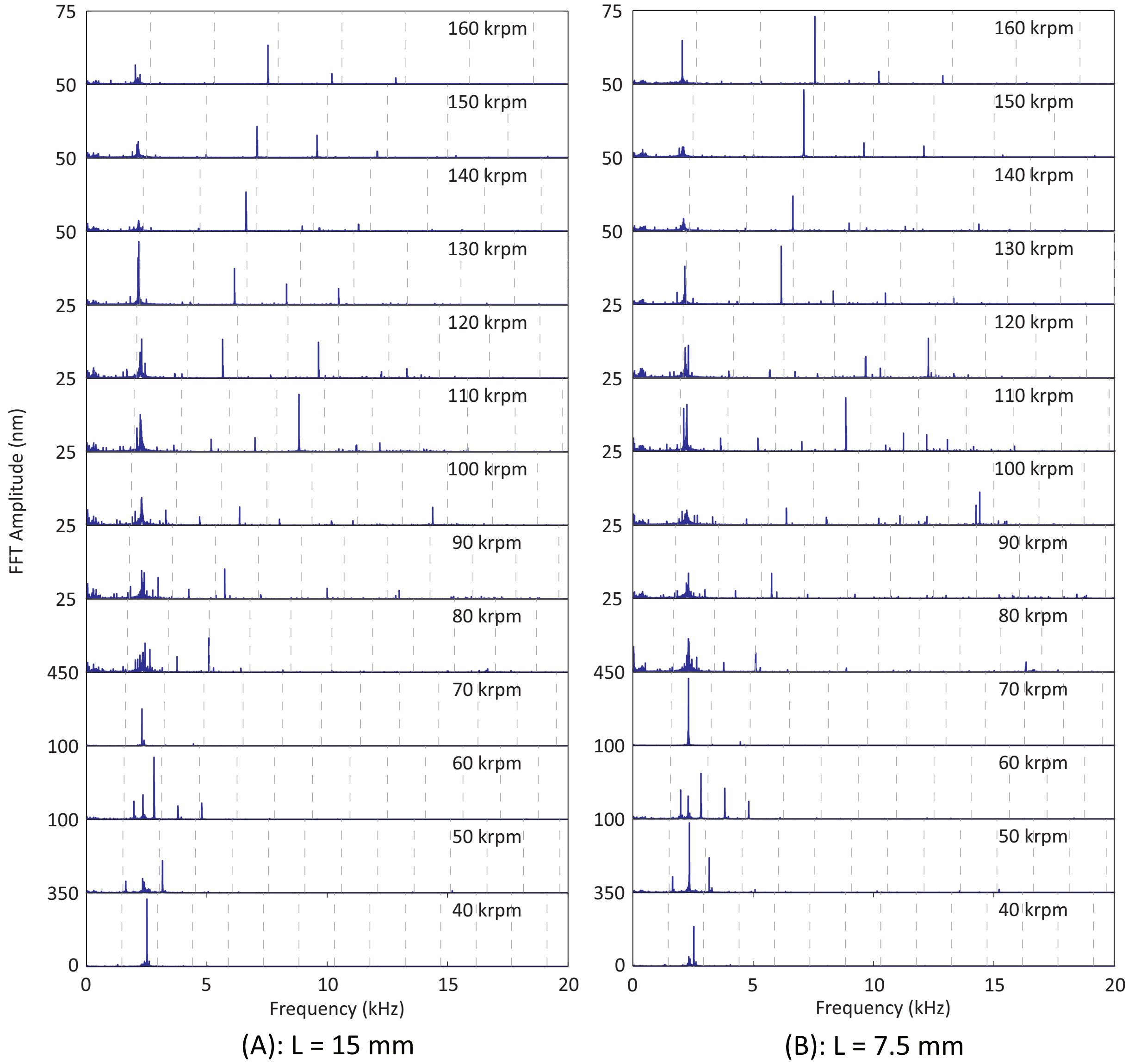

Figure 6.20: Magnitude of the Fourier transforms of asynchronous axial error motion at all spindle speeds: (A) Over-hang length = 15 mm, (B) Over-hang length = 7.5 mm.

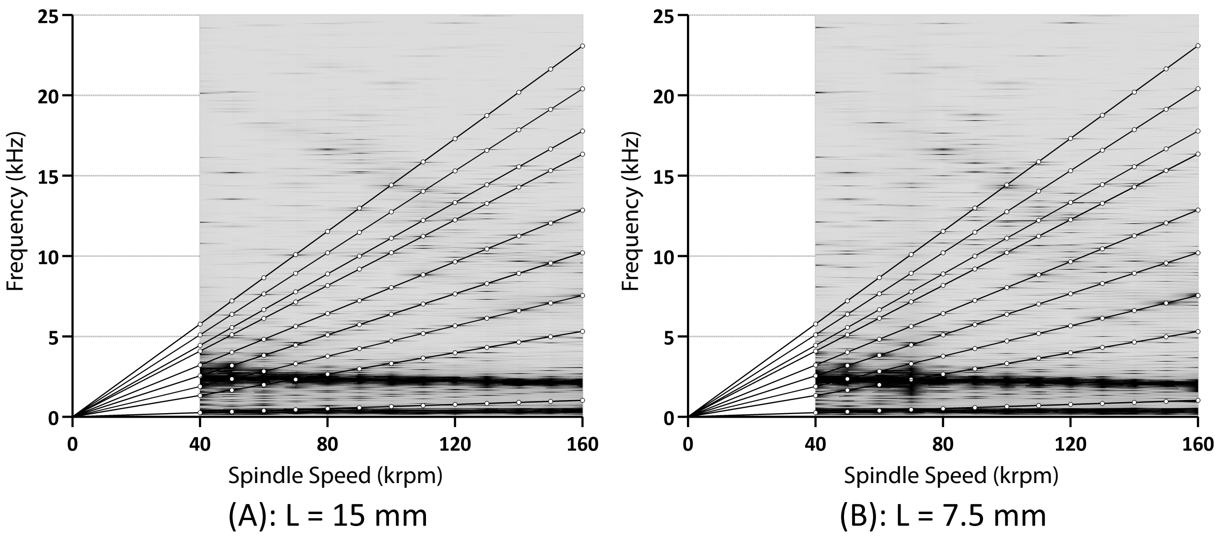

Figure 6.21: Magnitude of the Fourier transform of asynchronous axial error motion: (A) Over-hang length = 15 mm, (B) Over-hang length = 7.5 mm. Darker regions indicate higher amplitudes levels.

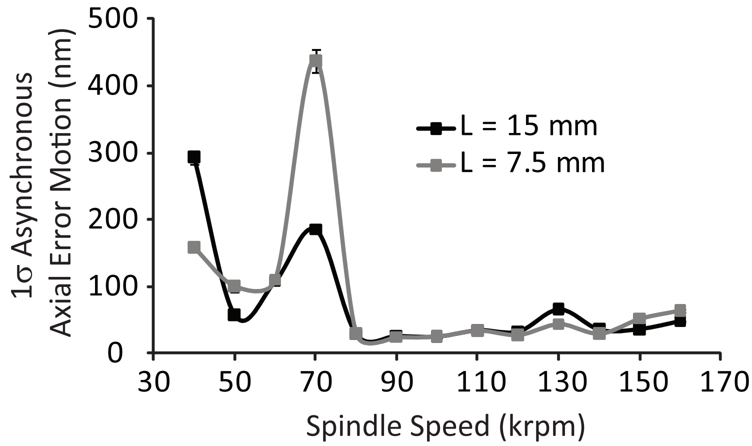

Figure 6.22: 1σ of asynchronous axial error motion versus spindle speed at both over-hang lengths.

6.4.3 Effect of Repeated Artifact Attachment on Radial Motions

The fundamental frequency components of the radial motions along fixed-sensitive directions are composed of centering errors. The errors in attaching the artifact to the precision collet induce a radial shift (eccentricity) and rotation (tilt) to the artifact (tool) axis with respect to the axis of rotation. In addition to quasi-static effects, the centering errors (eccentricity and tilt) induce dynamic effects due to the rotating unbalance. Each time the artifact is removed and re-attached, the centering errors vary, causing changes in both the quasi-static and dynamic effects. Further, the collet torque could have an effect on the dynamic behavior.

To quantify the effect of repeated artifact attachments on the radial motions, the sphere-on-stem artifact is removed and reattached with the same over-hang length of 15 mm at least 30 times and the collet is tightened with the same nominal torque of 0.75 Nm using a torque wrench. For each attachment, three sets of (X,Y) radial motions are collected at two speeds of 80 krpm and 120 krpm. Before each attachment, the artifact and the collet are handled with care using gloves and cleaned with alcohol to make sure that they are free of dust particles. To ensure the repeatability of over-hang length during these tests, each time the artifact is removed and re-attached, the axial position of the artifact is adjusted such that the strength of the X-laser beam reflected from the stationary surface of the sphere (read as a voltage signal from the laser controller) is maximized within 0.01 V. This corresponds to an over-hang length resolution of 2 μm.

Figures 6.23(a), 6.23(b) and 6.23(c) show the variation of the fundamental amplitudes, synchronous radial error motion values and 1σ of the asynchronous radial error motion, respectively, versus the artifact attachment number at 80 krpm and 120 krpm spindle speeds. The fundamental amplitudes are shown only for (X,Y) fixed-sensitive directions, while the values for synchronous and asynchronous error motions are shown for fixed-sensitive and rotating-sensitive (referred to as R) directions. Since sufficient care was taken during experimentation to ensure that all other sources of variation were minimized, the observed variability is hypothesized to be mainly governed by the performance of the collet and how well it controls the centering errors and the boundary conditions.

To check if the variations observed in the different frequency components could be explained by a *normal* distribution, Anderson-Darling normality tests are conducted on each of these different quantities [151]. The null hypothesis during this test is that the distribution is normal. For a 95% confidence level, if the calculated p-value exceeds 0.05, then the hypothesis of normality can be accepted. Table 6.4 shows the p-values calculated for the fundamental amplitudes, synchronous

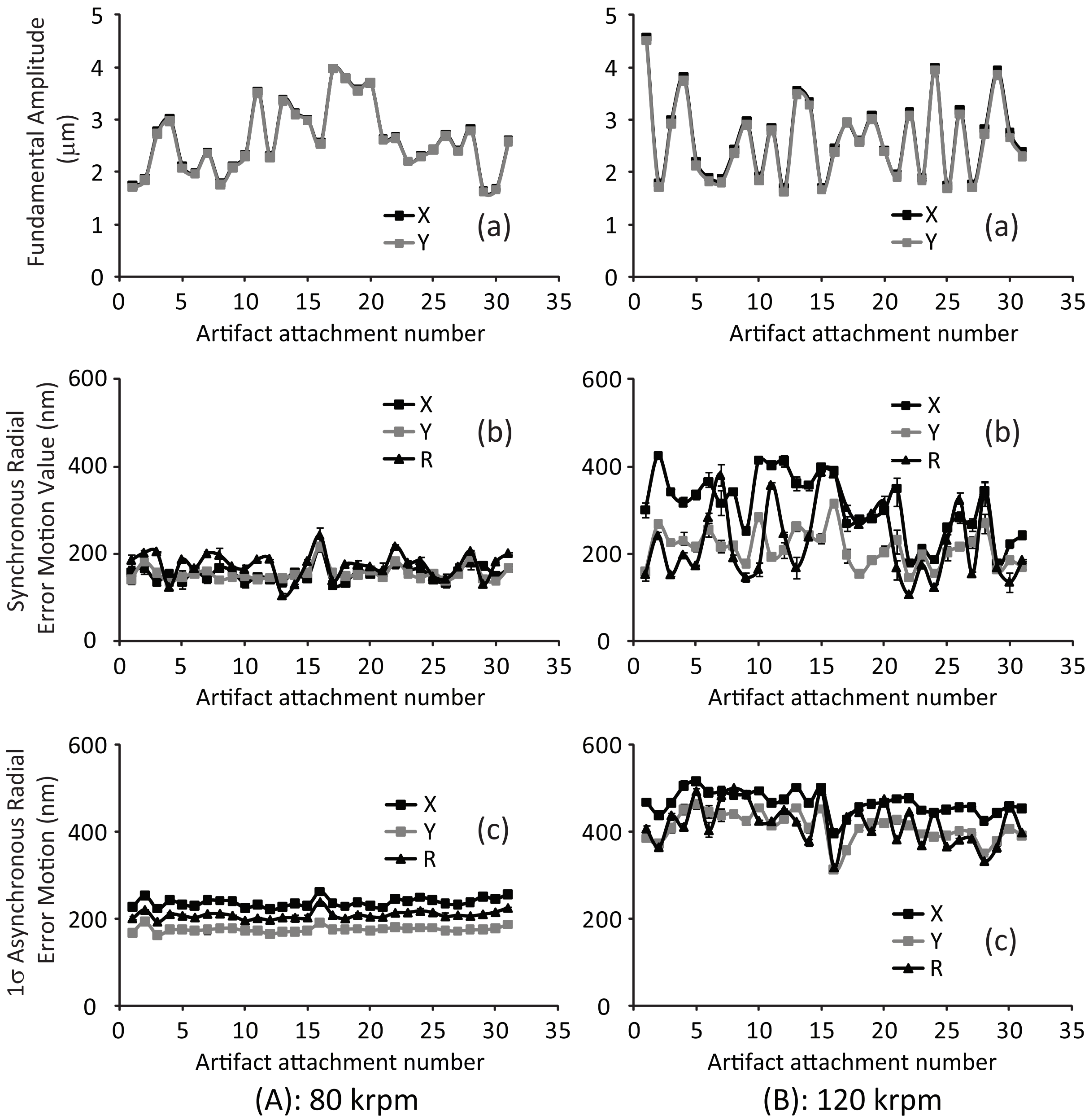

Figure 6.23: (a) Amplitudes of motion at the fundamental frequency along fixed-sensitive X- and Y-directions versus artifact attachment number, (b) Synchronous radial error motion values along fixed-sensitive X- and Y-directions and the rotating-sensitive direction versus artifact attachment number, (c) 1σ of asynchronous radial error motion along fixed-sensitive X- and Y-directions and the rotating-sensitive direction versus artifact attachment number: (A) Spindle speed = 80 krpm, (B) Spindle speed = 120 krpm.

error motion values and 1σ asynchronous error motions. Except for the p-value for rotating-sensitive synchronous error motion value at 120 krpm, the p-values for all other components at both speeds

Table 6.4: The p-values calculated from Anderson-Darling Normality test to assess distribution characteristics of the spindle attachment variations.

		80 krpm	**120 krpm**
Fundamental Amplitude	X	0.327	0.106
	Y	0.331	0.113
Synchronous error motion value	X	0.201	0.69
	Y	0.851	0.898
	R	0.203	0.023
1σ Asynchronous error motion	X	0.76	0.85
	Y	0.137	0.888
	R	0.959	0.293

Table 6.5: Descriptive statistics of the various components of the radial motion due to spindle attachment variations.

		80 krpm		**120 krpm**	
		μ_{data}	Range	μ_{data}	Range
Fundamental Amplitude (nm)	X	2614	±1278	2601	±1385
	Y	2593	±1283	2539	±1385
Synchronous error motion value (nm)	X	153	±28	309	±141
	Y	149	±16	210	±73
	R	174	±48	221	+160/-114
1σ Asynchronous error motion (nm)	X	236	±17	468	±45
	Y	174	±8	412	±58
	R	207	±12	424	±84

show that the null hypothesis is true and that the variations observed in all these quantities can be explained by using normal distributions.

Table 6.5 shows the mean (μ_{data}) and the range for each of the different components at both speeds. For all the cases which have a normal distribution, the range containing 95% of the values is reported by calculating $\pm 1.96\ \sigma_{data}$, where σ_{data} is the standard deviation of the data of that particular component. For the rotating-sensitive synchronous error motion values at 120 krpm, the true range around the mean is calculated from the data and reported.

It can be observed that the range of variation of the fundamental amplitude is quite large at both speeds (close to 50% of the mean value on either side). Also, the synchronous error motion values at 120 krpm vary by up to 45% of the mean value along fixed-sensitive directions and by up to 73% of the mean value along rotating-sensitive direction. The synchronous error motions at 120 krpm are more sensitive to the variations in the attachment error compared to 80 krpm.

Table 6.6: Total combined standard uncertainty and total expanded uncertainty for motions measured at various frequencies.

Contributing Sources	**Combined Standard Uncertainty, u_c (nm)** **Fundamental**		**Synchronous**		**Asynchronous**	
	Radial	**Axial**	**Radial**	**Axial**	**Radial**	**Axial**
Measurement Device and Hardware	0	0	19	0	5	5
Environmental Effects	50, 85	50, 85	2	2	15	15
Laser beam-alignment and Curvature effects	0	0	3	8	0	0
Data Processing	0	0	0	0	0	0
Total Combined Standard Uncertainty, u_{Total}	50, 85	50, 85	19	8	16	16
Total Expanded Uncertainty, U_{Total} (k=2)	100, 170	100, 170	38	16	32	32

6.5 Uncertainty Analysis of the Radial and Axial Motions

The uncertainties associated with each of the fundamental, synchronous and asynchronous motion components are obtained by following the procedure described in the previous chapter. Table 6.6 summarizes the combined standard uncertainty contributions. Note that the two values reported for the fundamental frequency correspond to speeds other than 160 krpm and 160 krpm, respectively. The combined standard uncertainty due to data processing is considered to be negligible as compared to the other sources and hence its value is taken as zero.

The expanded uncertainty in the measurement of radial motions along the rotating-sensitive direction is calculated using the Law of Propagation of Uncertainty (LPU) as outlined in [130]. The procedure described in our previous work [139] was followed to obtain this uncertainty. It should be noted the uncertainties in the synchronous and asynchronous frequencies cannot be separated for the calculations along the rotating-sensitive direction. Using the values for the uncertainties given above (for the fixed-sensitive directions), and by assuming a worst case uncertainty of 0.19^o in the rotation angle along with a value of 0.12^o for the maximum misalignment from 90^o between the X- and Y-laser beams, the expanded uncertainty in the motions measured along the rotating-sensitive direction is 112 nm for all speeds except 160 krpm and is 177 nm for 160 krpm.

It is to be noted that the total expanded uncertainty calculated for the synchronous frequencies is the uncertainty in determining the true error motions of the spindle. However, if the same artifact is used and measurements are conducted without disturbing the location of the laser spot relative to the sphere, the artifact's contribution to the measured radial motion at a given angle would be similar across various operating conditions (e.g., at different speeds and different thermal states of the spindle). Therefore the uncertainty in the relative changes observed at a certain rotation angle due to changes in operating conditions will not have any contribution from the artifact.

6.6 Summary and Conclusions

This chapter presented a thorough experimental analysis approach to analyze and quantify the sources affecting the radial and axial motions of the electrically-driven hybrid-ceramic-bearing UHS spindle used on the dual-stage polishing test-bed. The effect of temperature cycling and artifact over-hang length on the spindle motions are analyzed at different spindle speeds. The repeatability of artifact (tool) attachment to the collet and the associated effect on spindle motions are also studied. The uncertainty of measurements and analysis are quantified. The measured axial and radial motions were seen to be strongly dependent upon the spindle speed, thermal-state of the spindle, and the over-hang length of the artifact (tool). At certain speeds, the measured spindle motions may induce significant dimensional errors, shape distortions, and surface roughness to the polished surfaces. Therefore, effective application of the mandrel-based polishing process necessitates analysis of the UHS spindle motions and associated selection of favorable process conditions.

The experimental analysis approach presented in this work enables (a) rigorous quantification of the performance of any UHS spindle under various operating conditions, (b) identification of the different sources (along with their relative contributions) contributing to the fundamental, synchronous and asynchronous frequency components of the axial and radial motions, and (c) assessment of the suitability of a given UHS spindle for micromachining processes. For the specific spindle studied, the following conclusions can be drawn. Some of these conclusions could be generalized to the class of UHS spindles with contact-bearings:

- Even under steady-state conditions, the on-off nature of the coolant controller imposes a cyclic behavior to spindle temperatures, which results in up to $\pm 30\%$ variation in synchronous radial error motion value, and up to $\pm 40\%$ change in the fundamental axial error motion amplitude. The effect of thermal cycling on other motion components is less than $\pm 10\%$.
- The *fundamental component of the radial motions* is dominated by the quasi-static effects of the centering errors for speeds up to 100 krpm. Above 100 krpm, the dynamic effects become dominant, resulting in increased amplitude at higher spindle speeds. In many cases, the two

radial motion components (X and Y) exhibited amplitude and phase (from 90^o) differences at the fundamental frequency. This is considered to arise from the non-axisymmetric stiffness of the spindle, resulting in variation of deflections (from the rotating unbalance) at different angular locations.

- The *synchronous components of the radial motions* also vary strongly with the spindle speed. Both the shape (orbit) and amplitude of motions change significantly with the spindle speed. Furthermore, the effect of spindle speed is confounded with that of the over-hang length. *Consistently, longer over-hang length produces higher synchronous radial error motion values.*
- A majority of the *asynchronous radial motions* of the spindle arise from the bearing frequencies, which result in a linear shift in dominant frequencies with the spindle speed. Few other dominant frequencies are also observed, which may be arising from the natural frequencies of the spindle, artifact and/or structure. The over-hang length also has a significant effect on asynchronous motions: Except for a few speeds, the 1σ values of asynchronous radial error motions are 30% to 80% lower for the shorter over-hang length. For both over-hang lengths, large asynchronous motion amplitudes are observed at 60 krpm, reaching 2.5μm and 1.3μm 1σ values, respectively, for 15 mm and 7.5 mm over-hang lengths.
- The *synchronous axial error motions* are highly sensitive to the spindle speed. At speeds below 90 krpm, the motions are dominated by multiple harmonics, whereas above 90 krpm, the motions are mainly composed of the fundamental axial error motion. The synchronous axial error motion values do not vary with the over-hang length. Two peaks were observed at 130 krpm and 70 krpm with values of 2 μm and 750 nm, respectively. At all other speeds, the synchronous axial error motion values are less than 500 nm.
- The frequencies arising from the bearing error motions also dominate the *asynchronous axial error motions*. For spindle speeds greater than 80 krpm, the 1σ values of asynchronous axial error motions are less than 50 nm, and do not vary with the over-hang length. A maximum 1σ value of 425 nm is observed at 70 krpm for 7.5 mm over-hang length.
- The variations caused by artifact attachment to the collet have a critical effect in the radial motions of the spindle. Generally, the variations arising from the artifact attachment exhibit normal distributions. The amplitude of the fundamental component varies up to $\pm 50\%$ of the mean value. The sensitivity of the motions to attachment variations are higher at higher speeds, especially for the synchronous error motions. The artifact attachment variations cause up to 75% error in synchronous error motion values.

Chapter 7

Error-Separation Techniques Implemented on UHS Spindles to Determine True Spindle Error Motions

The radial motions measured from the UHS spindle also include the surface profile (form error or out-of-roundness) of the artifact around the circumferential measurement track. For the measurements shown in the previous chapters, the form error has been considered as a source of uncertainty in the measurement of synchronous radial error motions of the spindle. Since the motions measured at synchronous frequencies are of the same order of magnitude as the sphericity specification of the sphere, the uncertainties in the measurement of synchronous radial error motions are relatively high.

In this chapter, we have implemented two different error separation techniques - Multi-Orientation Technique and Donaldson Reversal Method, on UHS spindles. Both techniques have been successfully demonstrated to remove artifact form error from radial motions measured at speeds up to 150 krpm. First section of the chapter describes the multi-orientation technique implementation. The second section illustrates the implementation of the Donaldson reversal method as applied to UHS spindles.

7.1 Background

In order to reduce the uncertainty due to artifact form error, and accurately determine the spindle errors, i.e., eliminate the artifact form errors from the measurements, various error separation techniques have been developed in literature [152–165]. Error separation techniques can be broadly classified into three categories: (1) Reversal techniques [152–157]; (2) Multi-probe techniques [156–160]; and (3) Multi-step techniques [157, 161–163]. A detailed and thorough description of these techniques has been clearly summarized in [152,154]. All these techniques require extremely precise and rigid fixturing, as well as precise angular measurements in order to achieve accurate and repeatable separation. Reversal techniques are the only ones that allow for perfect separation of artifact and spindle errors. The other two techniques are limited in terms of accuracy due to the issue of harmonic suppression [154,162]. Full separation cannot be achieved by using these methods. Many works have attempted to minimize the effect of harmonic suppression. Angle probes along with displacement probes have been tried to obtain high accuracy roundness measurements [164]. Judicious choice of the angles and the number of probes/steps have also been used to enable higher bandwidth of separation [154, 156, 161, 163]. As a result, all these techniques have been successfully implemented to measure spindle error motions at the sub-nanometer level of ultra-precision spindles [156, 157].

Even though the error separation techniques mentioned above have been effective in separating errors for macro-scale spindles, implementation of those techniques to miniature UHS spindles pose considerable challenges. Those challenges arise from the smaller size (typically $\phi 3$ mm or 0.125 in.) of the artifact and the associated curvature effects, and the need to measure at higher speeds, since majority of the UHS spindles cannot be operated below a specific speed (usually more than 10 krpm). Another difficulty arises from repeatable attachment of the artifact. Most error separation techniques require very precise re-attachment and orientation of the artifact relative to the spindle.

7.2 Multi-Orientation Technique for Error Separation

A single-probe multi-orientation technique is implemented to remove the artifact form error from the radial measurements to obtain the radial spindle errors of miniature UHS spindles. The approach involves measurements of radial motions using a single LDV by keeping it stationary, and conducting measurements at multiple orientations of the artifact. Although this technique has been theoretically shown to work and has been implemented for a two-orientation case [154,165], it is not widely used. In this thesis, we have established an unique implementation scheme of this technique that allows its application using multiple *arbitrary* orientations of the artifact, without the need for any extra fixtures. For each orientation, the orientation angle of the artifact with respect to an angular reference on the spindle is measured *in-situ* from the reflectivity signal of another LDV. This implementation has been experimentally demonstrated to measure the spindle error motions of a typical miniature UHS spindle across its operational speeds. Although the implementation scheme has been demonstrated for miniature UHS spindles, the same approach can be readily used for error separation on macro-scale spindles as well.

This section is organized as follows. First, a brief introduction of the multi-orientation technique is provided. Then, the details of the implementation scheme developed in this thesis are described, with a focus on measuring spindle error motions of UHS spindles. Next, using a typical UHS spindle, measurements are conducted (a) to demonstrate the functionality of the implementation scheme by measuring spindle error motions from the sphere and stem portions of the sphere-on-stem artifact (note that the artifact form profile for the sphere and stem portions are significantly different), and (b) to study the effect of the number of orientations (used for error separation) on both the repeatability and bandwidth of error separation. Finally, to demonstrate the effectiveness of the implementation scheme across a wide range of speeds, radial spindle error motions of the tested UHS spindle are obtained at four speeds (40 krpm, 90 krpm, 120 krpm, and 150 krpm) that span the entire operating range of the spindle along both the fixed- and rotating-sensitive directions.

7.2.1 Description of the Single-probe Multi-Orientation Technique

The details of the single-probe multi-orientation technique have been described in [154]. This technique requires measurements from at least two orientations of the artifact. It involves using a single displacement sensor to measure the radial motions from the surface of an artifact that is attached to an axis of rotation provided by the spindle. The motions measured when the spindle is run at the operating speeds can be decomposed into motions at the fundamental frequency, synchronous motions and asynchronous motions [114,115]. The synchronous motions consist of the artifact form error and the speed-dependent synchronous spindle error motions [114,115]. In order to obtain the true synchronous spindle error motions, the synchronous radial motion measurements from multiple orientations of the artifact are combined to calculate and separate the artifact form error.

A description of the steps involved in the multi-orientation technique is shown in Fig. 7.1 for

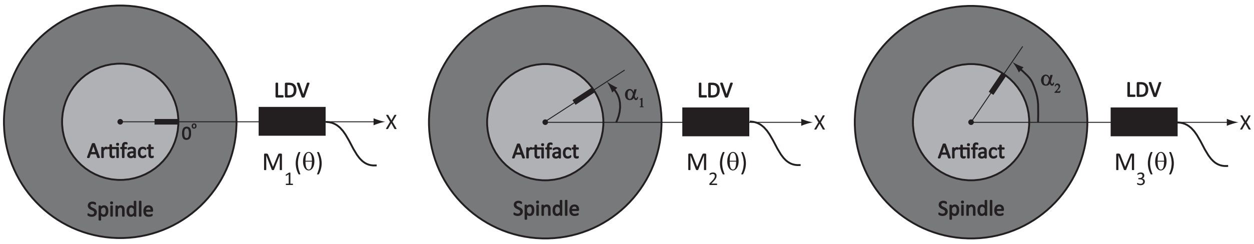

Figure 7.1: Steps involved in multi-orientation technique when using three orientations.

an implementation along the fixed-sensitive X-direction. After conducting the first measurement, the artifact is removed and rotated by a certain angle and re-attached to the spindle for the second measurement. This step is repeated until all the measurements from the desired number of orientations are completed. The measured displacement data from each orientation is post-processed to obtain the synchronous radial motions for each orientation.

Denoting the spindle error motions and artifact form error measured along the fixed-sensitive Y-direction as $S(\theta)$ and $A(\theta)$, respectively, the synchronous radial motions for the three orientations $M_1(\theta)$, $M_2(\theta)$, $M_3(\theta)$ can be related to $S(\theta)$ and $A(\theta)$ as

$$\begin{aligned} M_1(\theta) &= A(\theta) \ + S(\theta) \\ M_2(\theta) &= A(\theta - \alpha_1) \ + S(\theta) \\ M_3(\theta) &= A(\theta - \alpha_2) \ + S(\theta) \end{aligned} \tag{7.1}$$

where α_1 and α_2 are the rotation angles of the artifact (with respect to the first orientation) in the second and third orientations, respectively, as shown in Fig. 7.1. It is important to note that the angular reference (θ=0) between the different orientations corresponds to the same physical orientation of the spindle.

Mathematically, we can eliminate the spindle error motions, $S(\theta)$, from the three measurements by considering a combined sum $T(\theta)$ which can be written as

$$\begin{aligned} T(\theta) &= 2M_1(\theta) - M_2(\theta) - M_3(\theta) \\ &= 2A(\theta) \ - A(\theta - \alpha_1) \ - A(\theta - \alpha_2). \end{aligned} \tag{7.2}$$

Since the measured synchronous motion data is sampled at finite number of angular locations (θ_i, with i=*1,2,...N*, where N is the total number of angular sampling points), by taking the discrete Fourier transform of the sequence $T(\theta_i)$ and rearranging it, we obtain the discrete Fourier transform of the artifact form error as

$$A_k = \frac{T_k}{2 - e^{-jk\alpha_1} - e^{-jk\alpha_2}}, \qquad k = 1, 2, ...N. \tag{7.3}$$

The artifact form error, $A(\theta_i)$, is obtained by taking the inverse discrete Fourier transform of A_k, and the spindle error motion is then calculated as

$$S(\theta_i) = M_1(\theta_i) - A(\theta_i). \tag{7.4}$$

It can be clearly seen from Eqn. 7.3 that the denominator term can approach zero for certain values of k that satisfy $k\alpha_1 = 2\pi N_1$ and $k\alpha_2 = 2\pi N_2$ simultaneously, where N_1 and N_2 are integers. The artifact form error and hence the spindle error motion cannot be separated at these k^{th} harmonics. This is the main drawback of the multi-orientation technique. The harmonics that cannot be separated are commonly referred to in the literature as the *harmonic losses* and this issue is referred to as *harmonic suppression.* The highest value of k until which all the harmonics are separated can be referred to as the *bandwidth* of the error separation technique. If the number of orientations is kept fixed, in order to extend the bandwidth, researchers have suggested choosing specific rotation angles (or range of angles) [156, 165]. Another way to improve the bandwidth (as suggested by [154]) is to increase the number of orientations. For example, if N orientations are used, the equation for calculating the artifact form error becomes

$$A_k = \frac{T_k}{(N-1) - \sum_{c=1}^{N-1} e^{-jk\alpha_c}}, \tag{7.5}$$

where T_k is the discrete Fourier transform of the sequence given by $T(\theta_i) = (N-1)M_1(\theta_i) - \sum_{c=1}^{N-1} M_{c+1}(\theta_i)$ and α_c is rotation angle of the artifact in the $(c+1)^{th}$ orientation with respect to the first orientation. The first value of k at which $\sum_{c=1}^{N-1} e^{-jk\alpha_c} = (N-1)$ is potentially higher for a larger N, thus allowing for a higher bandwidth with greater number of orientations.

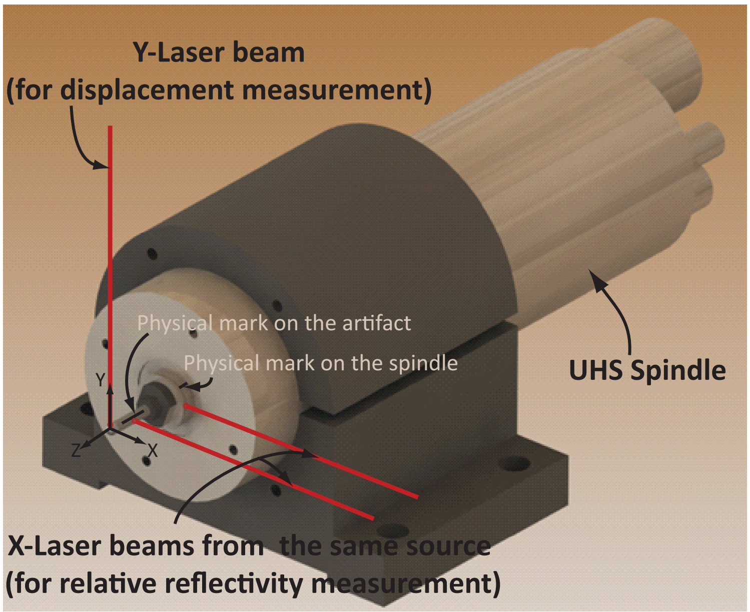

Figure 7.2: Measurement setup used for implementation of the multi-orientation technique on UHS spindles along radial Y-direction.

7.2.2 Implementation of the Multi-Orientation Technique

7.2.2.1 Measurement Setup

The measurement setup used for implementation of the multi-orientation technique on UHS spindles is shown in Fig. 7.2. An LDV in the single-point measurement mode is used to measure the motions along a fixed-sensitive radial direction from the surface of a rotating sphere-on-stem artifact attached to a miniature UHS spindle. As mentioned in [127, 139], the LDV can measure displacements at picometer-level accuracy with a frequency bandwidth up to 350 kHz. A high-magnification microscope is used to ensure that the artifact over-hang length is within $\pm$ 2.5 μm across various orientations. After attaching the artifact to the spindle, the measurement location of the laser spot on the sphere is fine-tuned using translation adjustments on the 6-axis precision kinematic mount such that the reflectivity signal is maximized and the laser beam is perpendicular to the average surface of rotation on the sphere. This procedure ensures that the axial measurement location on the sphere is repeated across multiple orientations within $\pm$ 2.5 μm.

In addition to the displacement measurement, another LDV is setup in the relative measurement mode (as shown in Fig. 7.2) to measure the relative angle between the artifact and spindle for a given orientation. When the LDV is used in the relative mode, a single laser source is split into two laser beams, each of which is focused independently on different measurement surfaces. The laser beams are arranged such that one of the laser beams is focused on a rotating surface of the spindle near the collet, and the other laser beam is focused on the stem portion of the artifact. The procedure used for the relative angle measurement is explained in the following section.

7.2.2.2 Measurement of Relative Angle between Artifact and Spindle

The measurement of the relative angle between the artifact and the spindle is conducted in-situ when the spindle is running at its operating speed. The LDV controller outputs a voltage signal (reflectivity signal) that corresponds to the intensity of the reflected laser beam from the measurement surface. In the case of relative measurement mode, the reflectivity signal corresponds to the combined intensities of the reflected lasers from the two measurement surfaces.

Physical marks are engraved and painted black at an arbitrary angular location on the stem portion of the artifact as well as a rotating component of the spindle. The locations of the laser beams are axially adjusted such that the physical marks pass through the respective laser spots when the spindle is rotated. When the spindle rotates at a certain speed, the reflectivity signal is fairly steady except for the angular locations when either of the marks pass through their respective laser spot. At such angular locations, the reflectivity signal drops sharply, causing two drops in signal for each revolution corresponding to the physical marks on the artifact and the spindle.

For a given speed, the shape and character of the signal drop depends on the physical nature of the mark (width and speckle within the mark). Since the two marks are fairly distinct, each of the two resulting signal drops have an unique pattern. Pattern templates (referred to here as *spindle search-pattern* and *artifact search-pattern*) for the two marks are obtained from one of the orientations during one of the revolutions. A signal processing technique using a pattern-matching algorithm is developed and implemented to search for the exact locations of these two search-patterns in each revolution. This technique scans through each successive revolution of the relative reflectivity signal and identifies the locations within the revolution where the signal shows the maximum correlation with each of the search-patterns. The indices corresponding to these locations are stored as *spindle-* and *artifact-markers* for that revolution. Figure 7.3 shows a typical reflectivity signal for five revolutions of data, along with the spindle and artifact search-patterns. The effectiveness of the search algorithm used in finding the locations of these search-patterns within the reflectivity signal can be seen in the exact pattern-matches accomplished for both spindle and artifact search-patterns in other revolutions. The spindle-markers for every revolution corresponding

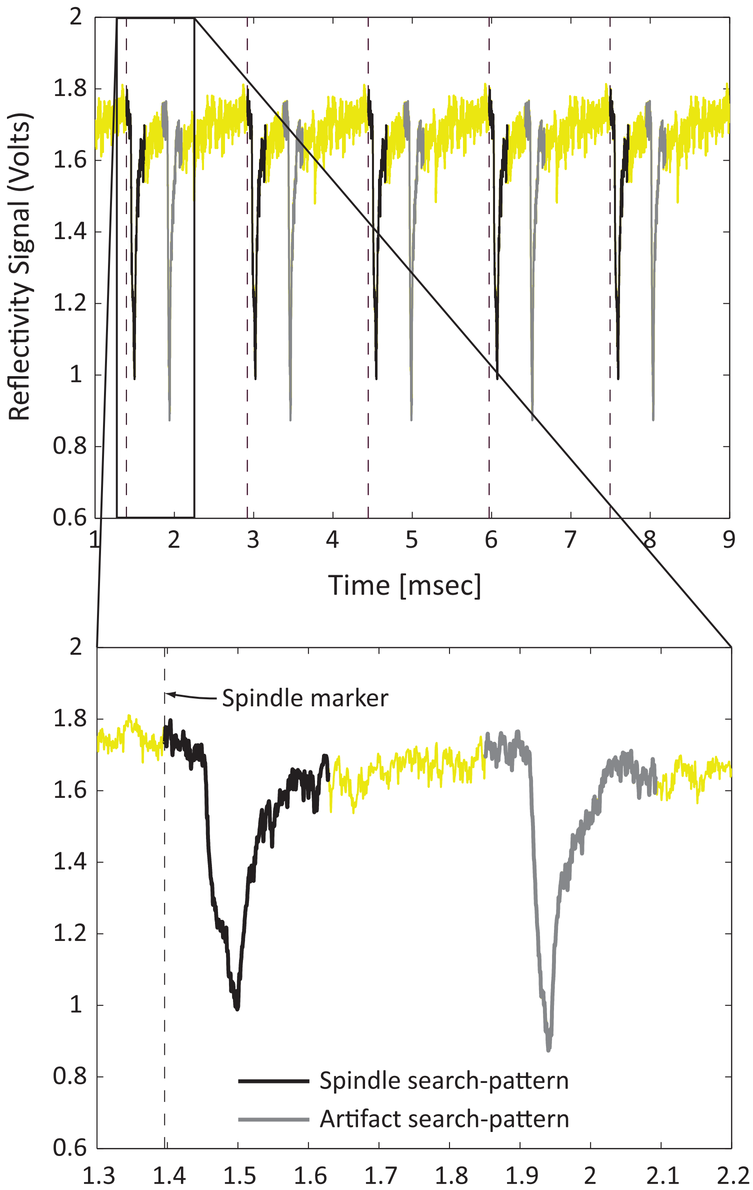

Figure 7.3: Typical spindle and artifact search-patterns and effectiveness of the search algorithm in pattern-matching.

to the matched locations are shown as dotted lines.

Within a revolution, using the spindle-marker as a reference, the relative angle of the artifact-marker is calculated. These calculations are repeated over all the acquired number of revolutions for that particular orientation. The mean value of all the calculated relative angles is defined as the relative angle of the artifact with respect to the spindle for that particular orientation. Whenever the orientation is changed, similar relative angle measurements are conducted for the new orientation with the same artifact and spindle search-patterns. The difference between the two relative angles gives the rotation angle between the orientations. Thus, the rotation angle of the artifact between orientations can be directly measured in-situ by acquiring the relative reflectivity signal.

7.2.2.3 Data Acquisition

For each orientation, the displacement and reflectivity data are acquired using NI 6259 (set to 1.25 MHz sampling rate) and NI 6115 (set to 10 MHz sampling rate) data acquisition cards, respectively. Data acquisition from the two cards at the different sampling rates is synchronized and simultaneously acquired using a LabView code.

7.2.2.4 Data Processing

The data post-processing technique used to separate the fundamental, synchronous and asynchronous components of the radial motion is explained in detail in our previous work [139]. The only difference in this work is that in order to map data from time-domain to angular-domain (to eliminate the effect of spindle-speed fluctuations), instead of using the pulse-signal from an infra-red sensor corresponding to each revolution, the spindle markers obtained by searching for the spindle search-pattern are used. The data in the angular-domain is averaged across all the revolutions at each angular location. A sine function is fitted to this data in a least-squares sense and the fundamental component is removed. The remaining data is the synchronous radial motion, which includes both the artifact form error and the synchronous radial spindle error motions. Further post-processing is done by following the mathematical formulation shown in Section 7.2.1.

As mentioned in the Section 7.2.1, the multi-orientation method suffers from the issue related to harmonic suppression at certain harmonics where the denominator approaches zero. Ideally, the harmonics that would be suppressed for a given set of orientations, say for the three-orientation case, are the set of ks (with k=*1,2,...*N) that simultaneously satisfy

$$|e^{-jk\alpha_1}| = 1 \quad and \quad |e^{-jk\alpha_2}| = 1. \tag{7.6}$$

However, from a numerical stand-point even as the denominator gets closer to zero, it could cause increased uncertainty in the accurate estimation of certain harmonics. Hence, in order to be conservative, we discarded the k^{th} harmonics that satisfied the following condition

$$|e^{-jk\alpha_1}| > 0.85 \quad and \quad |e^{-jk\alpha_2}| > 0.85. \tag{7.7}$$

The bandwidth for a given set of orientations is the first value of k in this set of k^{th} harmonics. Further, since we are interested in measuring a maximum of up to only the first 50 harmonics, a zero phase-shift low pass filter is used to discard all the harmonics greater than 50 throughout the analysis.

7.2.3 Evaluation of the Method

A successful implementation of the multi-orientation technique (i.e., accurate separation of the artifact form and spindle error motions) requires (a) accurate displacement measurements, keeping all the factors affecting the spindle error motions constant, (b) measurement at the same axial plane of the artifact (i.e., the same circumferential track on the artifact for all orientations), and (c) accurate measurement of the artifact rotation angle between the different orientations.

The fundamental assumption behind any error-separation technique is that the spindle error motions do not change between the different orientations. There are many important factors that are known to influence the spindle error motions. These factors include the artifact over-hang length, spindle speed and spindle thermal state. In addition to the factors, in the case of UHS spindles, due to the ultra-high speeds, the dynamic effects due to the rotating unbalance could also affect motions measured at the synchronous frequencies. The centering errors (radial offset and tilt) of the artifact are the most significant contributors to the rotating unbalance.

While the artifact over-hang length and spindle speed could be prescribed, and the thermal state could be controlled using a closed-loop temperature controller across different orientations, the difference in centering errors between orientations is almost entirely governed by the collet-type used for attaching the artifact to the spindle. Based on the performance of the collet in controlling the repeatability of attachment, the centering errors could change between orientations, thus resulting in different dynamic effects and hence possibly different contributions to the motions measured at synchronous frequencies. All these factors should be addressed while implementing the multi-orientation technique (or any other error separation technique) on UHS spindles.

The multi-orientation technique is implemented on the Fischer Precise spindle that would be used on the dual-stage polishing test-bed. This spindle has an operational speed range between 40 krpm and 160 krpm. The artifact over-hang length and the circumferential track corresponding to

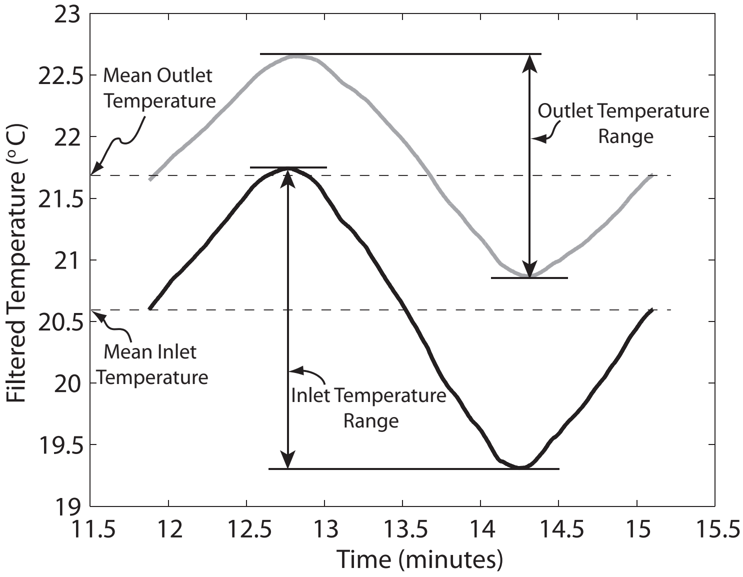

Figure 7.4: Thermal cycling observed in the tested spindle.

the artifact form error are held within $\pm$ 2.5 μm across various orientations. Spindle speed, except for small fluctuations of $\pm$ 100 rpm, is fairly constant and is set using the spindle controller.

Although this spindle is continuously cooled with a coolant and refrigeration unit, even at the steady state, i.e., after the spindle has equilibrated with the ambient conditions, the thermal state of the spindle (as characterized by the inlet/outlet temperatures of the coolant) is known to fluctuate due to the on/off cycling of the coolant temperature controller (see Fig. 7.4). This thermal cycling could potentially cause fluctuations in the synchronous error motions of the spindle. In order to reduce this effect, the inlet temperature is monitored real-time and the displacement data for each orientation is acquired at multiple (at least ten) thermal states (corresponding to various inlet temperatures) spanning the range of thermal fluctuations, with at least three repetitions for each state. The synchronous motions used for the mathematical formulation shown in Section 7.2.1 are the average of the synchronous motions measured at the multiple thermal states, including all the repetitions. Thus, any potential changes in the spindle error motions due to thermal cycling effects are averaged out for each orientation before going through the error separation calculations. Once the artifact form error is calculated from these averaged synchronous motions, the synchronous spindle error motions for a specific thermal state are calculated by using the original synchronous motions measured for that particular thermal state.

The main factor that could not be controlled for the spindle tested in this paper are the centering errors between different orientations. The spindle uses a thread-in style collet, which has been seen to cause relatively large variations (up to 100% change) between repeated attachments. Hence, in order to minimize the dynamic effects due to differences in centering errors across orientations, the lowest operational speed of the UHS spindle is used to implement the error separation technique and obtain the artifact form error. The obtained artifact form would remain the same across different speeds and can be directly subtracted from the synchronous motions measured at higher speeds to obtain the spindle error motions.

7.2.3.1 Effectiveness of the Implementation

To evaluate the effectiveness of the multi-orientation technique in error-separation for UHS spindles, measurements are conducted on the Fischer Precise spindle at its lowest operational speed of 40 krpm along a fixed-sensitive Y-direction for fifteen different (arbitrary) orientations of the artifact. All tests are conducted on the custom-made sphere-on-stem artifact, from both the sphere and stem (cylinder) ($\approx$ 3 mm away from the sphere) regions of the artifact for all the fifteen orientations. For each orientation, displacement and reflectivity data are acquired for ten different thermal states covering the total temperature fluctuation range, with three repetitions for each state. The average of the synchronous motions across all these thermal states and repetitions is used within the mathematical formulation of the multi-orientation technique to calculate the artifact form error.

The data obtained from the fifteen orientations is used to characterize the effect of different combinations and the number of orientations (used for error separation) on the bandwidth of error separation and the repeatability of measuring the artifact form error. For a certain fixed number of orientations, different combinations of the number of orientations are picked from the set of fifteen orientations. For a given combination, the corresponding rotation angles are used in respective equations to calculate the bandwidth. Those combinations that result in a bandwidth less than 50 harmonics are considered invalid for further processing. For the valid combinations, the average synchronous motions corresponding to each of the orientations of a certain combination are used within the framework of the mathematical formulation described in Section 7.2.1 to obtain the artifact form error for that particular combination. After discarding extreme outliers (using the quartile-based outlier detection method [151]), repeatability of the calculated artifact form error is analyzed for a given number of orientations. Beginning from three-orientation implementation, all possible number of orientations up to fifteen-orientation implementation are studied.

In addition to this study, the acquired data also allows for a direct evaluation of the effectiveness of the technique in error separation from different regions on the artifact (sphere and stem) that

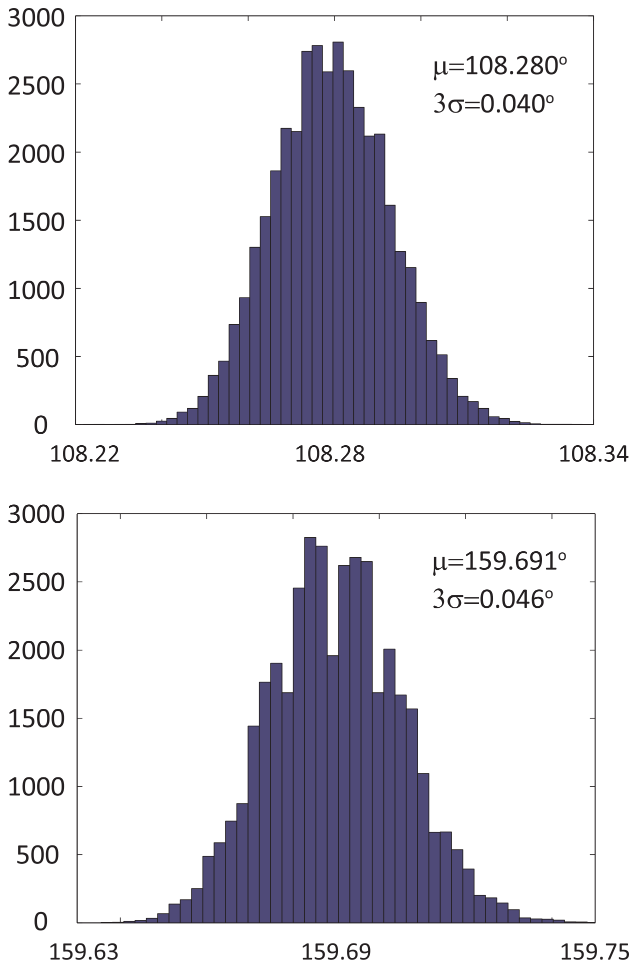

Figure 7.5: Histograms of the measured relative angles for two of the fifteen orientations.

have significantly different form errors. The spindle error motions obtained from the two regions of the artifact are compared and analyzed.

7.2.3.2 Results and Discussion

The relative angle for a given orientation is defined as the mean of the relative angles between the artifact- and spindle-markers, measured across all the revolutions for that particular orientation. The mean includes data from both the sphere and stem measurements which corresponds to $\approx$ 33,000 revolutions for each orientation. Histograms of the relative angles for two of the fifteen orientations are shown in Fig. 7.5. It can be clearly seen that the distribution is nearly of *normal* type. This was the case for all orientations. Hence, we can use the standard deviation of the relative angle measurements to characterize the variability and angular resolution.

Table 7.1: Descriptive statistics of the measured relative angles and the rotation angles for all orientations.

Orientation	**Relative angle statistics (in degrees)**		**Rotation angle (in degrees)**
	μ	3σ	(Total range: -89^o - 219^o)
1	108.280	0.040	0
2	66.474	0.092	-41.806
3	91.116	0.067	-17.163
4	19.224	0.096	-89.056
5	118.853	0.075	10.573
6	300.617	0.152	192.337
7	236.772	0.046	128.493
8	274.997	0.109	166.718
9	255.078	0.093	146.798
10	270.953	0.059	162.673
11	159.691	0.046	51.411
12	185.157	0.061	76.877
13	219.863	0.104	111.583
14	37.430	0.095	-70.850
15	327.084	0.131	218.805

Table 7.1 shows relative angles for all the orientations, including their 3σ values. The measured 3σ values are less than 0.1^o, indicating that that the resolution of the reflectivity-based pattern-detection technique to identify spindle- and artifact-markers, and hence the rotation angles is better than or equal to $\pm 0.1^o$. By arbitrarily setting the rotation angle of the first orientation to be zero, the rotation angles of the remaining fourteen orientations with respect to the first one are calculated. During these tests, while changing orientations, specific attention was paid to turn the artifact in such a manner that it covers a wide range of angles (-89^o - 219^o). This can be observed from the measured rotation angles.

Figure 7.6 plots the percentage of the number of combinations, for a given number of orientations, whose bandwidth lies within specified harmonic ranges. The harmonic range of the bandwidth increases in a highly non-linear fashion when the number of orientations is increased. The specific percentage values are strong functions of the angles used in the implementation of the multi-orientation technique. For the given set of angles used in this study, the harmonic range for almost all of the two-orientation implementations is less than 10 harmonics. However, when the number of orientations is increased to five, close to 90% of the five-orientation combinations have bandwidths whose harmonic range is greater than 100 harmonics. To ensure that the first 50 harmonics are captured as accurately as possible, we have considered only those combinations with a bandwidth greater than 50 harmonics.

Figure 7.7 shows the repeatability of the artifact form errors (for the sphere and stem portions)

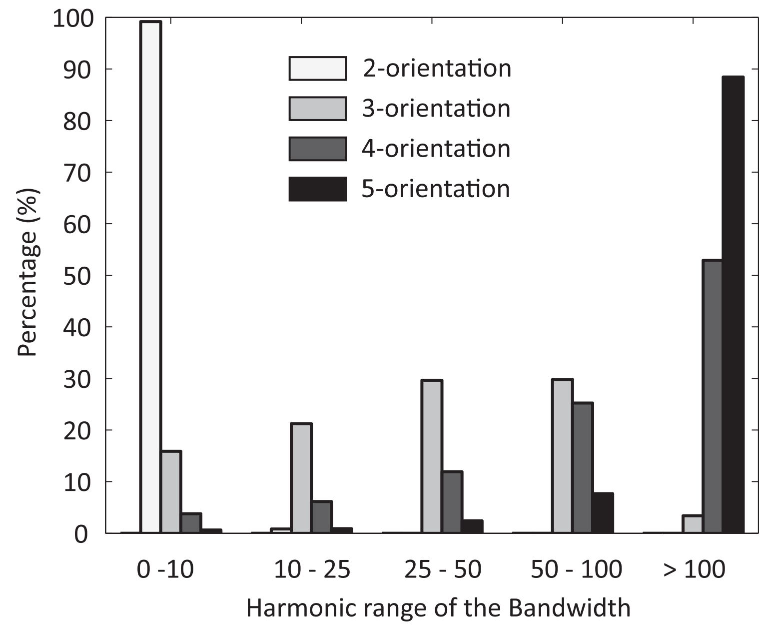

Figure 7.6: Percentage of combinations for a given number of orientations whose bandwidths lie within a specific harmonic range.

as obtained from valid combinations of five-orientations after rejecting the outliers. The associated histograms display the range of variation of the artifact form errors across one full revolution. The artifact form error of the sphere shows slightly lower variations compared to the form error of the stem portion.

There could be a few reasons for the observed variability. First, the artifact form error could be measured from slightly different circumferential tracks due to small differences (within ± 2.5 μm) in the axial measurement locations for the various orientations. Second, even though the lowest operational speeds of the spindle was used, the fundamental component of the measured motions (caused by the centering errors and the resulting dynamic effects) between orientations varied as much as 100%. These variations in centering errors and their effects could result in differences in the synchronous motions between orientations, and hence, cause variability in the measured artifact form error when different sets of orientations are used. Finally, any noise in the measurement of the synchronous motions (due to environment effects, data acquisition and processing related effects (see [127, 139]) could also be causing these variations.

The average value of the range of variation is plotted versus the number of orientations in Fig. 7.8. As the number of orientations increases, the mean value reduces significantly. This could be explained by the fact that when greater number of orientations are used, the formulation of the

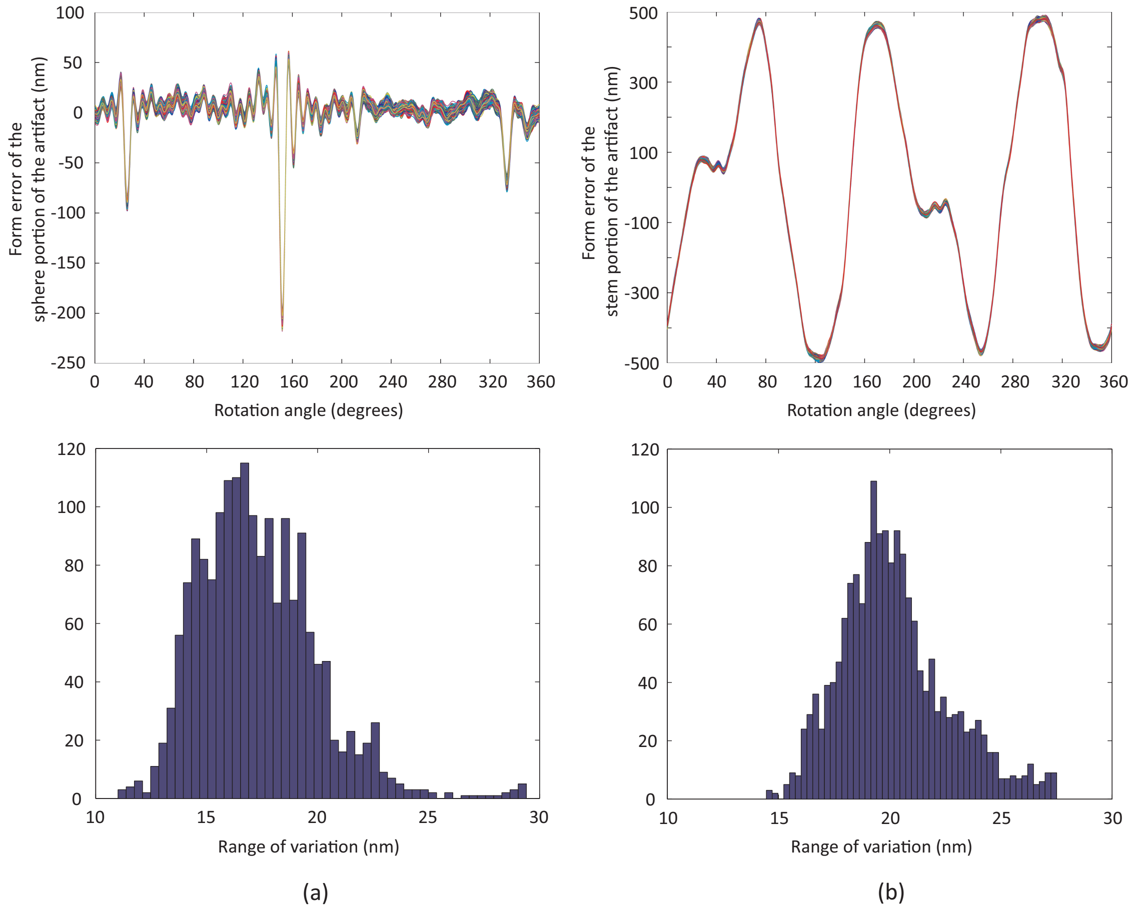

Figure 7.7: Repeatability of the measurement of artifact form errors for the five-orientation implementation: (a) Measurement from the sphere, (b) Measurement from the stem.

combined sum (Eqn. 7.2) naturally causes an averaging effect, thus reducing the effect of the various sources causing differences and uncertainty in measurements between orientations (see [166]). In the case of lower number of orientations, variations between orientations would not be completely averaged out and thus could be amplified at certain harmonics, causing increased variability between the artifact form errors obtained from different combinations. It was further observed that when the number of orientations is increased, the average artifact form error (calculated from all valid combinations) seems to converge to the artifact form error obtained from combining all the 15-orientation measurements.

For ease of practical implementation of the multi-orientation technique, we desire to choose the minimum number of orientations that allows calculation of the artifact form error within an average repeatability of ± 10 nm (i.e., an average range of 20 nm). From Fig. 7.8, the desired repeatability level is attained if a five-orientation implementation is used. Hence, for further analysis within

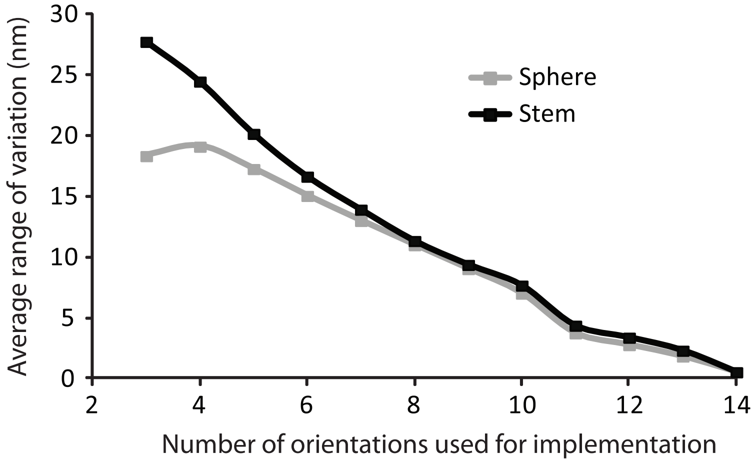

Figure 7.8: Average range of variation of the artifact form errors across valid combinations for the different number of orientations.

this thesis, the artifact form error is obtained as an average from different combinations of the five-orientation implementation.

To demonstrate the effectiveness of the multi-orientation technique in calculating the spindle error motions, the artifact form errors for the sphere and stem portions are subtracted from their respective synchronous motions measured at various thermal states for a certain orientation. The synchronous motions and the calculated spindle error motions (after form removal) as measured from the sphere and the stem are shown for ten different thermal states (with three repetitions per state) in Fig. 7.9. Even though the artifact form errors on the sphere and stem portions are significantly different (up to ten times), the multi-orientation technique is very effective in removing the form errors. This can be observed by noting that certain characteristic features of both the form errors are completely removed from their synchronous motions. Also, it can be seen that the spindle error motions measured from the sphere and the stem are quite similar in shape and magnitude. The slight differences that are observed could be due to the tilt error motions of the spindle, since the measurement locations on the sphere and stem are axially offset by ≈ 3 mm.

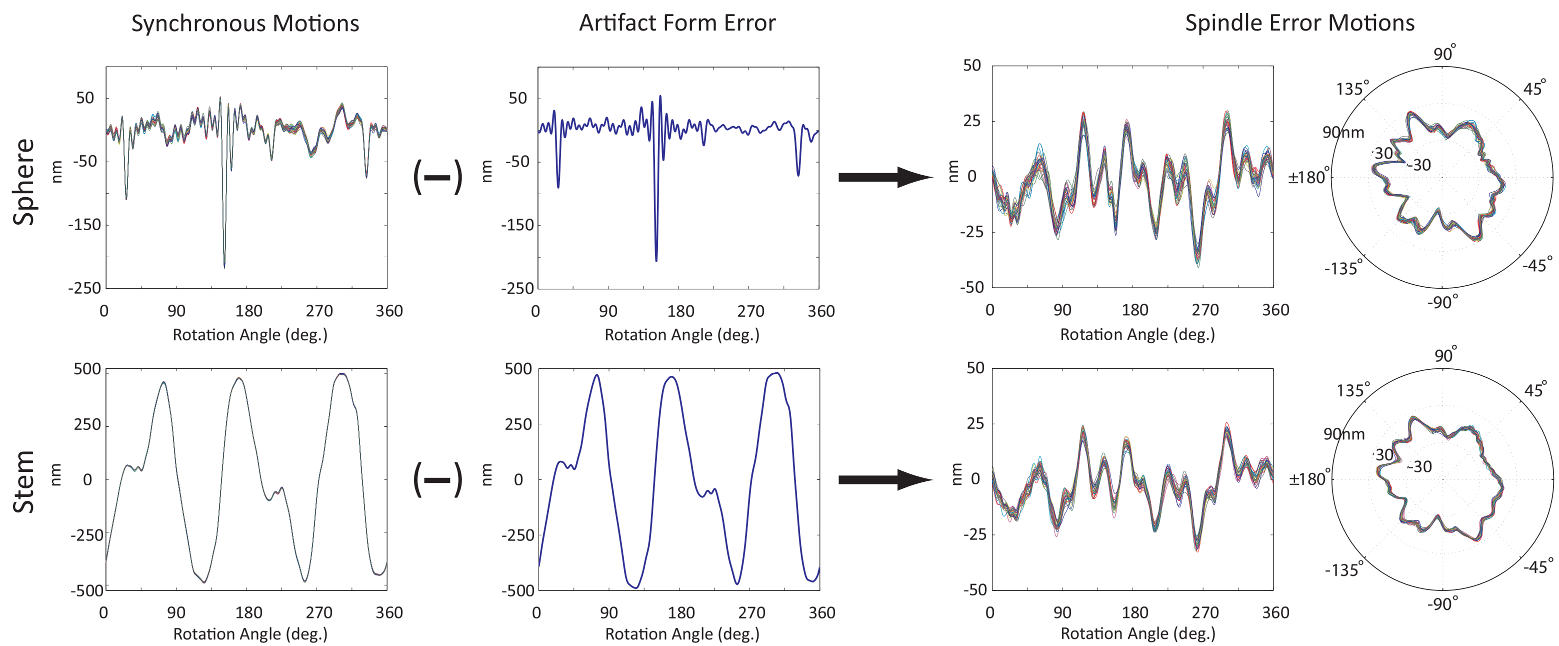

Figure 7.9: Synchronous motions and calculated spindle error motions for ten different thermal states (superimposed), as measured from (A) sphere and (B) stem portions of the artifact.

7.2.4 Error Motions at Ultra-high Speeds

The previous section demonstrated the effectiveness of the artifact form error removal at the lowest operating speed of the spindle. The procedure for obtaining the error motions at ultra-high speeds is similar to what was explained in the previous section. The multi-orientation method is implemented with a certain number of orientations and the average artifact form error with the desired number of harmonics is obtained for the lowest operational speed. Using this form error as a template, it is first accurately aligned and interpolated to the angles at which synchronous motion is measured for the ultra-high speed. Spindle error motions at the ultra-high speed are then calculated by subtracting the artifact form from the synchronous motion data.

To demonstrate this procedure, spindle error motions are determined along two orthogonal fixed-sensitive radial directions (X and Y) at four spindle speeds (40 krpm, 90 krpm, 120 krpm and 150 krpm). Because we have only two LDV systems, the X- and Y-measurements have to be conducted separately. The multi-orientation error separation procedure is first completed along one of the directions (say Y-direction). Then, the same procedure, however with a different set of (arbitrary) orientations is repeated by measuring the synchronous motion along the X-direction.

Prior to conducting any measurements, X- and Y-laser beams have to be aligned perpendicular to each other. The setup shown in Fig. 7.2 is used as the starting point for alignment. The X-laser beam that will be used later for displacement measurement is kept open, while the other X-laser beam is blocked off with a pentaprism and mirror arrangement (as explained in [139]). Using the kinematic mounts on which the laser beams are mounted, the angular alignments are adjusted such that both the X- and Y-laser beams are perpendicular to two of the surfaces of a three-faced corner cube retroreflector*, while simultaneously being perpendicular to the average surface of rotation (i.e., axis average line). This procedure is iterative and is explained clearly in [139].

Once the alignment procedure is complete, the measurement lasers along X and Y are perpendicular with respect to each other and with respect to the axis average line. The pentaprism and mirror arrangement used to block the second X-laser beam is removed and the laser beams are moved such that one of them is focused on the stem portion of the artifact that has the physical mark, while the other is moved to the rotating surface of the spindle that has the physical mark. Once all the Y-measurements are completed, without disturbing the Y-laser, the X-laser is shifted from a relative mode to single-point mode by capping off the second laser with a mirror. The measurement X-laser beam is then focused on the sphere portion of the artifact. Since the

*The faces of the corner cube are orthogonal to each other within an angle of 10 seconds

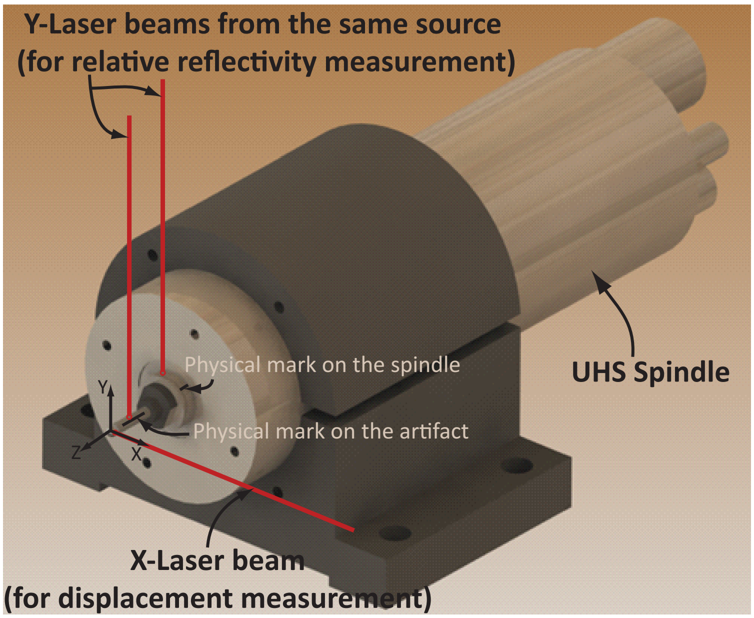

Figure 7.10: Measurement setup for implementation of the multi-orientation technique on UHS spindles along radial X-direction.

Y-laser remains untouched throughout this process, we use it as a reference. The corner-cube is used again and one its faces is made perpendicular to the Y-laser. The alignment of the X-laser is then fine-tuned such that it becomes perpendicular to the adjacent face of the corner-cube, and thus to the measurement that was conducted along the Y-direction. The Y-laser is then split into two lasers (by removing the mirror-cap from of one of the lasers). The two lasers are arranged in a parallel fashion, with one of them focused on the stem portion of the artifact with the black mark, while the other is moved to the same axial location on the rotating surface of the spindle that has the physical mark. The setup for the X-measurements is shown in Fig. 7.10. By going through this procedure, initially all the measurements are completed along the Y-direction, followed by the measurements along X-direction. Spindle error motions along the rotating-sensitive direction are calculated by projecting the error motions along X- and Y-directions onto a rotating vector (as per [114, 115]).

Five different orientations are measured for each direction. Just after the measurements from all orientations are completed, using the calculated rotation angles, it is checked if there is any suppression of harmonics that are below the 50^{th} harmonic. If there is, then additional measurements are conducted as needed from more orientations of the artifact, until a valid combination of at least five orientations could be obtained without harmonic losses below 50 harmonics. The artifact form error is then calculated from the measurements conducted at 40 krpm, using the valid

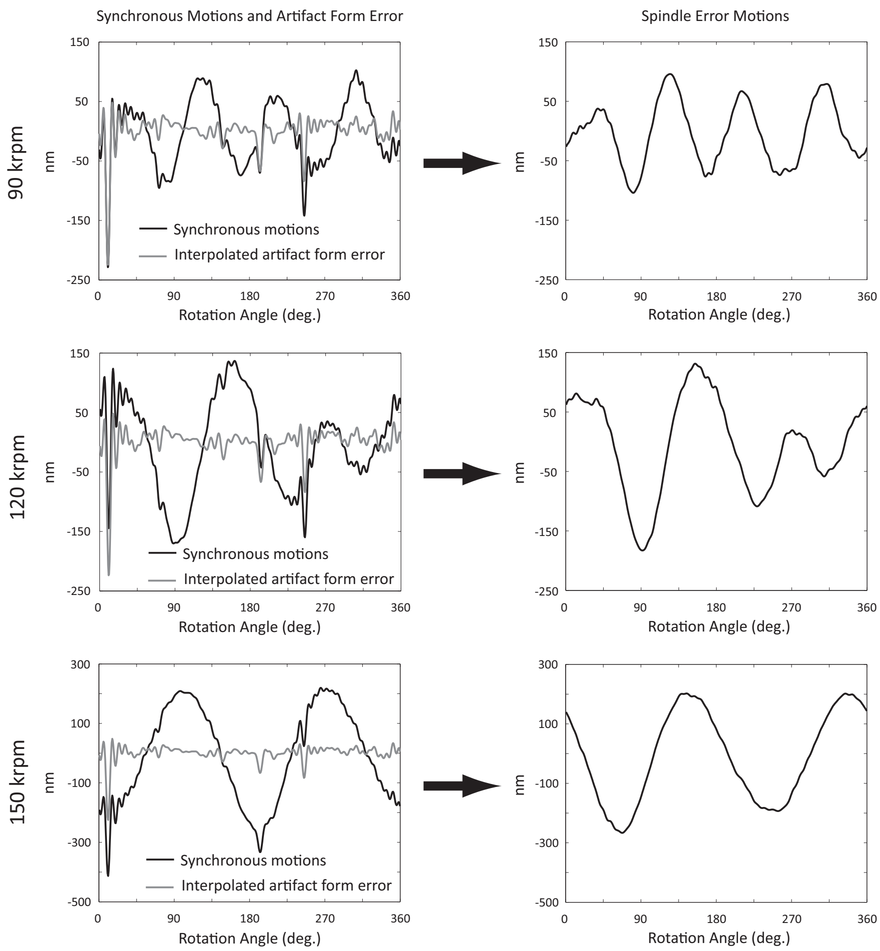

Figure 7.11: Synchronous motions and calculated spindle error motions along radial Y-direction for 90 krpm, 120 krpm and 150 krpm.

combinations of five orientations. This form error is used as a template and its interpolated version is removed from the synchronous motions measured at the four tested speeds. The effectiveness of this procedure is demonstrated in Fig. 7.11 at 90 krpm, 120 krpm and 150 krpm, for measurements conducted along the Y-direction. Both the synchronous motions as well as the spindle error motions (after form error removal) are shown for a given thermal state. It can be clearly seen that all the features of the artifact form (notches etc.) are completely removed at the higher speeds and the procedure is quite successful in accurately determining the spindle error motions at ultra-high speeds. The spindle error motions along X and Y fixed-sensitive directions as well as along the rotating-sensitive direction are shown in Fig. 7.12 for all the four speeds. The speed-dependent nature of both the shapes as well as the magnitudes of these error motions is quite evident from the plots.

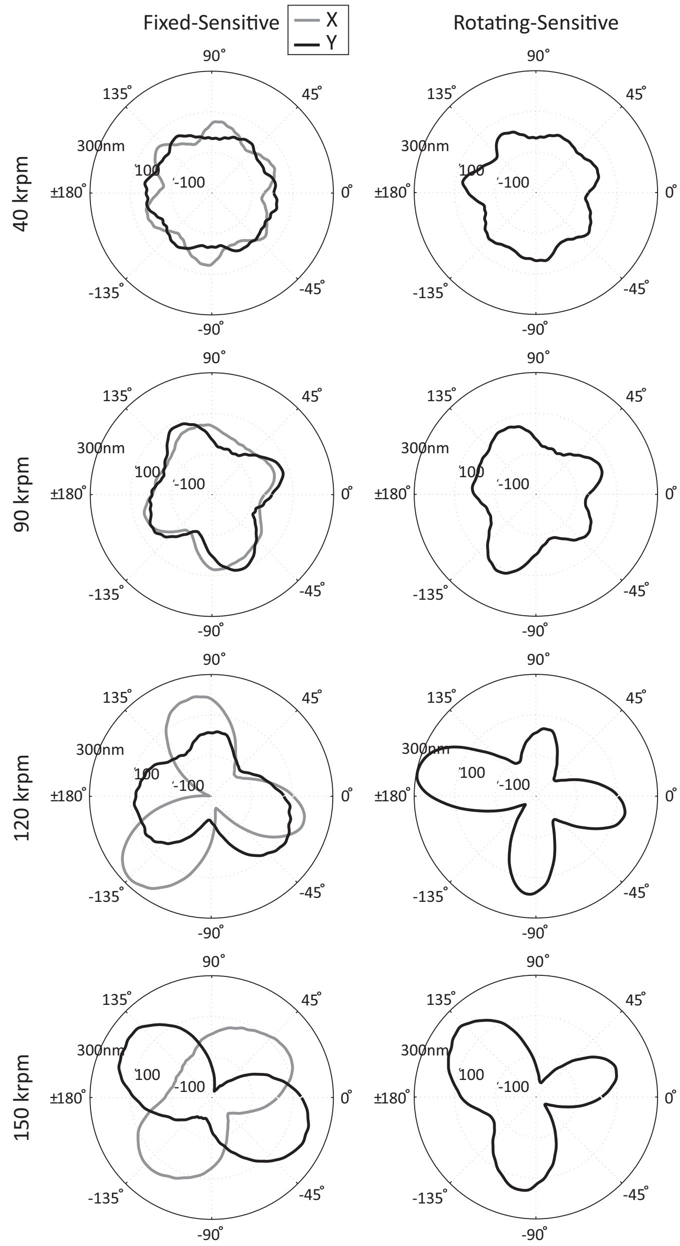

Figure 7.12: Spindle error motions along fixed-sensitive directions (X and Y) as well as along the rotating-sensitive direction for all the tested speeds.

7.3 Donaldson Reversal Method for Error Separation

This section describes an effective implementation of a slightly modified Donaldson reversal method using two LDV systems to remove artifact form error from the measured synchronous motions. Unlike the multi-orientation technique, this method allows complete separation of the artifact form

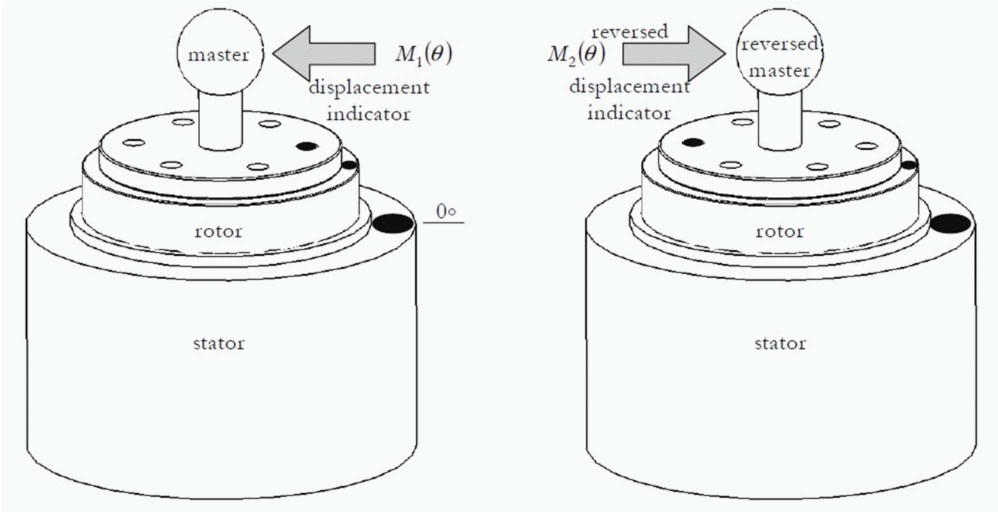

$$M_1(\theta) = A(\theta) + S(\theta)$$
$$M_2(\theta) = A(\theta) - S(\theta)$$
$$S(\theta) = (M_1(\theta) - M_2(\theta))/2$$

Figure 7.13: Standard implementation of Donaldson reversal procedure.

error and the synchronous spindle error motions.

The standard implementation of Donaldson reversal procedure (as given in [114, 167]) is illustrated in Fig. 7.13. The method requires two measurements ($\mathrm{M}_1(\theta)$ and $\mathrm{M}_2(\theta)$) from two different configurations as shown in the figure, where θ is the rotation angle. It is assumed that the physical angular orientation of the spindle corresponding to $\theta = 0^{\mathrm{o}}$ is the same for both configurations. For the second configuration, both the master (artifact) and the displacement indicator have to be reversed by 180$^{\mathrm{o}}$ relative to the spindle. The relative position of master (artifact) and the displacement indicator is unchanged while the spindle radial error motion as seen by the displacement indicator at both configurations is equal and opposite. The specific quantities measured in the two configurations are shown in Fig. 7.13, where $\mathrm{A}(\theta)$ refers to the artifact form error, and $\mathrm{S}(\theta)$ refers to the true spindle error motions, both as a function of the rotation angle. The true spindle error motions can be computed as the average difference between the measurements from the two configurations.

In order to conduct the Donaldson reversal procedure on the Fischer Precise UHS spindle, the spindle is retro-fitted with custom-designed precision fixtures as shown in Fig. 7.14. The two measurement configurations used for the Donaldson reversal method are shown in Fig. 7.15. At each configuration, simultaneous displacement measurements are conducted using two laser beams (from

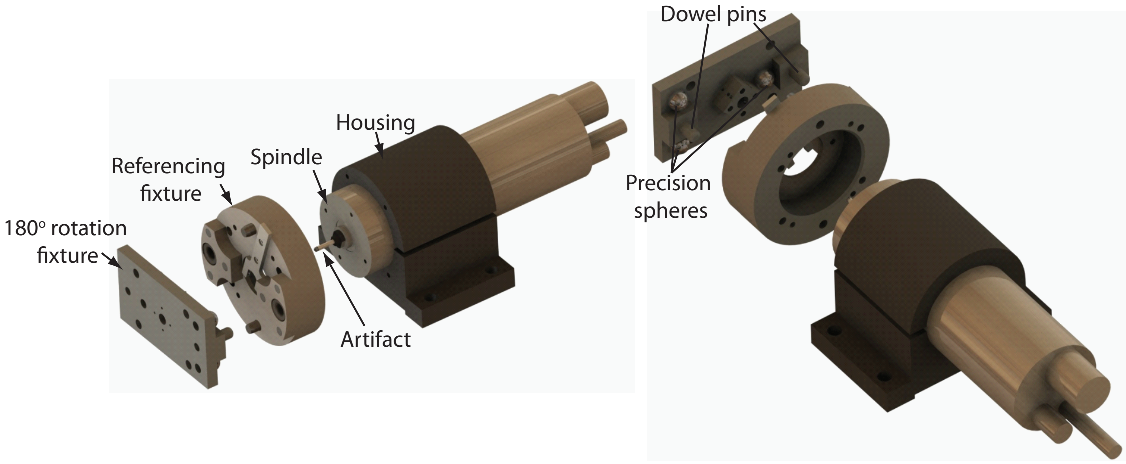

Figure 7.14: Fixture designs for implementation of Donaldson reversal method on the UHS spindle.

two different LDV systems) that are coincident and aligned to be within $180 \pm 0.08^{\circ}$. The referencing fixture provides a reference plane perpendicular to axis of the outer body of spindle. Three spheres on the 180° rotation fixture contact this plane so that the artifact's axial position could be repeatedly controlled. Under ideal conditions, this allows for the perimeter of measurement to be repeated (i.e., the same circumferential measurement track on the artifact) for both configurations of the reversal procedure. The tolerance of the pin-in-hole arrangement with the two dowel pins is strictly controlled so that the two configurations are within $180 \pm 0.1^{\circ}$ with respect to each other.

The UHS spindle used on the dual-stage polishing test-bed has a collet that is tightened (or loosened) through a nut to hold the artifact. While attaching or detaching the artifact between configurations, the relative angular position between the spindle and artifact should not be disturbed. Hence, a wrench is used to lock the spindle and a special set-screw arrangement is used to lock the artifact to the 180° rotation fixture, before changing configurations.

The implementation of the Donaldson reversal procedure on the UHS spindle is shown in Fig. 7.16. The implemented technique has some modifications compared to the standard procedure. The main difference comes from the fact that the reference angle $\theta = 0^{\circ}$ for a given configuration is defined as the passing of a black reference mark on the artifact as sensed by the stationary IR sensor. When the artifact is rotated by 180° between configurations, the reference locations for the two configurations do not correspond to the same physical angular location of the spindle (they are rotated by 180°). Hence, the spindle error motions cannot be calculated directly from the measurements. One of the measurements has to be phase-shifted by 180° before taking the average difference with the other measurement to obtain the spindle error motions.

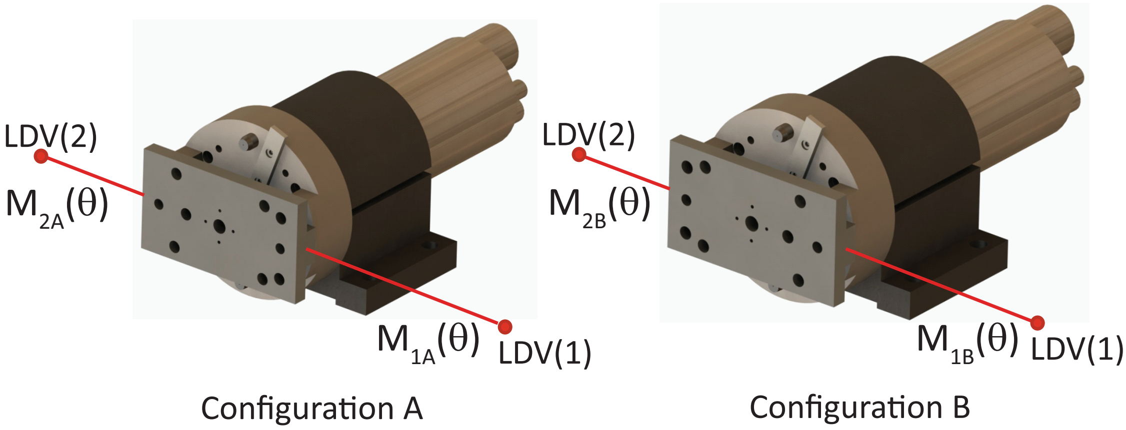

Figure 7.15: The two configurations during Donaldson reversal procedure.

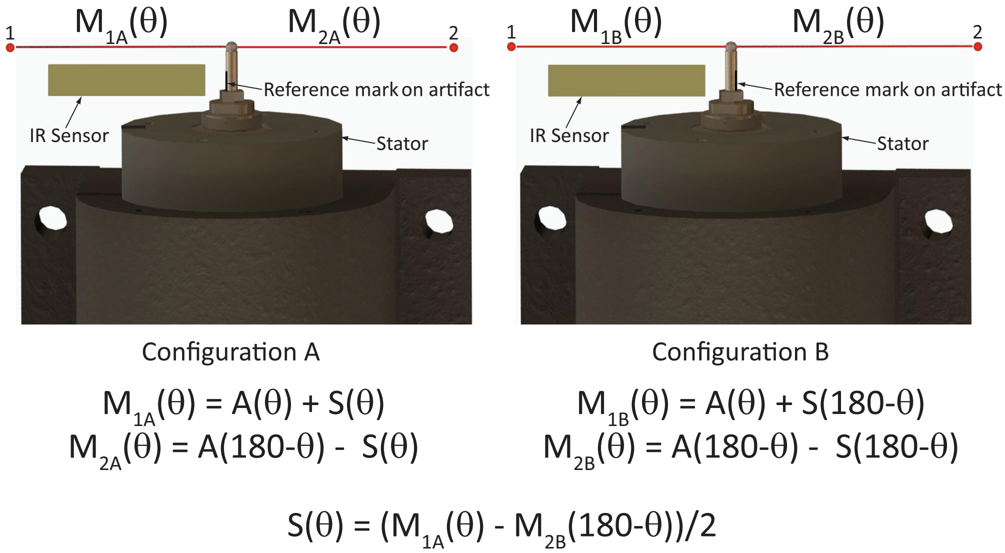

Figure 7.16: Implementation of Donaldson reversal procedure on the UHS spindle.

To assess the feasibility of this implementation, experiments from both the configurations are conducted from a tungsten-carbide cylindrical artifact on the Fischer Precise UHS spindle at speeds of 40 krpm and 80 krpm. Fig. 7.17 shows the results of the error separation after going through the reversal procedure conducted at both speeds. The success and validity of the implementation can be clearly seen from the fact that the artifact form errors obtained at the two spindle speeds are the same, with the spindle error motions being quite different.

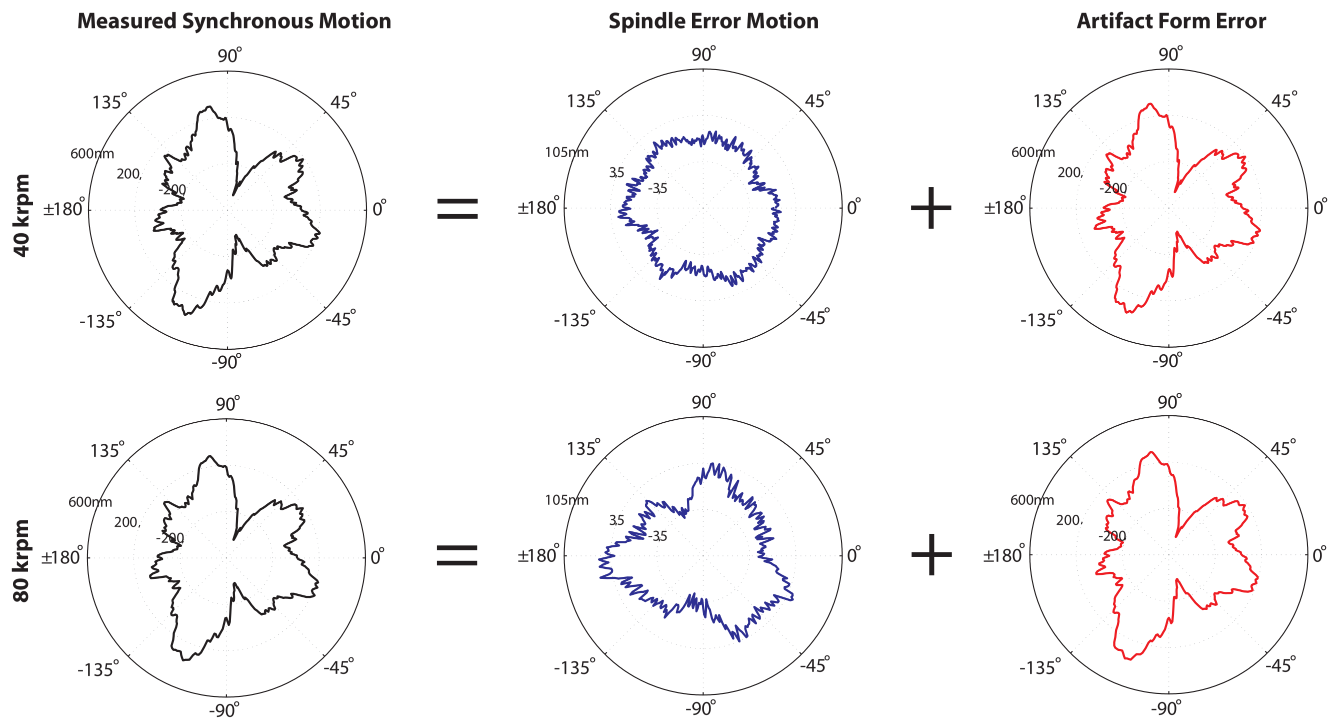

Figure 7.17: Results of the error separation using Donaldson reversal procedure at 40 krpm and 80 krpm.

7.4 Summary

This chapter presented implementations of two error separation techniques - Multi-Orientation Technique and Donaldson Reversal Method that are utilized to remove the artifact form error from the measured synchronous radial motions from an UHS spindle. A thorough experimental evaluation of the multi-orientation technique and its effectiveness at ultra-high speeds is presented.

The following specific conclusions can be drawn from the work presented in this chapter.

- For the implementation of the multi-orientation technique:
  - The harmonic range of the bandwidth increases in a highly non-linear fashion when the number of orientations is increased. For the given set of angles used in this work, the harmonic range for almost all of the two-orientation implementations is less than 10 harmonics, while for the five-orientation implementation, close to 90% of the combinations have bandwidths whose harmonic range is greater than 100 harmonics.
  - The average range of variation of the artifact form errors reduces significantly as the number of orientations increases. Based on the desired level of repeatability for the calculation of the artifact form error, we can choose the minimum number of orientations required to attain that level.
  - Even though the artifact form errors on the sphere and stem portions are significantly different (up to ten times), the spindle error motions obtained from both locations (that are axially offset by $\approx$ 3 mm) are very similar in shape and magnitude, thus demonstrating the effectiveness of the technique.
  - By using the form error at 40 krpm as a template, spindle error motions at ultra-high speeds were successfully quantified along both the fixed-sensitive (X, Y) and rotating-sensitive directions at 90 krpm, 120 krpm and 150 krpm.
- A slightly modified Donaldson reversal method using two LDV systems is successfully implemented by using two simultaneous displacement measurements for the two measurement configurations.
- The modified reversal method is shown to be quite effective in the removing the artifact form error at speeds up to 80 krpm.

Chapter 8

Conclusions

The research presented in this work aimed to gain an understanding of the mandrel-based polishing process and equipment to enable identifying favorable polishing conditions that will lead to accurate fabrication of micro-tools from single-crystal diamond and ceramics in a predictable fashion. The mandrel-based polishing process was demonstrated to be highly effective in polishing and shaping diamond to create smooth surfaces and sharp edges (≤ 1 μm edge radius). The polished surface quality was observed to be a strong function of polishing parameters such as grit size, polishing path (kinematics) and the boart material used during polishing. One critical issue identified with the process was the poor (dimensional and form) accuracy of removal. Mandrel-wear, elastic deflections within the structural-loop (including deflection of the mandrel, deflection of the spindle due to it radial stiffness and deflection of the precision slides), and the dynamic axial and radial motions of the miniature ultra-high-speed (UHS) air-bearing spindle were hypothesized to be the dominant factors affecting the accuracy.

A dual-stage polishing test-bed was designed and constructed as a hybrid-solution to include 1) the large-wheel based traditional diamond polishing system with high material removal rates for "rough" polishing, and 2) a rigid mandrel-based polishing configuration with capability to create intricate micro-scale features and high-aspect-ratio structures on single-crystal diamond and ceramics. The machine components of the mandrel-based polishing configuration were intentionally designed/chosen to be extremely rigid in order to address the issues identified earlier. The test-bed was also designed such that the entire tool-fabrication process, starting from a relatively large-sized roughly cut diamond to a finished micro-scale cutting tool with a specified shape and diameter as well as with smooth surfaces and sharp edges, is almost completely automated.

Finally, the polishing characteristics of various tool-grade ceramics were experimentally analyzed to evaluate their applicability for micro-scale cutting. Sharp (cutting) edges were created by lapping two adjacent surfaces of various tool materials using a two-stage lapping process under conservative conditions. Almost all the ceramic materials tested had a better surface roughness than sub-micron grade carbide. Two of the five materials (SiAlON and (Al_2O_3+TiC+TiN)) could be polished to surface roughness (Ra) values less than 5 nm. All ceramic materials were capable of being sharpened to edge radii less than 2 μm, which is less than the edge radius obtained for sub-micron grade carbide. SiAlON is the most sharpenable material, with an edge radius of approximately 0.5 μm.

For effective application of the mandrel-based polishing process to fabricate accurate features and smooth surfaces, a thorough experimental analysis of the radial and axial motions of the electrically-driven hybrid-ceramic-bearing UHS spindle used on the dual-stage polishing test-bed was seen to be essential. Due to the lack of a reliable spindle-metrology technique that could be applied to UHS spindles, a laser Doppler vibrometry (LDV)-based methodology for measuring the axial and radial error motions of UHS spindles was developed. The axial and radial motions were measured from the surface of a custom-fabricated sphere-on-stem precision artifact. A measurement setup and an alignment procedure were used to align three laser beams in a mutually orthogonal fashion, where the axial laser beam was aligned to coincide with the axis average line. The measured axial and radial motions were post-processed to obtain the synchronous and asynchronous components of the axial and radial error motions in both fixed-sensitive and rotating-sensitive directions. The sources and amounts of uncertainties in measuring the motions and in calculating the error motions were then analyzed.

A thorough experimental analysis of the radial and axial motions of the electrically-driven hybrid-ceramic-bearing miniature UHS spindle used on the dual-stage polishing test-bed was conducted using the LDV-based spindle metrology technique. The effect of temperature cycling and artifact over-hang length on the spindle motions were analyzed at different spindle speeds. The repeatability of artifact (tool) attachment to the collet and the associated effect on spindle motions were also studied. Some of conclusions that can be drawn are:

- Even under steady-state conditions, the on-off nature of the coolant controller imposes a cyclic behavior to spindle temperatures, which results in up to ±30% variation in synchronous radial error motion value, and up to ±40% change in the fundamental axial error motion amplitude.
- The *fundamental component of the radial motions* is dominated by the quasi-static effects of the centering errors for speeds up to 100 krpm. Above 100 krpm, the dynamic effects become

dominant, resulting in increased amplitude at higher spindle speeds.

- The *synchronous components of the radial motions* vary strongly with the spindle speed. Both the shape (orbit) and amplitude of these motions change significantly with the spindle speed. Furthermore, the effect of spindle speed is confounded with that of the over-hang length.

- A majority of the *asynchronous axial and radial motions* of the spindle arise from the bearing frequencies, which result in a linear shift in dominant frequencies with the spindle speed. Few other dominant frequencies are also observed, which may be arising from the natural frequencies of the spindle, artifact and/or structure. The over-hang length also has a significant effect on asynchronous radial motions.

- The *synchronous axial error motions* are highly sensitive to the spindle speed. At speeds below 90 krpm, the motions are dominated by multiple harmonics, whereas above 90 krpm, the motions are mainly composed of the fundamental axial error motion. The synchronous axial error motion values do not vary with the over-hang length. Two peaks were observed at 130 krpm and 70 krpm with values of 2 μm and 750 nm, respectively. At all other speeds, the synchronous axial error motion values are less than 500 nm.

Certain speed/over-hang length combinations were identified that could potentially induce significant dimensional errors, shape distortions, and surface roughness to the polished surfaces. Hence, this analysis provides a basis for selection of favorable process conditions for effective application of the mandrel-based polishing process.

The developed UHS spindle-metrology technique was advanced further by implementing error-separation methods to remove the artifact form error and quantify the true spindle error motions. Two different error separation techniques were implemented - Multi-Orientation Technique and a slightly modified Donaldson Reversal Method. For the implementation of the multi-orientation technique,

- The harmonic range of the bandwidth increases in a highly non-linear fashion when the number of orientations is increased.

- The average range of variation of the artifact form errors reduces significantly as the number of orientations increases. Based on the desired level of repeatability for the calculation of the artifact form error, we can choose the minimum number of orientations required to attain that level.

- Even though the artifact form errors on the sphere and stem portions are significantly different (up to ten times), the spindle error motions obtained from both locations (that are axially offset by ≈ 3 mm) are very similar in shape and magnitude, thus demonstrating the effectiveness of the technique.

- By using the form error at 40 krpm as a template, spindle error motions at ultra-high speeds were successfully quantified along both the fixed-sensitive (X, Y) and rotating-sensitive directions at 90 krpm, 120 krpm and 150 krpm.

The slightly modified Donaldson reversal method has also been shown to be quite effective in the removing the artifact form error at speeds up to 80 krpm.

Chapter 9

Future Work

The research conducted as part of this thesis has to be extended further in order to successfully fabricate accurate single-crystal diamond and ceramic micro-endmills in a repeatable fashion. Certain specific tasks have to be completed in the near-term to ensure that the potential high-impact nature of this work is realized. These tasks are described in the following sections.

9.1 Further Refinements to Multi-Orientation Technique for UHS Spindles

The implementation of the multi-orientation technique presented in this work has worked quite well in separation of artifact form errors. However, there are currently certain open issues that need to worked upon.

Specific objectives of this work are:

- Improving the accuracy of the relative angle measurement through more robust pattern-matching algorithms and fabrication of accurate physical marks.
- Using infra-red- and laser-based sensors to provide angular reference triggers every revolution that could be used for angle measurement as well as for synchronizing the data.
- Comparing the form errors obtained using this technique with a direct roundness error measurement.

9.2 Analysis of the Implementation of Donaldson Reversal Method on UHS Spindles

Even though the Donaldson reversal method has been shown to successfully remove artifact form error at ultra-high speeds, there were certain issues that we encountered during the experiments that require careful analysis. Further, after resolving these issues, we need to use this technique to determine the spindle error motions for various operating conditions.

Specific objectives of this work are:

- Resolve open issues that were encountered during the initial experiments.
- Conduct measurements to separate the artifact form errors from sphere-on-stem and cylindrical artifacts to obtain the true spindle error motions.
- Characterize the true spindle error motions at different spindle speeds and over-hang lengths.

The Donaldson reversal procedure should be implemented on the electrically-driven hybrid-ceramic-bearing UHS spindle to be used for mandrel-based polishing. The procedure should be implemented with different types of artifacts, at different overhang lengths and spindle speeds. The experimental matrix for these tests is given below (Table 9.1). For each case, the procedure should be carried out at least ten times to study the repeatability in error separation.

Table 9.1: Experimental matrix for Donaldson reversal studies.

Artifact Type	sphere-on-stem artifact, cylindrical carbide blank
Spindle Speeds	40 krpm - 160 krpm, in steps of 10 krpm
Over-hang length	7.5 mm, 15 mm

All artifacts should be attached to the spindle with the same collet-torque. For a given artifact, spindle speed and over-hang length, differences in the true spindle error motions are due to issues with the repeatability of the procedure and of the artifact attachment to the spindle. If the differences are negligible, then comparisons should be made across different over-hang lengths and artifact types. In all cases, the polar plots of the synchronous radial error motions and synchronous radial error motion values should be used as comparison metrics.

9.3 Studying the Effect of Spindle Error Motions on Polishing Accuracy

To understand the effect of axial and radial error motions on the geometric accuracy and surface roughness of the polished surfaces, numerical simulations should be conducted using the measured spindle error motions as an input. The polished surfaces should be generated through the simulation by taking into account only the polishing process kinematics with no forces/dynamics. These generated surfaces should be analyzed to correlate the influence of spindle error motions on the form errors and surface roughness at various polishing speeds.

9.4 Understanding Polishing Behavior of Single-crystal Diamond and Ceramics

A thorough understanding of the polishing characteristics of single-crystal diamond and ceramics when polished using the mandrel-based polishing process is essential to create smooth surfaces, sharp cutting-edges, and accurate micro-scale features on the respective materials.

Specific objectives of this work are:

- To experimentally correlate the polishing forces, geometric characteristics, and polishing rate/mandrel wear as a function of polishing parameters during mandrel-based polishing process of single-crystal diamond and ceramics.
- To develop semi-empirical mechanistic models of the mandrel-based polishing process for single-crystal diamond and ceramics in order to predict the polishing forces, polishing rates, surface roughness, polishing-tool wear, as a function of the polishing parameters.

Based on literature [36], the best edge radius is obtained with a tool orientation that has the rake and flank faces being the cube plane {100}. For the scope of the experiments that are envisioned in this work, the crystallographic orientation of the faces being polished should be restricted to the {100}. Two different sets of studies should be conducted to understand the polishing characteristics of single-crystal diamond.

The first set of studies should be conducted to investigate the effect of polishing directions on the {100} planes. In this study, single-crystal diamond workpieces should be polished along two of the {100} planes – (100) and (010). On each plane, the polishing direction should be changed in discrete steps of 30^o to obtain a total of 12 different polishing directions. For each plane, two different workpieces should be polished to ascertain repeatability. The polishing forces, polishing rate, polished surface roughness, and the polishing-tool wear should be studied. The mandrel type, the polishing speed, the size of abrasive particles, and the polishing path should be kept constant. The desired outcome of this study is an experimental understanding of the effects of polishing direction (crystallographic orientation) on polishing rate and surface roughness during mandrel-based polishing of single-crystal diamond.

The second set of studies should be conducted to analyze the effect of polishing parameters, while keeping the crystallographic orientation of the polished faces constant. This should be done by polishing the adjacent {100} faces – (100) and (010) in the "optimal" directions (the "optimal" direction should be the one that provides the lowest surface roughness) to obtain a cutting edge.

The polishing parameters that should be studied include the mandrel-type, polishing speed, the polishing depth, polishing feed rate, the size of abrasive particles, the polishing motion path, the polishing configuration relative to the edge, and the crystallographic orientation and direction (for diamond). A family of potential test conditions using which the experimental test matrix should be created is provided in Table 9.2. Each test should be repeated twice ensure the repeatability of the results.

Table 9.2: Experimental matrix for studying the effect of polishing parameters on single-crystal diamond.

Mandrel Type	Diamond-paste charged cast-iron, Bonded
Polishing Speed (m/sec)	20, 40
Prescribed polishing depth per pass (nm)	50, 100
Prescribed cross-feed rate (mm/sec)	1, 5
Size of abrasive particles (μm)	0-2, 5-10
Polishing motion path	Straight back-and-forth, Circles with discrete steps
Polishing configuration relative to the edge	Perpendicular, Parallel

The response parameters should include polishing forces, polished surface roughness, edge sharpness and condition, polishing rate, and the polishing-tool wear. The main and interaction effects of the polishing parameters on the response parameters should be analyzed. The desired outcome of these polishing tests is to obtain a thorough understanding of the mandrel-based polishing process when used in polishing single-crystal diamond.

A similar set of studies (as shown in Table 9.2 should be conducted on tool-grade ceramics as well.

9.5 Fabrication and Evaluation of Single-crystal Diamond Micro-endmills

Using the understanding obtained through the polishing studies, following these studies, complex micro-endmill geometries should be fabricated using the mandrel-based polishing process. The overall effectiveness of the process in creating functional endmills with accurate geometries (include the cross-sectional form, size, and aspect ratio) and sharp edges should be evaluated.

The specific objective of this work are:

- To plan the kinematics of the polishing process to efficiently fabricate single-crystal diamond micro-endmills.
- To perform cutting tests in order to evaluate the fabricated micro-endmills.

All of the micro-endmills that are planned to be fabricated include single straight cutting edges. Two different tool-designs with complex geometries should be considered, with a tool-diameter between 250 μm – 500 μm and an aspect ratio between 1.5 – 3. Each micro-endmill should be evaluated for geometric accuracy (form, waviness, surface roughness), edge sharpness and edge condition.

The fabricated endmills should be evaluated by conducting micromilling tests on different materials such as PMMA and naval brass. Full immersion cuts should be performed on each workpiece for each tool. The cutting forces, surface roughness of the machined surface, and the burr formation should be evaluated.

Bibliography

[1] X. Liu, R. E. DeVor, S. G. Kapoor, K. F. Ehmann, The mechanics of machining at the microscale: Assessment of the current state of the science, Transactions of the ASME: Journal of Manufacturing Science and Engineering 126 (2004) 666–678.

[2] K. F. Ehmann, D. Bourell, M. Culpepper, T. Hodgson, T. Kurfess, M. Madou, K. Rajurkar, R. E. DeVor, International assessment of research and development in micromanufacturing, World Technology Evaluation Center (WTEC), Inc. Panel Report, 2005.

[3] J. Chae, S. S. Park, T. Freiheit, Investigation of micro-cutting operations, International Journal of Machine Tools and Manufacture 46 (3) (2006) 313–332.

[4] D. Dornfeld, S. Min, Y. Takeuchi, Recent advances in mechanical micromachining, CIRP Annals-Manufacturing Technology 55 (2) (2006) 745–768.

[5] S. Filiz, C. M. Conley, M. B. Wasserman, O. B. Ozdoganlar, An experimental investigation of micro-machinability of copper 101 using tungsten carbide micro-endmills, International Journal of Machine Tools and Manufacture 47 (7) (2007) 1088–1100.

[6] S. Filiz, L. Xie, L. E. Weiss, O. B. Ozdoganlar, Micromilling of microbarbs for medical implants, International Journal of Machine Tools and Manufacture 48 (3-4) (2008) 459–472.

[7] M. Jun, R. E. DeVor, S. G. Kapoor, F. Englert, Experimental investigation of machinability and tool wear in micro-endmilling, Transactions of NAMRI/SME XXXVI (2008) 201–208.

[8] M. P. Vogler, R. E. DeVor, S. G. Kapoor, Microstructure-level force prediction model for micro-milling of multi-phase materials, Transactions of the ASME: Journal of Manufacturing Science and Engineering 125 (2) (2003) 202–209.

[9] C.-J. Kim, M. Bono, J. Ni, Experimental analysis of chip formation in micro-milling, Transactions of NAMRI/SME XXX (2002) 247–254.

[10] M. P. Vogler, On the modeling and analysis of machining performance in micro-endmilling, Ph.D. Thesis, University of Illinois at Urbana-Champaign (2003).

[11] D. A. Lucca, Y. W. Seo, Effect of tool edge geometry on energy dissipation in ultraprecision machining, CIRP Annals-Manufacturing Technology 42 (1) (1993) 83–86.

[12] C.-J. Kim, J. R. Mayor, J. Ni, A static model of chip formation in microscale milling, Transactions of the ASME: Journal of Manufacturing Science and Engineering 126 (2004) 710–718.

[13] J. Wilks, E. Wilks, Properties and applications of diamond, Butterworth-Heinemann Oxford, 1994.

[14] R. Komanduri, Friction and wear of ceramics, edited by Said Jahanmir: Ceramic Cutting Tools, CRC Press, 1994.

[15] E. D. Whitney, Ceramic cutting tools: materials, development, and performance, William Andrew, 1994.

[16] J. Hird, J. Field, Diamond polishing, Proceedings of the Royal Society of London. Series A: Mathematical, Physical and Engineering Sciences 460 (2052) (2004) 3547–3568.

[17] M. Tolkowsky, Research on the abrading, grinding or polishing of diamond, D.Sc. Thesis, City and Guilds College, University of London (1920).

[18] S. Grillo, J. Field, F. Bouwelen, Diamond polishing: the dependency of friction and wear on load and crystal orientation, Journal of Physics D: Applied Physics 33 (8) (2000) 985–990.

[19] F. Van Bouwelen, Diamond polishing from different angles, Diamond and Related Materials 9 (3) (2000) 925–928.

[20] Y. Enomoto, D. Tabor, The frictional anisotropy of diamond, Proceedings of the Royal Society of London. A. Mathematical and Physical Sciences 373 (1755) (1981) 405–417.

[21] L. Xiangdong, D. Xin, Diamond Tool Resharpening, SIMTech Technical Report, Singapore Institute of Manufacturing Technology, 2002.

[22] J. Hird, J. Field, A wear mechanism map for the diamond polishing process, Wear 258 (1) (2005) 18–25.

[23] J. Hird, M. Bloomfield, I. Hayward, Investigating the mechanisms of diamond polishing using Raman spectroscopy, Philosophical Magazine 87 (2) (2006) 267–280.

[24] F. Van Bouwelen, J. Field, L. Brown, Electron microscopy analysis of debris produced during diamond polishing, Philosophical Magazine 83 (7) (2003) 839–855.

[25] M. Couto, W. van Enekevort, B. Wichman, M. Seal, Scanning tunneling microscopy of polished diamond surfaces, Applied Surface Science 62 (4) (1992) 263–268.

[26] M. Couto, W. Van Enckevort, M. Seal, Diamond polishing mechanisms: an investigation by scanning tunnelling microscopy, Philosophical magazine. B. Physics of condensed matter. Structural, electronic, optical and magnetic properties 69 (4) (1994) 621–641.

[27] F. Van Bouwelen, W. Van Enckevort, A simple model to describe the anisotropy of diamond polishing, Diamond and Related Materials 8 (2) (1999) 840–844.

[28] F. Van Bouwelen, Polishing: mechanically induced degradation of diamond, Physica Status Solidi Applied Research 172 (1) (1999) 91–96.

[29] M. Jarvis, R. Pérez, F. Van Bouwelen, M. Payne, Microscopic mechanism for mechanical polishing of diamond (110) surfaces, Physical Review Letters 80 (16) (1998) 3428–3431.

[30] W. Zong, D. Li, K. Cheng, T. Sun, H. Wang, Y. Liang, The material removal mechanism in mechanical lapping of diamond cutting tools, International Journal of Machine Tools and Manufacture 45 (7) (2005) 783–788.

[31] L. Pastewka, S. Moser, P. Gumbsch, M. Moseler, Anisotropic mechanical amorphization drives wear in diamond, Nature Materials 10 (1) (2010) 34–38.

[32] W. Zong, T. Sun, D. Li, K. Cheng, Z. Li, Nano-precision diamond cutting tools achieved by mechanical lapping versus thermo-mechanical lapping, Diamond and Related Materials 17 (6) (2008) 954–961.

[33] W. Zong, D. Li, T. Sun, K. Cheng, Y. Liang, The ultimate sharpness of single-crystal diamond cutting tools – Part II: A novel efficient lapping process, International Journal of Machine Tools and Manufacture 47 (5) (2007) 864–871.

[34] W. Zong, T. Sun, D. Li, K. Cheng, Design criterion for crystal orientation of diamond cutting tool, Diamond and Related Materials 18 (4) (2009) 642–650.

[35] W. Zong, Z. Li, T. Sun, K. Cheng, D. Li, S. Dong, The basic issues in design and fabrication of diamond-cutting tools for ultra-precision and nanometric machining, International Journal of Machine Tools and Manufacture 50 (4) (2010) 411–419.

[36] W. Zong, D. Li, T. Sun, K. Cheng, Contact accuracy and orientations affecting the lapped tool sharpness of diamond cutting tools by mechanical lapping, Diamond and Related Materials 15 (9) (2006) 1424–1433.

[37] W. Zong, D. Li, T. Sun, K. Cheng, Y. Liang, The factors influencing on cutting edge radius of ultra-precision diamond cutting tools in mechanical lapping, Key Engineering Materials 304 (2006) 345–349.

[38] I. Miyamoto, T. Ezawa, K. Nishimura, Ion beam machining of single-point diamond tools for nano-precision turning, Nanotechnology 1 (1) (1990) 44–49.

[39] M. Vasile, R. Nassar, J. Xie, H. Guo, Microfabrication techniques using focused ion beams and emergent applications, Micron 30 (1999) 235–244.

[40] D. Adams, M. Vasile, T. Mayer, V. Hodges, Focused ion beam milling of diamond: Effects of H2O on yield, surface morphology and microstructure, Journal of Vacuum Science and Technology B: Microelectronics and Nanometer Structures 21 (6) (2003) 2334–2343.

[41] Y. Picard, D. Adams, M. Vasile, M. Ritchey, Focused ion beam-shaped microtools for ultra-precision machining of cylindrical components, Precision Engineering 27 (1) (2003) 59–69.

[42] X. Ding, G. Lim, C. Cheng, D. Butler, K. Shaw, K. Liu, W. Fong, Fabrication of a micro-size diamond tool using a focused ion beam, Journal of Micromechanics and Microengineering 18 (7) (2008) 75017–75026.

[43] S. Bhavsar, S. Aravindan, P. Rao, A critical review on microtools fabrication by focused ion beam (FIB) technology, Proceedings of the World Congress on Engineering 2 (2009) 1510–1515.

[44] D. Ramanathan, P. Molian, Micro-and sub-micromachining of type IIa single crystal diamond using a Ti: sapphire femtosecond laser, Transactions of the ASME: Journal of Manufacturing Science and Engineering 124 (2002) 389–396.

[45] C. Everson, P. Molian, Fabrication of polycrystalline diamond microtool using a Q-switched Nd: YAG laser, The International Journal of Advanced Manufacturing Technology 45 (5) (2009) 521–530.

[46] S. Shabouk, T. Nakamoto, Micro machining of single crystal diamond by utilization of tool wear during cutting process of ferrous material, Journal of Micromechatronics 2 (1) (2002) 13–26.

[47] S. Kim, Material properties of ceramic cutting tools, Key Engineering Materials 96 (1994) 33–80.

[48] X. S. Li, I.-M. Low, Ceramic cutting tools - an introduction, Key Engineering Materials 96 (1994) 1–18.

[49] E. Ezugwu, Manufacturing methods of ceramic cutting tools, Key Engineering Materials 96 (1994) 19–32.

[50] R. Komanduri, Advanced ceramic tool materials for machining, International Journal of Refractory Metals and Hard Materials 8 (2) (1989) 125–132.

[51] M. Szafran, E. Bobryk, D. Kukla, A. Olszyna, Si3N4-Al2O3-TiC-Y2O3 composites intended for the edges of cutting tools, Ceramics International 26 (6) (2000) 579–582.

[52] C. Xu, X. Ai, C. Huang, Fabrication and performance of an advanced ceramic tool material, Wear 249 (5-6) (2001) 503–508.

[53] C. Xu, M. Shang, H. Wang, Design of thermal shock resistance of Sic/Ti(C,N)/Al2O3 ceramic composite and its machining application, Journal of Basic Science and Engineering 14 (3) (2006) 384–389.

[54] C. Xu, H. Wang, Design of ceramic composite based on the impact resistance and its machining application, Key Engineering Materials 336 (2007) 2487–2489.

[55] B. Bitterlich, S. Bitsch, K. Friederich, Sialon based ceramic cutting tools, Journal of the European Ceramic Society 28 (5) (2008) 989–994.

[56] C. Huang, B. Zou, H. Liu, Development of self-toughening silicon nitride matrix nanocomposite ceramic tools and cutting performance, Key Engineering Materials 375 (2008) 128–132.

[57] D. Jianxin, D. Zhenxing, Y. Dongling, Z. Hui, A. Xing, Z. Jun, Fabrication and performance of Al2O3/(W,Ti)C + Al2O3/TiC multilayered ceramic cutting tools, Materials Science and Engineering A 527 (4-5) (2010) 1039–1047.

[58] J. R. Davis, Tool materials, ASM International, 1995.

[59] H. Z. Miao, L. H. Qi, G. W. Cui, Silicon nitride ceramic cutting-tools and their applications, Key Engineering Materials 114 (1996) 135–172.

[60] P. Mehrotra, Applications of ceramic cutting tools, Key Engineering Materials 138 (1998) 1–24.

[61] N. Camuscu, E. Aslan, A comparative study on cutting tool performance in end milling of AISI D3 tool steel, Journal of Materials Processing Technology 170 (1) (2005) 121–126.

[62] Z. Liu, X. Ai, H. Zhang, Z. Wang, Y. Wan, Wear patterns and mechanisms of cutting tools in high-speed face milling, Journal of Materials Processing Technology 129 (1) (2002) 222–226.

[63] A. Diniz, J. Ferrer, A comparison between silicon nitride-based ceramic and coated carbide tools in the face milling of irregular surfaces, Journal of Materials Processing Technology 206 (1) (2008) 294–304.

[64] A. Chakraborty, K. Ray, S. Bhaduri, Comparative wear behavior of ceramic and carbide tools during high speed machining of steel, Materials and Manufacturing Processes 15 (2) (2000) 269–300.

[65] I. Marinescu, H. Tönshoff, I. Inasaki, Handbook of ceramic grinding and polishing, William Andrew Publishing, 2000.

[66] B. Bandyopadhyay, The effects of grinding parameters on the strength and surface finish of two silicon nitride ceramics, Journal of Materials Processing Technology 53 (3) (1995) 533–543.

[67] H. Onishi, Y. Kondo, S. Yamamoto, A. Tsukuda, K. Ishizaki, Fabrication of porous cast-iron bonded diamond grinding wheels and their evaluation to grind hard-to-grind ceramics, Journal of the Ceramic Society of Japan 104 (211) (1996) 610–613.

[68] T. Liao, G. Sathyanarayanan, L. Plebani, M. Thomas, K. Li, Characterization of grinding-induced cracks in ceramics, International Journal of Mechanical Sciences 37 (9) (1995) 1035–1050.

[69] K. Li, T. Warren Liao, Surface/subsurface damage and the fracture strength of ground ceramics, Journal of Materials Processing Technology 57 (3) (1996) 207–220.

[70] T. Maksoud, A. Mokbel, J. Morgan, Evaluation of surface and sub-surface cracks of ground ceramic, Journal of Materials Processing Technology 88 (1) (1999) 222–243.

[71] B. Zhang, X. Zheng, H. Tokura, M. Yoshikawa, Grinding induced damage in ceramics, Journal of Materials Processing Technology 132 (1) (2003) 353–364.

[72] J. Mayer Jr, G. Fang, Effect of grinding parameters on surface finish of ground ceramics, CIRP Annals-Manufacturing Technology 44 (1) (1995) 279–282.

[73] K. Ramesh, S. Yeo, S. Gowri, L. Zhou, Experimental evaluation of super high-speed grinding of advanced ceramics, The International Journal of Advanced Manufacturing Technology 17 (2) (2001) 87–92.

[74] M. Huang, T. Lin, H. Chiu, Effect of machining characteristics on polishing ceramic blocks, The International Journal of Advanced Manufacturing Technology 26 (9) (2005) 999–1005.

[75] T. Bifano, T. Dow, R. Scattergood, Ductile-regime grinding: a new technology for machining brittle materials, Transactions of the ASME: Journal of Engineering for Industry 113 (2) (1991) 184–189.

[76] G. Wamecke, U. Rosenberger, J. Milberg, Basics of process parameter selection in grinding of advanced ceramics, CIRP Annals-Manufacturing Technology 44 (1) (1995) 283–286.

[77] Z. Zhong, Surface finish of precision machined advanced materials, Journal of Materials Processing Technology 122 (2) (2002) 173–178.

[78] H. Yasui, G. Yamazaki, Possibility of ultra-smoothness grinding of fine ceramics using a coarse grain size diamond wheel, Journal of the Japan Society for Precision Engineering 69 (1) (2003) 115–119.

[79] Z. Zhong, Ductile or partial ductile mode machining of brittle materials, The International Journal of Advanced Manufacturing Technology 21 (8) (2003) 579–585.

[80] J. Shen, C. Luo, W. Zeng, X. Xu, Y. Gao, Ceramics grinding under the condition of constant pressure, Journal of Materials Processing Technology 129 (1) (2002) 176–181.

[81] K. Mizutani, T. Kawano, Y. Tanaka, Piezoelectric-drive table and its application to micro-grinding of ceramic materials, Precision Engineering 12 (4) (1990) 219–226.

[82] B. Zhang, J. Wang, F. Yang, Z. Zhu, The effect of machine stiffness on grinding of silicon nitride, International Journal of Machine Tools and Manufacture 39 (8) (1999) 1263–1283.

[83] B. Zhang, An investigation of the effect of machine loop stiffness on grinding of ceramics, CIRP Annals-Manufacturing Technology 50 (1) (2001) 209–212.

[84] Z. Xie, R. Moon, M. Hoffman, P. Munroe, Y. Cheng, Role of microstructure in the grinding and polishing of α-sialon ceramics, Journal of the European Ceramic Society 23 (13) (2003) 2351–2360.

[85] K. Kitajima, G. Cai, N. Kurnagai, Y. Tanaka, H. Zheng, Study on mechanism of ceramics grinding, CIRP Annals-Manufacturing Technology 41 (1) (1992) 367–371.

[86] S. Malkin, J. Ritter, Grinding mechanisms and strength degradation for ceramics, Key Engineering Materials 71 (1992) 195–212.

[87] S. Malkin, T. Hwang, Grinding mechanisms for ceramics, CIRP Annals-Manufacturing Technology 45 (2) (1996) 569–580.

[88] K. Li, T. Liao, Modelling of ceramic grinding processes. Part I: Number of cutting points and grinding forces per grit, Journal of Materials Processing Technology 65 (1) (1997) 1–10.

[89] B. Zhang, X. Peng, Grinding damage prediction for ceramics via CDM model, Transactions of the ASME: Journal of Manufacturing Science and Engineering 122 (1) (2000) 51–58.

[90] X. Liu, B. Zhang, Machining simulation for ceramics based on continuum damage mechanics, Transactions of the ASME: Journal of Manufacturing Science and Engineering 124 (3) (2002) 553–561.

[91] J. Fleischer, M. Deuchert, C. Ruhs, C. Kühlewein, G. Halvadjiysky, C. Schmidt, Design and manufacturing of micro milling tools, Microsystem Technologies 14 (9) (2008) 1771–1775.

[92] X. Cheng, Z. Wang, K. Nakamoto, K. Yamazaki, Design and development of PCD micro straight edge end mills for micro/nano machining of hard and brittle materials, Journal of Mechanical Science and Technology 24 (11) (2010) 2261–2268.

[93] K. Egashira, S. Hosono, S. Takemoto, Y. Masao, Fabrication and cutting performance of cemented tungsten carbide micro-cutting tools, Precision Engineering 35 (4) (2011) 547–553.

[94] X. Cheng, Z. Wang, K. Nakamoto, K. Yamazaki, A study on the micro tooling for micro/nano milling, The International Journal of Advanced Manufacturing Technology 53 (5) (2011) 523–533.

[95] Z. Qin, C. Wang, Y. Lin, Y. Hu, Optimisation of tool angles and the relation between tool path and cutting force in high-speed milling with micro-endmill, International Journal of Computer Applications in Technology 28 (1) (2007) 20–26.

[96] J. Yan, K. Uchida, N. Yoshihara, T. Kuriyagawa, Fabrication of micro end mills by wire EDM and some micro cutting tests, Journal of Micromechanics and Microengineering 19 (2) (2009) 25004–25012.

[97] F. Fang, H. Wu, X. Liu, Y. Liu, S. Ng, Tool geometry study in micromachining, Journal of Micromechanics and Microengineering 13 (5) (2003) 726–731.

[98] O. Ohnishi, H. Onikura, S. Min, M. Aziz, S. Tsuruoka, Characteristics of grooving by micro end mills with various tool shapes and approach to their optimal shape, Memoirs of the Faculty of Engineering, Kyushu University 67 (4) (2007) 143–151.

[99] C. Morgan, R. Vallance, E. Marsh, Micro-machining glass with polycrystalline diamond tools shaped by micro electro discharge machining, Journal of Micromechanics and Microengineering 14 (12) (2004) 1687–1692.

[100] J. Fleischer, T. Masuzawa, J. Schmidt, M. Knoll, New applications for micro-EDM, Journal of Materials Processing Technology 149 (1) (2004) 246–249.

[101] C. Morgan, R. Vallance, E. Marsh, Micro-machining and micro-grinding with tools fabricated by micro electro-discharge machining, International Journal of Nanomanufacturing 1 (2) (2006) 242–258.

[102] G. Chern, Y. Wu, J. Cheng, J. Yao, Study on burr formation in micro-machining using micro-tools fabricated by micro-EDM, Precision Engineering 31 (2) (2007) 122–129.

[103] X. Cheng, Z. Wang, K. Nakamoto, K. Yamazaki, Design and development of a micro polycrystalline diamond ball end mill for micro/nano freeform machining of hard and brittle materials, Journal of Micromechanics and Microengineering 19 (11) (2009) 115022–115031.

[104] X. Cheng, Z. Wang, S. Kobayashi, K. Nakamoto, K. Yamazaki, Tool fabrication system for micro/nano milling function analysis and design of a six-axis wire EDM machine, The International Journal of Advanced Manufacturing Technology 46 (1) (2010) 179–189.

[105] H. Lee, H. Choi, S. Lee, J. Choi, H. Jeong, A study on the micro tool fabrication using electrolytic in-process dressing, Korean Society of Precision Engineering 19 (12) (2002) 171–178.

[106] K. Chou, A. Ogilvie, M. Ashford, E. Novak, An investigation into cutting edge geometry of uncoated and coated tools by optical profilometry, Transactions of NAMRI/SME XXXVIII (2010) 197–204.

[107] R. Grejda, E. R. Marsh, R. R. Vallance, Techniques for calibrating spindles with nanometer error motion, Precision Engineering 29 (1) (2005) 113–123.

[108] H. King-Fu, R. R. Vallance, R. D. Grejda, E. R. Marsh, Error motion of kinematic spindle, Precision Engineering 28 (2) (2004) 204–217.

[109] C.-H. Liu, W.-Y. Jywe, H.-W. Lee, Development of a simple test device for spindle error measurement using a position sensitive detector, Measurement Science and Technology 15 (9) (2004) 1733–1741.

[110] E. R. Marsh, R. D. Grejda, Experiences with the master axis method for measuring spindle error motions, Precision Engineering 24 (1) (2000) 50–57.

[111] E. Marsh, Precision Spindle Metrology, 2nd Edition, DEStech Publications, 2009.

[112] X. Lu, A. Jamalian, A new method for characterizing axis of rotation radial error motion: Part 1. Two-dimensional radial error motion theory, Precision Engineering 35 (1) (2011) 73–94.

[113] X. Lu, A. Jamalian, R. Graetz, A new method for characterizing axis of rotation radial error motion: Part 2. Experimental results, Precision Engineering 35 (1) (2011) 95–107.

[114] ASME B89.3.4-2010 Axes of Rotation: Methods for Specifying and Testing (2010).

[115] ISO 230-7:2006 Test code for machine tools Part 7: Geometric accuracy of axes of rotation (2006).

[116] M. Rantatalo, P. Norman, K. Tatar, Non-contact measurements of tool vibrations in a milling machine, SVIB vibrations Nytt 22 (2004) 22–29.

[117] M. Rantatalo, K. Tatar, P. Norman, Laser Doppler vibrometry measurements of a rotating milling machine spindle, IMechE Event Publications 2 (2004) 231–240.

[118] K. Tatar, M. Rantatalo, P. Gren, Laser vibrometry measurements of an optically smooth rotating spindle, Mechanical Systems and Signal Processing 21 (4) (2007) 1739–1745.

[119] W. Gao, S. Kiyono, E. Satoh, T. Sata, Precision measurement of multi-degree-of-freedom spindle errors using two-dimensional slope sensors, CIRP Annals-Manufacturing Technology 51 (1) (2002) 447–450.

[120] H. F. F. Castro, A method for evaluating spindle rotation errors of machine tools using a laser interferometer, Measurement 41 (5) (2008) 526–537.

[121] K. Fujimaki, K. Mitsui, Radial error measuring device based on auto-collimation for miniature ultra-high-speed spindles, International Journal of Machine Tools and Manufacture 47 (11) (2007) 1677–1685.

[122] W. Jywe, C. Chen, The development of a high-speed spindle measurement system using a laser diode and a quadrants sensor, International Journal of Machine Tools and Manufacture 45 (10) (2005) 1162–1170.

[123] Y. Park, S. Kim, Optical measurement of spindle radial motion by Moiré technique of concentric-circle gratings, International Journal of Machine Tools and Manufacture 34 (7) (1994) 1019–1030.

[124] H. Murakami, N. Kawagoishi, E. Kondo, A. Kodama, Optical technique to measure five-degree-of-freedom error motions for a high-speed microspindle, International Journal of Precision Engineering and Manufacturing 11 (6) (2010) 845–850.

[125] R. R. Vallance, E. R. Marsh, P. T. Smith, Effects of spherical targets on capacitive displacement measurements, Transactions of the ASME: Journal of Manufacturing Science and Engineering 126 (4) (2004) 822–829.

[126] P. Smith, R. Vallance, E. Marsh, Correcting capacitive displacement measurements in metrology applications with cylindrical artifacts, Precision Engineering 29 (3) (2005) 324–335.

[127] K. Anandan, A. Tulsian, A. Donmez, O. Ozdoganlar, A technique for measuring radial error motions of ultra-high-speed miniature spindles used for micromachining, Precision Engineering 36 (1) (2012) 104–120.

[128] I. Bucher, D. Ewins, Modal analysis and testing of rotating structures, Philosophical Transactions of the Royal Society of London. Series A: Mathematical, Physical and Engineering Sciences 359 (1778) (2001) 61–96.

[129] B. Knapp, D. Arneson, D. Oss, M. Liebers, R. Vallance, E. Marsh, The importance of spindle balancing for the machining of freeform optics, ASPE Spring Topical Meeting (2011).

[130] JCGM 100:2008, Evaluation of measurement data - Guide to the expression of uncertainty in measurement, Joint Committee for Guides in Metrology (JCGM), 2008.

[131] R. Ramesh, M. Mannan, A. Poo, Error compensation in machine tools - a review: Part I: Geometric, cutting-force induced and fixture-dependent errors, International Journal of Machine Tools and Manufacture 40 (9) (2000) 1235–1256.

[132] R. Ramesh, M. Mannan, A. Poo, Error compensation in machine tools - a review: Part II: Thermal errors, International Journal of Machine Tools and Manufacture 40 (9) (2000) 1257–1284.

[133] D. Martin, A. Tabenkin, F. Parsons, Precision spindle and bearing error analysis, International Journal of Machine Tools and Manufacture 35 (2) (1995) 187–193.

[134] T. Schmitz, J. Couey, E. Marsh, N. Mauntler, D. Hughes, Runout effects in milling: Surface finish, surface location error, and stability, International Journal of Machine Tools and Manufacture 47 (5) (2007) 841–851.

[135] T. Schmitz, J. Ziegert, J. Canning, R. Zapata, Case study: A comparison of error sources in high-speed milling, Precision Engineering 32 (2) (2008) 126–133.

[136] L. Uriarte, A. Herrero, M. Zatarain, G. Santiso, L. Lopéz de Lacalle, A. Lamikiz, J. Albizuri, Error budget and stiffness chain assessment in a micromilling machine equipped with tools less than 0.3 mm in diameter, Precision Engineering 31 (1) (2007) 1–12.

[137] W. Bao, I. Tansel, Modeling micro-end-milling operations. Part II: Tool run-out, International Journal of Machine Tools and Manufacture 40 (15) (2000) 2175–2192.

[138] Q. Bai, K. Yang, Y. Liang, C. Yang, B. Wang, Tool runout effects on wear and mechanics behavior in micro-endmilling, Journal of Vacuum Science & Technology B: Microelectronics and Nanometer Structures 27 (3) (2009) 1566–1572.

[139] K. Anandan, O. Ozdoganlar, An LDV-based methodology for measuring axial and radial error motions when using miniature ultra-high-speed (UHS) micromachining spindles, Precision Engineering, Submitted for Review.

[140] A. Baschin, P. Kahnis, D. Biermann, Dynamic analysis of the micromilling process - Influence of tool vibrations on the quality of microstructures, Materialwissenschaft und Werkstofftechnik 39 (9) (2008) 616–621.

[141] S. Filiz, O. Ozdoganlar, Microendmill dynamics including the actual fluted geometry and setup errors - Part II: Model validation and application, Transactions of the ASME: Journal of Manufacturing Science and Engineering 130 (3) (2008) 031120.

[142] N. Srinivasa, J. Ziegert, C. Mize, Spindle thermal drift measurement using the laser ball bar, Precision Engineering 18 (2) (1996) 118–128.

[143] H. Pahk, S. Lee, H. Kwon, Thermal error measurement and modelling techniques for the five-degree-of-freedom spindle drifts in computer numerically controlled machine tools, Proceedings of the Institution of Mechanical Engineers, Part C: Journal of Mechanical Engineering Science 215 (4) (2001) 469–485.

[144] J. Chen, W. Hsu, Characterizations and models for the thermal growth of a motorized high speed spindle, International Journal of Machine Tools and Manufacture 43 (11) (2003) 1163–1170.

[145] S. Yang, K. Kim, Y. Park, Measurement of spindle thermal errors in machine tool using hemispherical ball bar test, International Journal of Machine Tools and Manufacture 44 (2) (2004) 333–340.

[146] E. Creighton, A. Honegger, A. Tulsian, D. Mukhopadhyay, Analysis of thermal errors in a high-speed micro-milling spindle, International Journal of Machine Tools and Manufacture 50 (4) (2010) 386–393.

[147] J. Saedon, S. Soo, D. Aspinwall, Measurement of spindle thermal growth on a machine intended for micro/meso scale milling, Key Engineering Materials 447 (2010) 55–60.

[148] T. A. Harris, M. N. Kotzalas, Rolling Bearing Analysis (5th Edition): Essential concepts of bearing technology, Taylor & Francis Group-CRC Press, 2007.

[149] E. Marsh, V. Vigliano, J. Weiss, A. Moerlein, R. Vallance, Precision instrumentation for rolling element bearing characterization, Review of Scientific Instruments 78 (3) (2007) 035113.

[150] N. Lynagh, H. Rahnejat, M. Ebrahimi, R. Aini, Bearing induced vibration in precision high speed routing spindles, International Journal of Machine Tools and Manufacture 40 (4) (2000) 561–577.

[151] NIST/SEMATECH e-Handbook of Statistical Methods, http://www.itl.nist.gov/div898/handbook/, 2012.

[152] C. J. Evans, R. J. Hocken, W. T. Estler, Self-calibration: Reversal, redundancy, error separation, and absolute testing, CIRP Annals-Manufacturing Technology 45 (2) (1996) 617–634.

[153] R. R. Donaldson, A simple method for separating spindle error from test ball roundness error, Annals of CIRP 21 (1972) 125–126.

[154] D. Whitehouse, Some theoretical aspects of error separation techniques in surface metrology, Journal of Physics E: Scientific Instruments 9 (7) (1976) 531–536.

[155] J. Salsbury, Implementation of the Estler face motion reversal technique, Precision Engineering 27 (2) (2003) 189–194.

[156] E. R. Marsh, D. A. Arneson, D. L. Martin, A comparison of reversal and multiprobe error separation, Precision Engineering 34 (1) (2010) 85–91.

[157] E. R. Marsh, J. Couey, R. R. Vallance, Nanometer-level comparison of three spindle error motion separation techniques, Transactions of the ASME: Journal of Manufacturing Science and Engineering 128 (1) (2006) 180–187.

[158] M. Jansen, P. Schellekens, B. De Veer, Advanced spindle runout-roundness separation method, Series on Advances in Mathematics for Applied Sciences 57 (2001) 212–219.

[159] G. Zhang, R. Wang, Four-point method of roundness and spindle error measurements, CIRP Annals-Manufacturing Technology 42 (1) (1993) 593–596.

[160] G. Zhang, Y. Zhang, S. Yang, Z. Li, A multipoint method for spindle error motion measurement, CIRP Annals-Manufacturing Technology 46 (1) (1997) 441–445.

[161] C. Linxiang, W. Hong, L. Xiongua, S. Qinghong, Full-harmonic error separation technique, Measurement Science and Technology 3 (12) (1992) 1129–1132.

[162] C. Linxiang, The measuring accuracy of the multistep method in the error separation technique, Journal of Physics E: Scientific Instruments 22 (11) (1989) 903–906.

[163] S. Tong, Two-step method without harmonics suppression in error separation, Measurement Science and Technology 7 (1996) 1563–1568.

[164] W. Gao, S. Kiyono, T. Sugawara, High-accuracy roundness measurement by a new error separation method, Precision Engineering 21 (2) (1997) 123–133.

[165] W. Zhao, J. Tan, Z. Xue, S. Fu, SEST: A new error separation technique for ultra-high precision roundness measurement, Measurement Science and Technology 16 (3) (2005) 833–841.

[166] W. T. Estler, C. Evans, L. Shao, Uncertainty estimation for multiposition form error metrology, Precision Engineering 21 (2) (1997) 72–82.

[167] R. Grejda, Use and calibration of ultraprecision axes of rotation with nanometer level metrology, Ph.D. Thesis, The Pennsylvania State University (2002).